NASA-CR-173066
19830026689

# The Telecommunications and Data Acquisition Progress Report 42-74

## April–June 1983

E.C. Posner
Editor



August 15, 1983



NASA
National Aeronautics and
Space Administration

**Jet Propulsion Laboratory**
California Institute of Technology
Pasadena, California

# The Telecommunications and Data Acquisition Progress Report 42-74

## April–June 1983

E.C. Posner
Editor

August 15, 1983

NASA
National Aeronautics and
Space Administration

**Jet Propulsion Laboratory**
California Institute of Technology
Pasadena, California

The research described in this publication was carried out by the Jet Propulsion Laboratory, California Institute of Technology, under contract with the National Aeronautics and Space Administration.

# Preface

This quarterly publication provides archival reports on developments in programs managed by JPL's Office of Telecommunications and Data Acquisition (TDA). In space communications, radio navigation, radio science, and ground-based radio astronomy, it reports on activities of the Deep Space Network (DSN) and its associated Ground Communications Facility (GCF) in planning, in supporting research and technology, in implementation, and in operations. Also included is TDA-funded activity at JPL on data and information systems and reimbursable DSN work performed for other space agencies through NASA. The preceding work is all performed for NASA's Office of Space Tracking and Data Systems (OSTDS).

In geodynamics, the publication reports on the application of radio interferometry at microwave frequencies for geodynamic measurements. In the search for extraterrestrial intelligence (SETI), it reports on implementation and operations for searching the microwave spectrum. The latter two programs are performed for NASA's Office of Space Science and Applications (OSSA).

Finally, tasks funded under the JPL Director's Discretionary Fund and the Caltech President's Fund which involve the TDA Office are included.

This and each succeeding issue of the TDA Progress Report will present material in some, but not necessarily all, of the following categories:

OSTDS Tasks:

- DSN Advanced Systems
  - Tracking and Ground-Based Navigation
  - Communications, Spacecraft-Ground
  - Station Control and System Technology
  - Network Data Processing and Productivity
- DSN Systems Implementation
  - Capabilities for New Projects
  - Networks Consolidation Project
  - New Initiatives
  - Network Sustaining
- DSN Operations
  - Network Operations and Operations Support
  - Mission Interface and Support
  - TDA Program Management and Analysis
- GCF Operations and Implementation
- Data and Information Systems

OSSA Tasks:

- Search for Extraterrestrial Intelligence
- Geodynamics
  - Geodetic Instrument Development
  - Geodynamic Science

Discretionary Funded Tasks

This Page Intentionally Left Blank

# Contents

## DSN Operations

### NETWORK OPERATIONS AND OPERATIONS SUPPORT



### MISSION INTERFACE AND SUPPORT



### TDA PROGRAM MANAGEMENT AND ANALYSIS



## OSSA TASKS
## Search for Extraterrestrial Intelligence



## Geodynamics

### GEODYNAMIC SCIENCE

# Deep Space Navigation with Noncoherent Tracking Data

J. Ellis
Navigation Systems Section

*Navigation capabilities of noncoherent tracking data are evaluated for interplanetary cruise phase and planetary (Venus) flyby orbit determination. Results of a formal covariance analysis are presented which show that a combination of one-way doppler and ΔDOR yields orbit accuracies comparable to conventional two-way doppler tracking. For the interplanetary cruise phase, a tracking cycle consisting of a 3-hour doppler pass and ΔDOR (differential one-way range) from two baselines (one observation per overlap) acquired 3 times a month results in 100-km orbit determination accuracy. For reconstruction of a Venus flyby orbit, 10 days tracking at encounter consisting of continuous one-way doppler and ΔDOR sampled at one observation per overlap is sufficient to satisfy the accuracy requirements.*

## I. Introduction

The success of the ΔDOR data demonstration (Ref. 1) for Voyager interplanetary cruise navigation is expected to significantly alter the tracking data strategy for deep space missions. Since ΔDOR observations from two nearly orthogonal baselines effectively replace passes of two-way doppler as a source of geocentric angle and angle rate information, the role of coherent data for future navigation applications may be more limited. ΔDOR navigation typically requires a complementary data type, either two-way range or doppler, to resolve the geocentric radial and range rate components. In addition, navigation functions such as planetary flyby orbit reconstruction, planetary orbiter operations and maneuver reconstruction will still explicitly require some form of doppler. However, the success of the ΔDOR application for cruise navigation raises the question as to whether future missions can be navigated primarily with one-way or listen-only data types. This scenario would expand the use of the DSN's listen-only antennas for navigation applications and subsequently reduce the dependence on two-way tracking.

Several studies are currently being pursued to evaluate the performance of noncoherent data strategies for a variety of orbit determination situations including interplanetary cruise, planetary approach, maneuver support, and highly elliptic and low altitude circular planetary orbiters. This paper evaluates the navigation capabilities of noncoherent strategies for the interplanetary cruise and planetary flyby phases of a joint international mission which flies by Venus on its journey to an encounter with comet Halley.

The study was motivated by NASA's plans to provide an independent orbit determination capability to support a joint 1985 French Venus Balloon Experiment and a 1986 comet Halley "Pathfinder" concept. Both aspects entail independent DSN tracking of a Soviet Vega (Venus – Halley, but G≡H in Russian) spacecraft which encounters Venus, deploys a French balloon into the Venus atmosphere, and is subsequently targeted to encounter comet Halley. The comet encounter is scheduled to occur approximately one week before the ESA Giotto probe reaches the comet. The DSN's orbit determination role consists of reconstructing the Venus relative orbit of Vega during the balloon tracking period and determining the geocentric position of Vega at the Halley encounter.

The complete role of the DSN's participation in the Venus Balloon experiment entails using the DSN as part of a worldwide VLBI network for tracking the motion of the balloon in the Venus atmosphere. Wide and narrowband ΔVLBI data acquired between the balloon and the Vega spacecraft are used to determine the position and velocity of the balloon. Conceptually, the VLBI technique is similar to that used for Voyager—with the Vega signal serving as the known radio source for constructing relative angle differenced observations. The angular position and velocity of the balloon are referenced to the Vega flyby orbit—which must be estimated with accuracies of 10 km and 50 cm/sec during the balloon tracking phase.

The objective of the second phase of this task, the "Pathfinder" concept, is to improve the accuracy of the comet Halley ephemeris in time for the ESA Giotto targeting maneuver. Optical observations of the comet taken by Vega as it flies by the comet nucleus are combined with Vega trajectory information and ground-based comet observations to update the comet ephemeris knowledge. A critical element for the successful execution of this concept is an adequate determination (i.e., approximately 100-km geocentric position accuracy) of the Vega position at the time of comet encounter from earth-based tracking data.

One option being considered for determining the Vega trajectory entails independent DSN tracking of Vega using the 64-meter net. Unlike previous deep space missions which have relied on long spans of precise two-way doppler passes and occasional ranging for orbit determination, the Vega trajectory estimate will rely solely on data acquired by the DSN in a listen-only mode.

This paper presents results of a covariance analysis to evaluate one-way tracking strategies for both mission phases. Error model assumptions and data strategies are discussed and the navigation performance and its sensitivity to critical error sources are presented. Basically, results of the study are indicative of the capabilities of listen-only data strategies for typical cruise and planetary flyby orbit determination.

## II. Observational Error Model Assumptions

A USO (ultra stable oscillator) on board the Vega spacecraft is programmed to transmit an L-band signal at 1.668 GHz consisting of either a carrier or two subcarrier tones separated by 6.5 MHz. Total signal power is 5 watts. DSN plans call for the implementation of an L-band reception capability at the 64-meter antennas. This configuration will be capable of receiving one-way doppler (using the Blk IV Receiver and the MDA) and ΔDOR (using either the current Blk 0 or Blk I VLBI subsystem). Since the DSN will be operated in a listen-only mode, data types available for navigation are one-way doppler and the Very Long Baseline Interferometric (VLBI) data, i.e., wide and narrowband VLBI. Of the latter, the most useful and the simplest to implement for navigation is the wideband ΔVLBI (ΔDOR), which is constructed by differencing VLBI from a spacecraft with VLBI from a nearly natural radio source. The measurement determines the angular position of the two sources relative to each other. Table 1 summarizes the complete observational error model assumptions for both mission phases. Details are described in the following sections.

### A. One-Way Doppler Model Assumptions

Range rate measurements are made by estimating the doppler shift of a signal transmitted by the Vega USO. Based on experience with the signal from the Voyager USO, the received doppler signal will include errors due to an unknown frequency bias and linear frequency drift as well as errors due to USO instability and media effects. For the purpose of the covariance analysis the range rate error $\delta\dot{\rho}$ was assumed to be of the form

$$\delta\dot{\rho} = \delta f_b + \Delta t \delta f_d + \eta$$

where

$\delta f_b$ is the frequency bias

$\delta f_d$ is the frequency drift

$\eta$ is the random measurement noise

$\Delta t$ is a time difference between some arbitrary epoch and the current time

Although a possibility exists that precise estimates of the frequency bias and drift will be available during flight from two-way doppler measurements collected by Soviet stations, for the purpose of this analysis the bias and drift were both treated as essentially unknown constant parameters which are esti-

mated by the filter. Doppler measurement noise was assumed to be zero mean Gaussian white noise with a random error of 1.5 cm/sec based on a 60-second count time.

### B. ΔDOR Error Model Assumptions

The presence of a wideband 6.5-MHz spacecraft signal coupled with the availability of an adequate number of strong extragalactic radio sources (EGRS) near the Vega flight path provide the necessary conditions for acquisition of ΔDOR observations. ΔDOR is assumed to be acquired from the Goldstone-Madrid and Goldstone-Canberra baselines for maximum elevations angles during overlap greater than 8 degrees. This assumption limits the amount of data from the Goldstone-Madrid baseline for the Halley encounter phase.

The covariance analysis explicitly models the ΔDOR error sources to assess the effect of the individual errors on the navigation performance. ΔDOR error sources are characterized as either random or systematic. Random errors are combined into a single measurement noise quantity which is assumed to be Gaussian zero mean white noise. Systematic errors, which include troposphere, ionosphere, source position uncertainty, station location, UT1 and polar motion errors, are explicitly treated by the covariance analysis as unmodelled consider parameters. Such parameters are not modelled by the filter strategy but their a priori uncertainties are included in the computation of the statistics for the spacecraft state estimates. Details of the treatment of ΔDOR error assumptions are discussed below.

**Random ΔDOR errors.** The system noise for the spacecraft and for the natural radio source, dispersive instrumental phase and station oscillator instability errors are combined into a single random measurement noise. Estimates of the ΔDOR errors due to these sources are based on the analysis of J.B. Thomas. Table 1 summarizes the assumptions for the random errors for both mission phases, with the principal difference due to the strength of the natural radio sources used for each phase. For the Venus balloon phase, natural sources with source strengths greater than 0.5 Jy are available; the Pathfinder phase relies on sources with minimum strengths of 0.3 Jy.

**Ionosphere and troposphere errors.** At the time of this analysis our covariance analysis software did not have the capability to explicitly model troposphere and ionosphere calibration errors. A single ΔDOR bias was constructed for each baseline (Goldstone-Madrid and Goldstone-Canberra), which combined the total worst-case error expected for both error sources. Estimates of the errors are based on the analysis of S.Wu and assumed a worst-case minimum elevation angle for each phase.

**Source position uncertainty.** Natural source position errors included a frame tie error which characterizes the absolute uncertainty of the radio source reference catalog with respect to the planetary FK-4 frame and a relative error which describes the uncertainty of the source locations within the radio source reference frame. A correlated a priori error covariance was constructed based on this model. For the Venus flyby, a 500 nanoradian (nrad) frame tie was assumed. Postprocessing of the flyby data is expected to reduce the frame tie uncertainty to 100 nrad for the subsequent Pathfinder phase. Relative source errors were assumed to be 50 nrad.

**Station location, baseline, UT1 and polar motion errors.** Station location errors were also modelled in terms of absolute and relative errors. This model assumes station location estimates will be based on a combination of planetary encounter data and intercontinental baseline information derived from the VLBI radio source catalog determination. Errors due to UT1 and polar motion are combined into an "equivalent station location error." The absolute station location errors were assumed to be 2 m spin axis, 3 m longitude and 20 m z-height. An uncertainty of 0.8 m was assumed for the polar and equatorial components of the intercontinental baseline vector between the Goldstone-Madrid and Goldstone-Canberra sites.

## III. Heliocentric Cruise Analysis

### A. Cruise Model Assumptions

Noncoherent data strategies were evaluated for interplanetary cruise navigation based on tracking data for a 90-day heliocentric Vega trajectory terminating at Halley encounter. Dynamic parameters modeled in the covariance analysis included the probe position and velocity, solar radiation pressure acceleration and an arbitrary correction maneuver 30 days before encounter.

Tracking data was acquired during the 4 tracking periods shown in Fig. 1, which presents the trajectory profile during the 90-day arc. With the exception of the first tracking arc, the schedule is consistent with preliminary DSN plans for Giotto mission support. The earlier data was added to assess the effect of overall tracking geometry changes provided by the longer arc. Data included one-way doppler from Canberra and ΔDOR from the Goldstone-Canberra and Goldstone-Madrid baselines. The ΔDOR is sampled at one measurement per overlap period for elevation angles greater than 8°.

A batch least squares filter was used to determine the spacecraft state based on a simulated tracking schedule. The filter estimated the probe position and velocity, three components of the maneuver and the one-way doppler bias and drift. Source position uncertainty, station location errors, solar radiation pressure acceleration and ΔDOR biases were treated as unmodelled consider parameters. A priori error assumptions are given in Table 2.

## B. Cruise Navigation Performance

Based on the preceding dynamic and observational error model assumptions, covariance studies were conducted with the objectives of (1) understanding the relative tradeoffs and information content of the noncoherent data types for cruise navigation, (2) identifying data strategies which achieve acceptable performance with a minimum of tracking time and (3) assessing the sensitivity of estimates to unmodelled error sources. The navigation performance achievable with conventional two-way doppler tracking was first established as a reference. A two-way doppler random measurement accuracy of 1 mm/sec based on a 60-second count time was assumed. Information inherent in a single pass of doppler determines the geocentric range rate, right ascension and declination of the spacecraft. Successive passes over a sufficiently long arc resolve the geocentric range and the angular rate of change. The geocentric information combined with knowledge of the earth's ephemeris determines the heliocentric state.

Figure 2 compares the performance of two-way doppler (F2) passes with the following noncoherent data strategies: one-way doppler (F1) only passes, ΔDOR-only observations and a combination of one-way doppler and ΔDOR (F1 + ΔDOR). Daily tracking data acquired for the 4 spans shown in Fig. 1 includes 33 passes (330 hours) of doppler and ΔDOR from both baselines (one observation for each overlap period.) The combination of the low spacecraft declination and 8° station elevation angle constraint limited the ΔDOR acquisition from the Goldstone-Madrid baseline to the first 60 days. Results in Fig. 2 are expressed in terms of the geocentric position error (radial, right ascension and declination) at the time of Halley encounter.

The result of replacing two-way doppler passes with one-way doppler (F1-only) is to increase the position error by a factor of 6 due to noisier data and the inability of the filter to adequately estimate the one-way bias and drift. The ΔDOR-only strategy determines the angular position and velocity but is unable to provide acceptable radial information. A solution based on the combination of one-way doppler and ΔDOR yields results that are comparable if not better than two-way doppler. This is due to the complementary information content of the data types. An accurate independent determination of the angular position and velocity is provided by the ΔDOR, while the one-way doppler yields information in which the angular estimates are highly correlated with the radial components and the bias and drift terms. In effect, the ΔDOR angular information constrains the one-way doppler error ellipsoid. The result of the correlations and the angular accuracy constraint is an order of magnitude improvement in range estimates and a factor of 4 improvement in the bias and drift estimates.

Having demonstrated that noncoherent data strategies can perform as well as two-way doppler for cruise navigation, the next phase was to study the sensitivity of the estimates to the quantity of tracking data. A navigation tracking cycle can be defined consisting of a doppler pass from Canberra and a ΔDOR observation from each baseline (with maximum elevation angles exceeding 8°). Figure 3 shows that reducing the number of tracking cycles from 33 to 9 (distributed over the 4 scheduled tracking spans) does not affect the navigation accuracy.

The rationale for using full 8-10 hour doppler passes is based on the angular information inherent in a full doppler pass. When used in conjunction with ΔDOR, doppler primarily is a source of geocentric range and range rate. The effect of reducing the pass duration to 3 hours for the 9-cycle strategy is also shown in this figure. The shorter doppler passes increase the radial uncertainty from 69 to 92 km; however, the solution still satisfies the navigation requirements. For the remainder of the study, this 9-cycle, 3-hour doppler pass strategy with 8° constraint is treated as the nominal baseline strategy.

The opportunity to acquire ΔDOR from the Goldstone-Madrid baseline is limited due to the negative declination of the probe during the final days. Figure 4 compares the navigation accuracies for the 9-cycle (3-hour pass) strategy assuming no ΔDOR from this baseline, and an 8° and 6° elevation angle limit. The latter permits ΔDOR acquisition from both baselines during the entire trajectory. It is apparent that data from both baselines is needed to meet the 100-km requirement.

Cruise phase orbit determination typically requires two-way doppler observations of the spacecraft motion over a sufficiently long arc to detect the changes in range rate and the trajectory bending caused by the sun's gravitational field. The long arc tracking coupled with a model for the spacecraft dynamics resolves the radial position component. For the noncoherent tracking strategy, a reduction of the length of tracking arc from 3 months to 2 months (by eliminating the first tracking segment) increases the radial position error from 92 km to 175 km.

The analysis treated an arbitrary and essentially unknown midcourse maneuver. Applying the same noncoherent (F1 + ΔDOR) tracking strategy to a maneuver free arc (or assuming the maneuver can be independently determined from telemetry) improves the accuracy of all components. The radial error is reduced from 92 km to 44 km with a reduction in angular position errors from 30 to 20 km.

The sensitivities of geocentric position estimates to unmodelled error sources are displayed in Fig. 5. The position error is decomposed into a component due to measurement noise

and perturbations due to the considered error sources. Angular position errors are primarily influenced by the source position and intercontinental station baseline errors, which reflects the sensitivity of the ΔDOR to those error sources. The radial uncertainty is primarily corrupted by the station longitude error.

# IV. Planetary Flyby Analysis

## A. Flyby Model Assumptions

For the interplanetary cruise phase, we were primarily interested in determining the probe position and velocity with respect to either the earth or sun using ground-based observations. Planetary encounter navigation entails estimation of the probe's flight path relative to a target body. As the spacecraft approaches the target, the tracking data must be capable of detecting the accelerations induced by the planet's gravitational field and must be sufficiently sensitive to measure the trajectory bending.

The evaluation of noncoherent data strategies for planetary encounter orbit determination was based on an analysis of the Venus flyby for the Vega probe. The nominal trajectory is aimed for a Venus closest approach of approximately 40000 km. Two days before encounter the balloon is released and a bus deflection maneuver is executed, followed by a Halley targeting maneuver 7 days after encounter.

The covariance analysis models the following dynamic parameters: spacecraft state, Venus ephemeris (both position and velocity), Venus mass, solar radiation pressure accelerations and the two maneuvers. A priori error model assumptions are summarized in Table 3.

A nominal strategy was defined with a 10-day tracking arc—starting 5 days before encounter and ending 5 days after. Tracking data consisted of daily passes of one-way doppler from the three DSN complexes and ΔDOR observations from the Goldstone-Madrid and Goldstone-Canberra baselines. The 8° elevation angle constraint did not impact the ΔDOR availability for this phase. One ΔDOR observation was sampled from each baseline.

As in the cruise study, a batch least squares filter was used to assess the performance of noncoherent strategies. The performance criterion was the Venus relative position and velocity errors for the orbit segment starting one day before and ending two days after encounter. This corresponds to the balloon tracking phase which requires accurate knowledge of the flyby reference orbit for establishing the relative motion of the balloon. The filter estimated the spacecraft state, Venus ephemeris and mass, maneuver components and the one-way doppler bias and drift. Consider parameters were the same as in the cruise case—source position uncertainty, station location, solar radiation pressure and ΔDOR bias errors.

## B. Venus Flyby Performance

Two-way doppler has traditionally proved to be most effective for planetary flyby orbit reconstruction. The ability of doppler to sense the range rate changes caused by the planetary gravitational field establishes the planet relative spacecraft state. Figure 6 compares the two-way doppler performance with one-way doppler only, ΔDOR-only and a combination of one-way and ΔDOR data strategies. Venus relative position and velocity errors for the three-day encounter arc are plotted—with errors expressed in terms of an error component along the probe-earth direction and a second component in a plane orthogonal to this vector. The latter represents the RSS of the two plane-of-sky (POS) errors.

Two-way doppler tracking easily satisfies the Venus flyby orbit determination requirements. Position error is a minimum at closest approach with the error ellipse defocused on either side of encounter. In general, errors are increased by an order of magnitude when one-way doppler replaces the two-way data. This is primarily due to the inability of the filter to adequately determine the one-way bias and drift. The uncertainties of the bias and drift estimates are $1.0 \times 10^{-10}$ ($\Delta f/f$) and $1.6 \times 10^{-12}$ ($\Delta f/f$/day). Approximately an order of magnitude improvement is required for the one-way doppler to yield results comparable to two-way. The ΔDOR-only option determines the POS position and velocity (with the exception of an anomaly at encounter) but fails to provide information along the earth-probe line. The solution based on one-way doppler combined with ΔDOR yields results comparable to the two-way data.

In some respects this behavior is similar to the interplanetary cruise performance. One-way doppler provides information in which the radial components, bias and drift are highly correlated with the POS position and velocity. The addition of ΔDOR constrains the POS errors and determines the remaining components via the doppler correlations. The accuracy of the bias and drift estimates, which are key for determining radial information, are improved by factors of 10 and 4 respectively. Figure 7 illustrates the manner in which the ΔDOR and one-way doppler error ellipses combine for the position components.

Figure 8 plots the perturbations due to the unmodelled error sources for the estimates based on the F1 + ΔDOR strategy. The sensitivity is presented in terms of the total RSS position and velocity errors at E + 2d. The accuracy of the estimates are primarily dominated by the measurement error and

the a priori covariance assumptions for the Venus ephemeris and mass. The latter constrains the Venus relative position and velocity errors. Two-way doppler results are insensitive to considering or solving for the ephemeris and mass parameters. However, for the combined F1 + ΔDOR strategy, the ephemeris solution determines the planetary-radio source frame tie.

The sensitivities of the Venus relative estimates (based on the F1 + ΔDOR strategy) to the number of doppler tracking sites and to the duration of tracking are presented in Figs. 9 and 10. Results are expressed in terms of a single RSS position and velocity error. Reducing the number of doppler sites roughly increases the errors by the ratio of the square root of the number of measurements—which is characteristic of a situation in which the statistics are not dominated by unmodelled errors. The 10-km position requirement is only satisfied with tracking from three sites. Limiting the tracking span to 4 days at encounter also results in unacceptable performance. Only marginal improvement results from extending the arc to 20 days.

## V. Conclusions

The objectives of this study were to assess the capabilities of noncoherent data strategies for interplanetary cruise and planetary flyby orbit reconstruction. Results of the cruise phase analysis demonstrate that modest quantities of one-way doppler combined with ΔDOR from two baselines can yield navigation accuracies comparable to two-way tracking. A 100-km position requirement can be met with a navigation cycle consisting of a 3-hour one-way doppler pass and ΔDOR observations from two baselines scheduled three times per month. Necessary conditions for adequate performance include tracking over a sufficiently long arc and ΔDOR data from both baselines.

A noncoherent strategy consisting of continuous one-way doppler and ΔDOR from two baselines was also shown to be as effective as two-way doppler for planetary flyby orbit determination. The Venus relative position and velocity requirements of 10 km and 50 cm/sec are satisfied with tracking interval starting 5 days before and ending 5 days after encounter.

The effectiveness of the combined strategy is primarily due to the independent geocentric angular determination provided by the ΔDOR data which aids in the separation of the doppler angular information from the earth-line and bias and drift components. This enables an adequate determination of the latter components.

## Acknowledgement

The author would like to acknowledge the contributions of C. E. Hildebrand for his analysis of the ΔDOR error model and F. R. Bletzacker for providing the radio source catalog distribution.

## References

1. Border, J. S., Donivan, F. F., Finley, S. G., Hildebrand, C. E., Moultrie, B., and Skjerve, L. J., "Determining Spacecraft Angular Position with Delta VLBI: The Voyager Demonstration," paper 82-1471, presented at the AIAA/AAS Astrodynamics Conference, San Diego, Calif. August 1982.

**Table 1. Observational error model assumptions**

| One-way doppler | |
|---|---|
| Random measurement noise (60 sec count time) | 1.5 cm/sec |
| A priori bias error ($\Delta f/f$) | $1 \times 10^{-6}$ |
| A priori drift error ($\Delta f/f$/day) | $3 \times 10^{-6}$ |

| ΔDOR system | Cruise | Venus flyby |
|---|---|---|
| Random errors | | |
| System noise spacecraft | 2 cm | 2 cm |
| System noise radio source | 30 cm | 20 cm |
| Station oscillator | 5 cm | 5 cm |
| Dispersive instrument phase ($\epsilon = 2°$) | 52 cm | 52 cm |
| RSS random error | 60 cm | 56 cm |
| Ionosphere errors | | |
| Goldstone-Madrid | 26 cm | 17 cm |
| Goldstone-Canberra | 4 cm | 17 cm |
| Troposphere errors | | |
| Goldstone-Madrid | 55 cm | 30 cm |
| Goldstone-Canberra | 28 cm | 30 cm |
| Source position errors | | |
| Frame tie | 100 nrad | 500 nrad |
| Relative | 50 nrad | 50 nrad |
| Station location errors | | |
| Spin radius | 2 m | |
| Longitude | 3 m | |
| Z-height | 20 m | |
| Intercontinental baseline | 0.8 m | |

**Table 2. Cruise a priori error model assumptions**

| Parameters | A priori standard deviation |
|---|---|
| Estimated parameters | |
| VEGA position | $10^7$ km |
| VEGA velocity | 10 km/s |
| Doppler bias | 0.3 km/s |
| Doppler drift | $10^{-7}$ km/s$^2$ |
| Maneuver (E-30$^d$) | 1.0 m/s |
| Considered parameters | |
| Station spin radius | 2 m |
| Longitude | 3 m |
| Z-height | 20 m |
| Station baseline – (equatorial and polar components) | 0.8 m |
| Quasar FK-4 frame tie (right ascension/declination) | 0.1 μrad |
| Quasar relative position | 0.05 μrad |
| Solar radiation pressure acceleration | 10% of nominal |
| ΔDOR bias GLD-CAN | 28 cm |
| ΔDOR bias GLD-MAD | 60 cm |
| Random data noise | |
| One-way doppler | 1.5 cm/sec |
| ΔDOR | 60 cm |

**Table 3. Venus flyby a priori error model assumptions**

| Parameters | A priori standard deviation |
|---|---|
| Estimated parameters | |
| VEGA position | $10^7$ km |
| VEGA velocity | 10 km/s |
| Doppler bias | 0.3 km/s |
| Doppler drift | $10^{-7}$ km/s$^2$ |
| Maneuver (E-2$^d$) | 1.0 m/s |
| Venus ephemeris | |
| Position (RA, DEC, RADIAL) | 40, 40, 10 km |
| Velocity | $1 \times 10^{-5}$ km/sec |
| Venus mass | 1 km$^3$/sec$^2$ |
| Considered parameters | |
| Station spin radius | 2 m |
| Longitude | 3 m |
| Z-height | 20 m |
| Station baseline – (equatorial and polar components) | 0.8 m |
| Quasar FK-4 frame tie (right ascension/declination) | 0.5 μrad |
| Quasar relative position | 0.05 μrad |
| Solar radiation pressure acceleration | 10% of nominal |
| ΔDOR bias GLD-CAN | 34 cm |
| ΔDOR bias GLD-MAD | 34 cm |
| Random data noise | |
| One-way doppler | 1.5 cm/sec |
| ΔDOR | 56 cm |

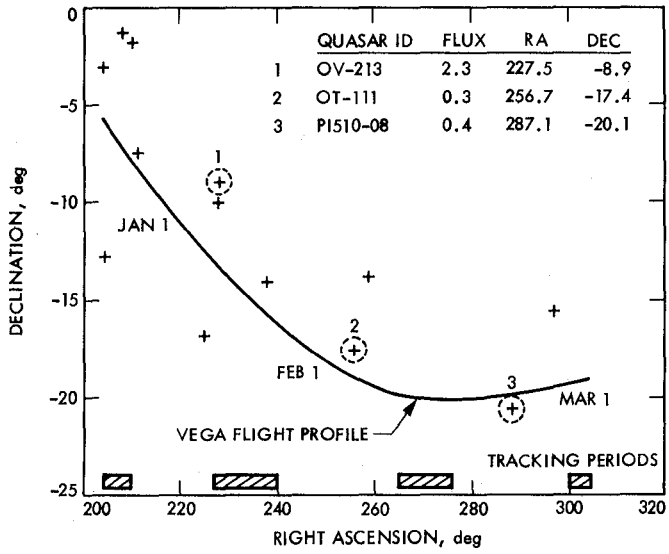


**Fig. 1. Cruise profile**

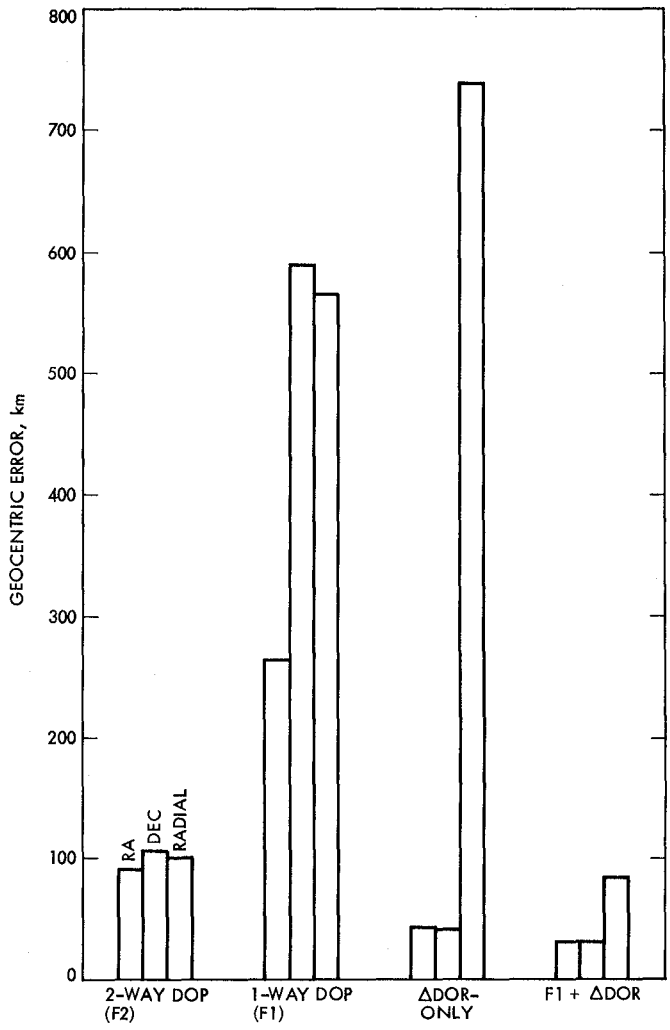


**Fig. 2. Comparison of strategies for cruise navigation**

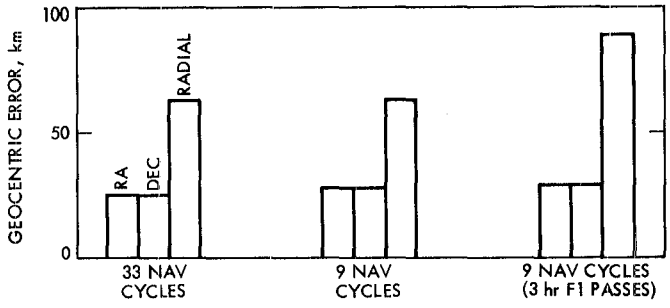


**Fig. 3. Effect of quantity of data**

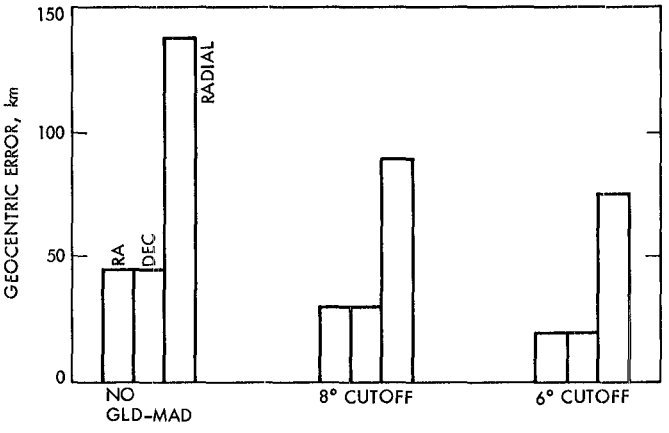


**Fig. 4. Sensitivity to Goldstone-Madrid ΔDOR**

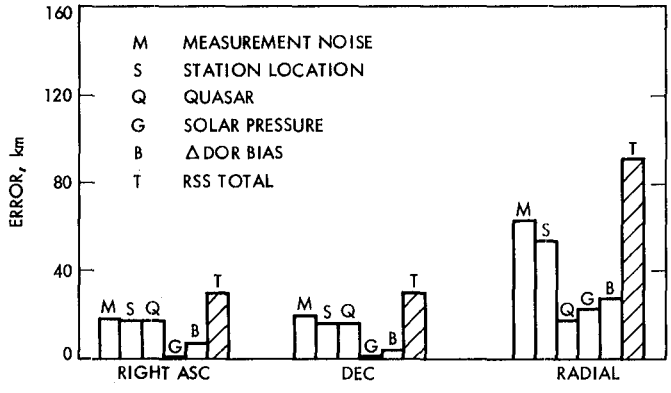


**Fig. 5. Sensitivity to consider errors**

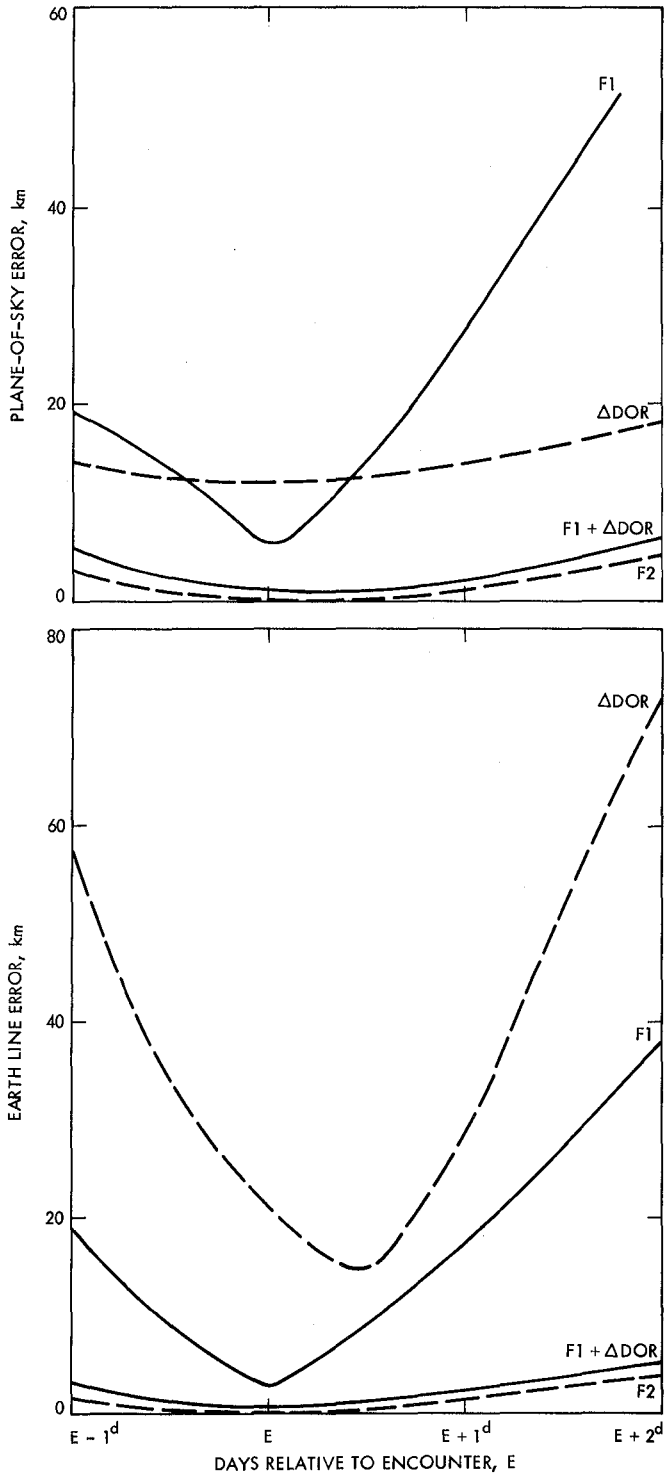


**Fig. 6(a). Comparison of strategies for Venus flyby reconstruction – Venus relative position errors**

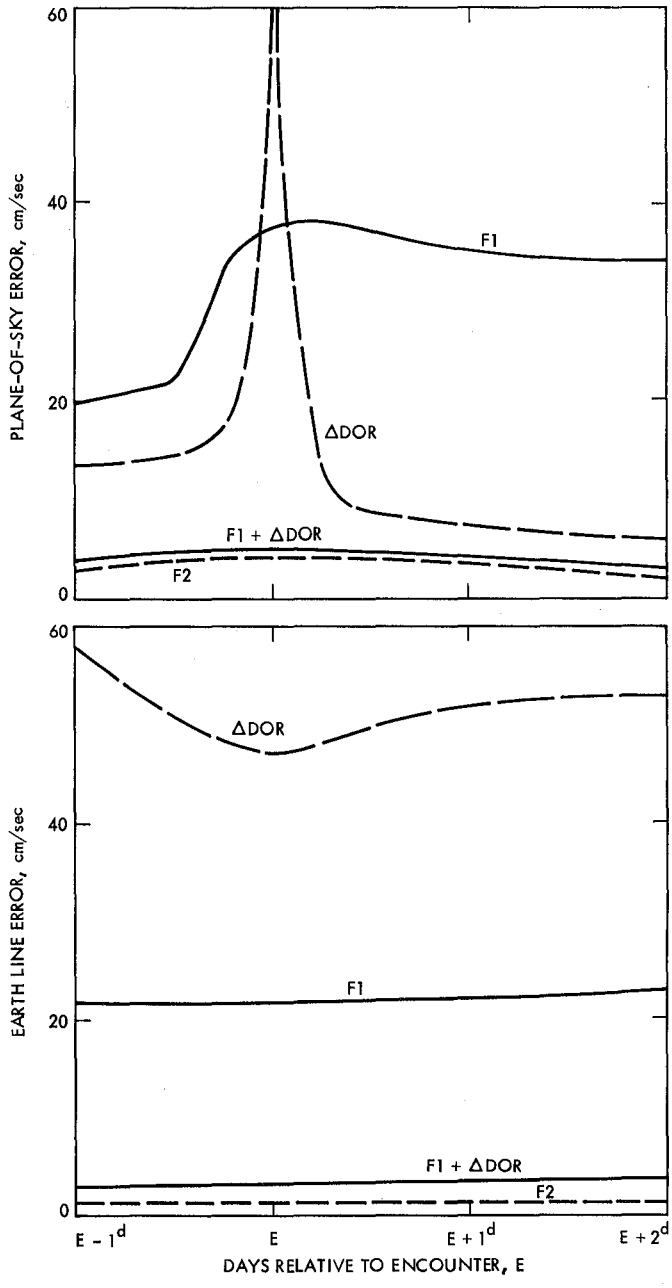


**Fig. 6(b). Comparison of strategies for Venus flyby reconstruction – Venus relative velocity errors**

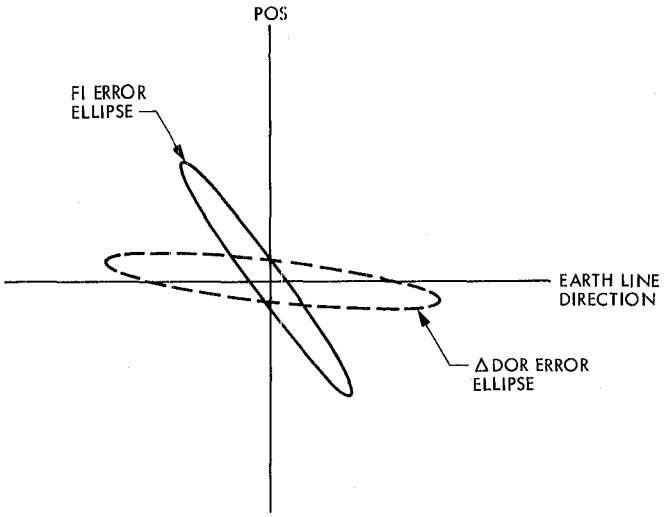


**Fig. 7. F1-ΔDOR two-dimensional error ellipse representation**

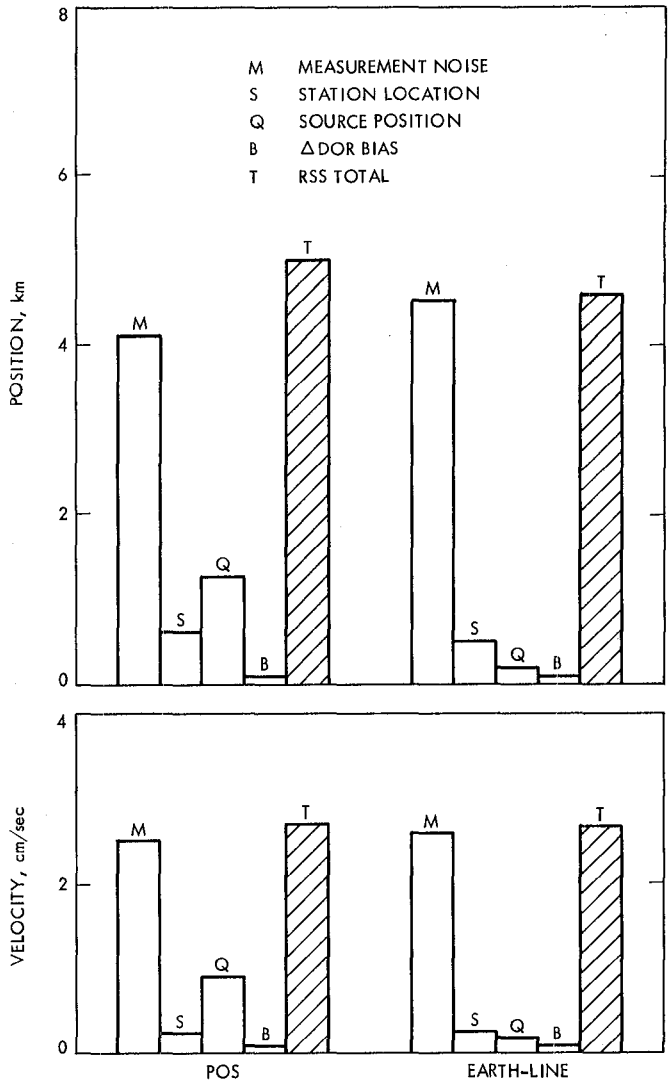


**Fig. 8. Sensitivity of solution at E + 2d to consider errors**

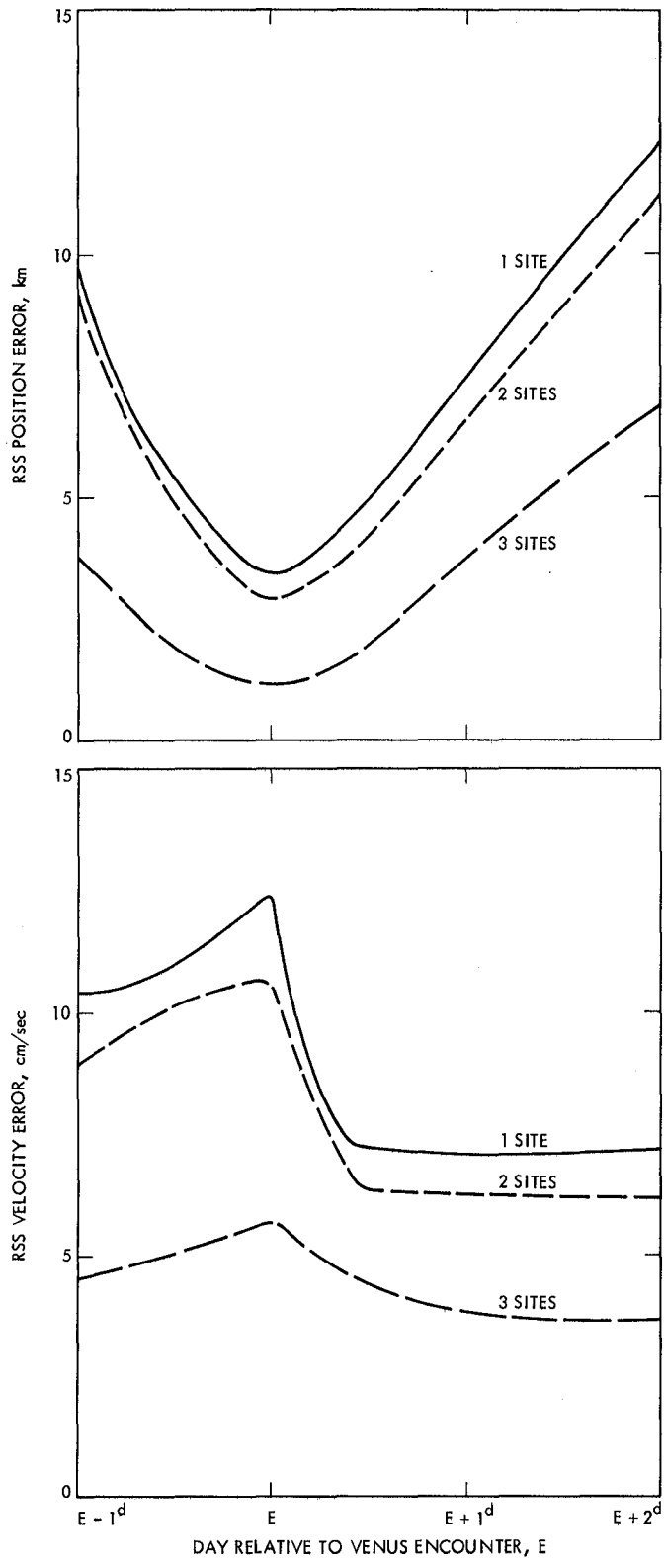


**Fig. 9. Sensitivity to number of doppler tracking sites**

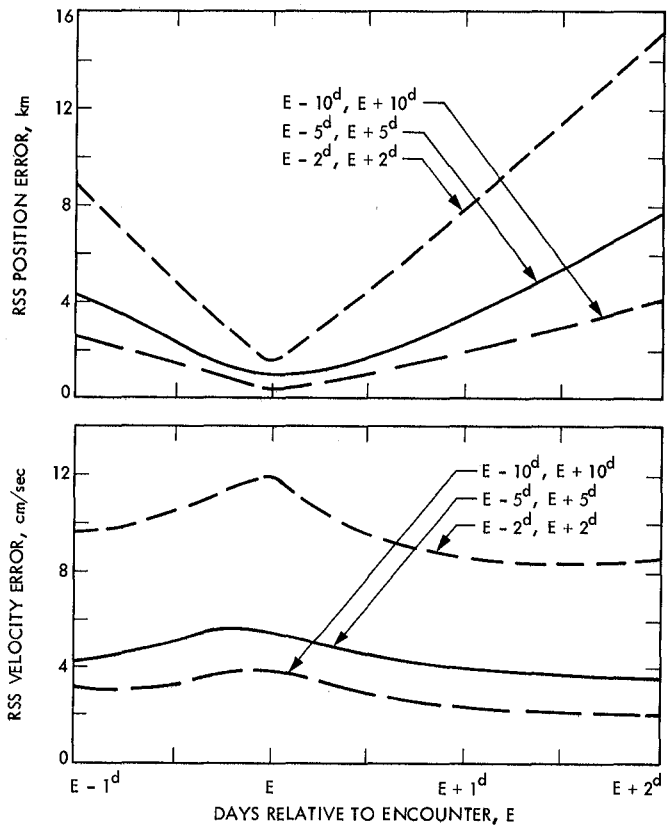


**Fig. 10. Sensitivity to length of tracking arc**

# Symbol Stream Combining Versus Baseband Combining for Telemetry Arraying

D. Divsalar
Communications Systems Research Section

*The objectives of this article are to investigate and analyze the problem of combining symbol streams from many Deep Space Network stations to enhance bit signal-to-noise ratio and to compare the performance of this combining technique with baseband combining. Symbol stream combining (SSC) has some advantages and some disadvantages over baseband combining (BBC). The SSC suffers almost no loss in combining the digital data and no loss due to the transmission of the digital data by microwave links between the stations. The BBC suffers 0.2 dB loss due to alignment and combining the IF signals and 0.2 dB loss due to transmission of signals by microwave links. On the other hand, the losses in the subcarrier demodulation assembly (SDA) and in the symbol synchronization assembly (SSA) for SSC are more than the losses in the SDA and SSA for BBC. It is shown that SSC outperforms BBC by about 0.35 dB (in terms of the required bit energy-to-noise spectral density for a bit error rate of $10^{-3}$) for an array of three DSN antennas, namely 64 m, 34 m(T/R) and 34 m(R).*

## I. Introduction

To capture signals from the Voyager spacecraft and potentially other space probes, signals from more than one antenna are combined. To reduce the cost of bringing the received signals from the Deep Space Network (DSN) and non-DSN facilities together, J. W. Layland of JPL has suggested combining quantized symbol streams in place of telemetry baseband combining.

The analysis of this article shows that symbol stream combining is superior to baseband combining. In baseband combining we require that the baseband signals from each antenna, after carrier demodulation, be brought to a signal processing center. Here the signals are delay adjusted, weighted, summed and then passed through the subcarrier demodulation assembly (SDA) and symbol synchronization assembly (SSA). The output of this processing is a quantized symbol stream which enters the maximum likelihood convolutional decoder (MCD). Since prior to decoding by the MCD all operations on the data signal are linear, it seems we might not be gaining anything by combining these signals before the SSA processing; i.e., symbols could be combined just before input to the MCD. This has the advantage of combining digital signals, which will be easier than combining baseband signals since the problems of time alignment, weighting and summing the symbol streams no longer exist. On the other hand, each station will have lower SNRs at its SDA and SSA than the SNRs from baseband combining. This article analyzes these methods of combining. It shows that these lower SNRs at the

SDA and SSA prior to combining do not present as much loss as was previously expected. On the contrary, when we compare these two methods under the same conditions, namely the same loop bandwidths for carrier tracking loop, SDA and SSA, and the same mod index, etc., we find that the overall total loss in symbol signal-to-noise ratio (SNR) for symbol stream combining is actually less than the loss in symbol SNR for baseband combining.

## II. Symbol Stream Combining

A system for combining symbol streams from $N$ stations is depicted in Fig. 1. The telemetry signal is an RF carrier that is phase-modulated by a squarewave subcarrier ($\mathrm{sin}\,\omega_{sc}t$) at a peak modulation index $\theta$. The subcarrier is bi-phase modulated with a binary data stream $D(t)$. This telemetry signal is received by $N$ ground stations. The received telemetry signal at the $i$th station is

$$r_i(t) = \sqrt{2P_i}\sin(\omega_c t + \Phi_{ci} + D(t+\tau_i)\theta \mathrm{sin}(\omega_{sc}t + \Phi_{sci})) + \tilde{\tilde{n}}_i(t) \quad (1)$$

where $P_i$ is the total received power at this station, $\omega_c$ is the carrier radian frequency, $\Phi_{ci}$ is the carrier phase, $\omega_{sc}$ is the subcarrier radian frequency, $\Phi_{sci}$ is the subcarrier phase and $\tilde{\tilde{n}}_i(t)$ is the additive white Gaussian noise with two-sided spectral density $N_{0i}/2$. The subscript $i$ refers to the $i$th station throughout this article. At the output of the receiver and carrier tracking loop (CTL) the signal can be represented as

$$s_i(t) = \sqrt{2P_i}\sin\theta\, D(t+\tau_i)\mathrm{sin}(\omega_{sc}t + \Phi_{sci})\cos(\omega_{IF}t + \phi_{ci}) + \tilde{n}_i(t) \quad (2)$$

where $\omega_{IF}$ is IF radian frequency, $\phi_{ci} = \Phi_{ci} - \hat{\Phi}_{ci}$ is carrier phase error and $\hat{\Phi}_{ci}$ is the phase locked loop (PLL) estimate of the carrier phase. $\tilde{n}_i(t)$ is white Gaussian noise with two-sided spectral density $N_{0i}/2$. The IF carrier reference signal is

$$r_{ci}(t) = \sqrt{2}\cos(\omega_{IF}t) \quad (3)$$

The subcarrier squarewave reference signal generated by the SDA is

$$r_{sci}(t) = \mathrm{sin}(\omega_{sc}t + \hat{\Phi}_{sci}) \quad (4)$$

where $\hat{\Phi}_{sci}$ is an estimate of $\Phi_{sci}$. After demodulating the signal $S_i(t)$ by the reference signals in (3) and (4), we obtain

$$W_i(t) = \sqrt{P_i}\sin\theta\, D(t+\tau_i)\left[1 - \frac{2}{\pi}|\phi_{sci}|\right]\cos\phi_{ci} + n_i(t) \quad (5)$$

which enters the SSA. The subcarrier phase error is $\phi_{sci} = \Phi_{sci} - \hat{\Phi}_{sci}$ and $n_i(t)$ is the baseband white Gaussian noise with two-sided spectral density $N_{0i}/2$.

The data waveform can be represented as

$$D(t) = \sum_{n=-\infty}^{\infty} a_n p(t - (n-1)T_s) \quad (6)$$

where $p(t)$ is unit power rectangular pulse shape with duration $T_s$ (symbol time) and $a_n$ is a binary channel symbol taking on values ±1. Passing this signal through the SDA, assuming $\phi_{ci}$ and $\phi_{sci}$ are very slowly varying with respect to symbol time $T_s$, we get

$$Q_{k+m_i,i} = \frac{1}{T_s}\int_{(k-1)T_s+\epsilon_i}^{kT_s+\epsilon_i} W_i(t)\, p(t-(k-1)T_s-\epsilon_i)\,dt$$

$$= \frac{\sqrt{P_i}}{T_s}\sin\theta\left[1 - \frac{2}{\pi}|\phi_{sci}|\right]\cos\phi_{ci} \int_{(k-1)T_s+\epsilon_i}^{kT_s+\epsilon_i} D(t+\tau_i)\, p(t-(k-1)T_s-\epsilon_i)\,dt + n_{k+m_i} \quad (7)$$

Let $\tau_i = m_i T_s + \epsilon_i'$ where $0 \leq \epsilon_i' < T_s$ for some integer $m_i$ and $\bar{\epsilon}_i \triangleq \epsilon_i - \epsilon_i'$; then

$$\int_{(k-1)T_s+\epsilon_i}^{kT_s+\epsilon_i} D(t+\tau_i)\, p(t-(k-1)T_s-\epsilon_i)\,dt = \begin{cases} (T_s - \bar{\epsilon}_i)\, a_{k+m_i} + \bar{\epsilon}_i a_{k+m_i+1} & 0 \leq \bar{\epsilon}_i < T_s/2 \\ (T_s + \bar{\epsilon}_i)\, a_{k+m_i} - \bar{\epsilon}_i a_{k+m_i-1} & -T_s/2 \leq \bar{\epsilon}_i < 0 \end{cases} \quad (8)$$

The worst case occurs if the symbol sequence consists of alternate symbol values ±1, because whenever there is no

symbol transition, a time synchronization error will not affect the signal amplitude. In this case, we have

$$Q_{k+m_i,i} = \sqrt{P_i}\sin\theta\left[1-\frac{2}{\pi}|\phi_{sci}|\right]\cos\phi_{ci}\,[1-2|\lambda_i|]$$

$$a_{k+m_i} + n_{k+m_i} \tag{9}$$

where

$$\lambda_i = \bar{\epsilon}_i/T_s \text{ and } -\frac{1}{2} < \lambda_i < \frac{1}{2}$$

Assuming the time delay for each station is perfectly estimated, then each symbol stream $Q_{k+m_i,i}$ can be delayed by $m_i$ seconds.

Samples of the signal at the output of the combiner for arraying of $N$ antennas are

$$z_k = \sum_{i=1}^{N} \beta_i Q_{k,i} \tag{10}$$

where $\beta_i$'s are weighting factors. The optimum values of $\beta_i$'s will be derived shortly. Now let us find the mean and variance of $z_k$. Given

$$\underline{\phi}_c \triangleq \{\phi_{c1}, \phi_{c2}, \ldots, \phi_{cN}\}, \underline{\phi}_{sc} = \{\phi_{sc1}, \phi_{sc2}, \ldots, \phi_{scN}\}$$

$$\underline{\lambda} \triangleq \{\lambda_1, \lambda_2, \ldots, \lambda_N\}$$

and $a_k$, we have the conditional mean and the conditional variance of $z_k$, respectively, as

$$\bar{z}_k = \sum_{i=1}^{N} \beta_i \sqrt{P_i}\sin\theta\, a_k \left[1-\frac{2}{\pi}|\phi_{sci}|\right]\cos\phi_{ci}\,[1-2|\lambda_i|] \tag{11}$$

and

$$\sigma^2_{z_k} = \frac{1}{2T_s}\sum_{i=1}^{N}\beta_i^2 N_{0i} \tag{12}$$

Then the conditional symbol SNR, conditioned on $\underline{\phi}_c$, $\underline{\phi}_{sc}$ and $\underline{\lambda}$ is

$$\text{conditional symbol SNR} = \frac{\bar{z}_k^2}{\sigma^2_{z_k}} \tag{13}$$

and the conditional bit SNR is

Conditional bit SNR = 2 × conditional symbol SNR

$$= \frac{\left[\sum_{i=1}^{N}\beta_i\sqrt{E_{bi}}\left(1-\frac{2}{\pi}|\phi_{sci}|\right)\cos\phi_{ci}\left(1-2|\lambda_i|\right)\right]^2}{\sum_{i=1}^{N}\beta_i^2 N_{0i}} \tag{14}$$

where $E_{bi} = 2P_iT_s\sin^2\theta$.

The bit error rate for $N$ arrayed antennas, given $\underline{\phi}_c$, $\underline{\phi}_{sc}$ and $\underline{\lambda}$, is

$$P_b(\underline{\phi}_c, \underline{\phi}_{sc}, \underline{\lambda}) = f(\text{conditional bit SNR}) \tag{15}$$

where

$$f(x) = \begin{cases} e^{\alpha_0 - \alpha_1 x} & ; \quad x \geq \dfrac{\alpha_0 + \ln 2}{\alpha_1} \\ 0.5 & ; \quad x < \dfrac{\alpha_0 + \ln 2}{\alpha_1} \end{cases}$$

$$\alpha_0 = 4.4514$$

$$\alpha_1 = 5.7230 \tag{16}$$

Letting $\beta_1 = 1$ and optimizing $\beta_i$'s; $i = 2, 3, \ldots, N$, in order to minimize the bit error rate, we get the optimum values for $\beta_i$'s:

$$\beta_i^* = \sqrt{\frac{E_{bi}}{E_{b1}}}\,\frac{N_{01}}{N_{0i}} \tag{17}$$

Let

$$\rho_i \triangleq \frac{P_i}{P_1}\cdot\frac{N_{01}}{N_{0i}} \tag{18}$$

and use (17) and (15); we obtain

$$P_b(\underline{\phi}_c, \underline{\phi}_{sc}, \underline{\lambda}) = f\left(\sum_{i=1}^{N}\frac{E_{bi}}{N_{0i}}y^2\right) \tag{19}$$

where

$$y \triangleq \frac{\sum_{i=1}^{N} \rho_i \left(1 - \frac{2}{\pi}|\phi_{sci}|\right) \cos\phi_{ci}(1 - 2|\lambda_i|)}{\sum_{i=1}^{N} \rho_i} \quad (20)$$

Note that when carrier phase, subcarrier phase and symbol time are all perfectly synchronized, the value of $y$ is one.

Assume $\phi_{ci}$'s, $\phi_{sci}$'s and $\lambda_i$'s are independent of each other, having density functions $p(\phi_{ci})$, $p(\phi_{sci})$ and $p(\lambda_i)$ respectively. Then the bit error rate can be expressed as

$$P_b = \int_{-\pi}^{\pi}\int_{-\pi}^{\pi}\int_{-1/2}^{1/2} P_b(\underline{\phi}_c, \underline{\phi}_{sc}, \underline{\lambda}) \left[\prod_{i=1}^{N} p(\phi_{ci})\, p(\phi_{sci})\, p(\lambda_i)\right] d\underline{\phi}_c\, d\underline{\phi}_{sc}\, d\underline{\lambda} \quad (21)$$

## III. Baseband Combining

A system for arraying baseband signals out of $N$ stations is shown in Fig. 2. Consider the baseband signals at the output of carrier tracking loops given by

$$s_i(t) = \sqrt{2P_i} \sin\theta\, D(t + \tau_i) \mathbf{S}\sin(\omega_{sc}t + \Phi_{sci}) \cos(\phi_{ci}) + \tilde{n}_i(t) \quad (22)$$

After estimating the time delays, we can align the signals in time (in practice there is about 0.2 dB loss for this alignment) and then combine them. For simplicity of analysis, assume that alignment is perfect; then at the output of the signal combiner we have

$$S(t) = \sum_{i=1}^{N} \beta_i S_i(t - \tau_i) \quad (23)$$

At SDA, after demodulating $S(t)$ by reference subcarrier squarewave reference signal,

$$r_{sc} = \mathbf{S}\sin(\omega_{sc}t + \hat{\Phi}_{sc}) \quad (24)$$

where $\hat{\Phi}_{sc}$ is the estimate of

$$\Phi_{sc} = \Phi_{sci} - \omega_{sc}\tau_i \quad (25)$$

we get

$$W(t) = \sum_{i=1}^{N} \beta_i \sqrt{P_i} \sin\theta\, D(t) \left[1 - \frac{2}{\pi}|\phi_{sc}|\right] \cos\phi_{ci} + n_i(t) \quad (26)$$

entering the SSA. The $\phi_{sc} = \Phi_{sc} - \hat{\Phi}_{sc}$ is the subcarrier phase error and $n_i(t)$ is baseband white Gaussian noise with two-sided spectral density $N_{0i}/2$.

Now if we proceed similarly to the previous section, at the output of SSA we get (for alternate symbol sequence)

$$Q_k = \sum_{i=1}^{N} \beta_i \sqrt{P_i} \sin\theta \left[1 - \frac{2}{\pi}|\phi_{sc}|\right] \cos\phi_{ci}\,[1 - 2|\lambda|]\, a_k + n_k \quad (27)$$

where $\lambda$ is symbol time error and $-1/2 < \lambda < 1/2$.

Continuing, also as in the previous section, we get

$$P_b(\underline{\phi}_c, \phi_{sc}, \lambda) = f\left(\sum_{i=1}^{N} \frac{E_{bi}}{N_{0i}} y^2\right) \quad (28)$$

where

$$y \triangleq \frac{\sum_{i=1}^{N} \rho_i \left(1 - \frac{2}{\pi}|\phi_{sc}|\right) \cos\phi_{ci}(1 - 2|\lambda|)}{\sum_{i=1}^{N} \rho_i} \quad (29)$$

Then the bit error rate for the BBC case is

$$P_b = \int_{-\pi}^{\pi}\int_{-\pi}^{\pi}\int_{-1/2}^{1/2} P_b(\underline{\phi}_c, \phi_{sc}, \lambda) \left(\prod_{i=1}^{N} p(\phi_{ci})\right) p(\phi_{sc})\, p(\lambda)\, d\underline{\phi}_c\, d\phi_{sc}\, d\lambda \quad (30)$$

## IV. Carrier Tracking Loop Performance

The performance of carrier tracking loop (CTL) can be summarized as follows. The density function for carrier phase error can be expressed as (Ref. 1)

$$p(\phi_c) = C \frac{\exp\{\rho_{CTL}\cos\phi_c + \rho_{CTL}\,\phi_c\phi_{cs}\}}{2\pi I_0(\rho_{CTL})};\quad -\pi < \phi_c < \pi \tag{31}$$

where $C$ is a normalization factor such that

$$\int_{-\pi}^{\pi} p(\phi_c)d\phi_c = 1.$$

The $\phi_c$ is carrier phase error, $\phi_{cs}$ is carrier static phase error and $\rho_{CTL}$ is carrier tracking loop SNR given by (Ref. 1)

$$\rho_{CTL} = \frac{P\cos^2\theta}{N_0 B_L \Gamma_c} \tag{32}$$

In (32) $P$ is power, and $B_L$ is $CTL$ loop bandwidth given by (Ref. 1)

$$B_L = B_{L0}\left(\frac{1 + r_0\alpha/\alpha_0}{1 + r_0}\right), \tag{33}$$

where $B_{L0}$ is loop bandwidth at threshold, $r_0$ is the damping parameter at threshold, and $\alpha$ is the loop suppression factor given by (Ref. 2)

$$\alpha = \sqrt{\frac{0.7854\,\rho_{in} + 0.4768\,\rho_{in}^2}{1 + 1.024\,\rho_{in} + 0.4768\,\rho_{in}^2}}, \tag{34}$$

and $\rho_{in}$ is the input signal-to-noise ratio to the bandpass limiter and an IF filter having bandwidth $B_{IF}$. Defining carrier margin (CM) by (Ref. 1)

$$CM = \frac{P\cos^2\theta}{N_0(2B_{L0})}, \tag{35}$$

then $\rho_{in}$ can be expressed as

$$\rho_{in} = CM\,\frac{2B_{L0}}{B_{IF}} \tag{36}$$

Finally $\Gamma_c$ is the limiter performance factor given by (Ref. 2)

$$\Gamma_c = \frac{1 + \rho_{in}}{0.862 + \rho_{in}} \tag{37}$$

For second-order loop with transfer function

$$F(s) = \frac{1 + \tau_2 S}{1 + \tau_1 S} \tag{38}$$

where $\tau_1$ and $\tau_2$ are loop filter time constants, assume that the instantaneous Doppler offset is expressed by

$$d(t) = \frac{\omega_c}{c}(\Omega_0 + \Lambda_0 t), \tag{39}$$

where $c$ is speed of light, $\Omega_0$ is spacecraft speed and $\Lambda_0$ is spacecraft acceleration. Then the static phase error $\phi_{cs}$ can be expressed as (Ref. 3)

$$\phi_{cs} \approx \frac{\omega_c}{c}\left[\frac{\Omega_0 + \Lambda_0 t + \Lambda_0\tau_1}{G}\right], \tag{40}$$

where $G$ is the loop gain

$$G = \frac{\sqrt{8}}{\pi}\alpha K \tag{41}$$

For a perfect second-order loop, or when $\tau_2 \ll r\tau_1$, expression (40) for $\phi_{cs}$ reduces to

$$\phi_{cs} \approx \frac{\omega_c}{c}\,\frac{\Lambda_0}{r}\left(\frac{1+r}{4B_L}\right)^2 \tag{42}$$

Note that $\Lambda_0$ at Uranus is about 0.204 m/sec$^2$ and at Neptune is about 0.434 m/sec$^2$. If at threshold the desired static phase error is $\phi_{cs0}$ then

$$\phi_{cs} = \frac{\alpha_0}{\alpha}\phi_{cs0} \tag{43}$$

where $\alpha_0$ is suppression factor at threshold.

## V. Performance of the SDA

The performance of the subcarrier demodulation assembly (Fig. 3) can be summarized as follows. The density function for subcarrier phase error can be expressed as (Ref. 1)

$$p(\phi_{sc}) = C \frac{\exp\{\rho_{SDA} \cos\phi_{sc} + \rho_{SDA}\phi_{sc}\phi_{ss}\}}{2\pi I_0(\rho_{SDA})}; \quad -\pi \leq \phi_{sc} \leq \pi \tag{44}$$

where

$C$ is a normalization constant as before,

$\phi_{sc}$ is the subcarrier phase error, $\phi_{ss}$ is the static phase error,

$\rho_{SDA}$ is subcarrier loop SNR given by (Ref. 1)

$$\rho_{SDA} = \frac{E_s}{N_0} \cdot \frac{R_s}{B_{LS}} \cdot \frac{1}{\Gamma_{SL}} \left(\frac{2\alpha'}{\pi}\right)^2 \tag{45}$$

The $\frac{E_s}{N_0}$ is symbol energy, $R_s$ is symbol rate and $\alpha' = \langle D(t)\hat{D}(t)\rangle$ is a suppression factor due to data aiding. This suppression factor for various symbol transition densities is given by (Ref. 4)

Symbol transition density

0% $$\alpha' = \operatorname{erf}\left[\sqrt{\frac{2}{3}\left(\frac{E_s}{N_0}\right)_e}\right] \tag{46}$$

50% $$\alpha' = 0.769 \left[\frac{0.887 + 0.2\left(\frac{E_s}{N_0}\right)_e^{1.2}}{1 + 0.2\left(\frac{E_s}{N_0}\right)_e^{1.2}}\right] \operatorname{erf}\left(\sqrt{\frac{2}{3}\left(\frac{E_s}{N_0}\right)_e}\right) \tag{47}$$

100% $$\alpha' = 0.538 \left[\frac{0.687 + 0.28\left(\frac{E_s}{N_0}\right)_e^{1.2}}{1 + 0.28\left(\frac{E_s}{N_0}\right)_e^{1.2}}\right] \operatorname{erf}\left(\sqrt{\frac{2}{3}\left(\frac{E_s}{N_0}\right)_e}\right) \tag{48}$$

for filter time constant to symbol time ratio 1/3.

The soft limiter "softness" parameter which depends on the physical parameters of the limiter and the input noise power is given by (Ref. 5)

$$D = \frac{\pi}{4} \nu^2 \, SNR \tag{49}$$

The soft limiter factor $\nu^2$ is

$$\nu^2 = \frac{1}{4} \quad \text{for Block III}$$
$$\nu^2 = \frac{1}{16} \quad \text{for Block IV,} \tag{50}$$

and the SNR is given by

$$SNR = \frac{E_s}{N_0} \frac{R_s}{B_{IFs}} \tag{51}$$

where $B_{IFs}$ is the bandwidth of the bandpass limiter

$$B_{IFs} = 500 \text{ Hz} \quad \text{for Block III}$$
$$B_{IFs} = 1000 \text{ Hz} \quad \text{for Block IV.} \tag{52}$$

Then $\Gamma_{SL}$, the soft limiter performance factor given in Ref. 6 (Eq. 65) can be approximated (Ref. 5) by

$$\Gamma_{SL} = \frac{1 + D}{0.862 + D} \tag{53a}$$

or by (Ref. 7)

$$\Gamma_{SL} = \frac{1 + 0.345\,\alpha'\,SNR + 50\,(\alpha'\,SNR)^5}{0.862 + 0.690\,\alpha'\,SNR + 50\,(\alpha'\,SNR)^5} \tag{53b}$$

The loop gain of SDA is

$$G' = \alpha' \alpha_{SL} G'_{MAX} \tag{54}$$

where $G'_{MAX}$ is the maximum gain ($G'_{MAX} = 400$) and $\alpha_{SL}$, the soft limiter average slope when the carrier tracking loop phase error is neglected, is given by (Ref. 8)

$$\alpha_{SL} = \sqrt{\frac{D}{1+D}} \exp\left[-\frac{R_{SL}}{2(1+D)}\right] \left\{ I_0\left[\frac{R_{SL}}{2(1+D)}\right] + I_1\left[\frac{R_{SL}}{2(1+D)}\right] \right\} \tag{55}$$

where (Ref. 8)

$$R_{SL} = \left(\frac{2\alpha'}{\pi}\right)^2 SNR\,(\phi_{ss}^2 + \sigma_{sc}^2)\,. \tag{56}$$

Since $R_{SL}$ is small, $\alpha_{SL}$ can be approximated as

$$\alpha_{SL} \approx \sqrt{\frac{D}{1+D}} \tag{57a}$$

or in Refs. 7 and 9 $\alpha_{SL}$ has been approximated as

$$\alpha_{SL} = \text{erf}\left[\frac{2\alpha'}{\pi}\sqrt{2D}\right]. \tag{57b}$$

$B_{LS}$ is the SDA loop bandwidth given by

$$B_{LS} = B_{LS0}\,\frac{1 + r_0' G'/G_0'}{1 + r_0'} \tag{58}$$

where $B_{LS0}$, $r_0'$, and $G_0'$ are SDA loop parameters at threshold. For the second-order loop with transfer function

$$F'(s) = \frac{1 + \tau_2' S}{1 + \tau_1' S}, \tag{59}$$

as for CTL, the SDA static phase error can be expressed as

$$\phi_{ss} \approx \frac{\omega_{sc}}{c}\left[\frac{\Omega_0 + \Lambda_0 t + \Lambda_0 \tau_1'}{G'}\right]. \tag{60}$$

For a perfect second-order loop, or when $\tau_2 \ll r'\tau_1$, (60) reduces to

$$\phi_{ss} = \frac{\omega_{sc}}{c}\,\frac{\Lambda_0}{r'}\left(\frac{1+r'}{4B_{LS}}\right) \tag{61}$$

If we set the desired static phase error at threshold as $\phi_{ss0}$ then

$$\phi_{ss} = G_0'\,\phi_{ss0}/G' \tag{62}$$

Finally, for SSC, the loss in data SNR due to carrier tracking loop is (Ref. 8)

$$L_{CTL,i} = \overline{\cos\phi_{ci}}^{\,2} \approx \left(\frac{I_1(\rho_{CTL,i})}{I_0(\rho_{CTL,i})}\cos\phi_{csi}\right)^2, \tag{63}$$

and the loss in data SNR due to subcarrier tracking loop is (Refs. 7, 8)

$$L_{SDA,i} = \left[1 - \left(\frac{2}{\pi}\right)^{1.5}\exp\left\{-\frac{\phi_{ssi}^2}{2\sigma_{sci}^2}\right\}\right.$$

$$\left.\sigma_{sci} - \frac{2}{\pi}\phi_{ssi}\,\text{erf}\left(\frac{\phi_{ssi}}{\sqrt{2}\,\sigma_{sci}}\right)\right]^2 \tag{64}$$

Then

$$\left(\frac{E_{si}}{N_0}\right)_e = \frac{E_{si}}{N_0} \times L_{SDA,i} \times L_{CTL,i}\,. \tag{65}$$

For BBC the loss in data SNR due to all carrier tracking loops is

$$L_{CTL} = \left[\frac{\sum_{i=1}^{N}\rho_i\,\frac{I_1(\rho_{CTL,i})}{I_0(\rho_{CTL,i})}\cos\phi_{csi}}{\sum_{i=1}^{N}\rho_i}\right]^2 \tag{66}$$

and loss in data SNR due to the SDA loop is

$$L_{SDA} = \left[1 - \left(\frac{2}{\pi}\right)^{1.5}\exp\left\{-\frac{\phi_{ss}^2}{2\sigma_{sc}^2}\right\}\right.$$

$$\left.\sigma_{sc} - \frac{2}{\pi}\,\phi_{ss}\,\text{erf}\left(\frac{\phi_{ss}}{\sqrt{2}\,\sigma_{sc}}\right)\right]^2 \tag{67}$$

Thus

$$\left(\frac{E_s}{N_0}\right)_e = \left(\sum_{i=1}^{N}\frac{E_{bi}}{N_{0i}}\right) \times L_{SDA} \times L_{CTL} \tag{68}$$

## VI. Performance of the SSA

The performance of the symbol synchronization assembly (Fig. 4) can be summarized as follows. The probability density function for symbol time error $\lambda$ can be expressed as

$$p(\lambda) = C\,\frac{\exp\left\{\frac{4\pi^2\lambda\lambda_s + \cos 2\pi\lambda}{(2\pi\sigma_\lambda)^2}\right\}}{I_0\left(\frac{1}{(2\pi\sigma_\lambda)^2}\right)};\ -\frac{1}{2} < \lambda < \frac{1}{2} \tag{69}$$

where $\lambda_s$ is the static time shift of the loop and $\sigma_\lambda^2$ can be expressed as (Ref. 2)

$$\sigma_\lambda^2 = \frac{\xi_0 B_{LSS}}{2\left(\frac{E_s}{N_0}\right)_e R_s} \mathscr{L} \tag{70}$$

where $\xi_0$ is the window size ($\xi_0 = 1/4$), and the SSA loop bandwidth is

$$B_{LSS} = B_{LSS0} \frac{1 + r_0'' \sqrt{\left(\frac{E_s}{N_0}\right)_e \Big/ \left(\frac{E_s}{N_0}\right)_0}}{1 + r_0''} \tag{71}$$

$(E_s/N_0)_e$ is the effective input SNR to the SSA and is given by (65) for SSC and (68) for BBC. $(E_s/N_0)_0$ is the data SNR at the design point and $r_0''$ is the SSA loop damping parameter at the design point ($r_0'' = 2$). $\mathscr{L}$ is the squaring loss, given by Ref. 2,

$$\mathscr{L} = \frac{h(0)}{k_g^2} \tag{72}$$

where

$$h(0) = 1 + \frac{\xi_0 \left(\frac{E_s}{N_0}\right)_e}{2} - \frac{\xi_0}{2}\left[\frac{1}{\sqrt{\pi}} e^{-\left(\frac{E_s}{N_0}\right)_e} + \sqrt{\left(\frac{E_s}{N_0}\right)_e}\, erf\left(\sqrt{\left(\frac{E_s}{N_0}\right)_e}\right)\right]^2 \tag{73}$$

and

$$K_g = erf\left(\sqrt{\left(\frac{E_s}{N_0}\right)_e}\right) - \frac{\xi_0}{2}\sqrt{\frac{1}{\pi}\left(\frac{E_s}{N_0}\right)_e}\, e^{-\left(\frac{E_s}{N_0}\right)_e} \tag{74}$$

For a perfect second-order loop the static time error

$$\lambda_s = \frac{R_s}{c} \frac{\Lambda_0}{r_{ss}} \left(\frac{1 + r_{ss}}{4 B_{LSS}}\right) \tag{75}$$

where $r_{ss}$ is the loop damping parameter.

The loss in data SNR due to the SSA alone is

$$L_{SSA} = \overline{(1 - 2|\lambda|)}^2 = \left[1 - 2\sqrt{\frac{2}{\pi}} e^{-\frac{\lambda_s^2}{2\sigma_\lambda^2}} \sigma_\lambda - 2\lambda_s \, \mathrm{erf}\left(\frac{\lambda_s}{\sqrt{2}\sigma_\lambda}\right)\right]^2 \tag{76}$$

## VII. Computation of Bit Error Rate

In order to compute Eq. (21) or (30), first we examine an approximate result for the large signal-to-noise ratio case, where

$$y \approx 1 \tag{77}$$

Therefore, we can make use of Taylor expansion for Eq. (19) as

$$f\left(\sum_{i=1}^{N} \frac{E_{bi}}{N_{0i}} y^2\right) = f\left(\sum_{i=1}^{N} \frac{E_{bi}}{N_{0i}}\right) + 2(y - 1) f^1\left(\sum_{i=1}^{N} \frac{E_{bi}}{N_{0i}}\right) \tag{78}$$

But

$$f^1(x) = \begin{cases} -\alpha_1 f(x) & ; \quad x > \dfrac{\alpha_0 + \ln 2}{\alpha_1} \triangleq T' \\ 0 & ; \quad x < \dfrac{\alpha_0 + \ln 2}{\alpha_1} \end{cases} \tag{79}$$

Therefore,

$$P_b = \overline{f\left(\sum_{i=1}^{N} \frac{E_{bi}}{N_{0i}} y^2\right)} = \begin{cases} f\left(\sum_{i=1}^{N} \frac{E_{bi}}{N_{0i}}\right)\left[1 + 2\alpha_1 (1 - \bar{y})\right] & ; \quad \sum_{i=1}^{N} \frac{E_{bi}}{N_0} > T' \\ 0.5 & ; \quad \sum_{i=1}^{N} \frac{E_{bi}}{N_0} < T' \end{cases} \tag{80}$$

For SSC,

$$\bar{y} = \frac{\sum_{i=1}^{N} \rho_i \left(1 - \frac{2}{\pi}\overline{|\phi_{sci}|}\right) \overline{\cos\phi_{ci}}\,(1 - 2\overline{|\lambda_i|})}{\sum_{i=1}^{N} \rho_i} \tag{81}$$

For BBC,

$$\bar{y} = \frac{\sum_{i=1}^{N} \rho_i \left(1 - \frac{2}{\pi}\overline{|\phi_{sc}|}\right) \overline{\cos\phi_{ci}}\,(1 - 2\overline{|\lambda|})}{\sum_{i=1}^{N} \rho_i} \tag{82}$$

Note

$$\overline{\cos\phi_{ci}} \approx \frac{I_1(\rho_{CTL,i})}{I_0(\rho_{CTL,i})} \cos\phi_{csi} \tag{83}$$

for large SNR

$$\overline{|\phi_{sc}|} \approx \sqrt{\frac{2}{\pi}}\, e^{\frac{-\phi_{ss}^2}{2\sigma_{sc}^2}} \sigma_{sc} + \phi_{ss}\,\mathrm{erf}\left(\frac{\phi_{ss}}{\sqrt{2}\sigma_{sc}}\right) \tag{84}$$

$$\overline{|\lambda|} \approx \sqrt{\frac{2}{\pi}}\, e^{\frac{-\lambda_s^2}{2\sigma_\lambda^2}} \sigma_\lambda + \lambda_s\,\mathrm{erf}\left(\frac{\lambda_s}{\sqrt{2}\sigma_\lambda}\right) \tag{85}$$

## VIII. Computation of Bit Error Rate Using Moment Technique

Note that the direct evaluation of Eq. (21) for $N$ antennas needs $(3N)$-tuple integration; for even the simple case $N = 3$ we need 9-tuple integration! Similarly, for evaluation of Eq. (30) we need $(N + 2)$-tuple integration. Using direct method of computation is very hard and consumes a lot of computer time (days and maybe weeks). Therefore, to solve the problem we use the moment technique of Ref. 10. Here we want to find

$$P_b = E\{f(x)\} = E\{g(y)\} \tag{86}$$

where

$$x = \sum_{i=1}^{N} \frac{E_{bi}}{N_{0i}} y^2 \tag{87}$$

and

$$g(y) = f(x)\,. \tag{88}$$

The $y$ is given by Eq. (20) for SSC and by Eq. (29) for BBC, and the expection $E$ is over all random variables-contained in $y$. Suppose we have $M + 1$ moments of $y$

$$\mu_k = E\{y^k\}; \quad k = 0, 1, 2, \cdots, M \tag{89}$$

Suppose we could expand $g(y)$ as

$$g(y) \approx \sum_{i=0}^{N} \alpha_i y^i \tag{90}$$

Then

$$E\{g(y)\} = \sum_{i=0}^{N} \alpha_i E\{y^i\} = \sum_{i=0}^{N} \alpha_i \mu_i \tag{91}$$

Unfortunately, expansion of $g(\cdot)$ given by (90) results in an alternating sum of moments with large coefficients $\alpha_i$; this results in numerical inaccuracies in summing. Thus, we cannot simply expand $g(y)$ and use moments of $y$. Therefore, we would like to find the smallest number of points $y_1$, $y_2, \cdots, y_\nu$ and weights $w_1, w_2, \cdots, w_\nu$ so that the approximate discrete probability distribution

$$\hat{p}_r\{y = y_\ell\} = \omega_\ell\,; \quad \ell = 1, 2, \cdots, \nu \tag{92}$$

satisfies the given moment constraints

$$\mu_k = \hat{E}(y_k) = \sum_{\ell=1}^{\nu} \omega_\ell y_\ell^k\,; \quad k = 0, 1, 2, \cdots, M \tag{93}$$

More details about the following summary of the moment technique can be found in Ref. 10.

Next define the polynomial

$$C(D) = \prod_{\ell=1}^{\nu} (1 - Dy_\ell) = C_0 + C_1 D + C_2 D^2 + \cdots + C_\nu D^\nu$$

$$C_0 = 1 \tag{94}$$

We can show

$$\mu_n = -\sum_{j=1}^{\nu} C_j \mu_{n-j} \tag{95}$$

This form of the relationship between moments can be interpreted as a linear feedback shift register generating the moments (Fig. 5). Note that the Berlekamp-Massey linear feedback shift register synthesis algorithm can find a smallest length feedback shift register that generates $\mu_0, \mu_1, \cdots, \mu_M$. This enables us to find $C(D)$. Having $C(D)$, we can find $y_1, y_2, \cdots, y_\nu$. Define the polynomial

$$P(D) = \sum_{\ell=1}^{\nu} \omega_\ell \prod_{\substack{j=1 \\ j\neq\ell}}^{\nu} (1 - Dy_j) = P_0 + P_1 D + \cdots + P_{\nu-1} D^{\nu-1} \tag{96}$$

Define the moment generating function polynomial as

$$\mu(D) \triangleq \sum_{k=0}^{\infty} \mu_k D^k \tag{97}$$

Then we can show

$$p(D) = \mu(D) C(D) \tag{98}$$

Finally it can be shown that

$$\omega_k = -\frac{y_k P(y_k^{-1})}{C'(y_k^{-1})}; \quad k = 1, 2, \cdots, \nu \tag{99}$$

where

$$C'(D) \triangleq \frac{d}{dD} C(D) \tag{100}$$

A summary of finding $E\{g(y)\}$ using the moment technique is shown in Fig. 6.

Define $y$ for SSC as

$$y \triangleq y_N = \left[\sum_{i=1}^{N} \rho_i \left(1 - \frac{2}{\pi}|\phi_{sci}|\right) \cos\phi_{ci} (1 - 2|\lambda_i|)\right] \Big/ \left[\sum_{i=1}^{N} \rho_i\right] \tag{101}$$

Then

$$y_N = y_{N-1} + \rho_N \left(1 - \frac{2}{\pi}|\phi_{SN}|\right) \cos\phi_{CN} (1 - 2|\lambda_N|) \Big/ \left(\sum_{i=1}^{N} \rho_i\right) \tag{102}$$

Finally

$$E\{y_N^k\} = \sum_{i=0}^{k} \binom{k}{i} E\{y_{N-1}^i\} \rho_N^{k-i} E\left\{\left(1 - \frac{2}{\pi}|\phi_{SN}|\right)^{k-i}\right\}$$

$$\times E\{\cos^{k-i}\phi_{CN}\} E\{(1 - 2|\lambda_N|)^{k-i}\} \tag{103}$$

Therefore, having certain moments of $[1 - 2/\pi\,|\phi_{si}|]$, $\cos\phi_{ci}$ and $(1 - 2|\lambda_i|)$, by iteration using Eq. (103) we can find all required moments of $y$. A faster method for computation of moments of $y$ is to use the so-called semi-invariants method given in Ref. 10. Having all moments of $y$ we can use the Berlekamp-Massey algorithm as discussed before to find required points $y_i$ and the weights $w_i$. Thus

$$P_b = E\{g(y)\} = \sum_{i=1}^{\nu} \omega_i\, g(y_i) \tag{104}$$

Example: Consider the arraying of three antennas, namely 64 m, 34 m (T/R) and 34 m (R). For a modulation index of 72°, a data symbol rate of 20 kbps (bit rate = 10 kbps), loop bandwidths at threshold of

$2B_{L0}$ (CTL) = 30 Hz

$B_{LS}$ (SDA) = 0.1 Hz

$B_{LSS}$ (SSA) = 0.05 Hz,

and window size = 1/4 in SSA, we have tabulated all data SNR losses and loop SNRs for SSC and BBC. From Table 1, if we include the losses of 0.2 dB from the microwave link and of 0.2 dB due to alignment in the BBC case, then the total loss in the data SNR in SSC will be 0.35 dB less than the data SNR loss in BBC. Finally, the bit error probability curve using the moment technique is given in Figs. (7) and (8) for the above case for SSC and BBC.

## IX. Conclusion

In this article, a system performance analysis of symbol stream and baseband combining is given. The performances of the carrier tracking loop, the subcarrier demodulation assem-

bly, and the symbol synchronization assembly have been determined. Numerical results are given for an example of arraying three antennas, namely a 64 m, 34 m (T/R) and 34 m (R) antennas of DSN. Final results show that symbol stream combining outperforms baseband combining by about 0.35 dB.

## Acknowledgments

The author wishes to thank J. H. Yuen, W. J. Hurd and J. W. Layland for their comments and discussions. Also he would like to thank M. K. Simon for providing the Berlekamp-Massey algorithm program.

## References

1. Yuen, J. H., *Deep Space Telecommunications Systems Engineering*, Publication 82-76, Jet Propulsion Laboratory, Pasadena, Calif., July 1982.

2. Lindsey, W. C., and Simon, M. K., *Telecommunication Systems Engineering*, Prentice-Hall, Inc., Englewood Cliffs, N.J., 1973.

3. Lindsey, W. C., *Synchronization Systems in Communication and Control*, Prentice-Hall Inc., Englewood Cliffs, N.J., 1972.

4. Brockman, M. H., "MMT Subcarrier Demodulator," *SPS 37-46*, Vol. III, Jet Propulsion Laboratory, Pasadena, Calif., July 1967, pp. 189-204.

5. Brown, D. W., *Signal Suppression in Bandpass Limiters,* Technical Report 32-1526, Vol. XVIII, Sept. and Oct. 1973, Jet Propulsion Laboratory, Pasadena, Calif., Dec. 15, 1973.

6. Lesh, J. R., "Signal-to-Noise Ratios in Coherent Soft Limiters," *IEEE Transactions on Communications,* Vol. COM-22, No. 6, June 1974.

7. Brockman, M. H., "MMTS: Performance of the Subcarrier Demodulator," *SPS 37-52,* Vol. II, Jet Propulsion Laboratory, Pasadena, Calif., July 1968, pp. 127-141.

8. Lesh, J. R., *A Re-Examination of Subcarrier Demodulator Performance,* Technical Report 32-1526, Vol. XVII, July and August 1973, Jet Propulsion Laboratory, Pasadena, Calif., Oct. 15, 1973.

9. Brockman, M. H., "An Efficient and Versatile Telemetry Subcarrier Demodulation Technique for Deep Space Telecommunications," Proc. 4th Hawaiian International Conference on System Science, January 1971.

10. Omura, J. K., and Simon, M. K., *Satellite Communication Performance Evaluation: Computational Techniques Based on Moments,* Publication 80-71, Jet Propulsion Laboratory, Pasadena, Calif., Sept. 15, 1980.

**Table 1. Comparison of performance of SSC and BBC**

$$\text{at} \sum_{i=1}^{3} \frac{E_{bi}}{N_{oi}} = 3.2 \text{ dB}$$

(all losses and loop SNR's in dB)

| Type of arraying | Antennas | Carrier tracking loop | | SDA | | SSA | | Microwave loss | Combining loss | Total loss in data SNR |
|---|---|---|---|---|---|---|---|---|---|---|
| | | $L_{CTL}$ | $\rho_c$ | $L_{SDA}$ | $\rho_s$ | $L_{SSA}$ | $\rho_{ss}$ | | | |
| SSC | 64 m | −0.22 | 13 | −0.044 | 40 | −0.01 | 44 | 0 | 0 | −0.43 |
| | 34 m (T/R) | −0.56 | 9.2 | −0.16 | 28 | −0.05 | 32 | 0 | 0 | |
| | 34 m (R) | −0.46 | 9.9 | −0.12 | 31 | −0.04 | 35 | 0 | 0 | |
| BBC | 64 m | −0.22 | 13 | | | | | | | |
| | 34 m (T/R) | −0.56 | 9.2 | −0.03 | 43 | −0.02 | 47 | −0.2 | −0.2 | −0.78 |
| | 34 m (R) | −0.46 | 9.9 | | | | | | | |

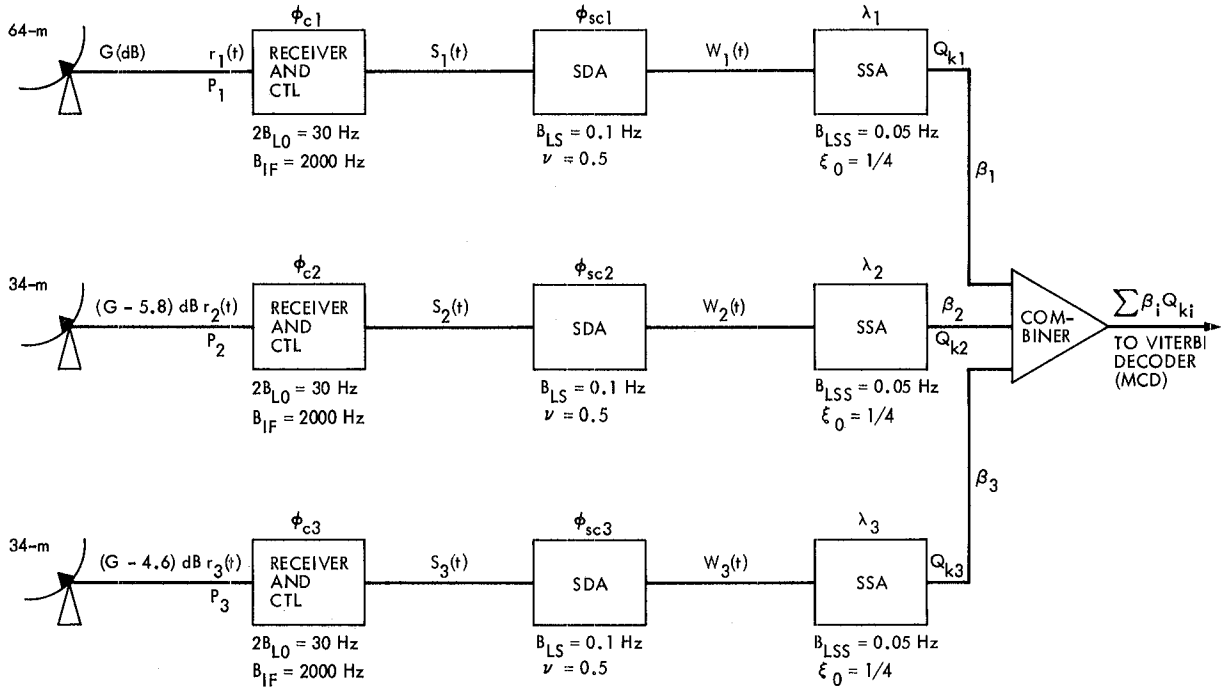


**Fig. 1. Block diagram of symbol stream combining system**

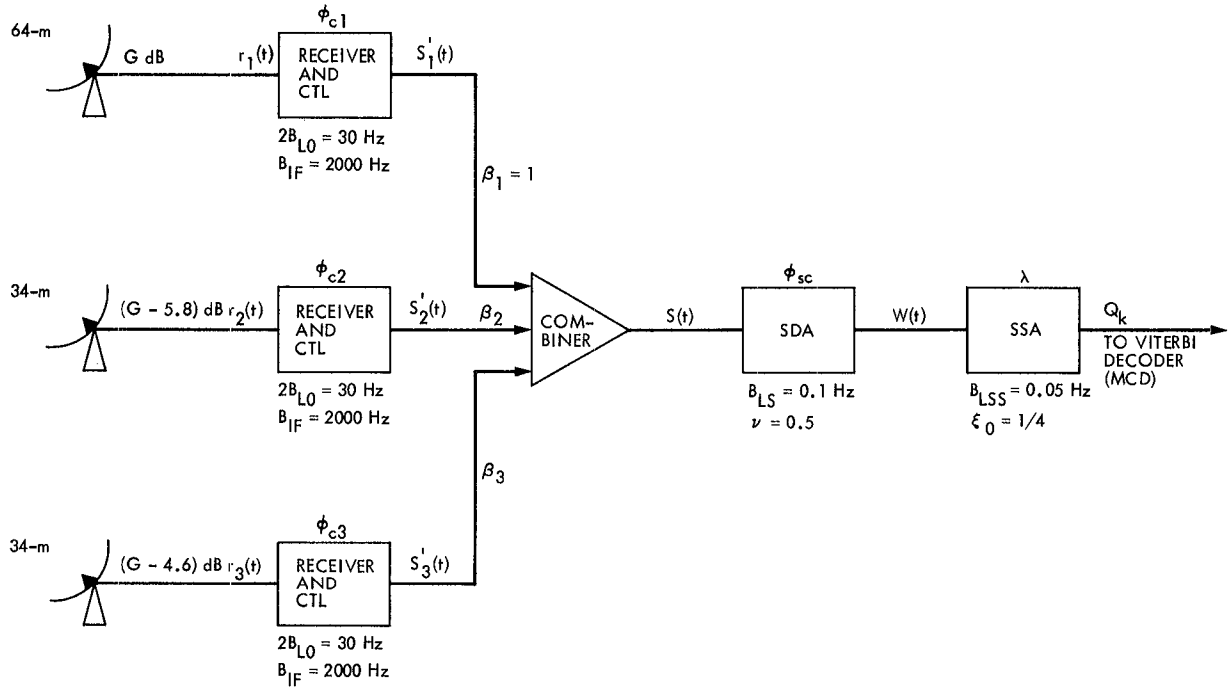


**Fig. 2. Block diagram of baseband combining system**

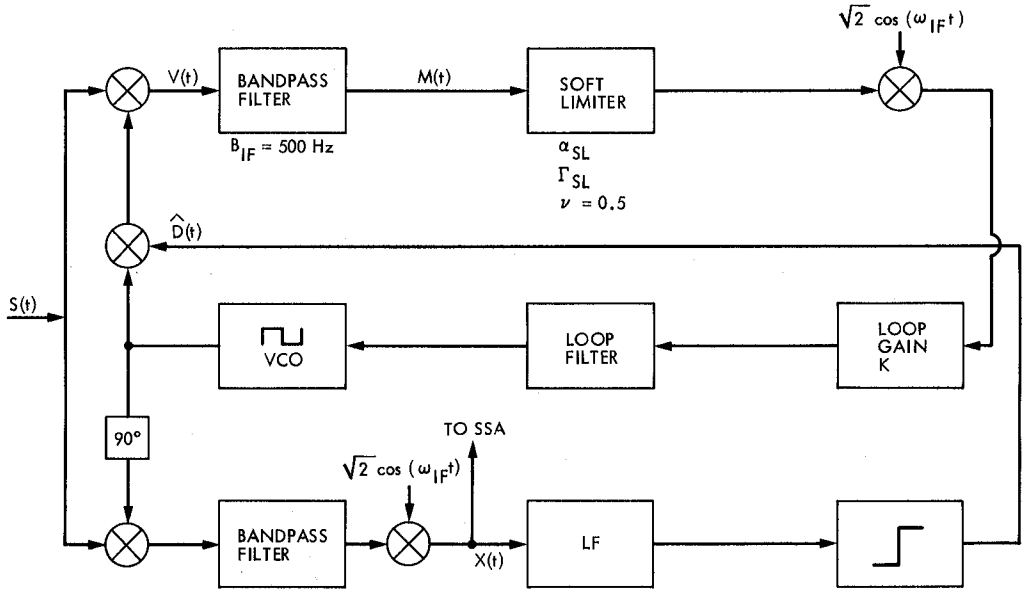


**Fig. 3. Block diagram of subcarrier demodulation assembly (SDA)**

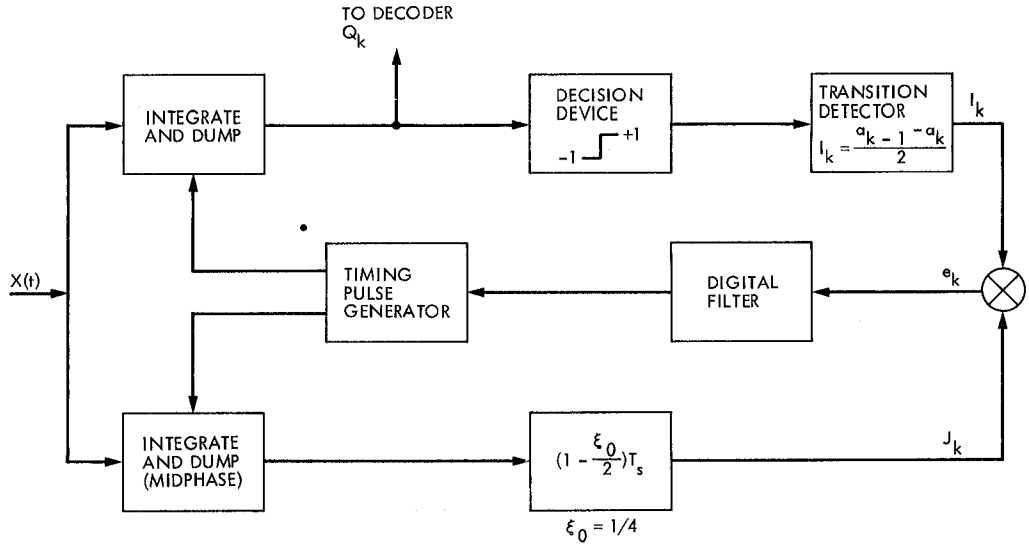


DIGITAL DATA TRANSITION TRACKING LOOP

**Fig. 4. Block diagram of symbol synchronization assembly (SSA)**

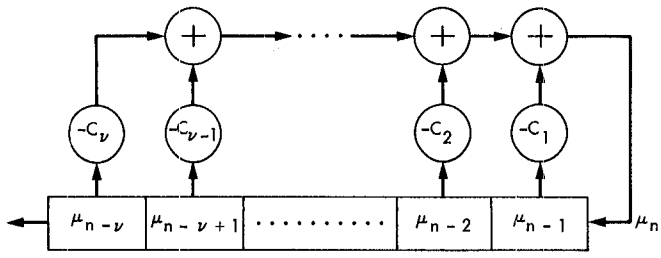


**Fig. 5. Moment generating linear feedback shift register**

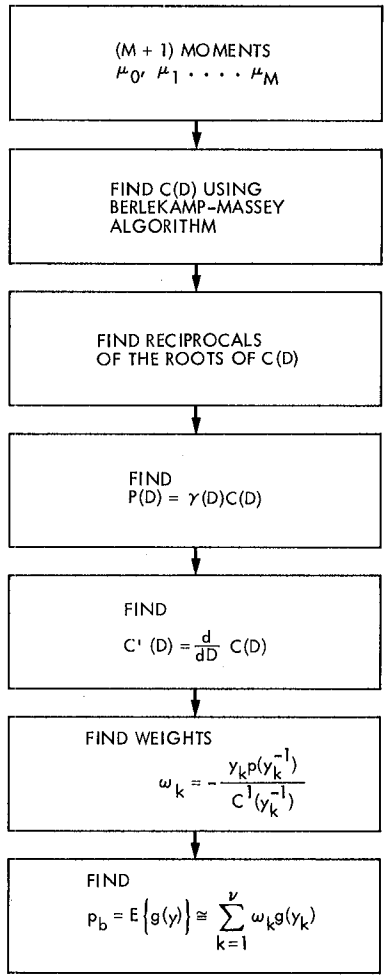


**Fig. 6. Flow chart for computation of $E\{g(y)\}$ using moment technique**

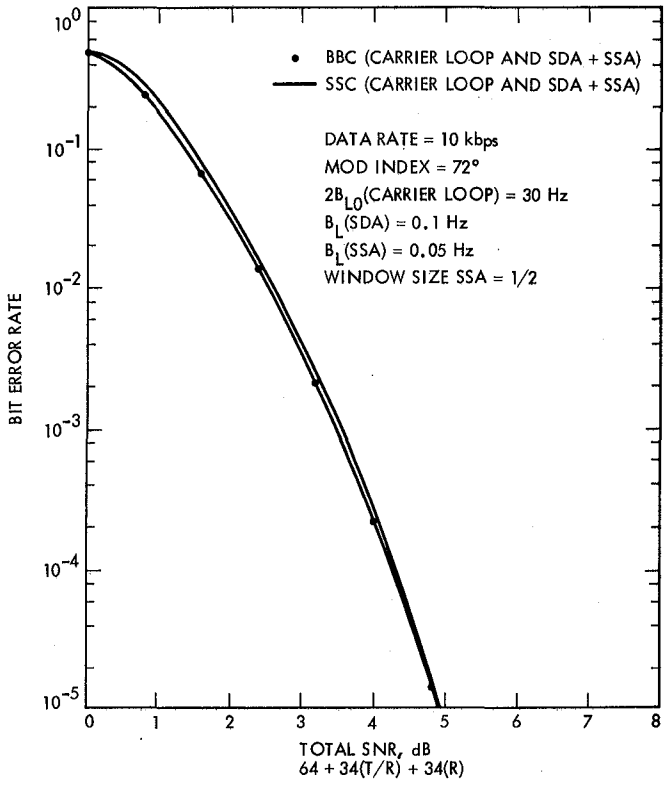


**Fig. 7. Bit error rate vs total SNR for symbol stream and baseband combining for window size 1/2 (microwave and combiner losses are not included)**

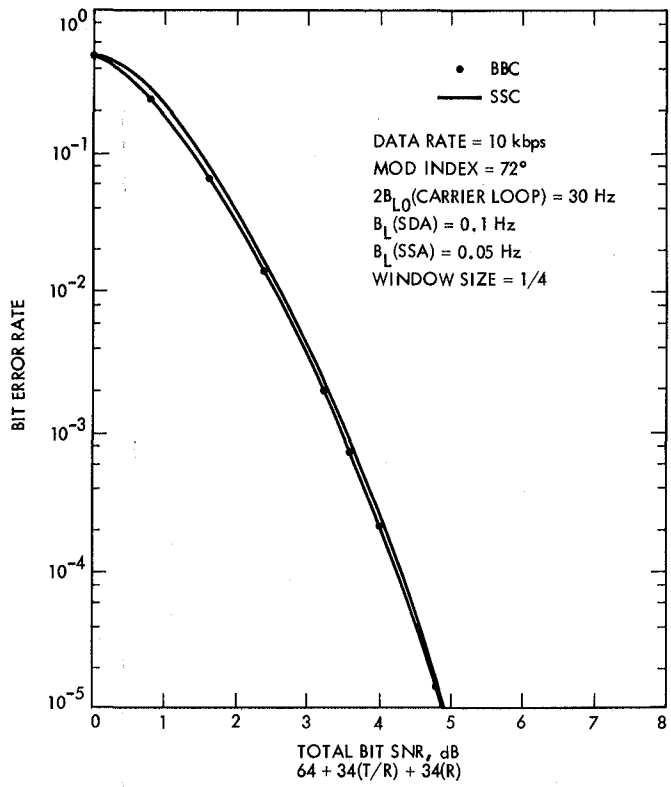


**Fig. 8. Bit error rate vs total SNR for symbol stream and baseband combining for window size 1/4 (microwave and combiner losses are not included)**

# Thermal Analysis of Antenna Structures Part II – Panel Temperature Distribution

D. Schonfeld and F. L. Lansing
Ground Antennas and Facilities Engineering Section

*This article is the second in a series that analyzes the temperature distribution in microwave antennas. An analytical solution in a series form is obtained for the temperature distribution in a flat plate analogous to an antenna surface panel under arbitrary temperature and boundary conditions. The solution includes the effects of radiation and air convection from the plate. Good agreement is obtained between the numerical and analytical solutions.*

## I. Introduction

In a previous article (Ref. 1) we have indicated that construction requirements for large Ka-band antennas are more stringent than those presently used for the S- or X-bands. In particular, for the Ka-band antennas, environmental factors such as temperature variations can have deleterious effects on the antenna panels setting, alignment, antenna pointing and tracking and therefore on the antenna performance.

In Ref. 1 we have presented a method of analysis that was used for thermal modeling of the links which make up the antenna's backup structure. The present article extends the thermal modeling by considering the antenna surface panels. In future articles we will tie the present panel temperature analysis to the thermal analysis of the backup structure. In this way we aim to obtain a temperature simulation of the complete antenna structure and, from this, calculate the thermal stresses in the antenna members.

## II. Analysis

To model a single antenna panel, we will be considering a two-dimensional rectangular plate of length $a$ and width $b$ as shown in Fig. 1. The two-dimensional assumption is warranted because the thickness of the antenna panel is much smaller than the other dimensions. We want to find the temperature distribution and the heat flux in this plate under the following assumptions:

(1) Arbitrary, steady-state temperature boundary conditions; these are labeled $T_N(x)$, $T_E(y)$, $T_S(x)$, and $T_W(y)$ in Fig. 1. for the north, east, south and west sides of the rectangle, respectively.

(2) Heat transfer in the plate occurs due to conduction, air convection and solar and IR radiation. The plate is characterized by a thermal conductivity $k$, a convection coefficient $h_c$ and a short wave solar absorptivity $\alpha$. No internal heat generation is assumed.

(3) Linearized approximation for the radiation heat transfer to ambient term as indicated in Ref. 1 results in a radiative heat transfer coefficient

$$h_r = \epsilon \sigma \mathbf{F} (T^2 + T_a^2)(T + T_a)$$

Under these conditions, the two-dimensional heat transfer equation is

$$\frac{\partial^2 T}{\partial x^2} + \frac{\partial^2 T}{\partial y^2} = \left(\frac{h_r + h_c}{k}\right) T + \left(\frac{\alpha I}{k} - \frac{h_r + h_c}{k} T_a\right) \quad (1)$$

or

$$\nabla^2 T = a_1 T + a_2 \quad (2)$$

where

$$a_1 = \frac{h_r + h_c}{k}$$

$$a_2 = \frac{\alpha I}{k} - \frac{h_r + h_c}{k} T_a \quad (3)$$

Equation (2) is a nonhomogeneous partial differential equation. The following nonhomogeneous boundary conditions are formed for Eq. (1):

$$\begin{aligned} T &= T_W(y) \quad \text{for } x = 0, \\ T &= T_E(y) \quad \text{for } x = a, \\ T &= T_S(x) \quad \text{for } y = 0, \\ T &= T_N(x) \quad \text{for } y = b. \end{aligned} \quad (4)$$

The following cases are studied to verify the accuracy limits between analytical solutions in series form and numerical solutions for homogeneous and nonhomogeneous forms of the equation.

Case 1. Simple Conduction Problem – Series Solution

When $a_1 = a_2 = 0$, Eq. (2) reduces to the conventional Laplace's equation and represents a two-dimensional temperature distribution due to conduction heat transfer only (Ref. 2). For this simplified case one obtains the following series solution.

$$T(x,y) = \frac{2}{a} \sum_{m=1}^{\infty} \frac{\int_0^a T_N(x) \sin \frac{m\pi x}{a}\, dx}{\sinh m\pi} \sin \frac{m\pi x}{a} \sinh \frac{m\pi y}{b}$$

$$+ \frac{2}{a} \sum_{m=1}^{\infty} \frac{\int_0^a T_S(x) \sin \frac{m\pi x}{a}\, dx}{\sinh(-m\pi)} \sin \frac{m\pi x}{a} \sinh \frac{m\pi(y-b)}{b}$$

$$+ \frac{2}{b} \sum_{m=1}^{\infty} \frac{\int_0^b T_E(y) \sin \frac{m\pi y}{b}\, dy}{\sinh m\pi} \sin \frac{m\pi y}{b} \sinh \frac{m\pi x}{a}$$

$$+ \frac{2}{b} \sum_{m=1}^{\infty} \frac{\int_0^b T_W(y) \sin \frac{m\pi y}{b}\, dy}{\sinh(-m\pi)} \sin \frac{m\pi y}{b} \sinh \frac{m\pi(x-a)}{a} \quad (5)$$

If one expands the temperature boundary conditions $T_N$, $T_S$, $T_E$ and $T_W$ in uniformly convergent Fourier series, the temperature distribution $T(X, Y)$ will no longer involve integrals. For this case, the solution is given in Ref. 2.

Case 2. Simple Conduction Problem–Numerical Solutions

The series solution, Eq. (5), can be truncated, and computed numerically for any arbitrary but finite number of terms. In this computation, as the number of terms and the arguments of the trigonometric functions become large, numerical errors can accumulate and cause instability. Therefore, when the computational programs were run on JPL's UNIVAC 1181, double precision was used for all the variables. The results of numerically computing the truncated series solution can be compared with those obtained by solving Laplace's equation by numerical means (Ref. 3). The two methods should give agreeable answers and thus serve as a check on each other. As an example, consider a square flat plate ($a = b = 1$) where the temperature boundary conditions (nonhomogeneous) are given by:

$$\begin{aligned} T_N(x) &= 150x + 50 \\ T_E(x) &= 100y + 100 \\ T_S(x) &= -200x + 300 \\ T_W(y) &= -250y + 300 \\ (0 < x < 1, 0 < y < 1) \end{aligned} \quad (6)$$

The resulting isotherms for this case are illustrated in Fig. 2. The series computation from Eq. (5) is truncated at the tenth term ($m = 10$) and the results show good agreement with those obtained by a numerical solution of Laplace's equation (results are listed in Table 1).

Case 3. The Nonhomogeneous Case–Series Solution

Where $a_1$ and $a_2$ are both nonzero, Eqs. (2) and (4) form a complex nonhomogeneous boundary value problem with nonhomogeneous differential equation and nonhomogeneous boundary conditions. However, taking advantage of linearity we use superposition to solve the nonhomogeneous boundary conditions and separation of variables to solve the nonhomogeneous differential equation as follows.

Let $T(x, y)$ be expressed as a sum of two functions:

$$T(x, y) = u(x, y) + f(a_1, a_2) \tag{7}$$

If the constant $f(a_1, a_2)$ is chosen such that:

$$f(a_1, a_2) = -\frac{a_2}{a_1} \tag{8}$$

then replacing (7) into (2) results in a homogeneous partial differential equation in $u(x, y)$:

$$\nabla^2 u(x, y) = a_1 u(x, y) \tag{9}$$

with the following four nonhomogeneous boundary conditions

$$\begin{aligned} u(x,0) &= T_X(x) + \frac{a_2}{a_1} \\ u(x,b) &= T_N(x) + \frac{a_2}{a_1} \\ u(a,y) &= T_W(y) + \frac{a_2}{a_1} \\ u(a,y) &= T_E(y) + \frac{a_2}{a_1} \end{aligned} \tag{10}$$

The linearity of Eq. (9) allows us to use superposition of four subproblems; each one has a single nonhomogeneous boundary condition. Write $u(x, y)$ as the sum

$$u(x, y) = s(x, y) + t(x, y) + v(x, y) + w(x, y) \tag{11}$$

which when inserted into (9) and (10) gives the following:

$$\nabla^2 s(x,y) + \nabla^2 t(x,y) + \nabla^2 v(x,y) + \nabla^2 w(x,y) =$$

$$a_1 s(x, y) + a_1 t(x, y) + a_1 v(x, y) + a_1 w(x, y) \tag{12}$$

with the following four boundary conditions:

$$\begin{aligned} s(x,0) + t(x,0) + v(x,0) + w(x,0) &= T_S(x) + \frac{a_2}{a_1} \\ s(x,b) + t(x,b) + v(x,b) + w(x,b) &= T_N(x) + \frac{a_2}{a_1} \\ s(0,y) + t(0,y) + v(0,y) + w(0,y) &= T_W(y) + \frac{a_2}{a_1} \\ s(a,y) + t(a,y) + v(a,y) + w(a,y) &= T_E(y) + \frac{a_2}{a_1} \end{aligned} \tag{13}$$

Therefore, the solution of homogeneous Eq. (9) with nonhomogeneous boundary conditions (10) can be obtained by solving four subproblems each one having at most one nonhomogeneity. These four subproblems are

Subproblem 1: $\Delta^2 s = a_1 s$

$$\begin{aligned} \nabla s(x,0) &= T_S(x) + \frac{a_2}{a_1} \\ s(x,b) &= 0 \\ s(o,y) &= 0 \\ s(a,y) &= 0 \end{aligned} \tag{14}$$

Subproblem 2: $\nabla^2 t = a_1 t$

$$\begin{aligned} t(x,0) &= 0 \\ t(x,b) &= T_N(x) + \frac{a_2}{a_1} \\ t(o,y) &= 0 \\ t(a,y) &= 0 \end{aligned} \tag{15}$$

Subproblem 3:

$$\nabla^2 v = a_1 v$$

$$v(x,0) = 0$$

$$v(x,b) = 0 \tag{16}$$

$$v(0,y) = T_W(y) + \frac{a_2}{a_1}$$

$$v(a,y) = 0$$

Subproblem 4:

$$\nabla^2 w = a_1 w$$

$$w(x,0) = 0$$

$$w(x,b) = 0 \tag{17}$$

$$w(0,y) = 0$$

$$w(a,y) = T_E(y) + \frac{a_2}{a_1}$$

The solution to subproblem 1 can be found in Ref. 4 as

$$s(x,y) = \frac{2}{a}\sum_{m=1}^{\infty} \frac{\sin \bar{x}_m \sinh((b-y)\gamma_m)}{\sinh b\gamma_m} \int_0^a \left[T_S(x) + \frac{a_2}{a_1}\right] \sin \bar{x}_m \, dx \tag{18}$$

where

$$\bar{x}_m = \frac{m\pi x}{a} \tag{19}$$

$$\gamma_m = \left(a_1 + \frac{m^2\pi^2}{a^2}\right)^{1/2} \tag{20}$$

By analogy with Eq. (18), the other subproblems have the following solutions.

For subproblem 2, the solution is:

$$t(x,y) = \frac{2}{a}\sum_{m=1}^{\infty} \frac{\sin \bar{x}_m \sinh(y\gamma_m)}{\sinh b\gamma_m} \int_0^a \left[T_N(x) + \frac{a_2}{a_1}\right] \sin \bar{x}_m \, dx \tag{21}$$

For subproblem 3, the solution is:

$$v(x,y) = \frac{2}{b}\sum_{m=1}^{\infty} \frac{\sin \bar{y}_m \sinh((a-x)\eta_m)}{\sinh a\eta_m} \int_0^b \left[T_W(y) + \frac{a_2}{a_1}\right] \sin \bar{y}_m \, dy \tag{22}$$

For subproblem 4, the solution is:

$$w(x,y) = \frac{2}{b}\sum_{m=1}^{\infty} \frac{\sin \bar{y}_m \sinh(x\eta_m)}{\sinh a\eta_m} \int_0^b \left[T_E(y) + \frac{a_2}{a_1}\right] \sin \bar{y}_m \, dy \tag{23}$$

where

$$\bar{y}_m = \frac{m\pi y}{a} \tag{24}$$

$$\eta_m = \left(a_1 + \frac{m^2\pi^2}{b^2}\right)^{1/2} \tag{25}$$

Therefore, the actual temperature field, $T(x,y)$, from Eq. (7) is given by adding Eqs. (18), (21), (22) and (23)

$$\begin{aligned} T(x,y) = {} & \frac{2}{a}\sum_{m=1}^{\infty} \frac{\sin \bar{x}_m \sinh((b-y)\gamma_m}{\sinh b\gamma_m} \int_0^a \left[T_S(x) + \frac{a_2}{a_1}\right] \sin \bar{x}_m \, dx \\ & + \frac{2}{a}\sum_{m=1}^{\infty} \frac{\sin \bar{x}_m \sinh(y\gamma_m)}{\sinh b\gamma_m} \int_0^a \left[T_N(x) + \frac{a_2}{a_1}\right] \sin \bar{x}_m \, dx \\ & + \frac{2}{b}\sum_{m=1}^{\infty} \frac{\sin \bar{y}_m \sinh((a-x)\eta_m)}{\sinh a\eta_m} \int_0^b \left[T_W(y) + \frac{a_2}{a_1}\right] \sin \bar{y}_m \, dy \\ & + \frac{2}{b}\sum_{m=1}^{\infty} \frac{\sin \bar{y}_m \sinh(x\eta_m)}{\sinh a\eta_m} \int_0^b \left[T_E(y) + \frac{a_2}{a_1}\right] \sin \bar{y}_m \, dy \\ & - \frac{a_2}{a_1} \end{aligned} \tag{26}$$

Equation (26) describes the temperature field throughout the plate, except at the corner points. For example, for the boundary $x = 0$, Eq. (26) reduces to

$$T(0,y) = \frac{2}{b} \sum_{m=1}^{\infty} \sin \bar{y}_m \int_0^b \left[ T_W(y) + \frac{a_2}{a_1} \right] \sin \bar{y}_m \, dy - \frac{a_2}{a_1} \tag{27}$$

If $T_W(y)$ is constant, Eq. (27) further simplifies to

$$T(0,y) = 2\left(T_W + \frac{a_2}{a_1}\right) \sum_{m=1}^{\infty} \sin y_m \frac{(1 - \cos m\pi)}{m\pi} - \frac{a_2}{a_1} = T_W \tag{28}$$

and the sum

$$\sum_{m=1}^{\infty} \sin \bar{y}_m \frac{(1 - \cos m\pi)}{m\pi}$$

can be evaluated numerically. The series converges to a value of 0.5 but the convergence is quite slow, as shown in Fig. 3, where after 200 terms, the value of the series is 0.498. The series converges to a value of 0.5 even close to the plate corners, but the closer one approaches these corners, the slower the convergence is (see Fig. 4).

Our model of the antenna surface panels and their backup structure assumes that the bars placed at the edges of each panel receive heat from the panels by conduction only. This means that we must calculate the heat flux $\phi$ at each edge, where

$$\phi_z = \frac{\partial T}{\partial x} + \frac{\partial T}{\partial y} \tag{29}$$

Using Eq. (26) and Leibnitz's rule, these edge fluxes are calculated as follows:

$$\phi_{y=0} = \frac{2}{a} \left[ \sum_{m=1}^{\infty} \frac{m\pi}{a} \left\{ \sin \bar{x}_m \int_0^a \overline{T}_S \cos \bar{x}_m \, dx + \cos \bar{x}_m \int_0^a \overline{T}_S \sin \bar{x}_m \, dx \right\} + \sin \bar{x}_m \int_0^a \sin \bar{x}_m \frac{\partial \overline{T}_S}{\partial x} \, dx \right]$$

$$+ \frac{2}{a} \left[ \sum_{m=1}^{\infty} \frac{-\gamma_m \sin \bar{x}_m}{\tanh b\gamma_m} \int_0^a \overline{T}_S \sin \bar{x}_m \, dx \right]$$

$$+ \frac{2}{a} \left[ \sum_{m=1}^{\infty} \frac{\gamma_m \sin \bar{x}_m}{\sinh b\gamma_m} \int_0^a \overline{T}_N \sin \bar{x}_m \, dx \right]$$

$$+ \frac{2}{b} \left[ \sum_{m=1}^{\infty} \frac{m\pi}{b} \frac{\sinh((a - x_m)\eta_m)}{\sinh a\eta_m} \int_0^b \overline{T}_W \sin \bar{y}_m \, dy \right]$$

$$+ \frac{2}{b} \left[ \sum_{m=1}^{\infty} \frac{m\pi}{b} \frac{\sinh x\eta_m}{\sinh a\eta_m} \int_0^b \overline{T}_E \sin \bar{y}_m \, dy \right] \tag{30}$$

$$\phi_{y=b} = \frac{2}{a} \left[ \sum_{m=1}^{\infty} \frac{m\pi}{a} \left\{ \sin \bar{x}_m \int_0^a \overline{T}_N \cos \bar{x}_m \, dx + \cos \bar{x}_m \int_0^a \overline{T}_N \sin \bar{x}_m \, dx \right\} + \sin \bar{x}_m \int_0^a \sin \bar{x}_m \frac{\partial \overline{T}_N}{\partial x} \, dx \right]$$

$$+ \frac{2}{a} \left[ \sum_{m=1}^{\infty} \frac{\gamma_m \sin \bar{x}_m}{\tanh b\gamma_m} \int \overline{T}_N \sin \bar{x}_m \, dx \right]$$

$$+ \frac{2}{a} \left[ \sum_{m=1}^{\infty} \frac{-\gamma_m \sin \bar{x}_m}{\sinh b\gamma_m} \int \overline{T}_S \sin \bar{x}_m \, dx \right]$$

$$+ \frac{2}{b} \left[ \sum_{m=1}^{\infty} \frac{m\pi}{b} \frac{\sinh((a - x)\eta_m)}{\sinh a\eta_m} (-1)^m \int \overline{T}_W \sin y_m \, dy \right]$$

$$+ \frac{2}{b} \left[ \sum_{m=1}^{\infty} \frac{m\pi}{b} \frac{\sinh x\eta_m}{\sinh a\eta_m} (-1)^m \int \overline{T}_E \sin \bar{y}_m \, dy \right] \tag{31}$$

$$\phi_{x=0} = \frac{2}{b} \left[ \sum_{m=1}^{\infty} \frac{m\pi}{b} \left\{ \sin \bar{y}_m \int_0^b \overline{T}_W \cos \bar{y}_m \, dy + \cos \bar{y}_m \int_0^b \overline{T}_W \sin \bar{y}_m \, dy \right\} \right.$$

$$+\sin\bar{y}_m \int_0^b \sin\bar{y}_m \frac{\partial \bar{T}_W}{\partial y}\, dy\Bigg]$$

$$+\frac{2}{b}\left[\sum_{m=1}^{\infty} \frac{-\eta_m \sin\bar{y}_m}{\tanh a\eta_m} \int_0^b \bar{T}_W \sin\bar{y}_m\, dy\right]$$

$$+\frac{2}{b}\left[\sum_{m=1}^{\infty} \frac{\eta_m \sin\bar{y}_m}{\sinh a\eta_m} \int_0^b \bar{T}_E \sin\bar{y}_m\, dy\right]$$

$$+\frac{2}{a}\left[\sum_{m=1}^{\infty} \frac{m\pi}{a} \frac{\sinh((b-y)\gamma_m)}{\sinh b\gamma_m} \int_0^a \bar{T}_S \sin\bar{x}_m\, dx\right]$$

$$+\frac{2}{a}\left[\sum_{m=1}^{\infty} \frac{m\pi}{a} \frac{\sinh\gamma_m y}{\sinh b\gamma_m} \int_0^a \bar{T}_N \sin\bar{x}_m\, dx\right] \qquad (32)$$

$$\phi_{x=a} = \frac{2}{b}\left[\sum_{m=1}^{\infty} \frac{m\pi}{b}\left\{\sin\bar{y}_m \int_0^b \bar{T}_E \cos\bar{y}_m\, dy\right.\right.$$

$$\left.+\cos\bar{y}_m \int_0^b \bar{T}_E \sin\bar{y}_m\, dy\right\}$$

$$+\sin\bar{y}_m \int_0^b \sin\bar{y}_m \frac{\partial T_E}{\partial y}\, dy\Bigg]$$

$$+\frac{2}{b}\left[\sum_{m=1}^{\infty} \frac{\eta_m \sin\bar{y}_m}{\tanh a\eta_m} \int_0^b \bar{T}_E \sin\bar{y}_m\, dy\right]$$

$$+\frac{2}{b}\left[\sum_{m=1}^{\infty} \frac{-\eta_m \sin\bar{y}_m}{\sinh a\eta_m} \int_0^b \bar{T}_W \sin\bar{y}_m\, dy\right]$$

$$+\frac{2}{a}\left[\sum_{m=1}^{\infty} \frac{m\pi}{b} \frac{\sinh((b-y)\gamma_m)}{\sinh b\gamma_m}(-1)^m \int_0^a \bar{T}_S \sin\bar{x}_m\, dx\right]$$

$$+\frac{2}{a}\left[\sum_{m=1}^{\infty} \frac{m\pi}{a} \frac{\sinh\gamma_m y}{\sinh b\gamma_m}(-1)^m \int_0^a \bar{T}_N \sin\bar{x}_m\, dx\right] \qquad (33)$$

In Eqs. (30) through (33), the following abbreviations were used:

$$\begin{aligned} \bar{T}_N &= T_N(x) + \frac{a_2}{a_1} \\ \bar{T}_S &= T_S(x) + \frac{a_2}{a_1} \\ \bar{T}_E &= T_E(x) + \frac{a_2}{a_1} \\ \bar{T}_W &= T_W(x) + \frac{a_2}{a_1} \end{aligned} \qquad (34)$$

## III. Summary

The purpose of this analysis is to determine the thermal influence of the antenna panels on the neighboring bars that make up the antenna backup structure. The problem analyzed is that of a flat rectangular plate under conductive, convective and radiative heat transfer. The plate is bounded by bars at its four edges. For arbitrary temperature boundary conditions we have determined the temperature distribution within the plate as well as the temperature flux at the edges. The analytical solutions are expressed in terms of trigonometric series. The panel heat fluxes at its edges represent, in turn, heat fluxes to or from the bars of the backup structure. Therefore, the interactions of fluxes obtained in this paper with fluxes from the bar model developed in Part I are necessary to develop the thermal behavior of the antenna reflector structure.

# References


1. Schonfeld, D., and Lansing, F. L., "Thermal Analysis of Antenna Backup Structure, Part I–Methodology Development," *TDA Progress Report 42-70*, Jet Propulsion Laboratory, Pasadena, Calif., Aug. 15, 1982.

2. Polozhiy, G. N., *Equations of Mathematical Physics*, Hayden Book Co., N.Y., 1967, p. 404.

3. Carnahan, B., Luther, H. A., and Wilkes, J. O., *Applied Numerical Methods*, J. Wiley & Sons, N.Y., 1969.

4. Carslaw, H. S., and Jaeger, J. C., *Conduction of Heat in Solids*, Oxford University Press, 1959, p. 169.

# List of Symbols

$a$ length of plate

$a_1$, $a_2$ coefficients in the generalized heat transfer equation

$b$ width of plate

F radiation shape factor

$h$ heat transfer coefficient

$I$ solar radiation intensity

$k$ thermal conductivity

$T$ absolute temperature

$\alpha$ solar radiative absorptance

$\epsilon$ radiative emittance

$\sigma$ Stefan-Boltzman constant

$\phi$ Flux from the edge of the plate

Subscripts

$a$ ambient

$c$ convective

$r$ radiative

**Table 1. Comparison of numerical and series results for conduction heat transfer only**

| | Temperature map in the plate–series solution | | | | | | | | | | |
|---|---|---|---|---|---|---|---|---|---|---|---|
| | $x/a$ | | | | | | | | | | |
| $y/b$ | 0.0 | 0.1 | 0.2 | 0.3 | 0.4 | 0.5 | 0.6 | 0.7 | 0.8 | 0.9 | 1.0 |
| 1.0 | 50.00 | 65.00 | 80.00 | 95.00 | 110.00 | 125.00 | 140.00 | 155.00 | 170.00 | 185.00 | 200.00 |
| 0.9 | 75.00 | 87.31 | 98.04 | 109.93 | 120.90 | 133.02 | 143.93 | 156.49 | 167.35 | 181.31 | 190.00 |
| 0.8 | 100.00 | 108.64 | 116.43 | 124.32 | 132.28 | 140.36 | 148.50 | 156.85 | 165.52 | 174.93 | 180.00 |
| 0.7 | 125.00 | 130.31 | 134.41 | 138.83 | 143.34 | 147.91 | 152.56 | 157.34 | 162.32 | 167.90 | 170.00 |
| 0.6 | 150.00 | 150.84 | 152.26 | 153.29 | 154.32 | 155.39 | 156.50 | 157.65 | 158.77 | 159.23 | 160.00 |
| 0.5 | 175.00 | 173.05 | 170.20 | 167.72 | 165.27 | 162.82 | 160.39 | 157.95 | 155.46 | 153.20 | 150.00 |
| 0.4 | 200.00 | 193.52 | 188.09 | 182.16 | 176.20 | 170.24 | 164.28 | 158.29 | 152.25 | 145.80 | 140.00 |
| 0.3 | 225.00 | 216.21 | 206.08 | 196.60 | 187.14 | 177.67 | 168.18 | 158.68 | 149.16 | 139.94 | 130.00 |
| 0.2 | 250.00 | 236.08 | 223.95 | 211.07 | 198.06 | 185.12 | 172.09 | 159.11 | 146.05 | 132.66 | 120.00 |
| 0.1 | 275.00 | 260.22 | 241.06 | 226.23 | 208.45 | 193.04 | 175.61 | 159.96 | 142.61 | 127.18 | 110.00 |
| 0.0 | 300.00 | 280.00 | 260.00 | 240.00 | 220.00 | 200.00 | 180.00 | 160.00 | 140.00 | 120.00 | 100.00 |
| | Temperature map in the plate–numerical solution | | | | | | | | | | |
| | $x/a$ | | | | | | | | | | |
| $y/b$ | 0.0 | 0.1 | 0.2 | 0.3 | 0.4 | 0.5 | 0.6 | 0.7 | 0.8 | 0.9 | 1.0 |
| 1.0 | 50.00 | 65.00 | 80.00 | 95.00 | 110.00 | 125.00 | 140.00 | 155.00 | 170.00 | 185.00 | 200.00 |
| 0.9 | 75.00 | 87.63 | 99.72 | 111.53 | 123.15 | 134.65 | 146.02 | 157.28 | 168.40 | 179.34 | 190.00 |
| 0.8 | 100.00 | 109.68 | 118.69 | 127.26 | 135.53 | 143.57 | 151.39 | 158.99 | 166.34 | 173.38 | 180.00 |
| 0.7 | 125.00 | 131.41 | 137.15 | 142.42 | 147.32 | 151.91 | 156.22 | 160.25 | 163.94 | 167.22 | 170.00 |
| 0.6 | 150.00 | 152.94 | 155.28 | 157.15 | 158.64 | 159.80 | 160.64 | 161.14 | 161.26 | 160.92 | 160.00 |
| 0.5 | 175.00 | 174.33 | 173.15 | 171.55 | 169.59 | 167.31 | 164.70 | 161.73 | 158.36 | 154.49 | 150.00 |
| 0.4 | 200.00 | 195.62 | 190.83 | 185.69 | 180.24 | 174.49 | 168.44 | 162.05 | 155.26 | 147.95 | 140.00 |
| 0.3 | 225.00 | 216.82 | 208.34 | 199.60 | 190.61 | 181.38 | 171.89 | 162.10 | 151.94 | 141.30 | 130.00 |
| 0.2 | 250.00 | 237.94 | 225.70 | 213.28 | 200.70 | 187.95 | 175.00 | 161.83 | 148.37 | 134.49 | 120.00 |
| 0.1 | 275.00 | 259.00 | 242.92 | 226.76 | 210.51 | 194.17 | 177.73 | 161.17 | 144.44 | 127.45 | 110.00 |
| 0.0 | 300.00 | 280.00 | 260.00 | 240.00 | 220.00 | 200.00 | 180.00 | 160.00 | 140.00 | 120.00 | 100.00 |

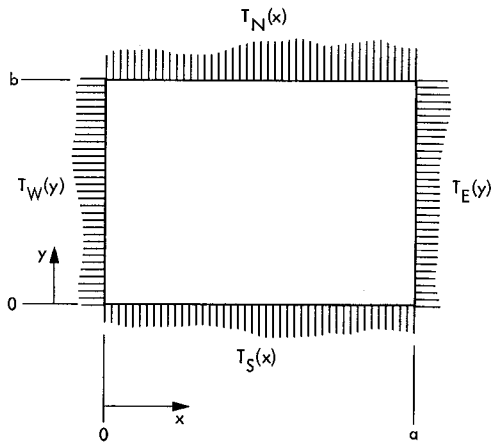


**Fig. 1. Geometry of panel analyzed**

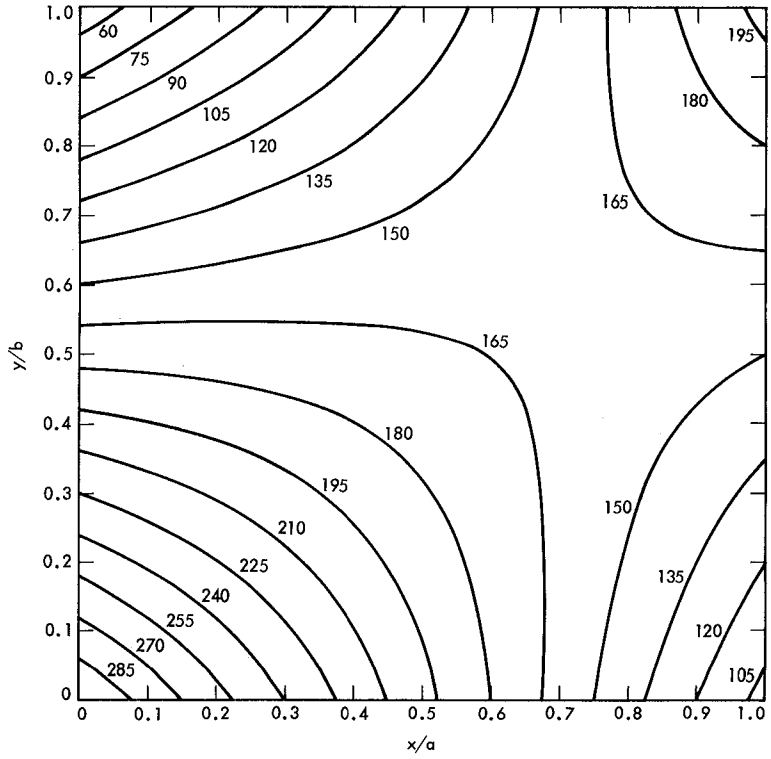


**Fig. 2. Isotherms in a plate with conduction heat transfer only**

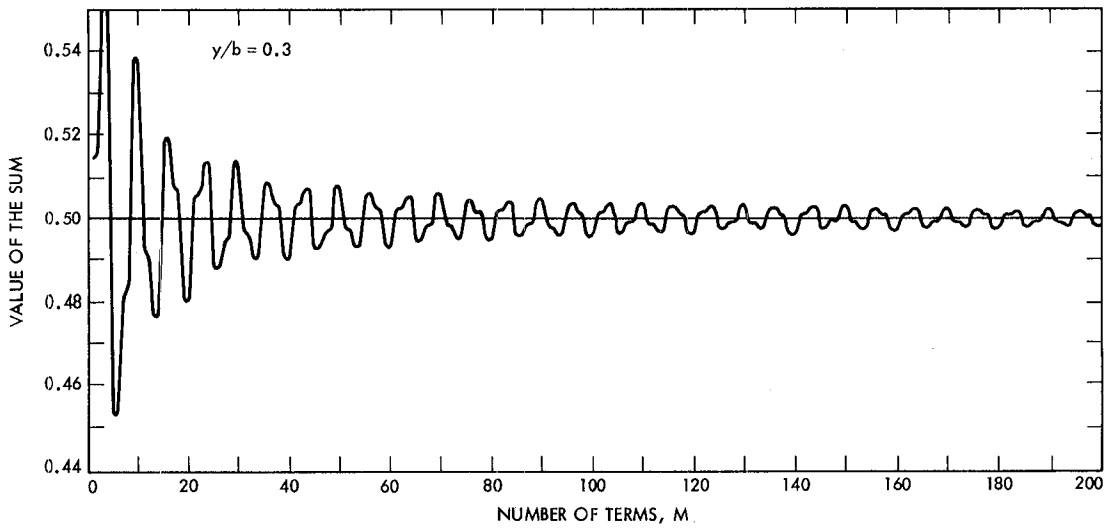


**Fig. 3. Series convergence for $y/b = 0.3$**

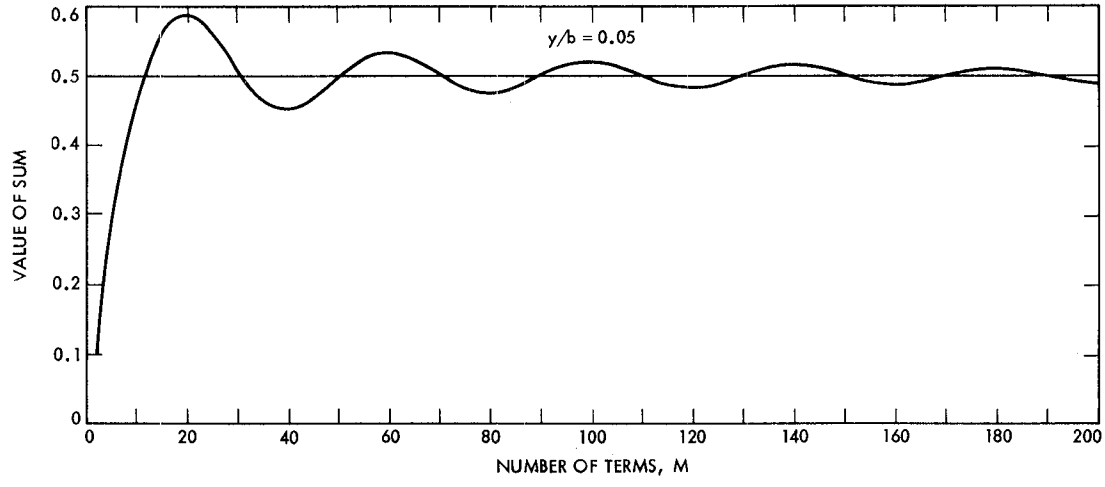


**Fig. 4. Series convergence for $y/b = 0.05$**

# New Syndrome Decoding Techniques for the (n, k) Convolutional Codes

I. S. Reed
Department of Electrical Engineering
University of Southern California

T. K. Truong
Communications Systems Research Section

*This paper presents a new syndrome decoding algorithm for the (n, k) convolutional codes (CC) which differs completely from an earlier syndrome decoding algorithm of Schalkwijk and Vinck. The new algorithm is based on the general solution of the syndrome equation, a linear Diophantine equation for the error polynomial vector E(D). The set of Diophantine solutions is a coset of the CC. In this error coset a recursive, Viterbi-like algorithm is developed to find the minimum weight error vector $\hat{E}(D)$. An example, illustrating the new decoding algorithm, is given for the binary nonsystemmatic (3, 1) CC.*

## I. Introduction

In this paper, a new syndrome decoding algorithm is developed which is analogous to the syndrome decoding algorithm of block codes. This new decoding method differs completely from that invented in 1976 by Schalkwijk and Vinck (Ref. 1).

In order to develop the new syndrome decoding algorithm it is necessary to first review and further treat the algebraic nature and structure of convolutional codes (CC). This background is then used to find the general solution of the syndrome equations for the error polynomial vector $e(D)$ where $D$ is the unit delay operator. In particular it is shown that these syndrome equations are linear Diophantine equations over the ring of polynomials $F[D]$ in $D$ and with coefficients in a finite field. The method for solving linear Diophantine equations for the integers is generalized and used to solve the syndrome equations for $e(D)$.

The set of Diophantine solutions of the syndrome equations constitutes a coset of the convolutional code space or group. The problem of syndrome decoding is to find the minimum-weight polynomial vector $\hat{e}(D)$ of this coset to subtract from the received polynomial vector $z(D)$ to yield an estimate $\hat{y}(D)$ of the transmitted polynomial vector. In order to find $\hat{e}(D)$ efficiently, a new recursive, Viterbi-like algorithm is devised. This new syndrome decoding algorithm is presented in this paper by example.

For a fixed convolutional code the new recursive syndrome decoder for a CC appears to be comparable in complexity to the Viterbi decoder except that in the new decoder fewer comparisons are required and the control logic is considerably simpler. However, if one wishes to design a CC decoder for several different rate codes of the same constraint length, it appears that the principles of the new syndrome decoder may yield a simpler system than could be achieved using the Viterbi

technique. For variable rate communication systems that utilize convolutional codes the new syndrome decoding concept appears to have an advantage over the standard Viterbi decoding techniques. A precise quantification of this comparison is a topic for future study.

## II. Algebraic Structure of Convolutional Codes

Let $a_0, a_1, a_2, \cdots$ be any sequence of symbols from the finite field $F = GF(q)$ of $q$ elements. Further let $D$ be the unit delay operator. $D$ operates on a function $x(n)$ of discrete time $n$ in accordance with the definition

$$D\,x(n) = x(n-1) \tag{1}$$

for all $n$. In terms of $D$ the sequence $\{a_j\}$ is conveniently represented by what is called its $D$-transform,

$$A(D) = a_0 + a_1 D + a_2 D^2 + \cdots, \tag{2}$$

in powers of the operator $D$.

The input to a convolutional encoder is a set of $k$ discrete-time input sequences. In terms of $D$-transforms this input is represented by the vector

$$x(D) = [x_1(D), x_2(D), \cdots, x_k(D)] \tag{3}$$

where $x_j(D) = x_{0j} + x_{1j} D + x_{2j} D^2 + \cdots$ for $(j = 1, 2, \cdots, k)$ with coefficients in $GF(q)$. (see Refs. 2, 3).

Very simply, an encoder for a CC is some *linear* sequential circuit over the finite field $GF(q)$ with vector input $x(D)$ and vector output

$$y(D) = [y_1(D), y_2(D), \cdots, y_n(D)] \tag{4}$$

where $n > k$ and $y_r(D) = y_{0r} + y_{1r} D + y_{2r} D^2 + \cdots$ for $1 \leqslant r \leqslant n$. For the standard $(n, k)$ convolutional code ($(n, k)$ *CC*) the linear relationship between the input and output is assumed to have finite memory so that it can be expressed as a matrix convolution of form

$$y(D) = x(D)\,G(D) \tag{5}$$

where $G(D)$ is a $k \times n$ matrix of polynomials of finite degree in $D$ over $GF(q)$. $G(D)$ in (5) is usually called the generating matrix of the $(n, k)$ *CC* of $k/n$ rate *CC*. $G(D)$ has the specific form, as a $k \times n$ matrix,

$$G(D) = \begin{bmatrix} g_{11}(D), & g_{12}(D), \cdots, & g_{1n}(D) \\ g_{21}(D), & g_{22}(D), \cdots, & g_{2n}(D) \\ \cdot & \cdot & \cdot \\ \cdot & \cdot & \cdot \\ \cdot & \cdot & \cdot \\ g_{k1}(D), & g_{k2}(D), \cdots, & g_{kn}(D) \end{bmatrix} \tag{6}$$

The maximum degree $M$ of the polynomials in $G(D)$ is called the *memory*, and the constraint length of the code is $L = M + 1$.

The elements of $G(D)$ in (6) are polynomials in $D$ over the finite field $F = GF(q)$. The set of all such polynomials in $D$ over a field $F$ is an infinite ring $F[D]$ as well as an integral domain since it has no divisors of zero. It can also be demonstrated that $F[D]$ is a Euclidean ring, e.g., see Ref. 4, sections 3.7 and 3.9.

If the elements of $G(D)$ in (6) are restricted to members of field $F$, the rows of $G(D)$ generate an $n$-dimensional vector space over field $F$. However, since $G(D)$ is a $k \times n$ matrix with elements in $F[D]$, the integral domain in $D$ over $F$, $G(D)$ generates what is called a *module* over the ring $F[D]$. A module has the same postulates as a vector space except that its scalars are elements of a ring rather than a field.

To characterize the algebraic properties of different generating matrices $G(D)$ over integral domain $F[D]$ we follow the lead of Forney in Ref. 3. Forney bases his study of CC on the well-known invariant-factor theorem of matrices over an integral domain. The statement of this theorem is reproduced for ring $F[D]$ as follows:

*Invariant-Factor Theorem*: If $F[D]$ is the integral domain and $G(D)$ is a $k \times n$ matrix over $F[D]$, then $G$ has the invariant-factor decomposition or Smith normal form[1],

$$G(D) = A(D)\,\Gamma(D)\,B(D) \tag{7}$$

where $A(D)$ is a $k \times k$ matrix over $F[D]$ with an inverse $A^{-1}(D)$ with elements in $F[D]$; $B(D)$ is a $n \times n$ matrix over $F[D]$ also with an inverse $B^{-1}(D)$ with elements in $F[D]$; and $\Gamma(D)$ is a $k \times n$ matrix over $F[D]$ of form

$$\Gamma(D) = [\Gamma_1(D), 0] \tag{8}$$

[1]The invariant-factor theorem was developed by the British mathematician H. J. S. Smith in the middle of the 19th century.

with 0, a $k \times (n-k)$ matrix of zeros and $\Gamma_1(D)$ a diagonal matrix

$$\Gamma_1(D) = \text{diag}\,[\gamma_1(D), \gamma_2(D), \cdots, \gamma_k(D)] \tag{9}$$

The diagonal elements $\gamma_i(D)$ in (9) for $1 \leqslant i \leqslant k$ are elements of $F[D]$ and are called the invariant factors of $G(D)$. The invariant factors are unique and can be computed as follows: Let $\Delta_0 = 1$. Let $\Delta_i$ be the greatest common divisor (GCD) of all $i \times i$ subdeterminants (minors) of $G$. Then $\gamma_i(D) = \Delta_i/\Delta_{i-1}$. If $\gamma_{i+1}(D) \neq 0$, then $\gamma_i(D)$ divides $\gamma_{i+1}(D)$ for $i = 1, 2, \cdots, k-1$.

Forney in Ref. 3 sketches a proof of this theorem. Other more elementary and detailed expositions of this theorem can be found in certain classic works on modern algebra, e.g., see Ref. 5, Sec. 10, Ch. III. Rather than give a proof of this theorem it is perhaps better to illustrate its use with an example.

For an example let $F = GF(2)$ and consider the generating matrix,

$$G(D) = G = \begin{bmatrix} 1 & 1+D & 1+D \\ 1+D & D & 0 \end{bmatrix} = A \begin{bmatrix} \gamma_1(D) & 0 & 0 \\ 0 & \gamma_2(D) & 0 \end{bmatrix} B \tag{10}$$

where $A$ is a $2 \times 2$ matrix and $B$ is a $3 \times 3$ matrix, both over $F[D]$. It is shown in Appendix A that the invariant-factor decomposition or Smith normal form of $G(D)$ in (10) is

$$G(D) = A\Gamma B = \begin{bmatrix} 1 & 0 \\ 1+D & 1 \end{bmatrix} \begin{bmatrix} 1 & 0 & 0 \\ 0 & 1 & 0 \end{bmatrix} \begin{bmatrix} 1 & 1+D & L+D \\ 0 & 1+D+D^2 & 1+D^2 \\ 0 & 1+D & D \end{bmatrix} \tag{11}$$

Let the generating matrix of a CC have the invariant-factor decomposition in (7). Then the output of the encoder in (5) can be expressed as

$$y(D) = x(D)G(D) = x(D)A(D)\Gamma(D)B(D) \tag{12}$$

where $A(D)$ and $B(D)$ have inverses $A^{-1}(D)$ and $B^{-1}(D)$, respectively, and $\Gamma(D)$ is the $k \times n$ matrix defined in (8).

For the encoding operation in (12) to be useful in the context of a communications system it is desirable that the mapping of $k$-vectors $x(D)$ onto $n$-vectors $y(D)$ over $F[D]$ be one-to-one and reversible. For this to be true there must exist a right inverse matrix $G^{-1}(D)$ of matrix $G(D)$. If $G^{-1}(D)$ exists, then

$$y(D)G^{-1}(D) = x(D)G(D)G^{-1}(D) = x(D)I_k = x(D) \tag{13}$$

where $I_k$ is the $k \times k$ identity matrix and $x(D)$ is uniquely recoverable from the encoded message $y(D)$. It will be assumed henceforth that the generating matrix $G(D)$ has a right inverse and that this inverse is realizable in finite delay time.

By the invariant-factor theorem $G(D) = A(D)\Gamma(D)B(D)$. Thus for $G^{-1}(D)$ to exist uniquely the last invariant factor of $\Gamma(D)$ must not be zero, i.e., $\gamma_k(D) \neq 0$. For otherwise, if $\gamma_k(D) = 0$, then $G(D)$ would have rank less than $k$ and as a consequence $G^{-1}(D)$ would be nonunique.

If $\gamma_k(D) \neq 0$, then it can be verified that

$$G^{-1}(D) = B^{-1}(D)\Gamma^*(D)A^{-1}(D) \tag{14}$$

is the right inverse of $G(D)$ where $\Gamma^*(D)$ is an $n \times k$ matrix with diagonal elements $\gamma_i^{-1}(D)$ of form

$$\Gamma^*(D) = \begin{bmatrix} \Gamma_1^*(D) \\ 0 \end{bmatrix} \tag{15}$$

with $\Gamma_1^*(D)$ the inverse of $\Gamma_1(D)$ in (9); i.e.,

$$\Gamma_1(D) = \text{diag}\,[\gamma_1^{-1}(D), \gamma_2^{-1}(D), \cdots, \gamma_k^{-1}(D)] \tag{16}$$

If deg $\gamma_k(D) > 0$, then by (16), (15) and (14) the circuit to realize (13) would not be feedback-free.

Massey and Sain (Ref. 6) proved that an inverse $G^{-1}(D)$ or some delayed version of it must be feedback-free in order to avoid CC that give rise to catastrophic error propagation. To avoid this problem it is desirable to make $G^{-1}(D)$ feedback-free. If $G^{-1}(D)$ is feedback-free, deg $\gamma_k(D) = 0$ and $\gamma_1(D) = \gamma_2(D), \cdots, \gamma_k(D) = 1$. Hence $\Gamma(D)$ must have the form

$$\Gamma(D) = [I_k, 0] \tag{17}$$

where $I_k$ denotes a $k \times k$ identity matrix and 0 denotes a $k \times (n-k)$ matrix of zeros.

The above properties needed for a useful encoder are recapitulated in the following definition of a basic encoder given by Forney (Ref. 3).

*Definition*: A *basic* encoder $G(D)$ is a CC with a feedback-free right inverse $G^{-1}(D)$. Both $G(D)$ and $G^{-1}(D)$ are polynomial matrices over $F[D]$ such that $G(D)G^{-1}(D) = I_k$.

It was shown in detail by Forney (Ref. 3) and briefly above that an encoder is basic if and only if it is polynomial over $F[D]$ and has all its invariant factors equal to one. Henceforth in this paper only basic encoders for a CC will be treated so that by (17) and the invariant-factor theorem the generating matrix for an $(n, k)$ CC has the form

$$G(D) = A(D)\,[I_k, 0]\,B(D) \tag{18}$$

where $I_k$ is the $k \times k$ identity matrix.

Forney [Ref. 3, Appendix I] exhibits a parity-check matrix $H(D)$ over $F[D]$ for a generating matrix which is equivalent to $G(D)$ in (18). It is shown here that this parity-check matrix is, in fact, the parity-check matrix of all generating matrices equivalent to (18) in the sense of Forney.

To treat the parity-check matrix the Euclidean ring $F[D]$ is extended to the field $F(D)$ of quotients or rational functions of polynomials in $F[D]$; e.g., see Ref. 5, Sec. 3.8. In terms of sequences field $F(D)$ is in one-to-one correspondence with the field $S$ of all possible infinite sequences that can be generated by an impulse passed through all finite memory linear circuits with or without feedback.

Let $g^{(1)}(D), g^{(2)}(D), \cdots, g^{(k)}(D)$ be the $k$ rows of matrix $G(D)$ in (18). Since $G(D)$ has rank $k$,

$$V = \left\{ \sum_{i=1}^{k} \alpha_j(D)\, g^{(i)}(D) \mid \alpha_j(D) \in F(D) \right\}$$

is a $k$-dimensional vector space with respect to the field $F(D)$ of scalars of its equivalent, to the field $S$ of sequences. The null space $V^{\perp}$ of $V$ is a vector space with field $F(D)$ of scalars of dimension $n-k$ (see [Ref. 7, Sec. 3.2]).

Let $H(D)$ be a matrix with coefficients in $F[D] \subset F(D)$ of rank $n-k$ which has its row space equal to $V^{\perp}$. Evidently any set of basis vectors in $V^{\perp}$ can be used to find $H(D)$ with components in $F[D]$. The rows of $H(D)$, found by this means, constitute a basis for $V^{\perp}$. Thus $V$ is a null space of $V^{\perp}$ if and only if for any vector, $y(D) \in V$,

$$y(D)\,H^T(D) = 0 \tag{19}$$

Since $g^{(j)}(D) \in V$ for $1 \leqslant j \leqslant k$ condition (19) implies,

$$G(D)\,H^T(D) = 0 \tag{20}$$

An explicit method due to Forney (Ref. 3, Appendix I) for constructing a parity matrix $H(D)$ of all generating matrices $G(D)$ with form (18) is now given. The coefficients of the parity-check matrix $H(D)$, developed by this technique, are polynomials in $D$, i.e., elements from the Euclidean ring $F[D]$.

Let the first $k$ rows of matrix $G$ in (18) be a submatrix $B_1$ and the last $(n-k)$ rows of $B$ be a submatrix $B_2$. Then $B$ is the matrix

$$B = [B_1, B_2]^T \tag{21}$$

in terms of submatrices $B_1$ and $B_2$. Similarly denote the first $k$ columns of the inverse matrix $B^{-1}$ of $B$ by $B'_1$ and denote the last $(n-k)$ columns of $B^{-1}$ by $B'_2$. Then the inverse of $B$ is the matrix

$$B^{-1} = [B'_1, B'_2] \tag{22}$$

Multiplying (21) and (22) yields

$$BB^{-1} = \begin{bmatrix} B_1B'_1, & B_1B'_2 \\ B_2B'_1, & B_2B'_2 \end{bmatrix} = \begin{bmatrix} I_k, & 0 \\ 0, & I_{n-k} \end{bmatrix} \tag{23}$$

and the matrix identities,

$$\begin{aligned} B_1B'_1 &= I_k, & B_1B'_2 &= 0; \\ B_2B'_1 &= 0, & B_2B'_2 &= I_{n-k}. \end{aligned} \tag{24}$$

Let

$$H(D) = (B'_2)^T, \tag{25}$$

where $T$ denotes transpose and $B'_2$ is defined in (22), be a candidate for the parity-check matrix of $G(D)$ in (18). Multi-

plying $G(D)$ in (18) by the transpose of $H(D)$ in (25) produces by (21) and (24),

$$G(D)\,H^T(D) = A\,[I_k, 0]\,[B_1, B_2]^T B_2' = [A, 0]\,[0, I_{n-k}]^T = 0 \tag{26}$$

Since the $n - k$ rows of $H(D)$ are the $n - k$ columns of the invertible matrix $B^{-1}(D)$, these rows must be linearly independent. Thus $H(D)$, as defined in (25), has rank $(n - k)$ and is a valid parity-check matrix for the general basic encoder $G(D)$, given in (18). $H(D)$ is clearly not unique since a matrix of form $H_1(D) = H(D)\,C(D)$, where $C(D)$ is a nonsingular matrix with elements in $F[D]$, is also a parity check matrix.

A parity-check matrix $H(D)$, associated with the general $k \times n$ generator matrix $G(D)$ of a basic encoder, is given by (25). However, for two special cases, the systematic $(n, k)$ CC and the nonsystematic $(n, 1)$ CC, a parity-check matrix can be found more directly. For example, for the systematic $(n, k)$ CC the parity-check matrix has form $G(D) = [I_k, P(D)]$ where $I_k$ is the $k \times k$ identity matrix and $P(D)$ is a $k \times (n - k)$ matrix of polynomials over $F = GF(q)$. In this case it is readily verified (Ref. 7) that $H(D) = [-P^T(D), I_{n-k}]$ is a parity-check matrix.

The generator matrix for the nonsystematic $(n, 1)$ CC has by (6) the form

$$G(D) = [g_1(D), g_2(D), \cdots, g_n(D)] \tag{27}$$

where for simplicity the first subscript of $g_{1j}(D)$ has been dropped. Condition (20) for the $(1 \times n)$ generating matrix $G(D)$ in (27) is easily shown to be satisfied by the $(n - 1) \times n$ matrix

$$H(D) = [L(D), R(D)] \tag{28}$$

where $L(D) = [g_2(D), g_3(D), \cdots, g_n(D)]^T$ and $R(D) = \text{diag}\,[g_1(D), g_2(D), \cdots, g_n(D)]$, so that it is a parity-check matrix of the $(n, 1)$ CC generated by $G(D)$ in (27).

To illustrate how to use (25) to compute a parity-check matrix consider again the example of a generating matrix, given in (10). By (A-2) in Appendix A the matrix $B^{-1}$ for this $G$ is

$$B^{-1} = \begin{bmatrix} 1 & 1+D & D+D^2 \\ 0 & D & 1+D^2 \\ 0 & 1+D & 1+D+D^2 \end{bmatrix} \tag{29}$$

so that by (22) and (25)

$$H(D) = (B_2')^T = [D+D^2, 1+D^2, 1+D+D^2], \tag{30}$$

the transpose of the last column of $B^{-1}$ in (29). It is easily verified that (30) satisfies (20), i.e., $G(D)\,H^T(D) = 0$, and that $H(D)$ is of rank one. Hence $H(D)$ in (30) is the parity-check matrix of the (3, 2) CC with generating matrix $G(D)$ in (10).

In the next section the parity-check matrix will be used to obtain the syndrome of the received CC. A new decoding algorithm will then be presented by example.

## III. Solutions of the Syndrome Equation for Convolutional Codes

Let $y(D)$ be transmitted CC in accordance with (5) where $G(D)$ is the generating matrix for a basic encoder. Next let $z(D) = y(D) + e(D)$ be the received code possibly corrupted by an error or noise sequence $e(D)$. The *syndrome* $s(D)$ of $z(D)$ is defined by

$$s(D) = z(D)\,H^T(D) \tag{31}$$

where $H(D)$ is syndrome (28) for the basic encoder.

Substituting (5) in syndrome (31) yields

$$s(D) = (y(D) + e(D))\,H^T(D) = e(D)\,H^T(D) + x(D)\,G(D)\,H^T(D) \tag{32}$$

But by construction (20) is satisfied; i.e., $G(D)\,H^T(D) = 0$. Hence the last term of (32) vanishes and

$$s(D) = e(D)\,H^T(D) \tag{33}$$

is the syndrome in terms of an error sequence or polynomial $e(D)$. The syndrome for a basic $(n, k)$ CC is by (33) totally independent of the transmitted coded message $y(D)$. Syndromes for block group codes also have this property so that

one might suspect that it is possible to use syndromes to decode CC in a manner similar to that used for block codes.

The first step towards achieving this goal for CC is to find the general solution for $e(D)$ of the syndrome equation (33), assuming that $s(D)$ is computed by (31). That is, given $s(D)$ by (31), solve for the set of all solutions $e(D)$ of the syndrome equation (33).

To find the general solution of (33) again use is made of the important invariant-factor theorem of the last section. This theorem is applied to the transpose of the parity-check matrix, $H^T(D)$ in (33). By construction the rank of $H(D)$ is $n - k$, the maximum possible rank. By the invariant-factor theorem

$$H(D) = R^T(D)\,[\Lambda, 0]\,L^T(D) \tag{34}$$

where $L(D)$ and $R(D)$ are invertible $n \times n$ and $(n-k) \times (n-k)$ matrices over $F(D)$,

$$\Lambda = \text{diag}\,(\lambda_1, \lambda_2, \cdots, \lambda_{n-k}) \tag{35}$$

and "0" denotes a $k \times (n-k)$ matrix of zeros. The $\lambda_j$'s in (35) are the invariant factors defined as follows: Let $\delta_0 = 1$, let $\delta_j$ be the *GCD* of all $j \times j$ minors of $H(D)$. Then $\lambda_j = \delta_j/\delta_{j-1}$ and $\lambda_j$ divides $\lambda_{j+1}$ for $j = 1, 2, \cdots, n-k-1$. Hence the transpose of $H(D)$ in (34) has the Smith normal form

$$H^T(D) = L(D)\,[\Lambda, 0]^T\,R(D) \tag{36}$$

A lemma, due to Forney (Ref. 3, Appendix I), is used to evaluate the diagonal matrix $\Lambda$ of invariant factors in (36). In the present terminology this lemma is stated as follows:

*Lemma (Forney)*: The $(n-k) \times (n-k)$ minors of $H(D)$ are equal up to scalar field elements in $F = GF(q)$ to the $k \times k$ minors of $G(D)$.

Since the basic encoder has a generating matrix $G(D)$ of form (18), the $k \times k$ minors of $G(D)$ have a *GCD* equal to 1. Hence by Forney's lemma the $(n-k) \times (n-k)$ minors of $H(D)$ also have a *GCD* equal to 1. Thus $1 = \delta_{n-k} = \delta_{n-k-1} = \cdots = \delta_1$ and the invariant factors of $H^T(D)$ are all 1. Therefore, $\Lambda = I_{n-k}$ and by (36)

$$H^T(D) = L(D)\,[I_{n-k}, 0]^T\,R(D) \tag{37}$$

is the Smith normal form of the transpose of a parity-check matrix for a basic encoder.

To solve for $e(D)$ first substitute expression (37) for $H^T(D)$ into (33). This yields

$$s(D) = e(D)\,L(D)\,[I_{n-k}, 0]^T\,R(D) \tag{38}$$

Next multiply both sides of (38) by $R^{-1}(D)$ to obtain

$$\sigma(D) = s(D)\,R^{-1}(D) = [e(D)\,L(D)]\,[I_{n-k}, 0]^T = \epsilon(D)\,[I_{n-k}, 0]^T \tag{39}$$

where

$$\sigma(D) = s(D)\,R^{-1}(D) = [\sigma_1(D), \cdots, \sigma_{n-k}(D)] \tag{40}$$

is an $(n-k)$-component transformed vector of $S(D)$ and

$$\epsilon(D) = e(D)\,L(D) = [\epsilon_1(D), \cdots, \epsilon_n(D)] \tag{41}$$

is an $n$-component transformed vector of the unknown polynomial error vector $e(D)$.

The component-by-component solution of (39) is obtained by equating components of the equation

$$\epsilon_j(D) = \sigma_j(D) \quad \text{for} \quad 1 \leqslant j \leqslant n-k \tag{42a}$$

and

$$\epsilon_j(D) = t_{j-n+k}(D) \quad \text{for} \quad n-k+1 \leqslant j \leqslant n \tag{42b}$$

where $t_i(D)$ for $1 \leqslant i \leqslant k$ is an arbitrary polynomial in the Euclidean ring $F[D]$.

Substituting (42a) and (42b) into the right side of (41) and solving for $e(D)$ yields finally

$$\begin{aligned} e(D) &= [e_1(D), \cdots, e_n(D)] \\ &= [\sigma_1(D), \cdots, \sigma_{n-k}(D), t_1(D), \cdots, t_k(D)] \\ &\quad L^{-1}(D) \end{aligned} \tag{43}$$

as the general solution of the syndrome equation (33) in terms of the $n-k$ components of the transformed syndrome $\sigma(D)$ in (39) and $k$ arbitrary polynomials parameters $t_j(D)$ of $F[D]$ for $1 \leqslant j \leqslant k$.

Some examples of the above technique for solving the linear Diophantine equations of the syndrome equation are now presented. Consider first the generating matrix

$$G(D) = [1+D^2, 1+D+D^2, 1+D+D^2] \tag{44}$$

of a (3, 1) CC with constraint length 3. Using the Forney method developed in the last section a parity-check matrix for $G(D)$ is readily calculated to be

$$H(D) = \begin{bmatrix} 1+D+D^2, & 1+D^2, & 0 \\ 1+D+D^2, & D^2, & 1 \end{bmatrix} \tag{45}$$

The Smith normal form for $H^T(D)$ is given by

$$H^T(D) = L \begin{bmatrix} 1 & 0 & 0 \\ 0 & 1 & 0 \end{bmatrix}^T \tag{46}$$

where the inverse of $L$ is

$$L^{-1} = \begin{bmatrix} D & 1+D & D \\ 0 & 0 & 1 \\ 1+D^2 & 1+D+D^2 & 1+D+D^2 \end{bmatrix} \tag{47}$$

Substituting (45) and (31) the syndrome is $s(D) = z(D)H^T(D)$. Hence by (33) and (46) the syndrome equation to solve is

$$s(D) = [s_1(D), s_2(D)] = ([e_1(D), e_2(D), e_3(D)]\, L) \begin{bmatrix} 1 & 0 & 0 \\ 0 & 1 & 0 \end{bmatrix}^T$$

$$= [\epsilon_1(D), \epsilon_2(D), \epsilon_3(D)] \begin{bmatrix} 1 & 0 & 0 \\ 0 & 1 & 0 \end{bmatrix}^T \tag{48}$$

By (42a, b) the solution of (48) for $\epsilon_j(D)$ is

$$\epsilon_1(D) = s_1(D), \epsilon_2(D) = s_2(D), \epsilon_3(D) = t(D) \tag{49}$$

where $t(D)$ is an arbitrary element of $F[D]$. Finally the $e_i(D)$ in terms of the solutions (49) is, using (47), $[e_1(D), e_2(D), e_3(D)] = [s_1(D), s_2(D), t(D)]\, L^{-1}$. This yields

$$\begin{aligned} e_1(D) &= Ds_1(D) + (1+D^2)t(D) \\ e_2(D) &= (1+D)s_1(D) + (1+D+D^2)t(D) \\ e_3(D) &= DS_1(D) + s_2(D) + (1+D+D^2)t(D) \end{aligned} \tag{50}$$

as the general solution of the syndrome equation (31) for the (3, 1) encoder in (44).

Another example of the general method for finding the general solutions of the syndrome equation is given in Appendix B for the (3, 2) CC with generating matrix (10). It is shown in the next section by an example how to use the solutions of the syndrome equation to perform optimum syndrome decoding.

## IV. Syndrome Decoding of (n,k) CC

Syndrome decoding of an $(n, k)$ CC involves finding a maximum likelihood estimate (MLE) $\hat{e}(D)$ of the actual error sequence in the coset, determined by (43), of all possible solutions of the syndrome equation (31). In order to accomplish this, both the weight or distance between codewords of a sequence and the type of channel need to be defined. For an $(n, k)$ CC a possible error sequence is of form $e(D) = [e_1(D), e_2(D), \cdots, e_n(D)]$ where $e_j(D)$ for $1 \leqslant j \leqslant n$ are finite degree polynomials over $GF(q)$. The usual weight for a discretized channel is the Hamming weight. The Hamming weight of $e(D)$ is

$$W_H[e(D)] = \sum_{j=1}^{n} W_H[e_j(D)] \tag{51}$$

where $W_H[e_j(D)]$, the Hamming weight of $e_j(D)$, is the number of nonzero coefficients of $e_j(D)$. It is convenient for this weight to assume that the channel can be approximated by a $q$-ary channel (see Ref. 2, Sec. 7.2).

If in (3) deg $[x_j(D)] \leqslant L-1$ for $1 \leqslant j \leqslant k$, codeword $y(D) = (y_1(D), y_2(D), \cdots, y_n(D))$ is said to be the $L$th truncation of an $(n, k)$ CC (see Ref. 2, p. 203). In this case

$$\deg [y_i(D)] \leqslant M + L - 1 \quad \text{for } 1 \leqslant i \leqslant n \tag{52}$$

where $M$ is the memory. Hence an $L$ truncated $(n, k)$ CC can be considered to be a block code where each word has length $n(L+M)$. Hence for a truncated $(n, k)$ CC the MLE of an error vector is what it would be for a linear block code. For a truncated $(n, k)$ CC transmitted over a $q$-ary symmetric channel the MLE of $e(D)$ is any vector $e(D)$ of form (43) such that

$$W_H[\hat{e}(D)] = \min_{t_1(D),\cdots,t_k(D)} (W_H[[\sigma_1(D),\cdots,\sigma_{n-k}(D), t_1(D),\cdots,t_k(D)]L^{-1}(D)]) \quad (53)$$

The above procedure for finding the MLE $\hat{e}(D)$ or the error vector, needed to correct a codeword, is equivalent to the usual technique for correcting block codes, e.g., see Ref. 7, Sec. 7.5. A recursive technique is developed now by example to perform the minimization required in (53). The iterative minimization procedure, needed to efficiently find $\hat{e}(D)$, is a Viterbi-like or dynamic programming type of algorithm.

As an example of the new syndrome decoding algorithm consider the (3, 1) CC with the generating matrix in (44). If (44) is substituted in (4), then

$$[y_1, y_2, y_3] = [x + D^2x, x + Dx + D^2x, x + Dx + D^2x] \quad (54)$$

is the output of the encoder. Assume the input sequence is

$$x = [0\ 1\ 0\ 0\ 1\ 0].$$

Then by (54),

$$y_1 = [0\ 1\ 0\ 1\ 1\ 0\ 1\ 0],$$

$$y_2 = [0\ 1\ 1\ 1\ 1\ 1\ 1\ 0],$$

and

$$y_3 = [0\ 1\ 1\ 1\ 1\ 1\ 1\ 0]$$

are the three components of the transmitted sequence. Let the corresponding three received sequences be

$$z_1 = [1\ 1\ 0\ 1\ 1\ 0\ 1\ 0],$$

$$z_2 = [0\ 1\ 0\ 1\ 1\ 1\ 1\ 0]; \quad (55)$$

$$z_3 = [0\ 1\ 1\ 0\ 1\ 1\ 1\ 0]$$

Next substitute the parity-check matrix (45) of the (3, 1) CC in (31) to obtain

$$s_1 = (1 + D + D^2)z_1 + (1 + D^2)z_2$$
$$s_2 = (1 + D + D^2)z_1 + D^2 z_2 + z_3 \quad (56)$$

as the syndrome of the code. A calculation of the syndromes in (56) in terms of the received sequence $[z_1, z_2, z_3]$ in (55) yields the syndrome sequences

$$s_1 = [1\ 1\ 0\ 0\ 1\ 0\ 0\ 0\ 0],$$
$$s_2 = [1\ 1\ 1\ 1\ 1\ 0\ 0\ 0\ 0] \quad (57)$$

for this example. Given the syndrome sequences (57) it is desired now to solve syndrome equation (33) for the vector sequence $e(D)$.

The explicit general solutions of the syndrome equation in (33) for the components of $e(D)$ were found in (50) of the last section. These solutions are explicitly

$$e_1 = Ds_1 + t + D^2t$$
$$e_2 = s_1 + Ds_1 + t + Dt + D^2t \quad (58)$$
$$e_3 = Ds_1 + s_2 + t + Dt + D^2t$$

where $t$ is an arbitrary polynomial in $F[D]$ and where for simplicity in notation the functional dependence on $D$ of such functions as $s_1(D)$, $t(D)$, etc., is deleted. Note that physically the functions $Ds_1$, $D^2t$, etc., in (57) can be interpreted as the function $s_1(D)$, delayed by one time unit, and the function $t(D)$, delayed by two time units, respectively.

The problem now is to find from (58) and the given syndrome sequences (57) the maximum likelihood estimate $\hat{e}$ of $e = [e_1, e_2, e_3]$. As in the Viterbi decoding algorithm $\hat{e}$ is found iteratively or sequentially with the aid of a trellis diagram (see Ref. 8). In the present case, the underlying trellis diagram is "universal" in the sense that it is identical for all $(n, k)$ CC of fixed $k$ and constraint length $L$.

For the present example the states of the trellis diagram are equivalent to the states of the shift register needed in (58) to store sequentially the delayed versions $Dt(D)$ and $D^2t(D)$ of the arbitrary function $t(D)$ on $F$. The block diagram of a shift register to hold $Dt$ and $D^2t$, the function $t$, delayed by one time unit and two time units, respectively, is shown in Fig. 1. The state table of the shift register in Fig. 2, when conceived to be a sequential circuit, is given in Fig. 3. Finally, in Fig. 3 the trellis diagram of the state table in Fig. 2 is presented. A solid-line transition in Fig. 3 corresponds to the input $t(D) = 0$; a dashed-line transition corresponds to the input $t(D) = 1$.

The new Viterbi-like syndrome decoding algorithm is illustrated by example in Fig. 4. The digits of the syndrome

sequences $s_1$ and $s_2$ computed in (57) are placed immediately over the corresponding transition paths of the trellis. The vectors $[e_1, e_2, e_3]$ are computed at each stage from Eqs. (58), using the syndrome data for $s_1$, $Ds_1$ and $s_2$ and data $t$, $Dt$ and $D^2t$, depending on the particular path taken.

To illustrate the above procedure, suppose that the algorithm has reached stage 2 at state $d = 11$. At stage 2 the required values of the syndrome sequence needed in (58) are

$$s_1 = 0, \quad Ds_1 = 1 \quad \text{and} \quad s_2 = 1. \tag{59}$$

Since the previous two values of $t$ leading to state $d$ at stage 2 are 1,

$$Dt = 1 \quad \text{and} \quad D^2t = 1. \tag{60}$$

If the $t = 0$ branch is taken in the trellis from stage 2 and state $d$, a substitution of Eqs. (59), (60) and $t = 1$ into (58) yields $[e_1, e_2, e_3] = [0, 1, 0]$ as the values of $e$ along that segment of the path which has attained stage 3 at state $b$.

After stage 2 in Fig. 3 there are always two possible transitions leading to a given node in the trellis. The transition chosen is the one of minimum weight. This is precisely the technique of dynamic programming to determine a minimum weight path. A similar method is used in the Viterbi-algorithm to find a transmitted codeword that is closest in Hamming weight to the received codeword.

The trellis diagram shown in Fig. 4 is completed by the above illustration and the dynamic programming rules for choosing the "survivor" segment of path. At state 9 the minimum weight path in the trellis diagram of Fig. 4 is clearly *a c d b c b a a a a*. The branches of this path yield $\hat{e}(D) = [\hat{e}_1(D), \hat{e}_2(D), \hat{e}_3(D)] = [1, D^2, D^3]$ as the estimate of error vector $e(D)$. Subtracting these estimates of the error from the components of $z$ in (55) produces

$$\begin{aligned} \hat{y}_1 &= [0\ 1\ 0\ 1\ 1\ 0\ 1\ 0] \\ \hat{y}_2 &= [0\ 1\ 1\ 1\ 1\ 1\ 1\ 0] \\ \hat{y}_3 &= [0\ 1\ 1\ 1\ 1\ 1\ 1\ 0] \end{aligned} \tag{61}$$

The Smith normal form of the (3, 1) CC generating matrix $G(D)$ in (44) is $G(D) = [1\ 0\ 0]B$ where

$$B^{-1} = \begin{bmatrix} 1+D & 1+D+D^2 & 1+D+D^2 \\ D & 1+D^2 & D^2 \\ 0 & 0 & 1 \end{bmatrix}$$

Thus the estimate $\hat{x}(D)$ of message in terms of the estimate of the transmitted codeword $\hat{y}(D)$ is $\hat{y} = \hat{x}G = \hat{x}[1\ 0\ 0]B$. Solving this relationship for $\hat{x}$,

$$\begin{aligned} \hat{x} &= \hat{y}G^{-1} = \hat{y}B^{-1}[1,0,0]^T \\ &= [\hat{y}_1, \hat{y}_2, \hat{y}_3] \begin{bmatrix} 1+D & 1+D+D^2 & 1+D+D^2 \\ D & 1+D^2 & 1+D^2 \\ 0 & 0 & 1 \end{bmatrix} \begin{bmatrix} 1 \\ 0 \\ 0 \end{bmatrix} \\ &= (1+D)\hat{y}_1 + D\hat{y}_2 \end{aligned} \tag{62}$$

since by (14) $G^{-1} = B^{-1}[1, 0, 0]^T$ is the right inverse of $G$. A substitution of the estimates of $\hat{y}_1$ and $\hat{y}_2$ in (61) into (62) yields finally $\hat{x} = [0\ 1\ 0\ 0\ 1\ 0]$ as the estimate of the original message.

In the above example the new syndrome decoding algorithm produces the original message. However, if the number of errors exceeds the free distance $d_f$ within any interval less than some multiple of the constant length, there may exist two or more paths of the same minimum error weight. In such a case a decoding failure and an erasure should be declared.

## V. Conclusions

In this paper a new syndrome decoding algorithm for an $(n, k)$ convolutional code with a basic encoder is found. To accomplish this, the method of Forney is extended and used to find the syndrome $H(D)$ of any basic encoder with generating matrix $G(D)$. Next, a general method based on the Smith normal form for matrices over the Euclidean ring $F[D]$ is used to solve the syndrome equation for all possible error vectors $e(D)$. This general solution of the syndrome equation for an $(n,k)$ code is shown in (43) to have the explicit form, $e(D) = [\sigma_1(D), \ldots, \sigma_{n-k}(D), \ t_1(D), \ldots, \ t_k(D)]L^{-1}(D)$ where $t_i(D)$ for $1 \leqslant i \leqslant k$ is an arbitrary polynomial in the $F[D]$ and $\sigma_j(D)$ for $1 \leqslant j \leqslant n-k$ are computable linear functions of the $(n-k)$ syndromes $s_1(D), \ldots, s_{n-k}(D)$.

To complete the new syndrome decoding algorithm, a Viterbi-like algorithm is developed to find the minimum Hamming-weight error-vector $\hat{e}(D)$ of all solutions of the syndrome equation. $\hat{e}(D)$ is the maximum likelihood estimate (MLE) of $e(D)$ within the coset of all solutions of the syndrome equation. The estimate $\hat{e}(D)$ is subtracted from the received codeword $z(D)$ to obtain the MLE $\hat{y}(D)$ of the transmitted codeword. Finally, the method of Forney (Ref. 3) and Massey and Sain (Ref. 7) is extended and applied to the basic

encoder to find the inverse circuit needed to obtain the decoded message $\hat{x}(D)$ from $\hat{y}(D)$.

The new syndrome decoder for the $(n, k)$ CC developed herein is comparable in complexity to the Viterbi decoder. The control logic and the computations associated with the trellis are somewhat simpler in the new decoder. An advantage of the new encoder is the ease with which codes of the same constraint length, but with different rates, can be switched. Detailed comparisons of the new syndrome decoder with the Viterbi decoder for both low and high rate codes are clearly topics for future study.

## Acknowledgement

The authors wish to thank Charles Wang of JPL for the suggestions he made during the preparation of this paper.

## References

1. Schalkwijk, J. P. M., and Vinck, A. J., "Syndrome Decoding of Binary Rate-½ Convolutional Codes," *IEEE Trans. Comm.*, COM-24, 1976, 977-985.
2. McEliece, R. J., *The Theory of Information and Coding*, Reading, Mass.: Addison-Wesley Publishing Co., 1974.
3. Forney, G. D., "Convolutional Codes I: Algebraic Structure," *IEEE Trans. Inform.*, IT-16, 1970, 720-738.
4. Herstein, I. M., *Topics in Algebra*, Xerox College Publishing, Lexington, Mass., 1975.
5. Albert, A. A., *Modern Higher Algebra*, University of Chicago Press, Chicago, Ill., 1947.
6. Massey, J. L., and Sain, M. K., "Inverses of Linear Circuits," *IEEE Trans. Comput.*, C-17, 1968, 330-337.
7. Peterson, W. W., and Weldon, E. J., Jr., *Error Correcting Codes*, 2nd Ed., Cambridge, Mass., MIT Press, 1972.
8. Viterbi, A., and Omura, J., *Digital Communication and Coding*, New York: McGraw-Hill Book Co., 1978.

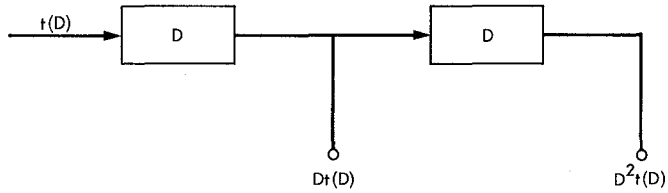


**Fig. 1. Shift register to generate delayed versions of *t(D)***

| | | Dt | $D^2t$ | t: 0 | t: 1 |
|---|---|---|---|---|---|
| a | = | 0 | 0 | 0 0 | 1 0 |
| b | = | 0 | 1 | 0 0 | 1 0 |
| c | = | 1 | 0 | 0 1 | 1 1 |
| d | = | 1 | 1 | 0 1 | 1 1 |

**Fig. 2. State table of shift register for *t(D)***

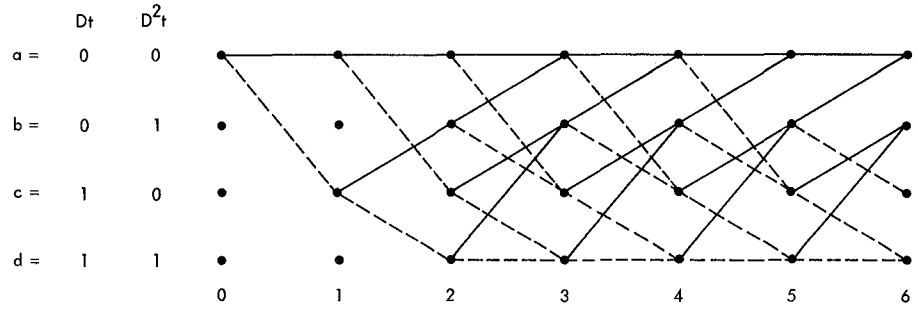


**Fig. 3. Trellis diagram of shift register for *t(D)***

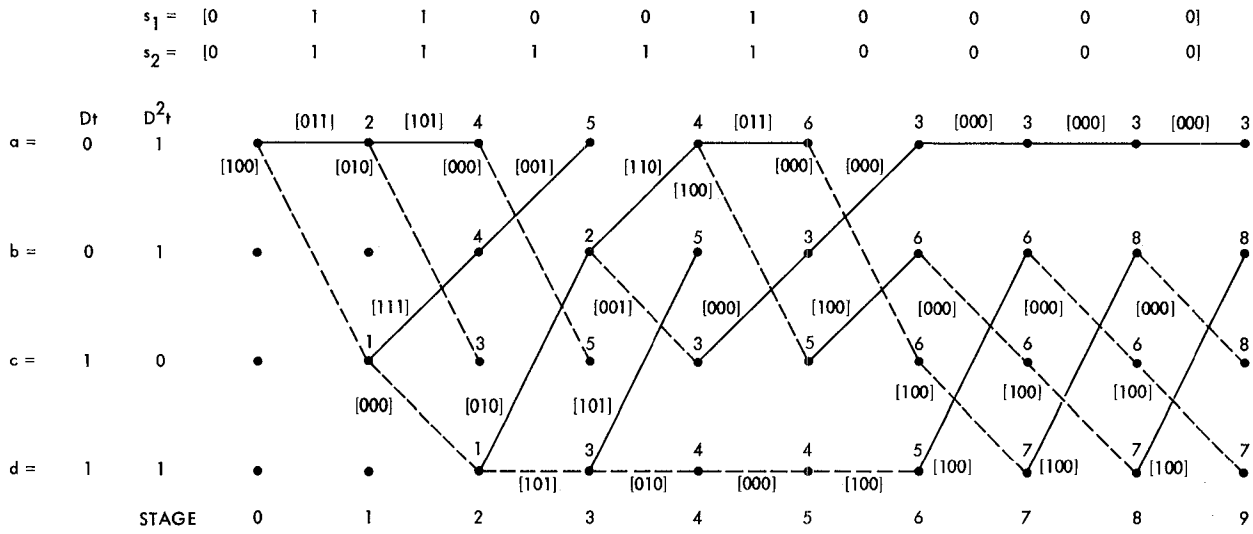


$\hat{e}$ = [100 000 010 001 000 000 000 000 000]
EACH BRANCH OF THE TRELLIS IS LABELED WITH $[e_1, e_2, e_3]$ WHERE $e_1 = Ds_1+t+Dt$, $e_2 = s_1+Ds_1+t+Dt+D^2t$, AND $e_3 = Ds_1+s_2+t+Dt+D^2t$. EACH NODE AT STAGE k IS LABELED WITH $W_H[e_1^{(k)}(D), e_2^{(k)}(D), e_3^{(k)}(D)]$ WHERE $e_i^{(k)}(D)$ IS POLYNOMIAL $e_i(D)$ TRUNCATED AT DEGREE k

**Fig. 4. A new Viterbi-like syndrome decoding algorithm for (3,1) CC**

# Appendix A

In this appendix an example of the invariant-factor decomposition for a generating matrix is given. It is shown that matrices $A$ and $B$ in (10) can be obtained by elementary row and column operations, respectively. The elementary operations are of three types (see, for example, Ref. 5):

(1) The interchange of any two rows (columns) is called an elementary operation of type 1.

(2) Let any row (column) be multiplied by an element of $F[D]$. The addition of this result to any other row (column) is called an elementary operation of type 2.

(3) The multiplication of any row (column) by a nonzero scalar of $F[D]$, i.e., a nonzero element of $F$ is called an elementary operation of type 3.

One procedure for finding $A$ and $B$ in (10) is to express (10) in the form,

$$\begin{bmatrix} 1 & 1+D & 1+D \\ 1+D & D & 0 \end{bmatrix} = \begin{bmatrix} 1 & 0 \\ 0 & 1 \end{bmatrix} G \begin{bmatrix} 1 & 0 & 0 \\ 0 & 1 & 0 \\ 0 & 0 & 1 \end{bmatrix} \qquad \text{(A-1)}$$

and reduce the left side to the form of $\Gamma$ in (10) by elementary transformation. To put zeros in the second column of the first row multiply the first column by $1+D$ and add the result to the second column of the matrix on the left. This same transformation is performed at the same time on the $3 \times 3$ identity matrix on the right side of the equation. The result is

$$\begin{bmatrix} 1, & 0, & 1+D \\ 1+D, & 1+D+D^2, & 0 \end{bmatrix} = \begin{bmatrix} 1 & 0 \\ 0 & 1 \end{bmatrix} G(D) \begin{bmatrix} 1 & 1+D & 0 \\ 0 & 1 & 0 \\ 0 & 1 & 1 \end{bmatrix} \begin{bmatrix} 1 & 0 & 0 \\ 0 & 1 & 0 \\ 0 & 0 & 1 \end{bmatrix}$$

where on the right a new $3 \times 3$ identity matrix multiplies the elementary transformation matrix

$$\begin{bmatrix} 1 & 1+D & 0 \\ 0 & 1 & 0 \\ 0 & 0 & 1 \end{bmatrix}$$

of type 2. Proceeding step by step in this fashion it is readily verified that the left side of (A-1) reduces finally to

$$\Gamma = \begin{bmatrix} 1 & 0 & 0 \\ 0 & 1 & 0 \end{bmatrix} = \begin{bmatrix} 1 & 0 \\ 1+D & 1 \end{bmatrix} G(D) \begin{bmatrix} 1 & 1+D & 0 \\ 0 & 1 & 0 \\ 0 & 0 & 1 \end{bmatrix} \begin{bmatrix} 1 & 0 & 1+D \\ 0 & 1 & 0 \\ 0 & 0 & 1 \end{bmatrix}$$

$$\times \begin{bmatrix} 1 & 0 & 0 \\ 0 & 1 & 1 \\ 0 & 0 & 1 \end{bmatrix} \begin{bmatrix} 1 & 0 & 0 \\ 0 & 1 & 0 \\ 0 & 1 & 1 \end{bmatrix} \begin{bmatrix} 1 & 0 & 0 \\ 0 & 1 & 0 \\ 0 & D & 1 \end{bmatrix} \begin{bmatrix} 1 & 0 & 0 \\ 0 & 1 & D \\ 0 & 0 & 1 \end{bmatrix}$$

$$= \begin{bmatrix} 1 & 0 \\ 1+D & 1 \end{bmatrix} G(D) \begin{bmatrix} 1 & 1+D & D+D^2 \\ 0 & D & 1+D^2 \\ 0 & 1+D & 1+D+D^2 \end{bmatrix}$$

$$= A^{-1}(D)\, G(D)\, B^{-1}(D) \qquad \text{(A-2)}$$

For $F = GF(2)$ it is easy to verify that an elementary matrix $E$ over $F[D]$ is its own inverse, i.e., $E^{-1} = E$ for an elementary matrix of types 1, 2 or 3. Thus solving for $G$ in (A-2) yields

$$G(D) = \begin{bmatrix} 1 & 0 \\ 1+D & 1 \end{bmatrix} \begin{bmatrix} 1 & 0 & 0 \\ 0 & 1 & 0 \end{bmatrix} \begin{bmatrix} 1 & 0 & 0 \\ 0 & 1 & D \\ 0 & 0 & 1 \end{bmatrix} \begin{bmatrix} 1 & 0 & 0 \\ 0 & 1 & 0 \\ 0 & D & 1 \end{bmatrix} \begin{bmatrix} 1 & 0 & 0 \\ 0 & 1 & 0 \\ 0 & 1 & 1 \end{bmatrix}$$

$$\times \begin{bmatrix} 1 & 0 & 0 \\ 0 & 1 & 1 \\ 0 & 0 & 1 \end{bmatrix} \begin{bmatrix} 1 & 0 & 1+D \\ 0 & 1 & 0 \\ 0 & 0 & 1 \end{bmatrix} \begin{bmatrix} 1 & 1+D & 0 \\ 0 & 1 & 0 \\ 0 & 0 & 1 \end{bmatrix}$$

$$= \begin{bmatrix} 1 & 0 \\ 1+D & 1 \end{bmatrix} \begin{bmatrix} 1 & 0 & 0 \\ 0 & 1 & 0 \end{bmatrix} \begin{bmatrix} 1 & 1+D & 1+D \\ 0 & 1+D+D^2 & 1+D^2 \\ 0 & 1+D & D \end{bmatrix}$$

$$= A(D)\, \Gamma(D)\, B(D) \qquad \text{(A-3)}$$

as the invariant-factor decomposition of $G(D)$ in (A-1).

# Appendix B

In this appendix an example for finding the general solution of syndrome equation for the (3, 2) CC is given. Consider the parity-check matrix, $H(D) = [D + D^2,\ 1 + D^2,\ 1 + D + D^2]$, found in (30) for the (3, 2) CC with generating matrix (10). A diagonalization of $H^T(D)$ yields for this example

$$L^{-1}(D) = \begin{bmatrix} 0 & 1+D & D \\ 1 & D+D^3 & D^2+D^3 \\ 0 & 1+D+D^2 & 1+D^2 \end{bmatrix} \quad \text{(B-1)}$$

where $L(D)$ is the left invertible matrix of the Smith normal form in (37) for $H^T(D)$. In this case the syndrome equation to solve for $e(D)$ is

$$\begin{aligned} s(D) &= [e_1(D), e_2(D), e_3(D)]\ L\ [1, 0, 0]^T \\ &= [\epsilon_1(D), \epsilon_2(D), \epsilon_3(D)]\ [1, 0, 0]^T \end{aligned} \quad \text{(B-2)}$$

The solution in (B-2) for $\epsilon(D)$ is

$$\epsilon_1(D) = s(D),\ \epsilon_2(D) = t_1(D),\ \epsilon_3 = t_2(D) \quad \text{(B-3)}$$

where $t_1(D)$ and $t_2(D)$ are arbitrary elements of parameters of $F[D]$. Solving $e(D)\ L = \epsilon(D)$ for $e(D)$ in terms of the solution (B-3) for $\epsilon(D)$ is, using (B-1)

$$[e_1(D), e_2(D), e_3(D)] = [s(D), t_1(D), t_2(D)] \times \begin{bmatrix} 0 & 1+D & D \\ 1 & D+D^3 & D^2+D^3 \\ 0 & 1+D+D^2 & 1+D^2 \end{bmatrix}$$

which yields, upon an equating of coefficients,

$$\begin{aligned} e_1(D) &= t_1(D) \\ e_2(D) &= (1+D)\,s(D) + (D+D^3)\,t_1(D) + (1+D+D^2)\,t_2^2(D) \\ e_3(D) &= Ds(D) + (D^2+D^3)\,t_1(D) + (1+D^2)\,t_2(D) \end{aligned} \quad \text{(B-4)}$$

as the general solution of the syndrome equation (31) for the (3, 2) encoder in terms of two arbitrary parameters $t_1(D)$ and $t_2(D)$ in $F[D]$. It is a straightforward exercise to verify that (B-4) satisfies (31).

# Phase Calibration for the Block I VLBI System

M. G. Roth
Setpoint Alaska Inc.
Anchorage, Alaska

T. F. Runge
Tracking Systems and Applications Section

*Very Long Baseline Interferometry (VLBI) in the DSN provides support for spacecraft navigation, earth orientation measurements, and synchronization of network time and frequency standards. An improved method for calibrating instrumental phase shifts has recently been implemented as a computer program in the Block I system. The new calibration program, called PRECAL, performs calibrations over intervals as small as 0.4 seconds and greatly reduces the amount of computer processing required to perform phase calibration.*

## I. Introduction

VLBI is a method of measuring the difference in arrival time of a radio signal at two widely separated antennas in order to determine other parameters of the observation. Radio signals from an extragalactic source (or from a spacecraft) are recorded simultaneously at two antennas on the earth's surface. Because of a difference in ray paths, the signal's arrival is delayed at one antenna relative to the other. This delay and its time derivative are of interest because they are observable parameters of a physical system which includes earth orientation, source location, and station clock parameters that cannot be observed directly. When a comprehensive mathematical model of this physical system is fitted to the delay parameters derived from VLBI observations, accurate estimates can be obtained for parameters such as the instantaneous rotation angle of the earth (UT1), polar motion, source positions, and the difference in clock epochs and rates at the two stations (Refs. 1-3).

The measured delay includes the delays experienced by the signals while passing through the station instrumentation. Phase calibration removes these components of the delay. Without phase calibration, the delays obtained using the bandwidth synthesis procedure (see below) contain unknown offsets due to frequency-dependent instrumental phase shifts. These instrumental delay offsets are indistinguishable from epoch differences between the station clocks and must be eliminated before absolute clock offsets can be measured.

Another benefit of phase calibration is that bandwidth synthesis delay ambiguities may be resolved independently for each source, using the simpler and more reliable process of single observation ambiguity resolution (Ref. 4). Without phase calibration, the resolution of BWS phase ambiguities is complicated by the presence of different instrumental phase shifts in different channels.

## II. Data Acquisition

In Fig. 1 the radio signal from a source is received at two DSN antennas. Both antennas observe one or more sources in an identical, simultaneous sequence. During each observation, both receiving stations repeatedly cycle through several 250-kHz bandwidth channels in unison to record data from several different frequencies for bandwidth synthesis. The radio data are 1-bit sampled and recorded at the Nyquist rate of 500,000 bits per second. After they are collected, the VLBI data from both stations are replayed over the Ground Communication Facility (GCF) wide band data (WBD) lines to the VLBI Processor Subsystem (VPS) at JPL and are filed on the VPS disks for processing.

## III. Cross Correlation

The two VLBI data streams are cross-correlated by the Block I VLBI Correlator Hardware Assembly under control of the VLBI Correlation Operational Program (VCOROP) (Ref. 5) as shown in Fig. 2. The correlation operation is performed simutaneously for each of 16 discrete time offsets, or "lags", between the streams. The lags are spaced at 2-microsecond intervals, which represent shifts of one bit in the 500,000-bps data streams.

Correlation reduces the data in each "correlation interval" to one pair of sine and cosine correlation sums per lag. During correlation the data streams are multiplied by a "fringe phase model" which counter-rotates the interferometer fringe phase to compensate for the earth's rotational doppler effect at the antennas, and the bitstream alignment is periodically shifted by one bit to offset the earth's rotational effect on the delay. The resulting "stopped fringe" correlation sums are then Fourier transformed from the lag domain to the frequency domain to obtain one complex correlation sum at each of 8 baseband frequencies for each correlation interval. The correlation and normalization sums and the correlator fringe phase model for each correlation interval are stored on the VPS disks in a file called the Post Correlation Record (PCR).

During cross correlation, as many as eight bandwidth synthesis (BWS) channels can be processed using time multiplexing. The dwell time on each channel defines a data segment that must be a multiple of 0.2 sec. The data from each channel in the multiplexing cycle are correlated over one or more correlation intervals, which must also be multiples of 0.2 sec. Data segments for a particular channel are often subdivided into two or more correlation intervals to allow for processing more than one calibration tone per channel, as explained below.

## IV. Fringe Phase

Each of the complex correlation sums can be represented by a phase and an amplitude. Phase calibration affects only the phase component of the correlation sums. Prior to phase calibration, the phases of the stopped fringe data points are given by (Ref. 4):

$$\psi_k = \omega_k (\Delta\tau_g + \tau_b + \tau_I) + \phi_I (\omega_k) + \Delta\phi_h, k = 0, 1, \ldots, 15$$

where

$\psi_k$ = uncalibrated fringe phase at frequency $\omega_k$

$\omega_k$ = baseband frequency

$\Delta\tau_g$ = group delay residual: observed delay minus modeled delay, including delays due to geometry, media and antenna offsets

$\tau_b$ = data recorder clock error, station 1-station 2

$\tau_I$ = instrumental delay, station 1-station 2

$\phi_I$ = instrumental phase shift, station 1-station 2

$\Delta\phi_h$ = heterodyne phase residual, station 1-station 2: observed phase minus modeled phase

Phase calibration removes the instrumental terms corresponding to $\tau_b$, $\tau_I$, $\phi_I$ and $\Delta\phi_h$. The physical interpretations of these terms are shown in Fig. 3.

## V. Phase Calibration

During the data collection, monochromatic phase calibration "tones" derived from the station frequency standards are injected into the first stage maser amplifiers and superimposed on the recorded radio signals. The tones are evenly spaced across the radio spectrum in such a way that each recorded frequency channel contains two or more tones whose differences in phase and frequency can later be used to calibrate the instrumental delays that are experienced by the signals at each station. The total delay between the two VLBI data streams includes the difference in instrumental delays experienced by the VLBI data between the antenna and the recording equipment at the two stations. The PRECAL program makes use of the relationship between the recorded tone phases and the known tone frequencies to calibrate the delays experienced by the tones at each station. However, the tone delays include the "uplink", or "cable," delay $\tau_u$, from the tone generator to the antenna, which does not affect the VLBI data, as well as the "downlink" instrumental delay $\tau_I$, from the antenna to the recording equipment as shown in Fig. 3. Therefore, the instru-

mental delay effect on the fringe phase is equal to the difference in the tone delays minus the difference in the uplink delays for the two stations. In practice, PRECAL corrects the fringe phase to compensate for the difference in the tone delays while the difference in the uplink delays, which are monitored and stabilized over each set of observations, is allowed to appear as an additional clock offset between the two stations. (This offset is later removed during the parameter estimation operations.)

As the data from each correlation interval are correlated, one phase calibration tone from each station is also correlated against an appropriate tone model. This produces two complex stopped tone data points per correlation interval. The phase difference between these stopped tone phases at the two stations at frequency $\omega_k$ is given by (Ref. 4):

$$\phi_k = \omega_k (\tau_b - \tau_c + \tau_I + \tau_u) + \phi_I + \Delta\phi_h, k = 0, 1, \ldots, 15$$

where

$\phi_k$ = tone phase difference, station 1-station 2

$\omega_k$ = baseband tone frequency

$\tau_c$ = clock reference point epoch offset, station 1-station 2

$\tau_u$ = calibration signal uplink delay, station 1-station 2

The fringe phase is calibrated by subtracting the tone phase from the fringe phase to obtain:

$$\psi_k^* = \psi_k - \phi_k = \omega_k (\Delta\tau_g + \tau_c - \tau_u), k = 0,1, \ldots, 15$$

Note that cancellation of the $\tau_b$ and $\tau_I$ terms depends on matching the calibration tone frequencies with the fringe function baseband frequency $\omega_k$, while cancellation of the $\Delta\phi_h$ terms depends on the use of the same heterodyne model for both fringe and tone phase. It is not practical to correlate a separate tone frequency for each of 16 $\omega_k$ in the Block I system. Instead, the instrumental phase is interpolated to each $\omega_k$ before phase calibration is performed. For linear interpolation, at least two calibration frequencies are needed in each channel. (It is assumed that the Block I hardware specifications are sufficient to ensure that linear interpolation using two tones per passband is adequate for this purpose.) However, the Block I correlator correlates only one tone from each station during each correlation interval. Therefore, the multiple tones that are required for each frequency channel are obtained by correlating a different tone over each of two or more successive correlation intervals for each frequency channel. PRECAL then uses the multiple tones obtained in this way to apply a single fringe phase correction to each such group of successive intervals from the same frequency channel.

For each group of successive correlation intervals from a given frequency channel, PRECAL approximates the tone phase at each station using a linear fit of phase against frequency for two or more tones. Any number of calibration frequencies may be used, subject to the restriction that all channels must be calibrated with the same number of frequencies.

Because only the fractional cycles of tone phase can be observed, PRECAL must rely on an independent calibration of the instrumental delay at each station to within less than one half cycle of the observed tone phase in order to resolve the integer cycle ambiguities. For a single tone in the 2000-MHz range, this would require an independent calibration of the delay to about one-fourth nanosecond, which is not feasible. However, PRECAL observes the phase and frequency differences between two or more tones from each station, thereby reducing the tone delay ambiguity to the reciprocal of the tone spacing and relaxing the independent calibration requirements proportionately (e.g., to 5 $\mu$sec for a tone spacing of 100 kHz).

In theory, phase calibration may be performed at any point of the data analysis following cross-correlation. In the past, the phase calibration data for an entire observation lasting up to several minutes were processed separately from the fringe data using the PCAL program. After the delay parameters were estimated from the fringe data by the PHASOR program and the calibration parameters were estimated from the tone data by PCAL, a single calibration was made to the delays at the mean time of the observation.

In the new system using the program PRECAL, the phase calibration data are combined with the correlation sums prior to estimation of the delay parameters by the program PHASOR as shown in Fig. 2. In this way, the delay parameters produced by PHASOR are completely phase calibrated and the extra processing required to obtain the tone parameters and combine them with the PHASOR results is eliminated. In addition, the PRECAL calibration is performed for each correlation interval, lasting only a few tenths of a second, instead of once for an entire observation.

## VI. Calibration Algorithm

The PRECAL program verifies that the stopped tone data required for phase calibration are available, calibrates the fringe phase to remove the effects of instrumental delays, and translates the fringe data into the format expected by the PHASOR program. PRECAL operates on a PCR file produced by the correlator and creates four output files containing

reformatted data. One of these contains the calibrated fringe data while a second contains the uncalibrated data for use if calibration is unsuccessful. Two other output files receive the tone data from one station each for use in analyzing tones. These output files are created in the form expected by the tone analysis program, PCAL. A listing file that summarizes the calibration status and results is also created.

PRECAL uses the shift in phase between two or more tones of known frequency to calculate the instrumental delay at each station. Because this delay varies with both frequency and time, it must be calculated for each channel and updated periodically in time. In practice, the delay for each channel and station is computed for each correlator cycle, which is the data interval over which the correlator cycles through all of the channels and tone models. This typically corresponds to a few seconds in time, which is a sufficient updating interval for the stopped fringes and tones produced by the correlator. PRECAL's first major operation is to ensure that two or more stopped tones are available in each channel for each correlator cycle.

The sequence in which data from the different channels are recorded and correlated is specified by a phase model table in the PCR file. The corresponding sequence of tone models used for tone stopping is specified by a tone model table. PRECAL checks the phase and tone model tables to verify that two or more stopped tones are specified for each channel. To facilitate calibration, PRECAL also verifies that all channels have the same number of stopped tones.

The next task of the phase calibration operation is to obtain a priori estimates of the instrumental delays at each station, for use in resolving the tone phase ambiguities. Ideally, these estimates would be read from the station catalog, and the PRECAL program does this if the estimates are found in the catalog. If an a priori instrumental delay estimate is not found in the station catalog, PRECAL derives its own estimate as described below.

If no a priori instrumental delay estimate for a given station is found in the station catalog, tone data from the first correlator cycle of the observation are used to derive an estimate. First, the tone phase ambiguities in each channel are resolved to align the tone data between zero and one cycle of phase shift for the narrowest tone pair in the channel, and the instrumental delay is estimated from the tone phase shifts. Then, this estimated delay for each channel is used to resolve the tone phase shift ambiguities in the other channels and derive delay estimates for them. When these two steps are completed for all of the channels, the individual channel delay estimate from the first step that produced the best agreement between the estimates for the other channels in the second step is chosen as the station a priori instrumental delay estimate. Although the instrumental delays are dispersive, the variation between channels is small compared to the magnitude of the delay, so the estimates for all channels should be in close agreement (except when they are corrupted by the presence of apparent tone delays, which are discussed below).

At present, the instrumental delays observed by tone tracking are severely corrupted by the presence of apparent tone delays which are caused by a lack of synchronization between the recorder clocks and the output pulses produced by the tone generators and are indistinguishable from $\tau_u$. These station-dependent apparent delays differ from the S-band channels to the X-band channels, but remain constant in each band over each observing session. However, they vary from one observing session to the next and their magnitude is known only to be a multiple of 200 ns and to be less than the reciprocal of the tone spacing (e.g., 10 $\mu$sec for 100-kHz tone spacing). Because accurate a priori estimates cannot be made for these apparent delays (without measuring them at the stations for each set of observations), no a priori instrumental delay estimates will be entered into the station catalog until the clock-tone generator asychronies are removed by the installation of new tone generator hardware at the stations. Prior to the installation of new tone generators (which are currently under development and are expected to be operational sometime in 1984), PRECAL'S calculation of a priori instrumental delay estimates may fail if the apparent delays in the S-band and X-band channels differ by more than one or two $\mu$sec, in which case no calibration will be performed. If, on the other hand, an a priori estimate can be calculated, the apparent delays will generally cause a different constant instrumental delay offset to remain in each band of channels after calibration. Therefore, the full advantage of the PRECAL method of calibration will not be realized until the new tone generators become operational.

After a priori instrumental delay estimates are determined for both stations, the fringe data from each correlator cycle are calibrated in sequence. The acceptability of the tone data is monitored by comparing the tone amplitudes against a threshold value which is calculated so that the probability of its being exceeded by noise alone is 0.001. For each station and channel in sequence, the acceptable tone data are aligned by resolving their phase shift ambiguities against the station's a priori estimate and the instrumental delay is calculated by a linear fit of tone phase against frequency. For each channel, the fitted tone phases for the two stations are used to interpolate the corresponding tone phases for each individual baseband frequency $\omega_k$ of the frequency domain fringe data. Finally, the difference between the station's instrumental phases for each baseband frequency of each channel is subtracted from the corresponding uncalibrated fringe phase to com-

pute the calibrated baseband fringe phase. The PRECAL phase calibration algorithm is summarized below:

if (correlation cycle is valid):

for (each observation):

if (no a priori instrumental delay estimate for a given station is found in the station catalog):

repeat until (a priori instrumental dealy estimate is acceptable)

(1) Estimate station's instrumental delay in each channel for next correlator cycle.

(2) Select individual channel delay estimate that best fits all channel's tone data for first correlator cycle as station a priori estimate.

for (each correlator cycle):

for (each station and channel):

(3) Verify sufficient tone signals.

(4) Resolve tone phase shift ambiguities against station a priori instrumental delay estimate.

(5) Calculate instrumental delay from linear fit of tone phase shift against frequency spacing.

for (each channel):

(6) Calculate stations' instrumental phases at each baseband fringe frequency.

(7) Subtract difference in stations' instrumental phases at each baseband fringe frequency from corresponding baseband fringe phase.

Two additional operations are performed during data reformatting to ensure that the data organization is acceptable to PHASOR. PHASOR requires that any repeated observations of a given channel within a correlator cycle must be adjacent. However, every channel must be repeated in each cycle to obtain the multiple stopped tones needed for calibration, and some observations may use a cycle that repeats the same sequence of channels two or more times, e.g.,

1 2 3 4 5 6 1 2 3 4 5 6

Because of the nonadjacent repetition of channels, PRECAL factors cycles of this type into two or more cycles for the PHASOR program, e.g.,

1 2 3 4 5 6 / 1 2 3 4 5 6

The PHASOR program also requires all correlation intervals to have the same length. If they do not, PRECAL factors them into uniform intervals equal to the greatest common divisor of the original lengths. For example, DSN clock synchronization scans typically use correlation intervals that are four times as long for the X-band channels (usually channels 4 through 6 at 8400-8440 MHz) as for the S-band channels (usually 1 through 3 at 2260-2300 MHz). Therefore, PRECAL factors each X-band interval of those scans into four shorter intervals and repeats the corresponding stopped fringe and tone data four times, transforming a cycle with variable length intervals such as

1 2 3 4 5 6

into an equivalent cycle with equal length intervals such as

1 2 3 4 4 4 4 5 5 5 5 6 6 6 6

## VII. BWS Ambiguity Resolution

The observed VLBI delay derived from the data in a single channel is called the bit stream alignment (BSA) delay or lag offset. Ideally, the residual BSA delays will be zero in all channels, when the data are correlated using perfect model parameters.

The precision with which the BSA delay can be estimated is limited by the effective bandwidth of the recorded signals. Because it is not practical to record an extremely wide-band channel, "bandwidth synthesis" is employed to extend the effective bandwidth. Data for bandwidth synthesis are obtained by recording a narrow-band channel and switching it rapidly over a wide range of channel frequencies. The phases for specified channel pairs are then combined into bandwidth synthesis (BWS) delays equal to the fringe phase difference divided by the difference in radio frequencies between the two channels. Bandwidth synthesis (BWS) delays provide the most accurate VLBI delay observations. BWS delays are ambiguous because they account for only the fractional phase differences between channels. Integer cycles of phase constitute a "delay ambiguity" equal to the reciprocal of the channel separation. By combining different pairs of channels to obtain varying separations, the ambiguities in the BWS delays may be resolved against the unambiguous BSA delay.

Since the same delay model is used for both BSA delays and BWS delays, they might be expected to have the same residuals. However, this will be true only for calibrated data. With uncalibrated data, instrumental delays severely corrupt the BWS delays and no meaningful comparisons between channel pairs for a single observation can be made. With calibrated data, the BWS delays represent the fractional part of the delay

residual after removal of an integer number of delay ambiguities. The delay ambiguity for each BWS channel pair in a band is the reciprocal of the channel pair separation, so we expect the BWS residuals to follow no particular pattern across pairs of channels. However, when the integer ambiguities are taken into account, the BSA delay residuals and all BWS residuals should agree to within their estimated errors.

An example of ambiguity resolution using calibrated data is shown in Table 1. The data are from observations of the radio source 4C 39.25 on the intercontinental baseline between the DSN 64-meter antennas located near Goldstone, California, and Canberra, Australia. Data in three S-band channels were calibrated using the PRECAL program and then were processed by the PHASOR program to obtain BSA and BWS delays. The mean of the three BSA delays is identified as channel 0 in Table 1. The ambiguities are resolved in order of increasing channel separation, starting with the narrowest channel pair, which is resolved against the mean BSA delay. The progressively smaller ambiguity in each ensuing channel pair is then resolved against the previous unambiguous BWS delay to obtain a sequence of increasingly accurate synthesized delay estimates. Successful resolution of the cycle ambiguities is indicated by agreement between successive channels to within the combined standard errors of the channels.

An independent verification of these results was obtained using the PCAL program to perform phase calibration on the uncalibrated fringe data. The calibrated delays obtained by this method were in agreement with the PRECAL results.

## VIII. Summary

An improved method of calibrating instrumental delays is available for the DSN Block I VLBI System. This method uses the newly implemented PRECAL program to process phase-calibration tone data and combine them with the VLBI correlation sums prior to estimation of the delay parameters by the PHASOR program. Thus a substantial amount of additional processing that was previously required to extract the instrumental delay parameters and combine them with the PHASOR results is eliminated. Furthermore, the PRECAL program performs instrumental delay calibration over intervals as small as 0.4 sec, while the previous method performed only a single calibration for each channel over an entire observation. However, the full advantage of the new method cannot be realized until asynchronies between the recorder clocks and the phase calibration "clocks" are removed by the installation of new tone generator hardware (which is currently under development) at the DSN receiving stations.

## References


1. Border, J. S., et al., "Determining Spacecraft Angular Position with Delta VLBI: The Voyager Demonstration", AIAA 82-1471, 1981.
2. Eubanks, T. M., et al., "An Analysis of JPL TEMPO Earth Orientation Results," Proceedings of the IAG General Meeting, Tokyo, Japan, 1982.
3. Roth, M. G., "Intercontinental Synchronization of Atomic Clocks," Proceedings of the Precise Time and Time Interval Applications and Planning Meeting, 1981.
4. Thomas, J. B., *An Analysis of Radio Interferometry with the Block 0 System*, Publication 81-49, Jet Propulsion Laboratory, Pasadena, Calif., December 1981.
5. Software Specification Document: VLBI Processor Subsystem, Block I VLBI Correlation Operational Program, DSN Document SSD-NVV-5137-OP, Revision B.

**Table 1. Ambiguity resolution using calibrated BWS data**

| | Channel | | | |
|---|---|---|---|---|
| | 0 | 1 | 2 | 3 |
| Bandwidth, MHz | 0.25 | 7.000 | 32.750 | 39.750 |
| Ambiguous delay, ns | – | 29.483 | -20.785 | 13.218 |
| Nx ambiguity, ns | – | 30 X 142.857 | 142 X 30.534 | 171 X 25.157 |
| Unambiguous delay (ns) | 4285 ±38 | 4315.19 ±0.83 | 4315.04 ±0.18 | 4315.06 ±0.16 |

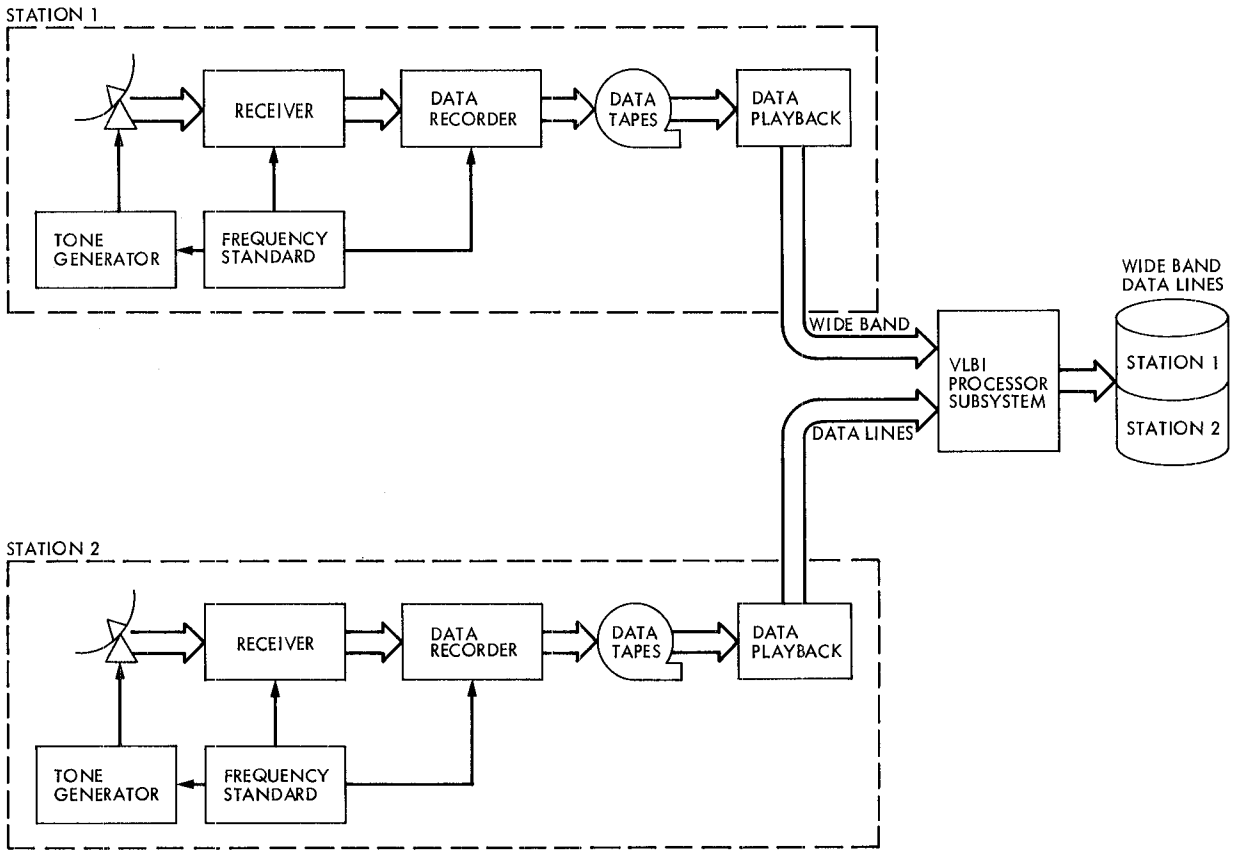


**Fig. 1. Overview of DSN Block I VLBI data acquisition system**

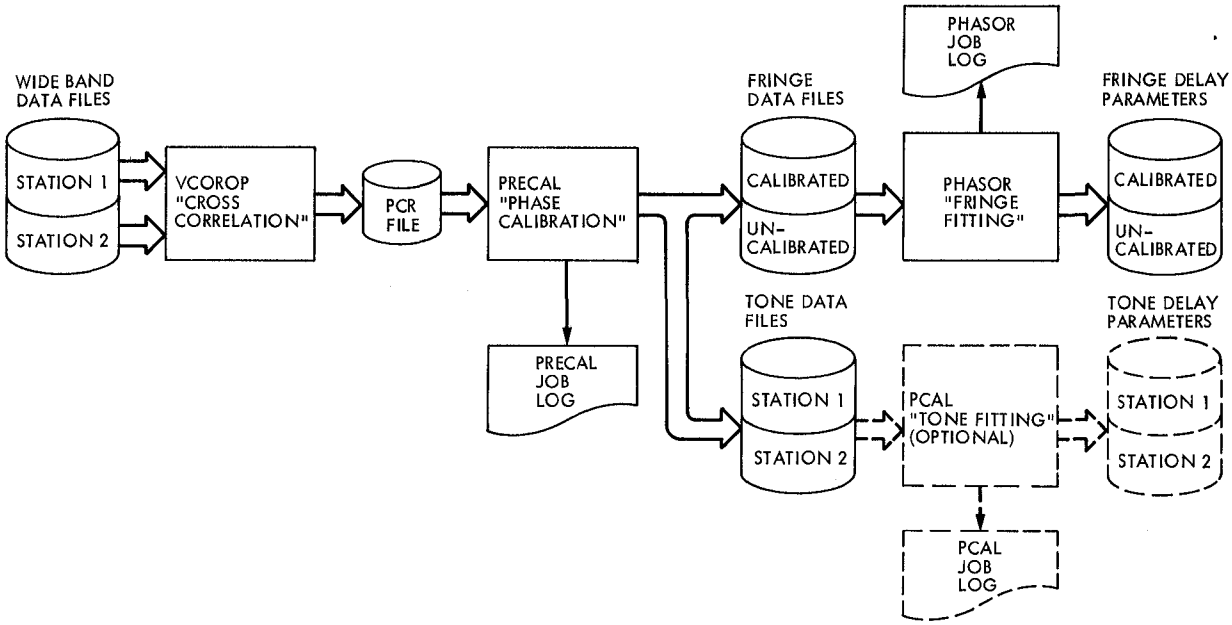


**Fig. 2. Processing steps for phase calibration operation. Dashed symbols indicate optional functions for diagnostic purposes**

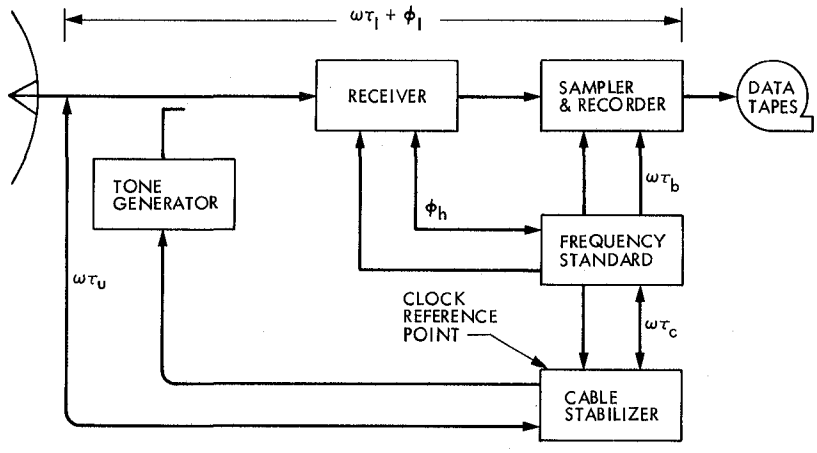


**Fig. 3. Phase shifts experienced by a signal at frequency $\omega$ passing through station instrumentation**

# Antenna Microwave Subsystem Controller

A. Freiley
Radio Frequency and Microwave Subsystems Section

*The development of a new microwave subsystem controller is discussed, and results of installing the equipment at the DSS 13 R&D station are reported. This controller is serving as the prototype for a new generation of microwave controllers for the DSN.*

## I. Introduction

The Antenna Microwave Subsystem Controller (Fig. 1) has been developed utilizing a microprocessor-based digital system to monitor and control microwave switch type equipment. This report details the results of the development and the implementation of the prototype equipment which controls the microwave equipment in the second-generation common aperture X- and S-band uplink feedcone (XSU, Ref. 1) at the DSS 13 Venus station, Goldstone, California.

The hardware consists of two major assemblies, the Microwave Switch Control Interface (USCI) and the Microwave Switch Controller (USC). The USCI is a control room rack-mounted assembly which accepts high level inputs and initiates corresponding subsystem changes and/or responses. The USC accepts direction from the USCI and translates the software commands into hardware switch commands which configure the microwave system, then reports the results.

The software consists of individual modules which have distinct and separate functions. The modular structure of the software lends itself well to timely delivery and clarity as the software evolves in the development process.

The operator controls the microwave equipment by entering commands to the USCI from a local terminal. The system responds with acknowledgments and results of his inputs. The interface with the host computer has been planned, but due to schedule constraints the interface was not fully developed and implemented initially.

Additional refinements and developments to the monitor and control equipment are needed to improve this prototype and implement all the functions that are required of a fully automated and integrated subsystem controller. These refinements and developments would resolve interface, timing, executive control, interrupt, power failure and equipment failure problems that have not been fully solved. Future application of this control system to the Deep Space Network (DSN) presents additional challenges when the more complicated 64-m UWV subsystem is considered. The ability to communicate with up to 5 USC's will present some additional difficulties.

## II. Hardware

The UWV subsystem controller functional block diagram is shown in Fig. 1. The USCI is the central focal point for all messages to and from the control room and interfaces with the local CRT terminal, the Host or station controller, the floppy disk memory and the USC.

The local CRT terminal provides the means for the operator to input commands or directives into the system, and receive response messages from the system. The physical interface between the local terminal and the USCI is a standard RS232C operating at 9600 baud. The station controller or HOST computer will also be able to input command to the USCI through the HOST interface. This physical input is the star switch standard interface also operating at 9600 baud.

The floppy disk memory provides permanent program storage for the USCI. During development the use of this disk drive was not intended to be a long-term solution to software storage but was an expedient short-term solution for the needed memory in light of schedule constraints. The drive will be replaced, as will be discussed later. The interface between the USCI and the floppy disk drive unit uses the disk control board and a standard 50-pin connector.

Transparent to the system but nevertheless important is the modem/fiber optic communications link between the USCI and USC. The Canoga Data Systems modems convert standard RS232C data and control signals to a stream of optical pulses for transmission over the optical cables. The data and handshaking signals are directly combined into a serial data stream. A light emitting diode driven by the data stream produces optical pulses which are carried over one of two channels in the optical cable extending from the control room up the antenna to the feedcone. At the feedcone the optical pulses are converted back to the standard RS232C data and control signals.

Internal to the USCI, a standard Intel rack mountable chassis, commercially available boards are used. A list of the boards is presented in Table 1. The intent of this design was to develop a system which used all standard components and avoided the use of special purpose boards, thus simplifying maintenance, sparing, and repairs.

The USC is the central focal point for the incoming commands, outgoing responses and the hardware command and indicate signals. The USC is mounted in the feedcone near the microwave equipment to be controlled. The interfaces to the USC are the USCI by way of the fiber optic link, the local CRT terminal (optional), two transmitter interlocks and inhibits, eight safety interlocks and 16 switch command and indicators.

The USC interface to the USCI is the same as was described for the USCI. The local CRT terminal is optional; that is, it is not needed for normal operations. Its main purpose is to provide local control if the feedcone were involved in ground test or if the USCI communication had failed and a direct control is needed for maintenance or other special tests. The USC was designed to interface with the two on-site transmitters. Through this interface, the transmitter indicates if the beam is on in order to inhibit the movement of critical switches in the transmit path. The interface also provides "safe to transmit" indication which means all critical switches and interlocks are in the correct configuration to radiate RF energy from either transmitter. The eight safety interlocks, which are part of the "safe to transmit" signal, monitor such items as feedcone doors, main dish hatch, nitrogen pressure, water flow, and three spares for expansion. The interface with the microwave equipment, such as waveguide switches, polarizer controllers, test oscillators and others, consists of 16 connectors, one connector for each component to be controlled.

The same philosophy of using standard commercially available boards was adopted for the USC. The USC assembly is a Hoffman enclosure. 24 X 36 X 10 inches. One of the key components within the USC is a bank of solid state relays. Half of the bank is devoted to switch command function; the other half is devoted to the indicated functions. Through these relays the software programs command and sense the switch functions. The boards used in the USC are listed in Table 2 along with their descriptions and functions.

## III. Software

The software for the USC and USCI was planned and developed in a modular form. The design approach expedited timely delivery and enhanced the clarity of the final software. For each module, a sufficiently detailed description was first generated so that coding could subsequently take place entirely from the description. Each description discussed six categories:

(1) The functional description addressed what the module was to accomplish.

(2) The entry requirements addressed the inputs to the module and the assumptions made of the outside world.

(3) The results provided were the output from the module and the assumptions made of the outside world.

(4) The exceptions enumerated the error conditions detected in the module and indicated any errors encountered.

(5) The external effects addressed the observable effects such as reading a file, displaying something on a CRT, and interacting with the physical environment.

(6) The processing addressed and expanded on the algorithm, explanatory remarks and the sequence of the steps of the algorithm used in the routine.

The flow charts in Figs. 2, 3, 4, and 5 illustrate the modular nature designed into the software structure. Figure 2 shows the flow for the initialization, self-test and executive routine of the USCI. Figure 3 expands the USCI executive routine into its major functions. Figure 4 shows the initialization, self-test, and executive routine for the USC. Figure 5 expands the executive routine into its major functions. A description of the software modules, along with the major subroutines, their location and brief functional narrative is given in Table 3.

## IV. Venus Site Application

The prototype X- and S-band uplink controller was installed into the second-generation common aperture feedcone XSU at DSS 13 during November 1981. The functional block diagram of the microwave subsystem is presented in Fig. 6.

This feed incorporated a geometrically symmetrical common aperture feedhorn and combiner which operates at both X- and S-band. Its capabilities include S-band transmit from 2110 to 2120 MHz and receive from 2200 to 2300 MHz and X-band transmit from 7145 to 7235 MHz and receive from 8200 to 8600 MHz with fully independent diplex functions.

The S-band labyrinth and combiner provide the "hard wired" right circular polarization while the X-band motorized polarizer can select either right or left circular polarization.

A combination of waveguide and coax switches as well as the motor driven polarizer is controlled by the microwave subsystem controller to configure the system. The useful system configurations were defined and mode names were assigned to allow a desired mode to be selected by simply specifying a mode name at the CRT terminal. Such modes could direct the RF energy from the transmitter into the water load or toward the feedhorn. Calibration signals can be routed from the signal sources to the TWMs. System noise calibrations are achieved by switching the TWM input between the feedhorn and the calibrated ambient load. Most useful configurations are accommodated by operator input of the desired mode. For those configurations not planned, the control system will accept changes to the hardware as specified by the MODIFY command.

The feed system will accommodate 20 kW of Rf radiated power at both S- and X-band. Safety interlocks and waveguide switch positions are monitored by the USC. From this information, "safe to transmit" or "inhibit" signals were designed to be sent to the transmitter through the transmitter interface and status reports to the operator, but due to the lack of field experience with software interlocks, a system of relay logic was implemented as a proven, reliable method of ensuring RF safety of personnel and equipment.

## V. Operator Interfaces

The operator may input commands to the microwave controller from either the local CRT terminal or from the station control terminal through the star switch interface. In November 1981 the star switch and station controller interface were not operational, so the local CRT terminal was the only viable means with which to interface with the USCI.

To communicate with the microwave subsystem controller, the operator has seven basic commands at his disposal for either the USC or the USCI. From these basic commands he can configure and modify the signal flow, change the polarization and inject test signal and noise signals for calibration. He may also request assistance to better understand the commands and modes at his disposal. He may inquire as to the health and status of the equipment or completely initialize the system.

Operator input of long command names could be a source of errors and delays in configuring any computer-controlled equipment, so a command name recognition scheme was developed. The command names can be abbreviated down to as few characters as needed to uniquely identify them. For example, CON is sufficient to uniquely identify CONFIGURE, since no other command begins with that letter sequence. The alternate command name text, CFG, is included for that particular command in order to handle entry of this commonly used abbreviation. Multiple word command designators can be similarly shortened. For example, ST COM successfully selects STATUS COMPRESSED. All characters typed in are verified against the referenced command, and misspelled command names, in whole or in part, are not accepted.

## VI. Additional Developments

The antenna microwave subsystem controller has been in operation at the Venus site for almost a year with no major problem. Operator acceptance of the commands and responses has been good and no operational difficulties have been encountered.

The implementation of this prototype has demonstrated that some areas need additional development. Some modifications are needed to this prototype to meet all the desired functions required to provide full control to the station controller and to provide the flexibility to accommodate changes to the microwave system.

The communication package used between the USC/USCI should operate under interrupt control. Preliminary software has been written to implement this interrupt control package and simulation tests have proven successful. As time permits,

this package will be integrated into the prototype at the Venus site and fully tested.

The area of software interlocks with the transmitter and station operator needs some improvements. The total software control of interlocks and inhibits may not be advisable but some software monitoring and automatic reporting as a back-up function should be considered. To accomplish these changes in a real-time executive program would result in timing questions to be resolved, because such a fail safe system requires periodic servicing within some time limits.

Most DSN systems change or evolve as the requirements change. To accommodate such changes the system-dependent data such as switch functions, channel assignments and configuration should be designed into table form. These tables should be readily adaptable to additions and changes. To implement a change, the data tables should be confined or isolated to a limited set of memory hardware. This gives the implementer the opportunity of changing the data table in the particular set of ROMs without disturbing any software routines. The field changes to the configuration control equipment will consist of replacing a relatively few number of ROMs containing configuration data tables without replacing the entire software programs. The operating programs should not be hardware dependent. After a given modification the man-machine interface should be no different except for the additions of the new equipment.

A maintenance routine is needed to cycle failed equipment for possible recovery. This routine would be called automatically if a switch failed to arrive in the commanded position. The switch would be commanded to reverse its direction, then return to the commanded position. After such an exercise, if the switch again failed, then the operator would be advised.

The USCI operating programs need to be transferred to PROMs and installed within the USCI chassis. The system has performed well using the floppy disk drive but a more permanent long-term solution is required.

## Acknowledgment

The author would like to acknowledge the work of Dave Nixon and Prentiss Knowlton, who devoted their time and effort to produce this first-generation Microwave Subsystem Controller.

## References

1. Withington, J. R., "Second-Generation X/S Feedcone: Capabilities, Layout and Components, *TDA Progress Report 42-63*, pp. 97-103, Jet Propulsion Laboratory, Pasadena, Calif., June 15, 1981.

**Table 1. Single board computer cards for the USCI**

| Part number | Card description | Function |
|---|---|---|
| BLC-80/204 | CPU | Program control |
| BLC-8064 | RAM, 64K | Read/write memory for USCI |
| iSBC-534 | Serial I/O 4 channels | USCI-USC communication, local maintenance, terminal interfaces |
| BLC/8201 | Disk control | Floppy disk program, memory control |

**Table 2. Single board computer cards for the USC**

| Part number | Card description | Function |
|---|---|---|
| BLC-80/204 | CPU | Program control |
| BLC-8064 | RAM, 64K | Read/write memory |
| BLC-8432 | ROM, 32K | Read only memory |
| iSBC-534 | Serial I/O 4 channels | USCI-USC communication, local maintenance, terminal interfaces |
| SBC-519 | Parallel I/O | Switch commands and indicates |

**Table 3. Software Module Descriptions**

| Routine name | Incorporated in | Description |
|---|---|---|
| BAD COMMAND | | |
| BAD & CMD | USC/USCI | Reports unrecognizable commands to operator |
| CONFIGURE | | |
| USCCFG | USC | Processes the USC configure command, verifies that it has been correctly specified, and that the functions can be performed before exeucting the command |
| DEBUG | | |
| DEBUG | USC/USCI | Provides software debugging as a tool for program development |
| DIRECTORY | | |
| USI DIR | USCI | Processes the USCI Directory command, verifies that it has been correctly specified, and displays detailed information to the USCI operator |
| EXEUCTIVE COMMAND | | |
| USI | USCI | Main executive program for the USCI which handles operator interaction through the maintenance terminal as well as the machine interaction through the Host, in order to process the high level requests for microwave switch control and to translate to the low level requests for processing by the USC. Status information is translated to high level responses. |
| USC | USC | Main executive program for the USC which handles operator interaction through the maintenance terminal as well as the machine interaction through the USCI, in order to process requests for microwave switch control for up to 16 four-position switches |
| HELP | | |
| USIHLP | USCI | Displays helpful information on USCI operation to the operator |
| USCHLP | USC | Displays helpful information on USC operation to the operator |
| INITIALIZE | | |
| USIINI/USCINI | USC/USCI | Performs initialization after a power up, or as a result of processing the initialize command |
| MODIFY | | |
| USIMOD | USCI | Processes the USCI MODIFY command, verifies that it has been correctly specified, and passes a detailed modification specification to the USC via the MODIFY command |
| SELF TEST | | |
| MTEST | USC/USCI | Provides memory test and report errors to operator |
| STATUS | | |
| USISTS | USCI | Generates a USCI switch status report for the operator |
| USISTI | USCI | Generates a USCI interlock status report for the operator |
| USISTC | USCI | Generates a USCI compressed status report (typically for use by a higher level processor) |
| USCSTC | USC | Generates a USC compressed status report (typically for use by the USCI) |
| USCSTA | USC | Generates a USC status report for the operator (typically at the maintenance terminal) |
| TRANSFER | | |
| USITRA | USCI | Processes the USCI transfer command, verifies that it has been correctly specified, and passes a detailed configuration via the configure command down to the USC. |

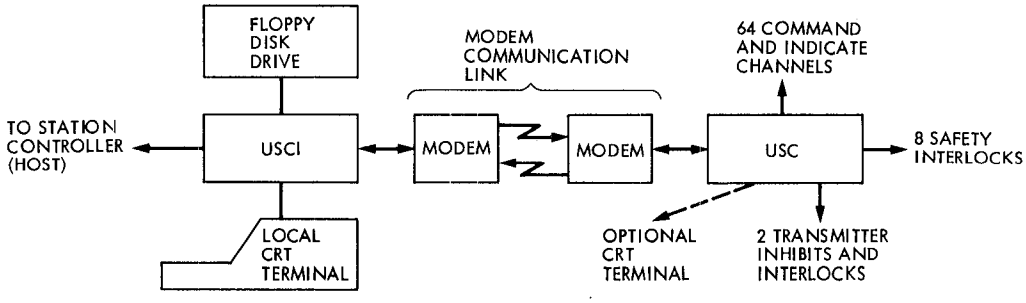


**Fig. 1. Antenna Microwave Subsystem Controller functional block diagram**

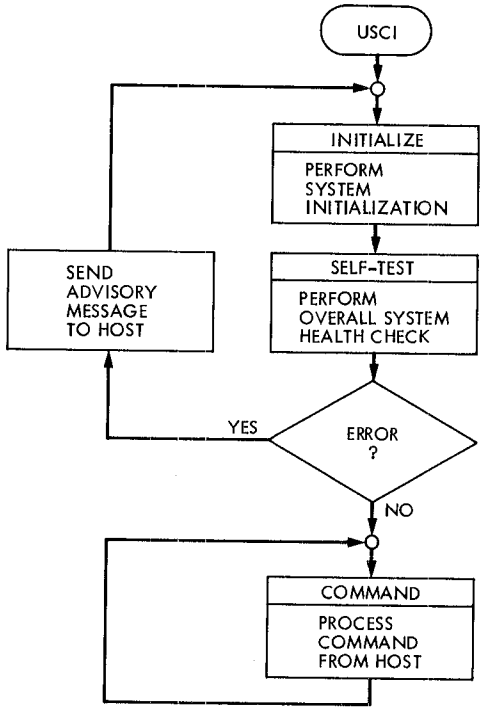


**Fig. 2. USCI software flow diagram: Initialize USCI and process USCI command sequence**

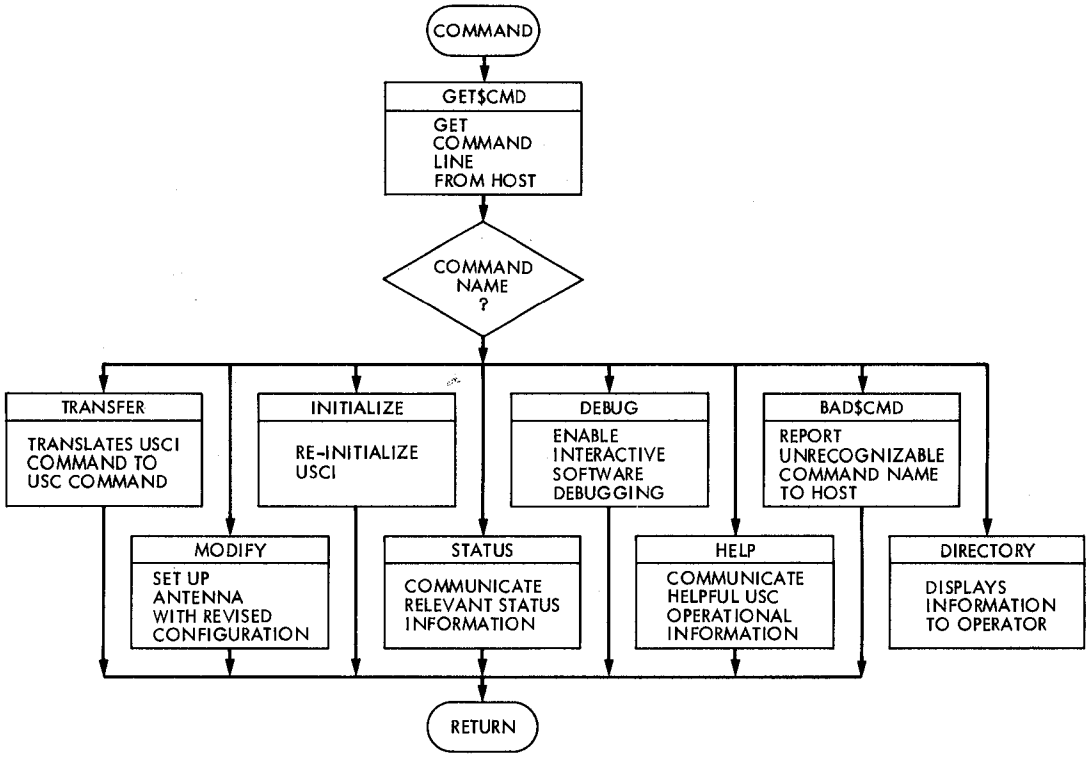


**Fig. 3. USCI software flow diagram: Process command from Host**

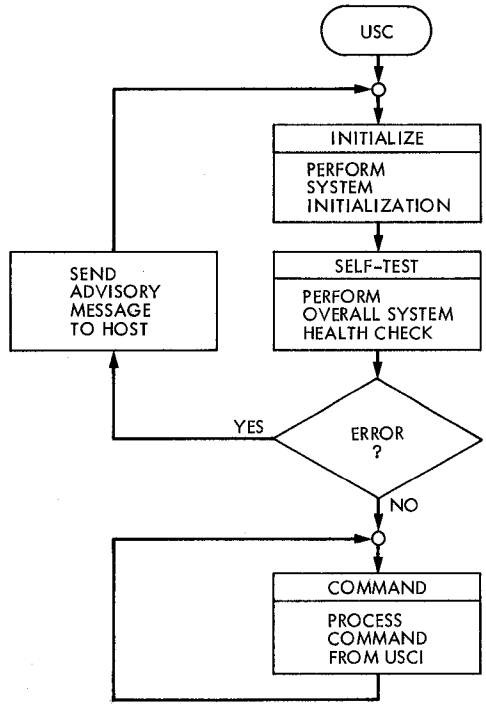


**Fig. 4. USC software flow diagram: Initialize USC and process USC command sequence**

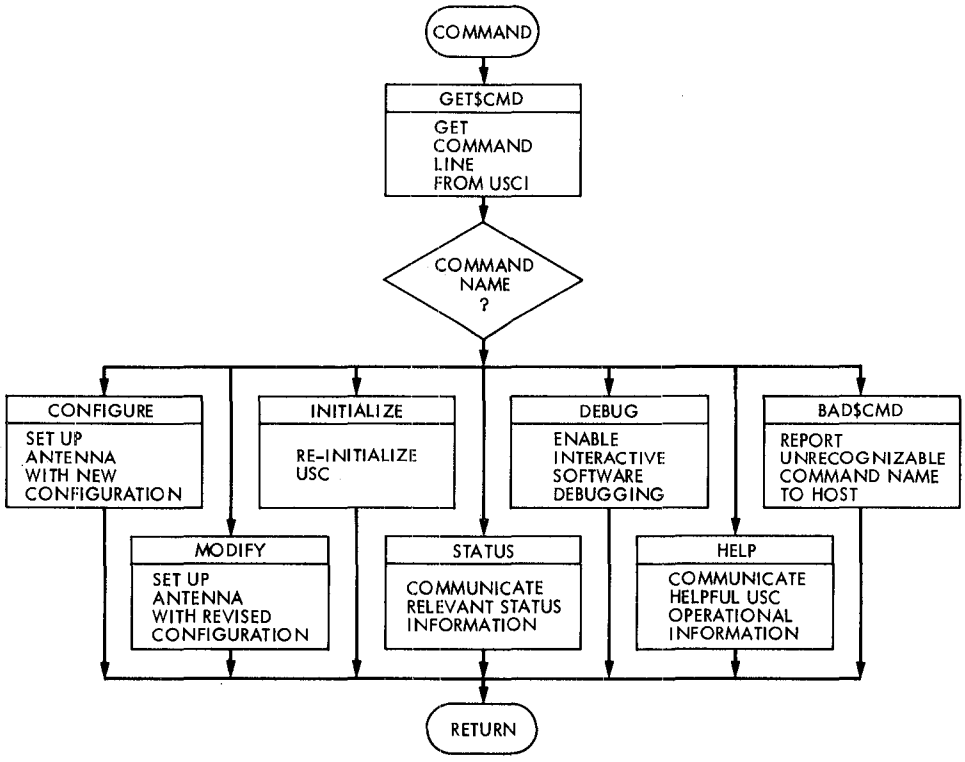


**Fig. 5. USC software flow diagram: Process command from USCI**

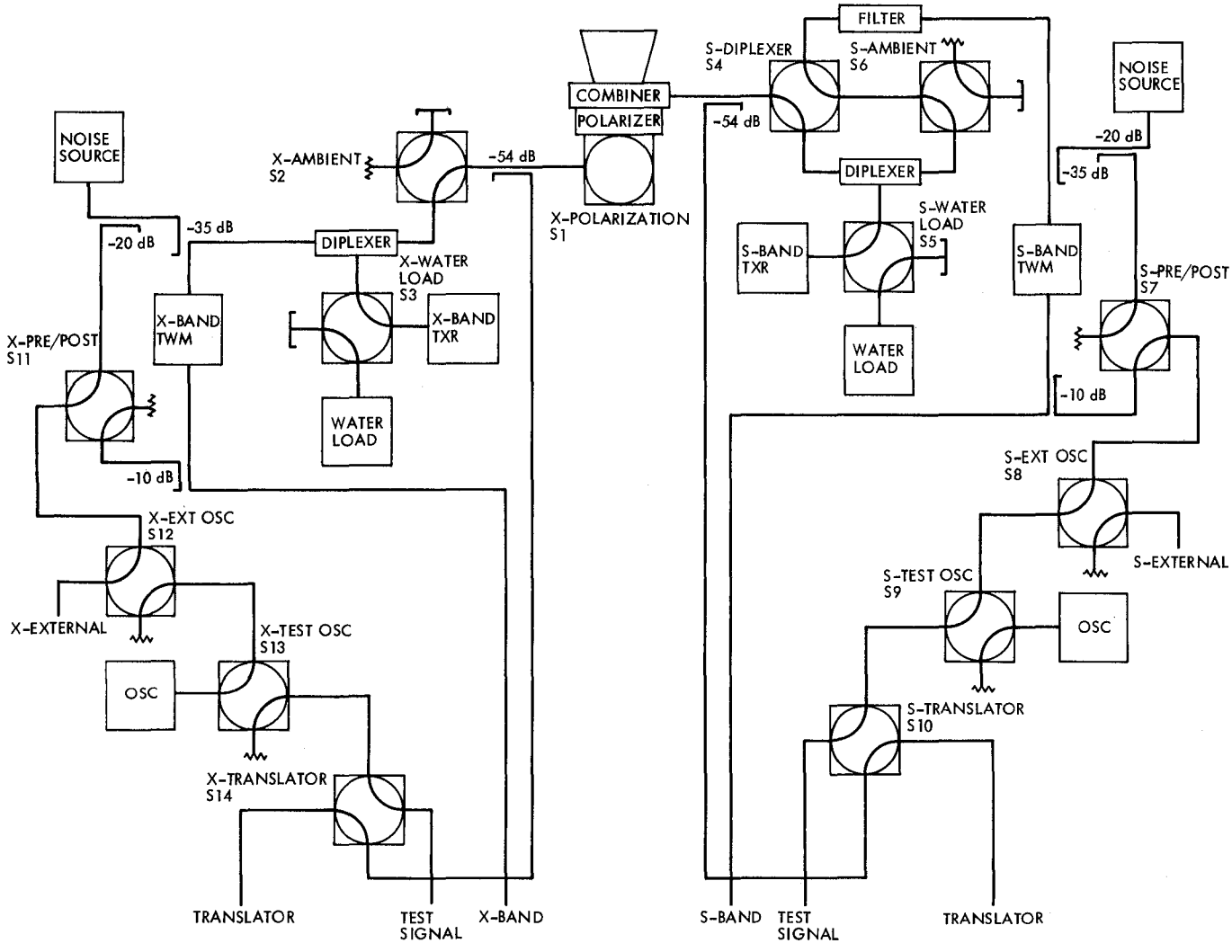


**Fig. 6. Antenna Microwave Subsystem functional block diagram for the feedcone**

# Thermal Analysis of the X-Band 34-Meter Antenna Feedcone

R. D. Hughes
Ground Facilities and Antenna Engineering Section

*A thermal analysis was done to describe feedcone shell temperature profiles and induced thermal stresses in waveguide components. IMP-SS, a steady-state version of the thermal analysis computer program employing the implicit alternating-direction numerical technique documented in a previous report, was used to analyze the two-dimensional regions of the feedcone. This portion of the analysis determined the free relative displacement of the feedcone for a worst-case thermal condition.*

## I. Introduction

A newly developed X-band (8.4-GHz) feedcone configuration has been designed for the latest generation of 34-meter antennas to be installed at the Goldstone, Canberra, and Madrid Deep Space Communication Complexes. A potential problem of excessive stress due to environmental thermal effects was identified when the feedcone and inside waveguide component design was under review. To make an accurate estimate of the stress, a detailed thermal analysis depicting temperature distributions along the feedcone shell was necessary. The remaining portion of this analysis then involved computing the free relative displacement between the waveguide and the feedcone structure to which it is attached for a given worst-case condition. The free relative displacement is the displacement of the reference point shown in the feedcone configuration in Fig. 1 that would occur if the shell was unconstrained by connections to the waveguide components. The calculated value of displacement will be used by a separate analysis to calculate stresses in waveguide members.

The temperature distribution calculations were performed by using a general-purpose two-dimensional thermal analysis computer program developed by R. Hughes (Ref. 1). The program used the implicit alternating-direction finite difference technique to analyze systems represented in lumped parameter, electrical analog form. A program version, called IMP-SS, which models a region having steady-state boundary conditions, was developed to suit this particular problem.

## II. Configuration Description and Assumptions

The thermal stability of the feedcone interior region is maintained within certain limits (18.3 to 25.6°C (65 to 78°F)) by an air-conditioning system, while the exterior is subject to environmental effects. This thermal analysis was based upon worst-case thermal conditions, assumed to be 54.4°C (130°F) average exterior ambient temperature and 26.7°C (80°F) interior ambient. Also, a "zero-stress" condition was assumed if both interior and exterior components are at 26.7°C. Thus, as the feedcone shell temperature increases above 26.7°C (80°F), thermally-induced stresses will occur by an amount $\delta_T$, the vertical displacement of the reference location shown in Fig. 1. This is the displacement that would occur if the shell were

free to expand (the maser/waveguide components were not connected to the feed horn). Therefore, the major portion of this analysis involved determining the temperature distribution of the shell. The feedcone shell consists of structural components covered by a thin aluminum skin insulated on the interior side.

The exterior ambient temperature was represented by the average of shell surface temperatures on the cone side facing the sun and the side away from the sun during peak solar levels. The temperature of a point on the shell surface facing furthest away from the sun was assumed to be 46.1°C (115°F), corresponding to the maximum expected air temperature at Goldstone, California. The temperature of a point on the surface facing most directly toward the sun was assumed to be 16.7°C (30°F) greater than the shady side, or 62.8°C (145°F). The assumption of a 16.7°C temperature difference was based upon field temperature measurements taken at the feedcone of the nearby 26-meter antenna located at Deep Space Station 13 (Venus), as well as from data in Ref. 2 pertaining to the instrument tower windshield of the 64-meter antenna located at Deep Space Station 14 (Mars).

The feedhorn component of the feedcone was assumed to also be exposed to an ambient exterior temperature of 54.4°C. Since the feedhorn is uninsulated, the representative horn wall temperature was assumed to be the average between the inside and outside ambient temperatures, $T_{horn}$ = 40.6°C (105°F).

The feedcone shell thermal expansion was assumed to be characterized by a one-dimensional temperature profile in the axial direction. Thus, the representative shell temperature was computed as the integrated average of the composite temperature profile in the axial direction:

$$\overline{T}_{shell} = \frac{1}{L}\int_0^L T\,dy$$

## III. Analysis

The IMP-SS computer program was used to determine the temperature distributions for three types of thermal regions of the feedcone shell (1) the intersection of the maser floor with the skin, (2) the intersection of a stiffening ring with the skin, and (3) the intersection of a vertical stiffener with the skin, as indicated in Fig. 1. The skin was represented as a one-dimensional thermal region in these analyses as shown in the thermal node networks of Figs. 2 through 4. These thermal networks are either horizontal (skin-stiffener intersection) or vertical (skin-floor and skin-ring intersections) cuts through the shell. In both cases, the curvature of the shell was neglected so that the analysis could be done in rectangular coordinates. Figs. 5 through 7 show the actual configurations before being transformed to the representative ones used in the model.

The following four boundary conditions were applied to each of the three thermal networks in Figs. 2 through 4: (1) a line of symmetry, (2) an interior ambient temperature of 26.7°C, (3) an exterior ambient temperature of 54.4°C, and (4) a prescribed temperature profile at a sufficient distance from a "thermal disturbance" (i.e., the intersection of ring and skin) so that the temperature distribution from the inside to the outside across the wall thickness, including insulation, becomes one dimensional and may be predicted analytically for a composite wall. This analytical composite wall result is shown in Fig. 8 for two inside and outside temperatures. The computations and material properties are described in the Appendix.

## IV. Results

The resulting temperature distributions for pertinent nodes of the three thermal region types are shown in Tables 1 through 3. The parts of the tables enclosed in solid lines indicate temperatures in the skin and the attached structural component (ring, stiffener, and floor). The vertical stiffeners appear to have an influence on the skin temperature of only about 0.5°C (1°F) and therefore the effect of stiffeners on skin temperature was neglected. The skin temperature profiles for the skin-ring and skin-floor intersection regions are shown in Fig. 9. These profiles indicate a significant thermal influence upon skin temperature. Note that both are asymptotic to the undisturbed skin temperature, and are reasonably close to it at the boundary of the thermal network modeled.

These profiles were mapped onto appropriate regions of the feedcone skin, resulting in an overall skin temperature profile that is a composite of the individual profiles. Although the various stiffening rings differ in dimension, it was felt that the ring configuration modeled was typical, and the use of one profile for all ring regions provided an acceptable level of detail for this analysis. The skin temperature profile was integrated along the axial length of the feed cone surface to determine an integrated average skin temperature of 48.6°C (119.4°F).

The average temperature of the stiffener cross section was estimated from Table 1 to be 51.4°C (124.5°F). This temperature was combined with the average skin temperature to give a weighted average shell temperature based on cross-sectional area:

$$\overline{T}_{shell} = 49.7°C\ (121.3°F)$$

The resulting shell expansion in the axial direction was 0.196 cm (0.077 in.). This expansion would be directed upward in Fig. 1. The axial thermal expansion of the feedhorn was calculated to be 0.038 cm (0.015 in.), directed downward. Thus, the net displacement of the reference location is:

$$\delta_T = 0.157 \text{ cm } (0.062 \text{ in.})$$

based on the assumptions made in this analysis. Calculation details regarding the skin temperature profile and deflections are given in the appendix.

## References


1. Hughes, R. D., "The Application of the Implicit Alternating Direction Numerical Technique to Thermal Analysis Involving Conduction and Convection," *Telecommunications and Data Acquisition Progress Report 42-73*, Jet Propulsion Laboratory, Pasadena, Calif., May 1983.

2. McGinness, H. D., "210-Ft. Antenna Tower Positional Stability," *DSN Space Programs Summary No. 37-50*, Vol. II, Jet Propulsion Laboratory, Pasadena, Calif., March 1968.

**Table 1. Skin-stiffener region temperature distribution, °C**

| Vertical node, $I$ | Horizontal nodes, $J$ [a] | | | | | | | | | | | |
|---|---|---|---|---|---|---|---|---|---|---|---|---|
| | 1 | 2 | 3 | 4 | 5 | 6 | 7 | 8 | 9 | 10 | 11 | 12 |
| 1 | 26.7 | 26.7 | 26.7 | 26.7 | 26.7 | 26.7 | 26.7 | 26.7 | 26.7 | 26.7 | 26.7 | 26.7 |
| 2 | 47.5 | 51.3 | 47.5 | | | | | | | | | |
| 3 | 49.5 | 51.4 | 49.6 | | | | | | | | | |
| 4 | 50.3 | 51.4 | 50.3 | | | | | | | | | |
| 5 | 50.6 | 51.4 | 50.6 | | | | | | | | | |
| 6 | 50.9 | 51.4 | 50.9 | | | | | | | | | |
| 7 | 51.1 | 51.5 | 51.1 | | | | | | | | | |
| 8 | 51.2 | 51.5 | 51.2 | | | | | | | | | |
| 9 | 51.4 | 51.5 | 51.4 | | | | | | | | | |
| 10 | 51.5 | 51.6 | 51.5 | 51.4 | 51.2 | 50.8 | 50.0 | | | | | |
| 11 | 51.6 | 51.6 | 51.6 | 51.6 | 51.6 | 51.6 | 51.1 | 50.9 | 50.9 | 50.9 | 50.9 | 51.0 |
| 12 | 51.6 | 51.6 | 51.6 | 51.6 | 51.6 | 51.6 | 51.7 | 51.8 | 51.9 | 52.0 | 52.0 | 52.2 |
| 13 | 54.4 | 54.4 | 54.4 | 54.4 | 54.4 | 54.4 | 54.4 | 54.4 | 54.4 | 54.4 | 54.4 | 54.4 |

[a]Refer to Fig. 2 for node network configuration.

**Table 2. Skin-floor region temperature distribution, °C**

| Vertical node, $I$ | Horizontal nodes, $J$ [a] | | | | | | | | | | | | |
|---|---|---|---|---|---|---|---|---|---|---|---|---|---|
| | 1 | 2 | 3 | 4 | 5 | 6 | 7 | 8 | 9 | 10 | 11 | 12 | 13 |
| 1 | 26.7 | 26.7 | 26.7 | 26.7 | 26.7 | 26.7 | 26.7 | 26.7 | 26.7 | 26.7 | 26.7 | 26.7 | 26.7 |
| 2 | 26.7 | 27.8 | 26.7 | | | | | | | | | | |
| 3 | 26.7 | 29.0 | 26.7 | | | | | | | | | | |
| 4 | 26.7 | 30.3 | 26.7 | | | | | | | | | | |
| 5 | 26.8 | 31.9 | 26.8 | | | | | | | | | | |
| 6 | 26.8 | 34.1 | 26.8 | | | | | | | | | | |
| 7 | 31.2 | 36.0 | 31.2 | | | | | | | | | | |
| 8 | 36.1 | 36.9 | 36.1 | | | | | | | | | | |
| 9 | 39.6 | 37.5 | 39.6 | 42.8 | 45.0 | 46.5 | 47.5 | 48.2 | 49.0 | 49.4 | 49.6 | 49.7 | 49.9 |
| 10 | 40.8 | 37.8 | 40.8 | 44.4 | 46.8 | 48.5 | 49.7 | 50.4 | 51.2 | 51.7 | 52.0 | 52.1 | 52.2 |
| 11 | 54.4 | 54.4 | 54.4 | 54.4 | 54.4 | 54.4 | 54.4 | 54.4 | 54.4 | 54.4 | 54.4 | 54.4 | 54.4 |

[a]Refer to Fig. 3 for node network configuration.

**Table 3. Skin-ring region temperature distribution, °C**

| Vertical node, $I$ | Horizontal nodes, $J$[a] | | | | | | | | | | | | |
|---|---|---|---|---|---|---|---|---|---|---|---|---|---|
| | 1 | 2 | 3 | 4 | 5 | 6 | 7 | 8 | 9 | 10 | 11 | 12 | 13 |
| 1 | 26.7 | 26.7 | 26.7 | 26.7 | 26.7 | 26.7 | 26.7 | 26.7 | 26.7 | 26.7 | 26.7 | 26.7 | 26.7 |
| 2 | 26.7 | 43.6 | 26.7 | | | | | | | | | | |
| 3 | 26.7 | 43.7 | 26.7 | | | | | | | | | | |
| 4 | 26.7 | 43.8 | 26.7 | | | | | | | | | | |
| 5 | 33.4 | 43.9 | 33.4 | | | | | | | | | | |
| 6 | 40.1 | 44.2 | 40.1 | | | | | | | | | | |
| 7 | 44.6 | 44.3 | 44.6 | 46.0 | 47.2 | 48.0 | 48.5 | 48.9 | 49.3 | 49.6 | 49.7 | 49.8 | 49.9 |
| 8 | 46.1 | 44.4 | 46.1 | 48.0 | 49.3 | 50.1 | 50.8 | 51.2 | 51.6 | 51.9 | 52.0 | 52.1 | 52.2 |
| 9 | 54.4 | 54.4 | 54.4 | 54.4 | 54.4 | 54.4 | 54.4 | 54.4 | 54.4 | 54.4 | 54.4 | 54.4 | 54.4 |

[a]Refer to Fig. 4 for node network configuration.

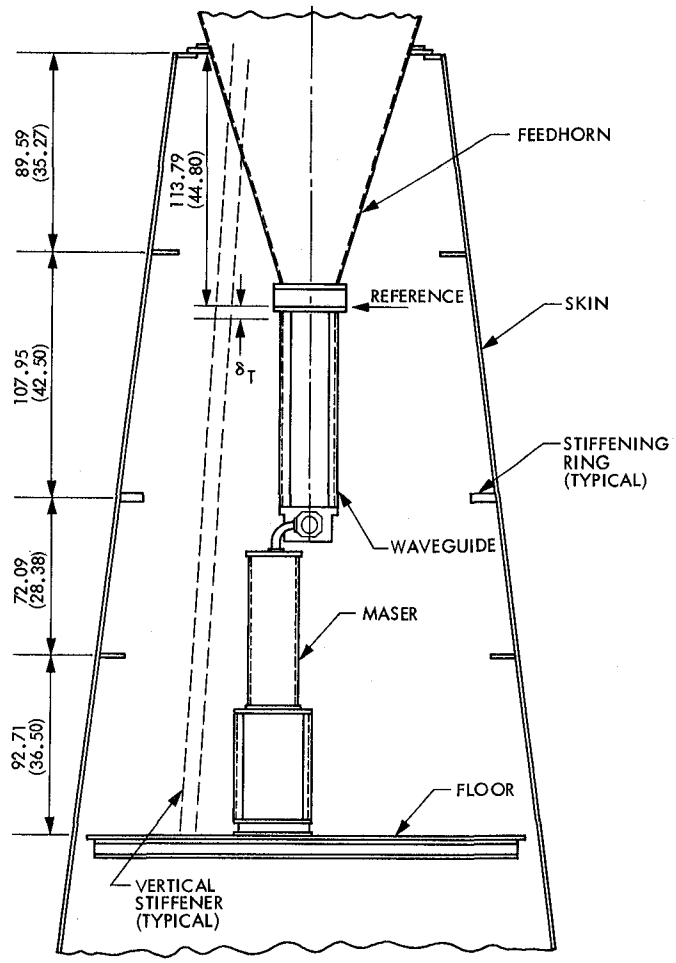


**Fig. 1. 34-meter antenna feedcone configuration**

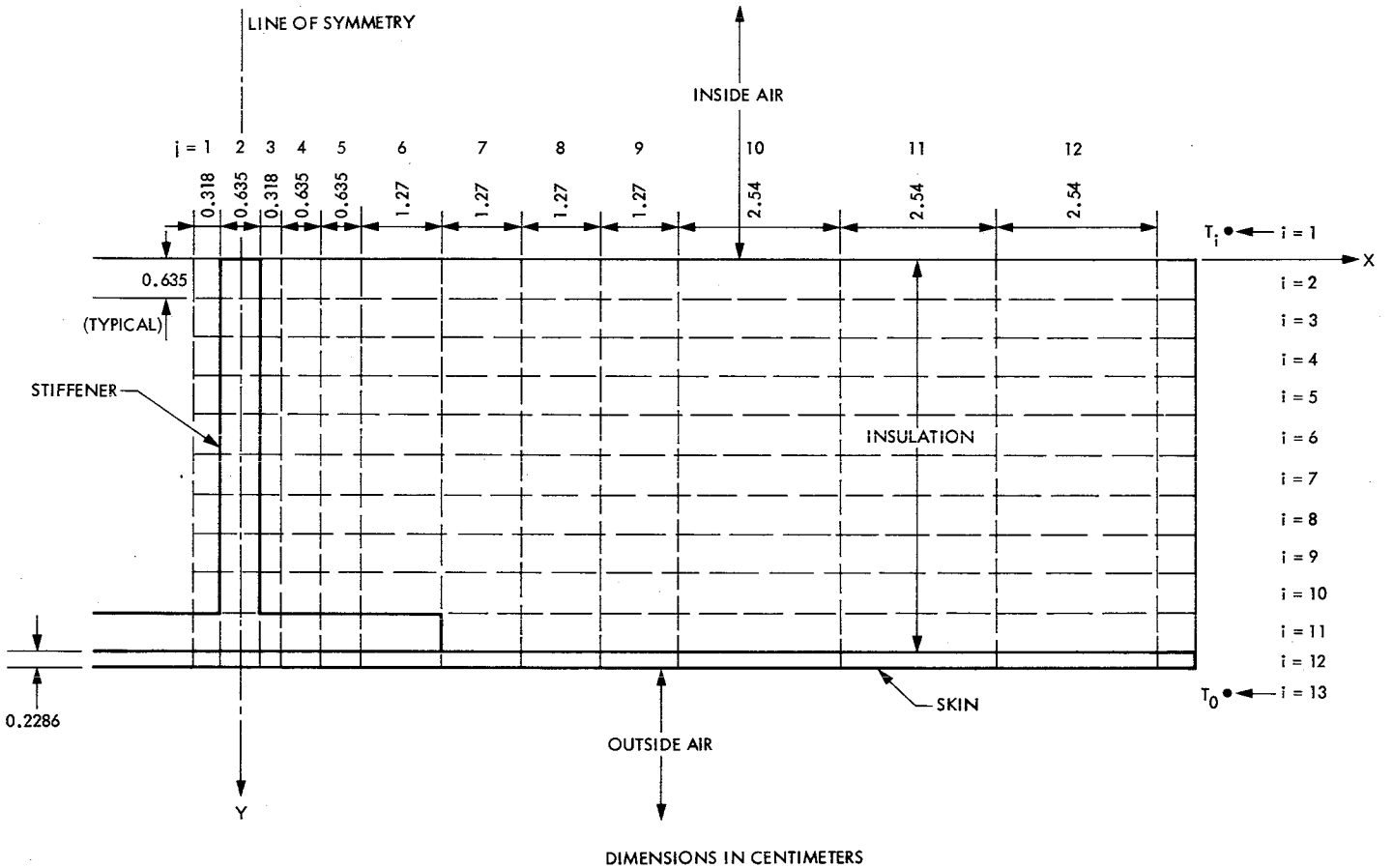


**Fig. 2. Thermal cells: skin with vertical stiffener**

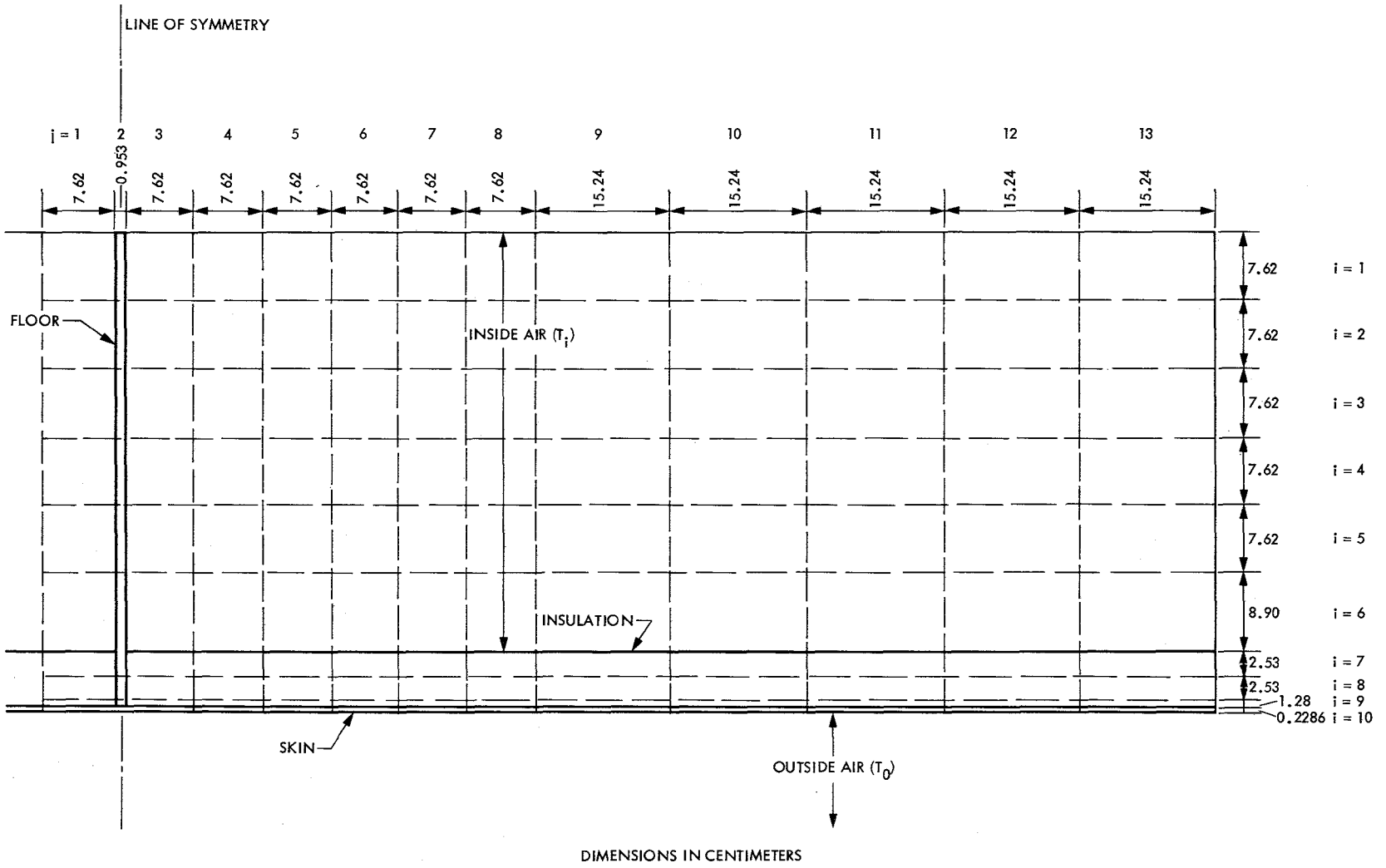


**Fig. 3. Thermal cells: skin and floor intersection**

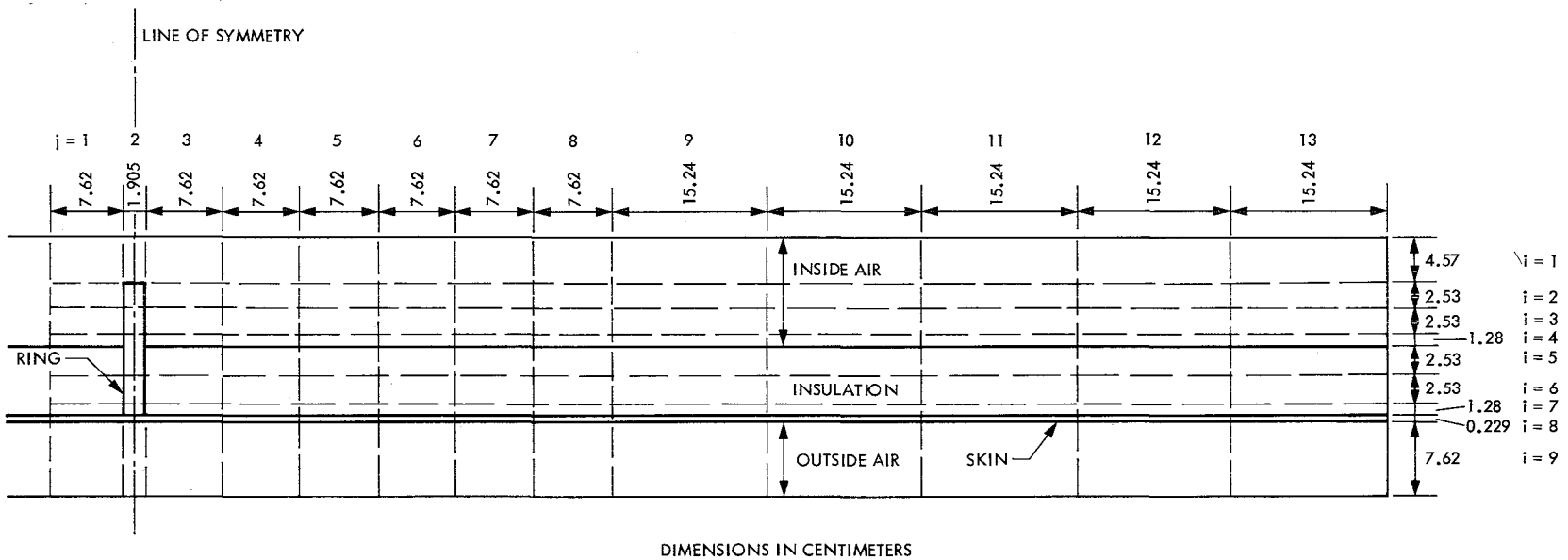


**Fig. 4. Thermal cells: skin and ring intersection**

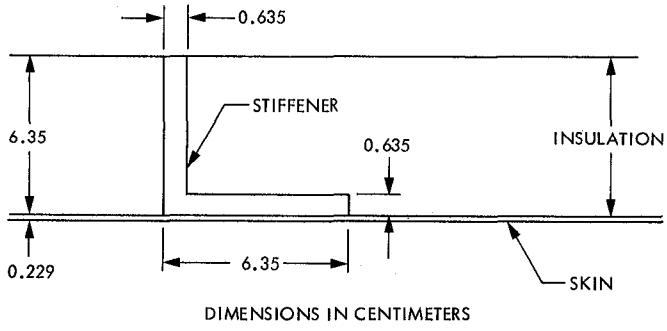


**Fig. 5. Vertical stiffener actual configuration**

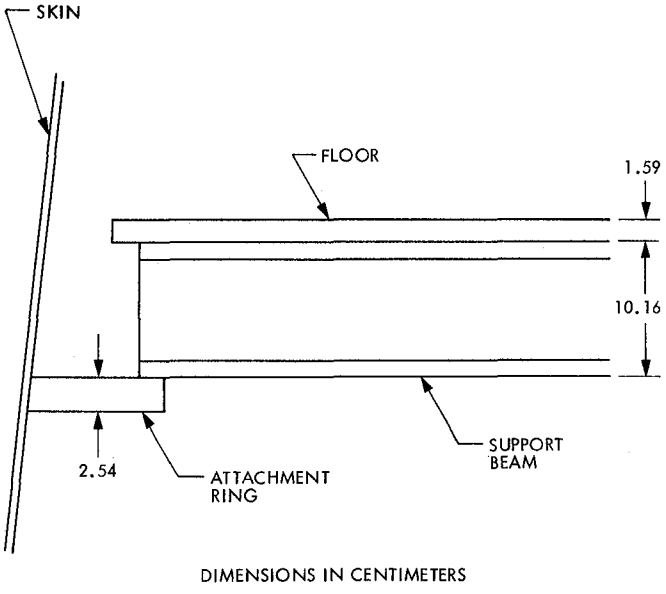


**Fig. 6. Skin: floor region actual configuration**

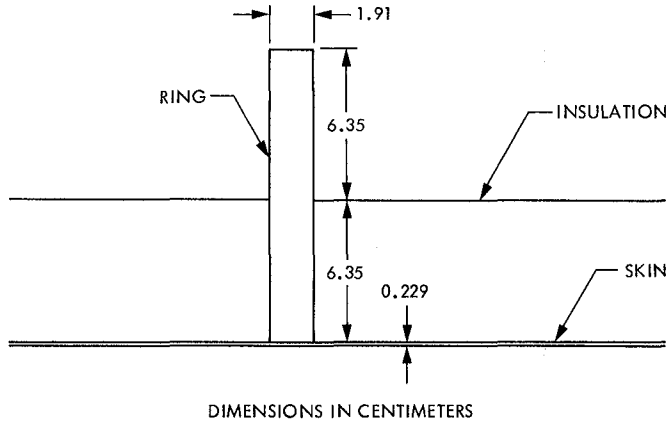


**Fig. 7. Skin: ring region actual configuration**

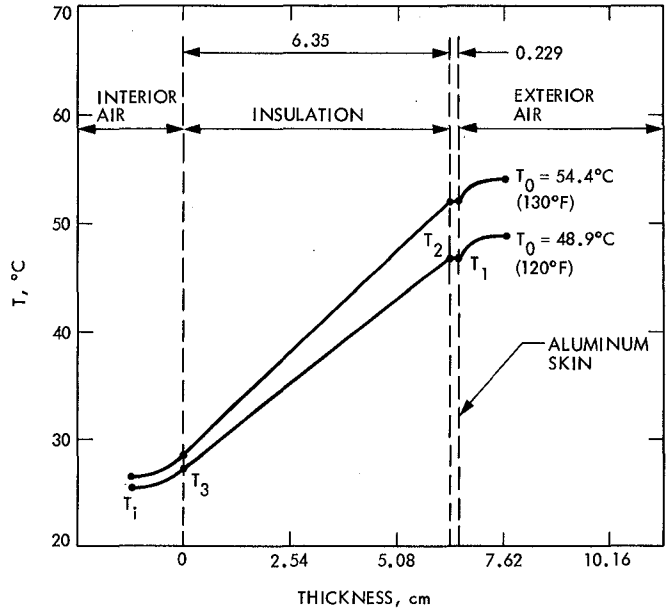


**Fig. 8. One-dimensional wall temperature profiles**

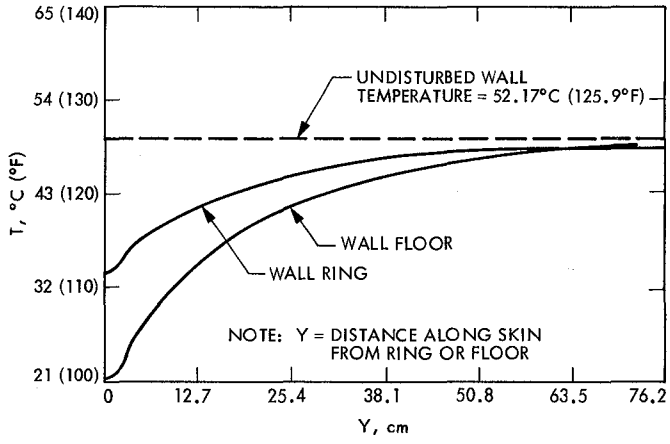


**Fig. 9. Skin temperature profiles**

# Appendix

# Computational Procedure

## I. One-Dimensional Wall Temperature Profile

The temperature profiles shown in Fig. 8 are derived by first calculating the steady-state heat flux according to the relationship for a composite wall:

$$q = \frac{T_0 - T_i}{\frac{1}{h_0} + \frac{X_1}{k_{sk}} + \frac{X_2}{k_{ins}} + \frac{1}{h_i}}$$

where:

$q$ = heat flux into the wall, W/m$^2$

$h_0$ = outside heat transfer coefficient = 8.29 W/m$^2$ - C

$k_{sk}$ = conductivity of skin = 154.9 W/m - C

$k_{ins}$ = conductivity of insulation = 0.052 W/m - C

$X_1$ = thickness of skin = 0.00229 m

$X_2$ = thickness of insulation = 0.0635 m

$h_i$ = inside heat transfer coefficient = 8.29 W/m$^2$ - C

$T_0$ = outside air temperature = 54.4°C (130°F)

$T_i$ = inside air temperature = 26.7°C (80°F)

which gives:

$$q = 18.94 \text{ W/m}^2.$$

Local temperatures, as depicted in Fig. 8, are calculated from the relations:

$$T_1 = t_0 - \frac{q}{h_0}$$

$$T_2 = T_1 - \frac{q X_1}{k_{sk}}$$

$$T_3 = T_2 - \frac{q X_2}{k_{ins}}$$

which give:

$$T_1 = 52.2°\text{C}, T_2 = 52.2°\text{C}, T_3 = 29.06°\text{C}.$$

## II. Skin Temperature Profile Calculation

The feedcone skin was divided into regions as shown in Fig. A-1. The appropriate temperature profile (Fig. 9) was applied to each region, and the integrated average in each region was determined by:

$$\bar{T}_i = \frac{1}{L} \int_0^L T \, dy$$

The results are as follows:

| Region | $L$, cm | $T$, °C |
|---|---|---|
| 1 | 46.36 | 46.50 |
| 2 | 46.36 | 48.89 |
| 3 | 36.04 | 48.39 |
| 4 | 36.04 | 48.39 |
| 5 | 53.98 | 49.22 |
| 6 | 53.98 | 49.22 |
| 7 | 44.96 | 48.83 |
| 8 | 44.96 | 48.83 |

Although this procedure involved "cutting off" the profiles to conform to the distances between rings, the temperatures at the locations on the skin furthest from the rings differed from the "undisturbed wall temperature" (52.17°C) by only a maximum of 1°C. Thus, no attempt was made to refine the model to take this condition into account, since any error would be well within the scope of accuracy already incorporated.

Note also that the cone angle (~ 7 deg) was neglected in mapping the temperature profiles onto the skin; the profiles were integrated in terms of axial length. This represents an error of less than 1%.

The overall integrated average skin temperature was then calculated by:

$$\bar{T}_{skin} = \sum_i (\bar{T}_i L_i) / \sum_i L_i$$

which gives:

$$\overline{T}_{skin} = 48.6°C$$

The average stiffener temperature, as given in the text was 51.4°C. The representative shell temperature was taken to be the weighted average of the skin and stiffener temperatures according to cross-sectional area. Representative areas were taken at midheight of the cone where: diameter = 197.9 cm, the cross-sectional area of the skin between two stiffeners = 11.85 $cm^2$, and the cross-sectional area of a stiffener = 7.66 $cm^2$.

The resulting weighted average shell temperature is $\overline{T}_{shell}$ = 49.7°C.

## III. Free Relative Displacement

The axial expansion of the shell is given by:

$$\delta_s = \mu L \Delta T$$

where:

$\mu$ = coefficient of thermal expansion = 0.0000234/°C for 6061-T6 aluminum

$L$ = axial length (height) of cone section from floor to top of feed horn = 362.7 cm

$\Delta T$ = temperature differential = 49.7°C - 26.7°C = 23°C

which gives:

$$\delta_s = 0.195 \text{ cm}$$

Note that this displacement would be upward in Fig. A-1.

The axial displacement of the feedhorn is determined according to the conditions:

$$L = 113.8 \text{ cm}$$

$$\Delta T = 40.6°C - 26.7°C = 13.9°C$$

which gives: $\delta_h$ = 0.0381 cm downward. The net free relative displacement of the reference location at the bottom of the feed horn is:

$$\delta_T = 0.195 \text{ cm} - 0.0381 \text{ cm}$$

or

$$\delta_T = 0.157 \text{ cm}$$

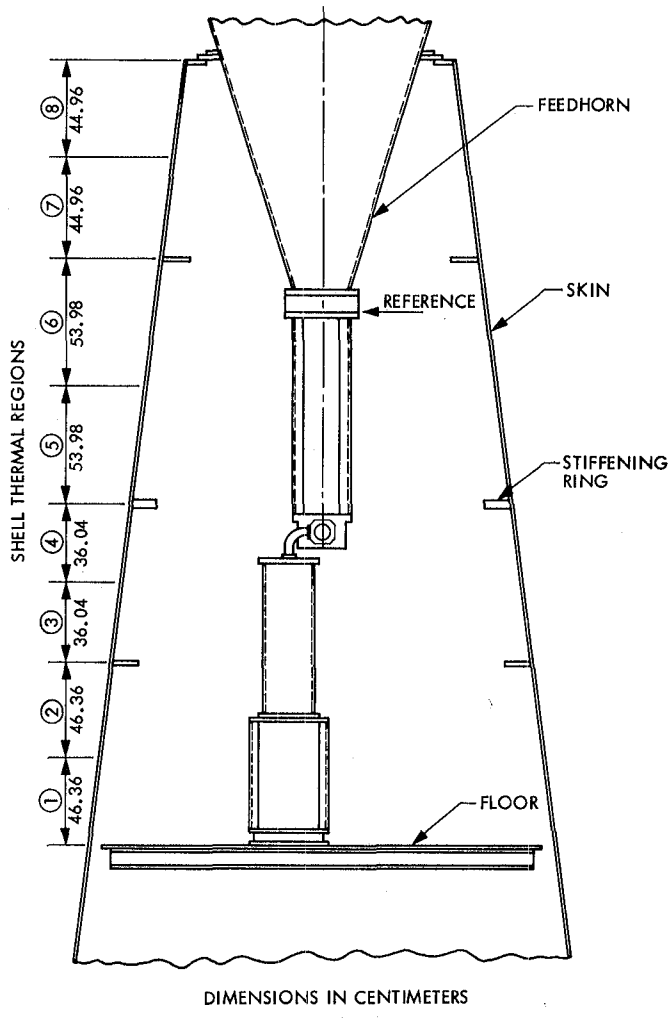


**Fig. A-1. Feed cone thermal regions**

# NASTRAN Structural Model for the Large 64-Meter Antenna Pedestal, Part I

C. T. Chian, M. S. Katow, and H. McGinness
Ground Antennas and Facilities Engineering Section

*Static analysis and a computer structural model for the large 64-m antenna pedestal are developed using the MSC version of the NASTRAN program. This model was necessary to conduct a variety of hydrostatic bearing rehabilitation studies. The results obtained from the model show that the top surface deflections due to pad loads are in good agreement with the results previously obtained from a simplified "shortcut" analytical model, and also in agreement with field measurements. In addition, the displacement and force distributions as well as the state of stress and strain are obtained.*

## I. Introduction

The hydrostatic bearing of the large 64-m antenna of the NASA Mars Deep Space Station (DSS 14) at Goldstone has experienced some oil leakage problems. A computer structural model, using the MSC version of NASTRAN, has been developed in order to support the current rehabilitation efforts of the hydrostatic bearing.

This article is the first in a series of reports on the static analysis performed for the pedestal under pressure loadings at the three hydrostatic bearing pads. The displacement and force distribution throughout the model as well as the state of stress and strain are obtained.

A separate model for the hydrostatic bearing runner is also being developed. The two models will be combined to form a runner-pedestal system for further hydrostatic bearing studies.

## II. Pedestal Description

A general arrangement of the hydrostatic bearing system for the 64-m antenna is shown in Fig. 1. The azimuth hydrostatic bearing, set on the pedestal top, supports the full weight of the moving parts of the antenna and permits a very low friction azimuth rotation on a pressurized oil film (Ref. 1). Three movable pad-and-socket assemblies float on the oil film over a stationary runner and support the three corners of the alidade base triangle as shown in Fig. 2. The stationary runner for the bearing and the three bearing pads are completely enclosed in an oil reservoir. The three hydrostatic bearing pads are equidistant from the central axis of the pedestal as shown in Fig. 3.

The pedestal is a two-story, reinforced concrete building 25.3 m (83 ft) in diameter, with a diaphragm top which has a concrete collar in the center; the pedestal supports the movable structure of the antenna. The wall thickness is 1.1 m (3.5 ft).

The three principal forces from the antenna alidade which act on the pedestal are: (1) vertical forces from the azimuth hydrostatic bearing pads, (2) rotational forces from the azimuth drives, and (3) horizontal forces on the azimuth radial bearing.

The three hydrostatic bearing pads, made of carbon steel, are 1.016 m (40 in.) wide, 1.524 m (60 in.) long, and 0.508 m

(20 in.) deep. There are six recesses in the bottom of each pad as indicated in Fig. 4, with the two center recesses being larger than the corner recesses. According to the original design specification, the pedestal concrete is required to have a Young's modulus of elasticity $E$ of $3.5 \times 10^{10}$ N/m$^2$ ($5.0 \times 10^6$ psi). However, it is believed that the current Young's modulus of elasticity for the pedestal concrete is less than this value, and a reduced value, consistent with current core-sample measurements, is assumed for this report.

## III. Model Description

All three pads are assumed to support the same amount of loads. Therefore, the pedestal is divided into three identical segments. Moreover, due to the symmetry with respect to the center line of the pad, each segment can be further divided into two segments.

As a consequence, a one-sixth segment of the pedestal, with angular span of 60°, is being developed in the present structural model as shown in Fig. 5. Appropriate boundary conditions are being applied to reflect the aforementioned symmetry.

The computer model comprises 630 six-sided solid elements with a total of 880 grid points as shown in Fig. 6.

It is pointed out in Appendix A that one of the three bearing pads (Pad No. 3) does support more load than the other two. The actual ratios of the loads in the three pads are approximately 9:9:11. However, in our modeling, the three pads are assumed to carry equal amounts of loading. A FORTRAN program was used to generate the grid. The model can be further modified to obtain a finer grid, if necessary.

The pedestal concrete is assumed to be homogeneous, with a reduced Young's modulus of elasticity $E$ of $2.8 \times 10^{10}$ N/m$^2$ ($4.0 \times 10^6$ psi). The hydrostatic pressure in the pad is exerted on the first three rows of the top pedestal surface, with an angular span of 3.75° as shown in Fig. 6. A uniform pressure of $6.9 \times 10^6$ N/m$^2$ (1000 psi) is assumed under the pad. The MSC (Macneal Schwendler Corp.) version of NASTRAN is used in the present static analysis of the pedestal model.

## IV. Comparison with Previous Work

Three approaches were followed to determine the pedestal surface deflection: a detailed NASTRAN computer model, an independent shortcut model, and field measurements.

First, the deflection map of the pedestal top surface, using NASTRAN for a uniform pad pressure of $6.9 \times 10^6$ N/m$^2$ (1000 psi), is shown in Figs. 7 and 8. The negative sign indicates a downward deflection (compressive) which is in the same direction as the applied pressure, while the positive sign indicates an upward deflection (tensile). The average deflection distribution for the top surface, as a function of the angular increment, is given in Fig. 9. The maximum deflection occurs at the outer edge. It has a relative deflection of 1.064 mm (0.0419 in.). If the average deflections are considered, the maximum deflection becomes 0.917 mm (0.0361 in.).

Second, a simplified shortcut analytical model was used which considered the pedestal as a semi-infinite plate (Appendix B and Fig. 10). The deflection at the pad center, for a pad pressure of $6.9 \times 10^6$ N/m$^2$ (1000 psi), was found to be 0.914 mm (0.036 in.). The pad center deflection derived from the present NASTRAN model is 0.935 mm (0.0368 in.). Third, a level measurement was conducted at the DSS 14 pedestal in which the maximum deflection was found to be 1.067 mm (0.042 in.). Hence, the comparison shows a good agreement among results obtained from the three different methods.

In addition to the top surface deflection, the present NASTRAN model gives additional information about the deflection and force distribution, as well as the state of stress and strain throughout the pedestal.

## V. Conclusions

The good correlation of the top pedestal surface deflection among the NASTRAN computer model, the independent shortcut analytical model, and the field measurement assures the validity of the present pedestal NASTRAN computer model. This detailed pedestal structural model will be useful to the current rehabilitation studies of the large antenna pedestal.

Additional work is planned to improve the present pedestal NASTRAN computer model by including the haunch areas in the new pedestal model and the actual pressure pattern of the oil under the pad.

The top surface deflection of the pedestal obtained from the newly proposed NASTRAN model will then be used as an input to an in-house computer program to determine the minimum oil film height under the pad.

## Acknowledgement

The authors acknowledge the assistance given by H. Phillips, F. Lansing, S. Rocci, V. Lobb, A. Riewe, D. McClure, F. McLaughlin, D. Wells, and J. Dyson during the various execution steps of this work.

## References

1. *The NASA/JPL 64-Meter-Diameter Antenna at Goldstone, California: Project Report*, Technical Memorandum 33-671, Jet Propulsion Laboratory, Pasadena, Calif., July 15, 1974.

2. Timoshenko, S., *Theory of Elasticity*, 1st ed., p. 92, McGraw-Hill, New York, 1934.

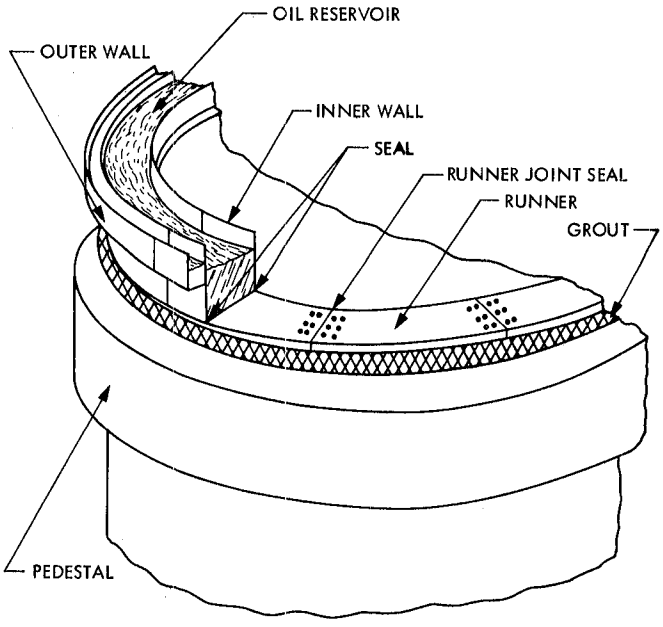


**Fig. 1. General arrangement of 64-m antenna hydrostatic bearing**

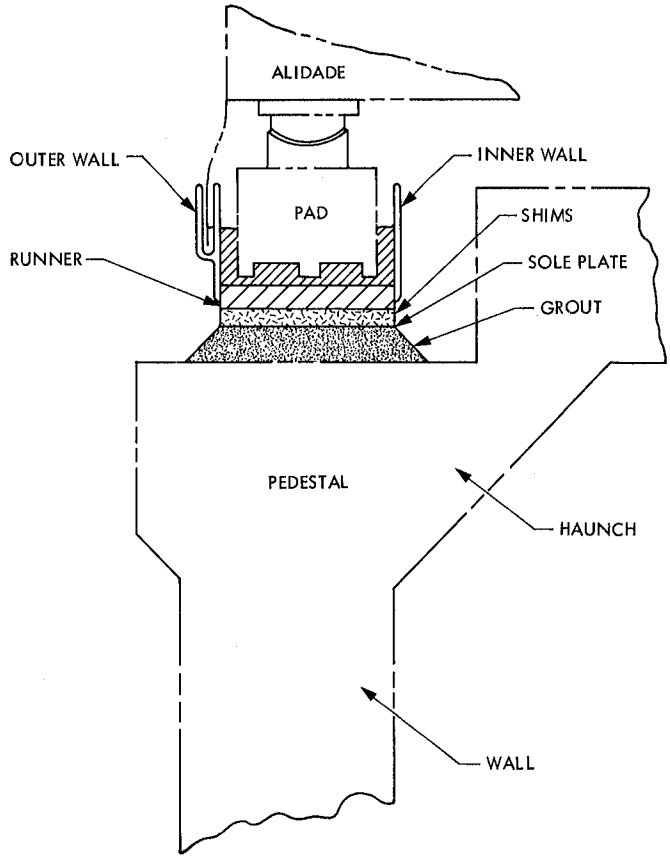


**Fig. 2. Cross section of hydrostatic bearing system**

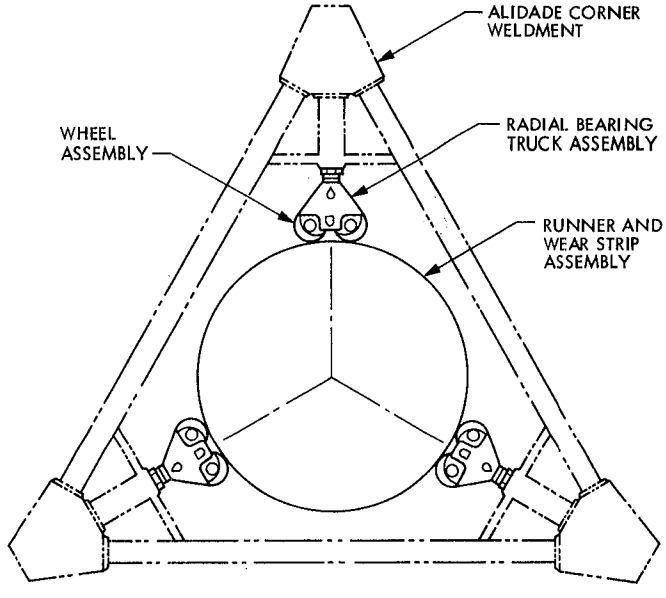


**Fig. 3. Alidade base triangle and radial bearing assembly**

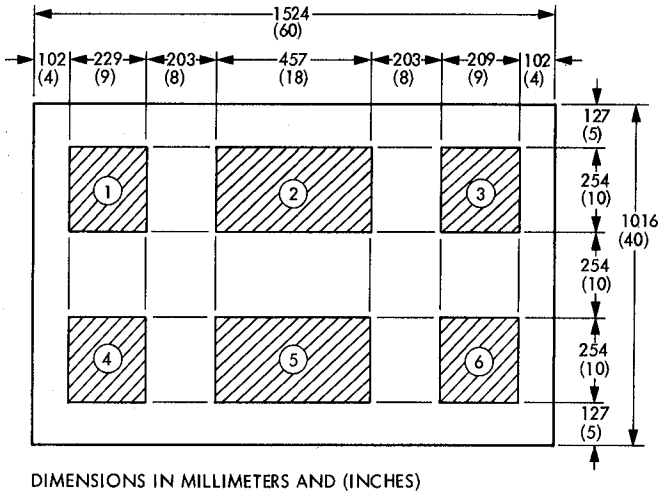


DIMENSIONS IN MILLIMETERS AND (INCHES)

**Fig. 4. Recess pattern of hydrostatic bearing pad**

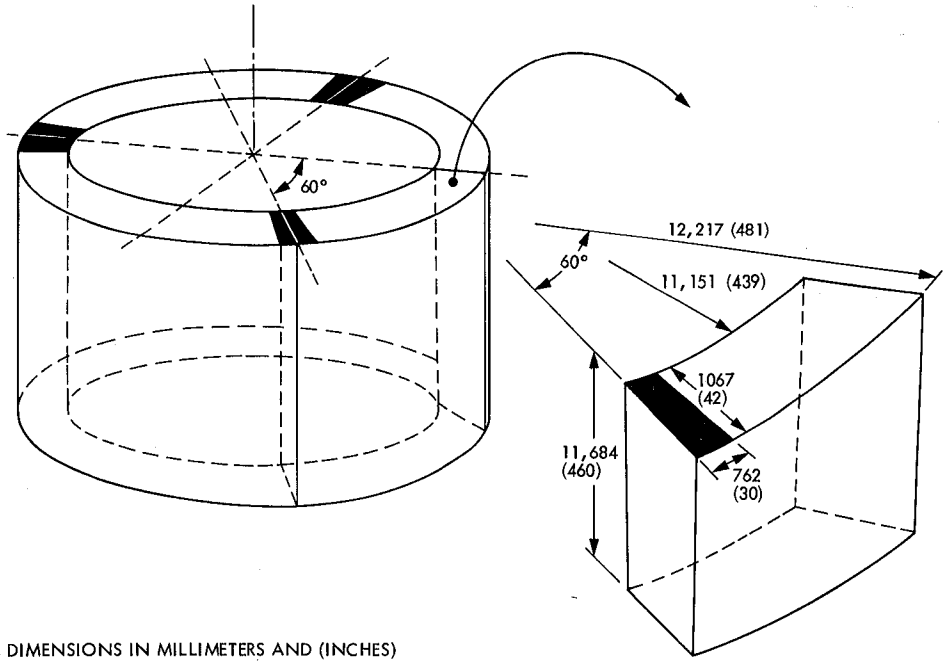


DIMENSIONS IN MILLIMETERS AND (INCHES)

**Fig. 5. One-sixth segment of the pedestal mode**

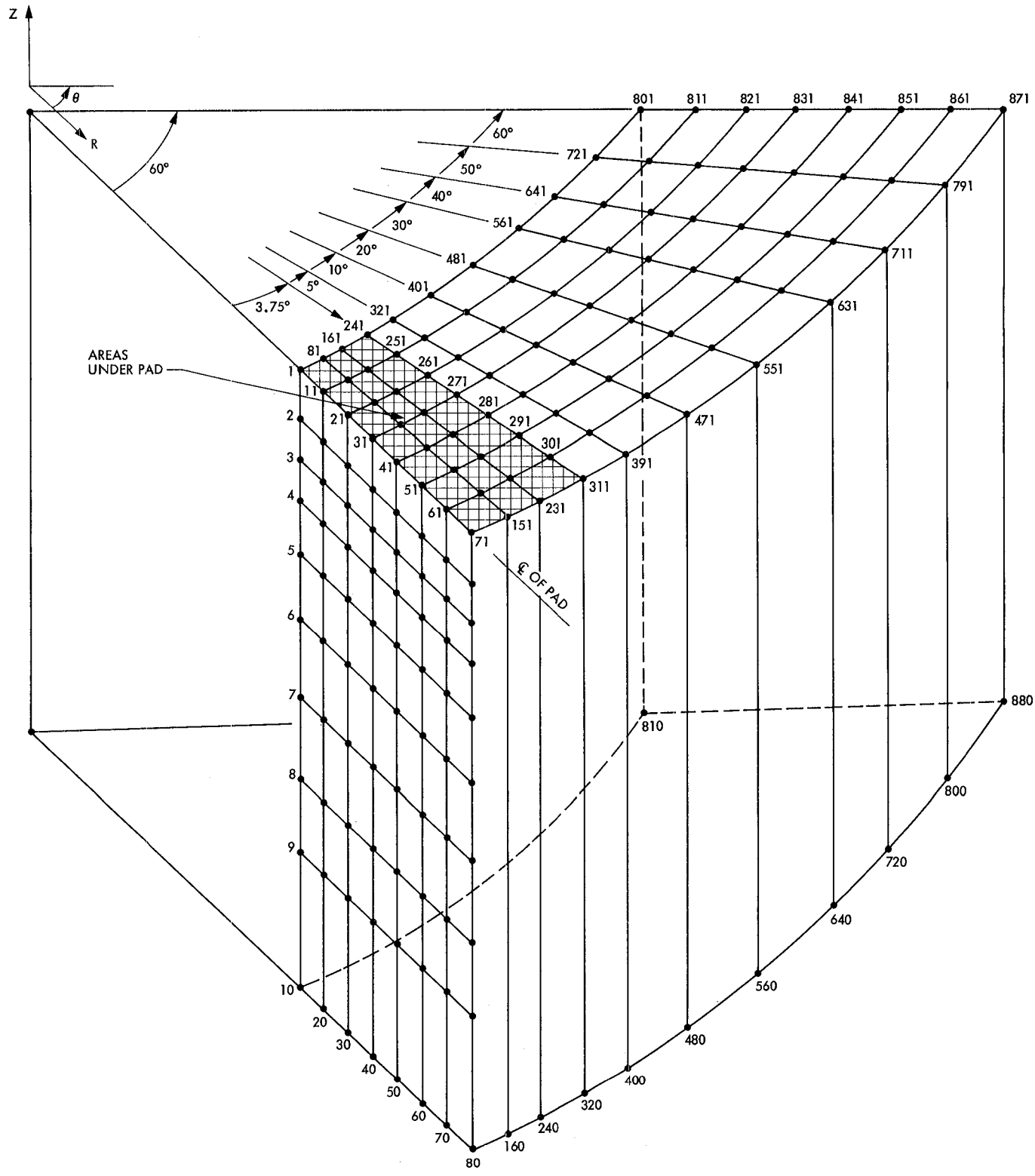


**Fig. 6. NASTRAN pedestal model and nodal points**

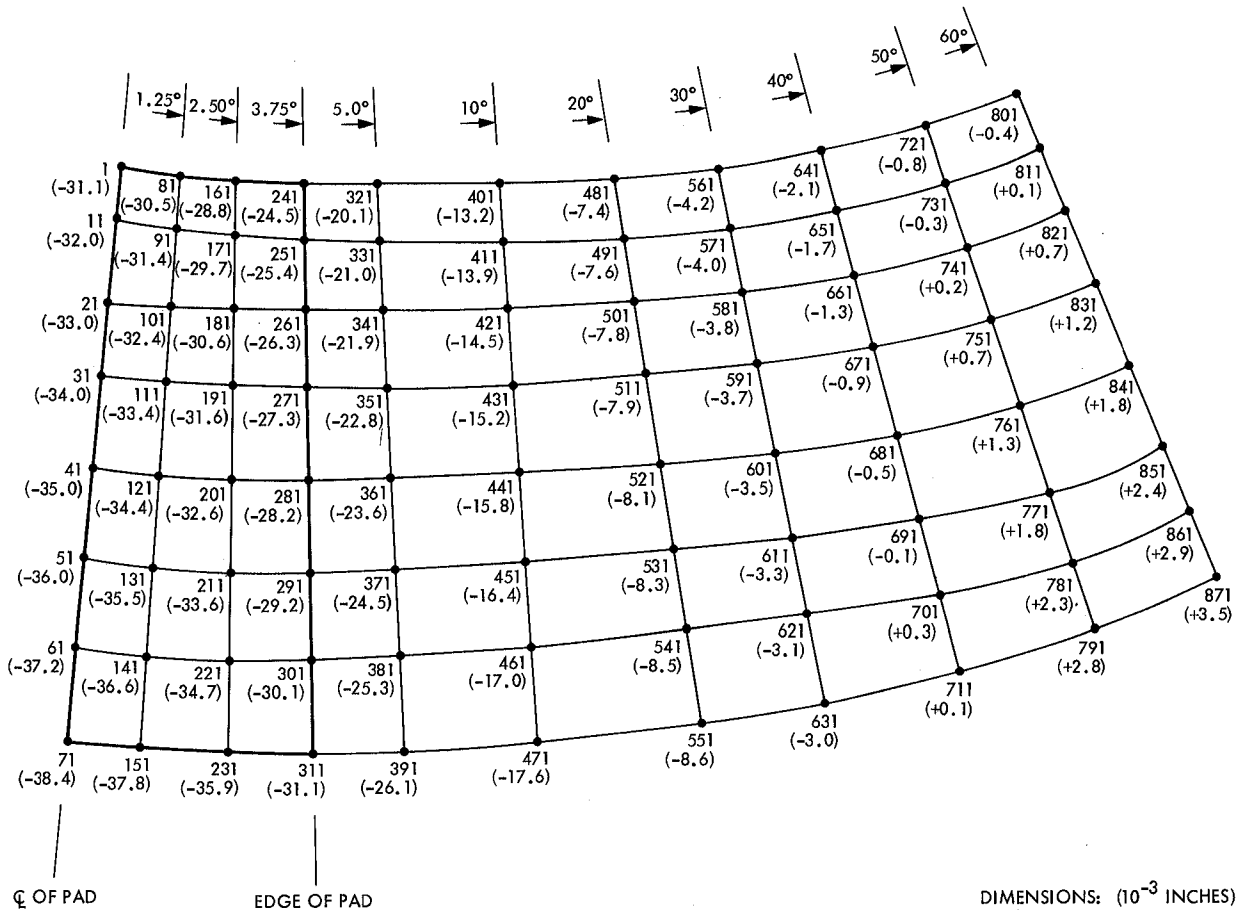


**Fig. 7. Deflection map of pedestal top surface**

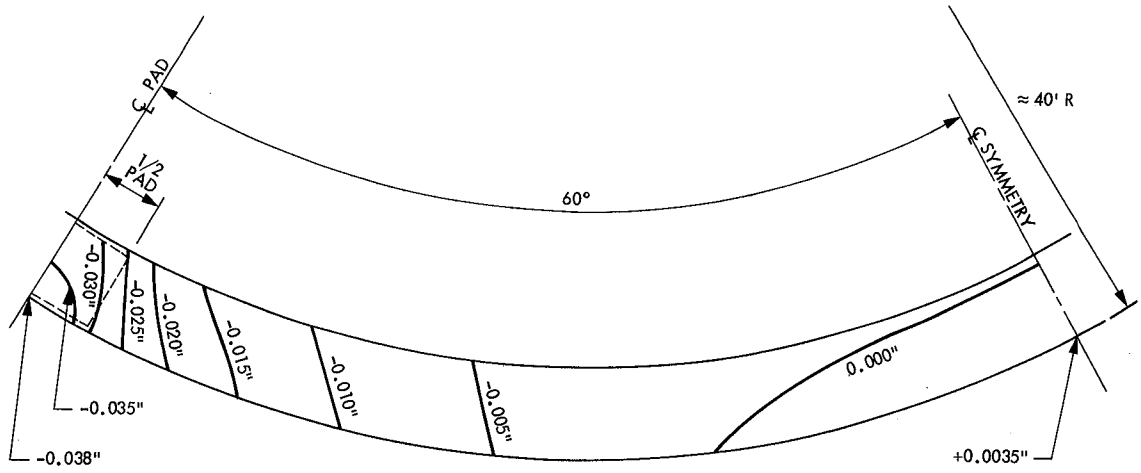


**Fig. 8. Pedestal deflection under hydrostatic bearing runner**

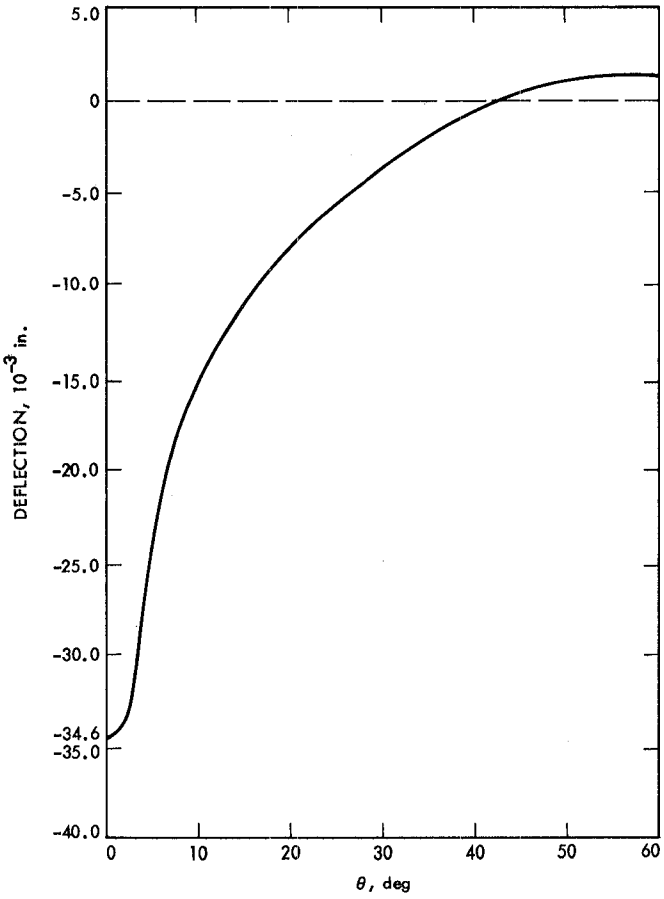


**Fig. 9. Average top surface deflection**

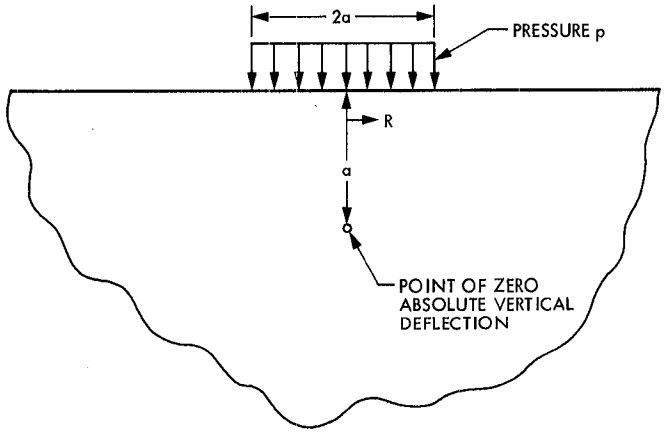


**Fig. 10. Semi-infinite plate under pressure**

# Appendix A

# Field Measurements of Pad Pressure

The three hydrostatic bearing pads, made of carbon steel, are 1.016 m (40 in.) wide, 1.524 m (60 in.) long, and 0.508 m (20 in.) deep. There are six recesses in the bottom of each pad as indicated in Fig. 4, with the two center recesses being larger than the corner recesses. Two sets of recess pressure field measurements were obtained at DSS 14, (Tables A-1 and A-2).

Based on the geometric configuration of the recess areas, a simple equation is derived to relate the load (in lb) on each of the three pads as a function of the six recess pressures (in psi);

$$L_i = 264\,(p_1 + p_3 + p_4 + p_6) + 455\,(p_2 + p_5) \quad \text{(A-1)}$$

where

$i = 1, 2, 3.$

The load $L_i$ and the average pressure $\langle P_i \rangle$ on each pad, calculated from the pad recess pressures, are given in Tables A-3 and A-4. The total load of the three pads is also obtained.

It is noted that the ratios of the pressures among the three pads are about

$$\langle P_1 \rangle : \langle P_2 \rangle : \langle P_3 \rangle = 9 : 9 : 11$$

**Table A-1. First set of pad recess pressures[a]**

| Recess pressure | Pad No. 1 | Pad No. 2 | Pad No. 3 |
|---|---|---|---|
| $p_1$ | 9,135,000 (1325) | 8,101,000 (1175) | 10,859,000 (1575) |
| $p_2$ | 6,722,000 (975) | 7,067,000 (1025) | 7,757,000 (1125) |
| $p_3$ | 8,101,000 (1175) | 8,446,000 (1225) | 11,894,000 (1725) |
| $p_4$ | 7,757,000 (1125) | 6,722,000 (975) | 11,894,000 (1725) |
| $p_5$ | 6,378,000 (925) | 6,722,000 (975) | 9,480,000 (1375) |
| $p_6$ | 7,412,000 (1075) | 7,412,000 (1075) | 9,825,000 (1425) |

Dimensions: $N/m^2$ (psi).

[a]Data taken in 1966.

**Table A-2. Second set of pad recess pressures[a]**

| Recess pressure | Pad No. 1 | Pad No. 2 | Pad No. 3 |
|---|---|---|---|
| $p_1$ | 9,997,000 (1450) | 8,791,000 (1275) | 9,997,000 (1450) |
| $p_2$ | 6,378,000 (925) | 8,446,000 (1225) | 7,067,000 (1025) |
| $p_3$ | 8,446,000 (1225) | 8,274,000 (1200) | 11,721,000 (1700) |
| $p_4$ | 8,791,000 (1275) | 6,550,000 (950) | 12,066,000 (1750) |
| $p_5$ | 6,205,000 (900) | 6,205,000 (900) | 7,757,000 (1125) |
| $p_6$ | 8,963,000 (1300) | 7,757,000 (1125) | 8,791,000 (1275) |

Dimensions: $N/m^2$ (psi).

[a]Data taken in Jan. 1982. Wind speed about 25 mph, control room azimuth 180°, oil temperature 84°F.

**Table A-3. First set of pad loads and average pressures[a]**

| Load and ave pressure | Pad No. 1 | Pad No. 2 | Pad No. 3 |
|---|---|---|---|
| Load, N (lb) | 9,373,000 (2,106,240) | 9,281,000 (2,085,690) | 12,645,000 (2,841,590) |
| Total load, N (lb) | 31,300,000 (7,033,520) | | |
| Ave pressure $N/m^2$ (psi) | 6,054,000 (878) | 6,000,000 (869) | 8,164,000 (1184) |

[a]Corresponds to pad recess pressures in Table A-1.

**Table A-4. Second set of pad loads and average pressures[a]**

| Load and ave pressure | Pad No. 1 | Pad No. 2 | Pad No. 3 |
|---|---|---|---|
| Load, N (lb) | 9,868,000 (2,217,425) | 9,652,000 (2,168,985) | 11,613,000 (2,609,685) |
| Total load, N (lb) | 31,133,000 (6,996,095) | | |
| Ave pressure, $N/m^2$ (psi) | 6,371,000 (924) | 6,233,000 (904) | 7,495,000 (1087) |

[a]Corresponds to pad recess pressures in Table A-2.

# Appendix B

# "Shortcut" Analytical Pedestal Model

The deflection of the grout beneath the runner will be estimated based upon the following assumptions.

The runner has a negligible bending stiffness in comparison to the foundation beneath it. Thus, ignore the runner and assume the pad load is applied directly to the foundation which is composed of concrete and grout, each having the same elastic modulus of $E = 2.8 \times 10^{10}$ N/m$^2$ (4,000,000 psi). It will be assumed that at ground level, 11.68 m (460 in.) below the top of the foundation, the absolute vertical deflection is zero.

The pedestal or foundation will be considered as a semi-infinite plate with a uniformly distributed load applied to the top surface. By superposing various uniform loads, any loading normal to the surface can be simulated.

From Ref. 2, the following expressions for deflection will be employed:

$$V_c = \frac{2aP}{\pi E}\left[(1-\nu) + 2\ln\frac{d}{a} - (1-\lambda)\ln(1-\lambda) - (1+\lambda)\ln(1+\lambda)\right], \lambda < 1 \quad \text{(B-1)}$$

$$V_0 = \frac{2aP}{\pi E}\left[(1-\nu) + 2\ln\frac{d}{a} + (\lambda-1)\ln(\lambda-1) - (\lambda+1)\ln(\lambda+1)\right], \lambda > 1 \quad \text{(B-2)}$$

where $V_c$ and $V_0$ are the vertical deflections at the surface within the loaded area and outside the loaded area respectively, and $\lambda = R/a$.

The deflection at the pad center, for a pad pressure of $6.9 \times 10^6$ N/m$^2$ (1000 psi), was found to be 0.914 mm (0.036 in.).

# Syntax Editing for Mark IV-A System Performance Test Software

G. N. Jacobson
Operations Sustaining Engineering Section

*This article describes the syntax editing concepts used by the Operations Sustaining Engineering Section in implementing System Performance Test software for the Mark IV-A era. The processing functions are discussed, as well as the necessary data structures and table generation macros used in implementing those functions. In addition, the procedural and software interfaces which have been developed for users of the syntax editor are described, including the forms required for establishing directive and parameter characteristics.*

## I. Introduction

The System Performance Test (SPT) software package being developed by the Operations Sustaining Engineering Section for the Mark IV-A DSN implementation will reside in the backup Complex Monitor and Control (CMC) computer, a Modcomp 7845. It consists of a test executive and a set of six application tasks. Basically, the executive distributes input data to the applications, provides resource allocation services, and performs common processing such as data block dumping, display generation, test procedure reading, and syntax editing. The application tasks are each designed to test a particular DSN system. Tracking, Telemetry, Command, Monitor and Control, Very Long Baseline Interferometry, and Radio Science will all be supported by SPT software for the Mark IV-A configuration. (Frequency and Timing will not require SPT software for performance testing.)

Approximately 300 SPT input directives will be required to control the SPT software. These directives may be entered by the operator or may be read from a test procedure file residing on disk. In prior versions of SPT software, each application developed its own syntax editing functions, based on the formats of its own directives. For Mark IV-A, the bulk of the syntax checking will be done by the SPT test executive.

To accomplish this, there is a set of resident subroutines that perform common syntax editing functions such as limit checking, default assignments, existence of required fields, illegal characters, etc. In addition, there is a set of subroutines that perform functions peculiar to a single directive or a small group of directives. These subroutines are referred to as Individual Directive Processors (IDPs). If the directive has passed all the checks made by the syntax editor, then the appropriate IDP will be executed. The IDP can make additional syntax checks pertinent only to this directive (if applicable). If the directive is syntactically correct, the IDP will then perform the intended function of the directive or set the applicable flag(s) for use by the applications task.

## II. Syntax Editor Output Buffer

The primary interface between the resident syntax editor and the IDPs is the 100-word syntax editor output buffer. The first six words of the buffer contain execution time, the overall status of the syntax check, the number of words in the buffer required for this particular directive, and the CAN code (compressed alpha-numeric code) for the directive name. The remainder of the buffer is defined by the programmer implementing the directive. The detailed contents of the remaining words in the buffer are itemized on the Directive Characteristics Description form (see Fig. 1.) The programmer defines a canonical form of the directive. This means that all fields are shown on the Directive Characteristics Description form and that they appear in the same sequence as desired for the output buffer. The output buffer contains a parameter status word for each parameter. The parameter itself is passed in a format specified by the user.

To specify the characteristics of each parameter in detail, a Field Characteristics Description form is used (see Fig. 2.) The entries made on this form determine the actual syntax checks which will be made by the syntax editor. A field listed as required must obviously be included with each occurrence of the directive. The field may be interrelated to other fields in the sense that at least one, exactly one, or at most one of a series of fields may be entered. This can be easily recorded on the Field Characteristics Description form and checked by the syntax editor.

The programmer must next define whether the field consists of a value, a self-identifying variable, or a variable identifier equalling a value. In the third case, there are two subfields involved, the variable identifier and the value. This is why the Field Characteristics Description allows two subfield entries per field.

The input format may be specified as alphanumeric, integer (including octal or hexadecimal), numeric (may include a decimal point), time (UTC or HMS format), text string, or expression. Man-machine interface standards provide for directives with the variable portion of the directive containing a text string. This is treated in SPT software as a single value with an input format type of "text string."

The range value column will be filled in with lower and upper boundaries if limit checks are to be performed by the syntax editor.

Legal output formats include CAN code (single or double word), floating point (double, triple, or quadruple word), fixed point (single, double, or quadruple precision), time (ASCII, deciseconds since beginning of year, or milliseconds since midnight), integer, and ASCII. In the latter case, a maximum length in bytes may also be specified.

The syntax editor is capable of checking a subfield against a list of acceptable entries. The valid entries are listed in the next-to-last column of the Field Characteristics Description. It is possible to request an indexed output format type. The syntax editor will output the index number corresponding to the position of the actual parameter in the list of acceptable entries.

If a subfield is to assume a default value when it is omitted from the directive, the desired default value is entered in the last column of the Field Characteristics Description.

## III. Syntax Definition Tables

The information contained on the Directive Characteristics Description and the Field Characteristics Description must be transcribed into tables for subsequent use by the syntax editor. SPT software design requires three tables for this purpose.

### A. Directive Definition Table

The Directive Definition Table contains a two-word entry per directive (see Fig. 3.) The first word of the two-word entry contains the CAN code for the three characters which identify the directive. (This is possible because all SPT directives consist of four characters, where the first character identifies the system under test, and the last three characters consist of a mnemonic name for the directive.) The second word contains a pointer to the appropriate entry in the Directive Characteristics Table.

### B. Directive Characteristics Table

Each entry in the Directive Characteristics Table consists of two parts. The first part is fixed in length, consisting of two words per directive (see Fig. 4.) The first word contains a series of flags to indicate for which subsystems this directive is allowable, whether it contains an expression or a text field, and if it is a fixed position type of directive. The second word contains the overall output size in words and the maximum number of subfields.

The second part of each entry in the Directive Characteristics Table is variable in length, based on the number of parameters in the directive. Each parameter requires two words in this part of the table (see Fig. 5.) The first word contains a series of flags which relate to information specified on the Field Characteristics Description form such as whether the field is required or optional, whether a default value applies, whether a list of acceptable values has been supplied, whether the field is to be range-checked, and whether any relational characteris-

tics (such as mutually exclusive fields) apply. Also contained in this word is the index for this parameter into the syntax editor's output buffer. The second word points to the address of the appropriate entry in the Parameter Characteristics Table, where all the detailed information relative to this parameter is stored.

### C. Parameter Characteristics Table

The Parameter Characteristics Table also contains a fixed length portion and a variable length portion per entry (see Fig. 6.) The first four words are required for each parameter characteristic entry. The first word contains a pair of codes to describe the input format and output format specified on the Field Characteristics Description form. The first eight bits of the second word contain the maximum length of an ASCII field (if specified) or the number of bits to the right of the binary point (if fixed point). The remainder of the second word contains the index into the Parameter Characteristics Table for the default value and the number of words required for the default value, if applicable. The third word contains the index of the lower limit and the number of words required for each of the two limit values, if range checking is desired. (The upper limit value will immediately follow the lower limit.) Similarly, the fourth word contains the index of the first word of the list of acceptable values and the number of words required for each element of the list. In this case, the total number of entries in the list will also be stored in the fourth word (in the first eight bits).

Following this comes the variable length portion of the Parameter Characteristics Table entry. If a default value has been specified for this parameter, it will be stored next in the table. If range checking is desired, the lower and upper limits will follow. Finally, if a list of acceptable values has been supplied, it will be stored at the end of each table entry. The elements in the list will be stored in the same order as specified by the user. This is because an indexed output type is available for such a parameter. As described earlier, this means that the syntax editor will return to the user an index corresponding to the position in the list of acceptable values where the actual parameter was located. The user is then able to use this index directly in subsequent processing. For this reason, the indexed output type is very commonly requested when a list of acceptable values is supplied for the input field.

## IV. Syntax Table Generation Macros

There is actually a missing step in the transcription process from the syntax definition forms to the syntax definition tables. It must be possible to generate the very detailed bit-oriented tables efficiently and accurately. The route selected was the use of macro techniques (Ref. 1).

Nine macros have been created for the purpose of syntax editor table generation. Two macros are for initialization and termination of the table generation process. The remaining seven are used for creating specific entries or parts of entries for the three tables described in the preceding section.

Four of the macros are used for creating entries in the Parameter Characteristics Table. The first of these is in fact called the parameter characteristics macro and is used to begin the definition of the characteristics of a particular parameter. It must be followed by corresponding default, range, and acceptable value macros, as appropriate, if the parameter has an associated default, range check, or list of acceptable values. The macros must occur in this specific sequence for any parameter.

The directive name macro is used for generating a directive name in CAN code format and a pointer to the corresponding entry in the Directive Characteristics Table. The two words become a complete entry in the Directive Definition Table. This macro must occur after all corresponding parameter characteristics macros.

The final two macros are required for creating entries in the Directive Characteristics Table. The first of these, the directive characteristics macro, begins the generation of an entry. It is used for creating the fixed length portion of each Directive Characteristics Table entry. This macro must appear immediately after its related directive name macro and must be immediately followed by any related parameter pointer macros. The parameter pointer macro generates the two-word subentry per parameter in the Directive Characteristics Table. A parameter pointer macro is required for each possible subfield of the directive and must appear in the same sequence as in the directive's canonical form.

Figure 7 shows a portion of the actual macros used in the Mark IV-A SPT software system for generating the three required tables for the syntax editor.

## V. Architectural Design

The syntax editor is used for checking both directives entered by the operator and directives read from a test procedure file. As such, it is actually invoked by two routines, the main directive processor control routine and a separate routine which processes directives from the procedure processor. The editor itself consists of 22 subroutines. Figure 8 contains a hierarchical tree for the editor.

The top level, of course, consists of the main control routine for the syntax editor. It in turn calls a series of subrou-

tines which performs initialization functions, validates the directive, retrieves and converts individual parameters, checks relational characteristics (such as mutually exclusive fields or existence of at least one or at most one of a series of fields), sets default values, and checks for required parameters.

Of these, the only major expansion is for the routine which retrieves and converts individual parameters, EOPARM. EOPARM itself consists primarily of a loop for processing each parameter in the directive. It calls a routine to obtain the next parameter (which is further modularized to retrieve alphanumeric, text, or numeric subfields); checks that the retrieved parameter is legal for the prior trailing character; and then calls EOFSUB to correlate the input parameter with the subfield data contained in the Directive Characteristics Table and Parameter Characteristics Table. EOFSUB contains several subroutines at three additional hierarchic levels to perform all of the necessary conversions, range checking, and acceptable value list searching.

If the directive passes all of the syntax editor's checks, the appropriate Individual Directive Processor is established and executed. The IDP often has additional syntax checks to make, peculiar to this particular directive. For example, certain directives or certain fields may be allowed only under one or more specific operating modes. Or some fields may become required if some other specific field has been entered. Depending on the directive entered, the IDP often has other functions to perform, such as setting flags or data in a global or private shared common area. To assist the programming staff in attending to all details in the design of an IDP, a checklist has been prepared of possible IDP processing functions. This is illustrated in Fig. 9.

## VI. Implementation Sequence

The Mark IV-A SPT software system is being implemented in a continually cycling, demonstrable fashion (Ref. 2). A Network of Demonstrable Functions (NDF) has been prepared, defining approximately 170 individual steps. Each step will demonstrate one specific function or group of functions and will normally require implementation of around a dozen new subroutines.

Development of the syntax editing routines and IDPs adheres to the SPT implementation philosophy. Each routine will be developed when it is required for demonstration of one of the specific functions laid out in the NDF. As an example, the syntax editor routine for retrieving a text subfield will not be implemented until the first scheduled step which requires a directive involving a text subfield. The IDP for enabling a long loop test will not be implemented until work begins on the long loop path of the NDF. Figure 10 shows a partial list of SPT directives and the NDF step in which they will be implemented.

When the design of each step is completed, a review is held internal to the Operations Sustaining Engineering Section. To assist in reviewing the design of the IDP, and to convey the proper syntax (and purpose) of each directive to the ultimate users of SPT software, a standard format has been established for use in the Software Operator's Manual (SOM). Figure 11 illustrates the required sections for one of the SPT directives used for running a Command test sequence. It should be noted that the directive response messages listed at the end of each SOM directive description are unique to that directive or a small subset of directives. Common messages, such as standard acknowledgements or errors detected by the syntax editor (as opposed to the IDP), will be listed and described once in a separate section of the SOM.

## VII. Concluding Remarks

At this point in time, 20 of the syntax editor's 22 routines have been developed and demonstrated. (The two routines for fixed point conversions are not required at this time on our implementation plan.) The editor has proven to be extremely reliable. Close to 100 steps on the Mark IV-A SPT Network of Demonstrable Functions have been demonstrated, and each one has exercised the capabilities of the syntax editor to varying degrees. During this interval, only a few minor anomalies related to the syntax editor have been detected.

Initial design of the syntax editor has proven to be extremely sound. Only one major new capability had to be added since the primary concepts were developed. This was the capability to have the syntax editor check for relational characteristics, such as mutually exclusive fields. The design of the editor was flexible enough to allow this to be added with comparative ease.

As the application tasks require new directives for upcoming steps on the NDF, the directives are incorporated into the system easily and efficiently. Design and implementation of most IDPs are also fairly straightforward. What used to be a significant, time-consuming task for each application has been reduced to a routine, standardized activity for Mark IV-A SPT software development.

# References


1. Spinak, A., "Syntax Table Generation Macros," Internal Memorandum No. SSG-FY82-257, Bendix Field Engineering Corporation, Pasadena, Calif., July 14, 1982.

2. Jacobson, G. N., and Spinak, A., "Top Down Implementation Plan for System Performance Test Software," *TDA Progress Report 42-70,* Jet Propulsion Laboratory, Pasadena, Calif., pp. 190-199, Aug. 15, 1982.

DIRECTIVE CHARACTERISTICS DESCRIPTION DATE:_____

REVISION:_____

1. NAME:_____ 2. STEP:_____

4. FUNCTION: 3. PROGRAMMER:_____

5. OVERALL GENERAL FORMAT:

6. LEGITIMATE SUBSYSTEM PREFIXES: C K T R M V

7. MAXIMUM EXPECTED NUMBER OF PARAMETER FIELDS:_____

8. SYNTAX OUTPUT BUFFER:

| | | | |
|---|---|---|---|
| 1 | TIME MSB | MLBTIM | ILBOUT HEADER |
| 2 | TIME LSB | MLBTIM | ILBOUT HEADER |
| 3 | OVERALL STATUS | ILBSTA | ILBOUT HEADER |
| 4 | OVERALL OUTPUT SIZE | ILBSIZ | ILBOUT HEADER |
| 5 | DIRECTIVE CAN CODE UPPER | MLBCAN | ILBOUT HEADER |
| 6 | DIRECTIVE CAN CODE LOWER | MLBCAN | ILBOUT HEADER |
| 7 | | | |
| 8 | | | |
| 9 | | | |
| 10 | | | |
| 11 | | | |
| 12 | | | |
| 13 | | | |
| 14 | | | |
| 15 | | | |
| 16 | | | |
| 17 | | | |
| 18 | | | |
| 19 | | | |
| 20 | | | |
| 21 | | | |
| 22 | | | |
| 23 | | | |
| 24 | | | |
| 25 | | | |
| 26 | | | |

9. FIXED POSITION INPUT (Y OR N): ____

10. OTHER CHARACTERISTICS:

**Fig. 1. Directive characteristics description**

## FIELD CHARACTERISTICS DESCRIPTION

1. DIRECTIVE NAME:_____ 2. PROGRAMMER _____

3. FIELD NUMBER:_____ 4. FIELD OPTIONAL (R OR O):_____
(R = REQUIRED, O = OPTIONAL)

5. FUNCTION:

6. DESCRIBE FIELD INTERRELATIONSHIPS (IF ANY)

NEXT RELATED FIELD NUMBER _____

AT MOST ONE _____ EXACTLY ONE _____ AT LEAST ONE _____

| SUB-FIELD | V,VI, SIV | INPUT FORMAT | RANGE VALUES | OUTPUT FORMAT | MAX. OUTPUT LENGTH | LIST OF ACCEPTABLE ENTRIES (IN INDEX ORDER) | DEFAULT |
|---|---|---|---|---|---|---|---|
| SF1 | | | | | | | |
| SF2 | | | | | | | |

7. OTHER CHARACTERISTICS:

Fig. 2. Field characteristics description

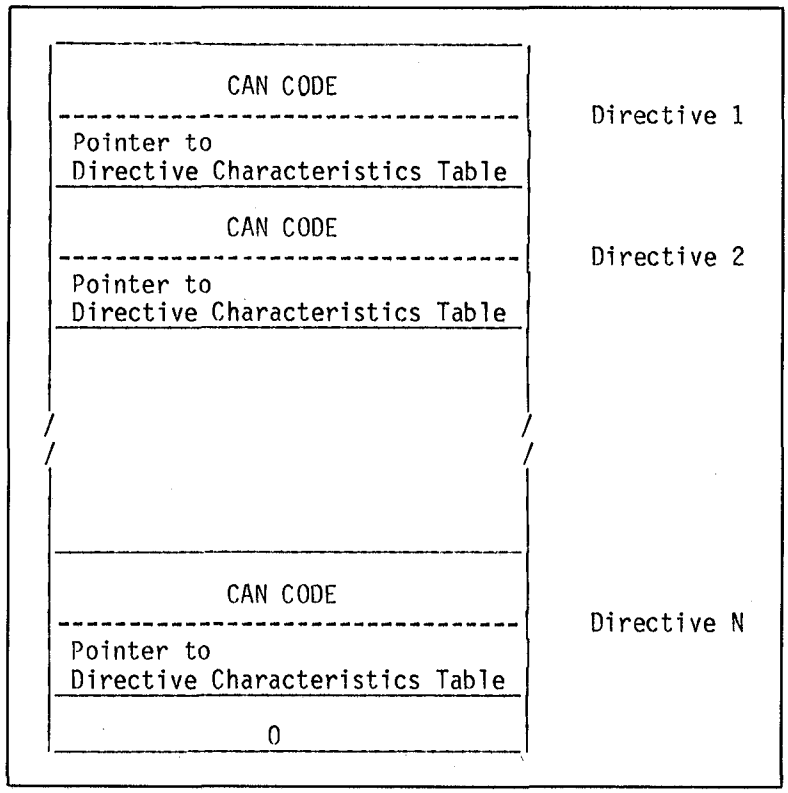


**Fig. 3. Directive definition table**

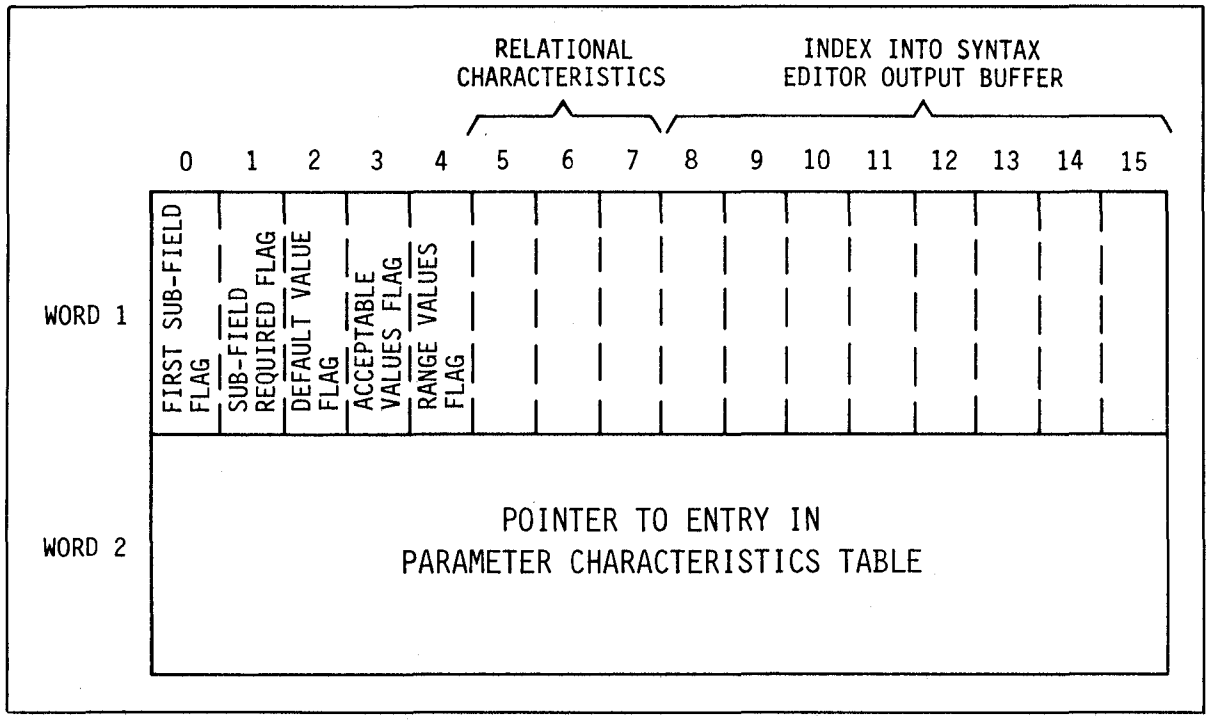


**Fig. 4. Directive characteristics table, directive description entry**

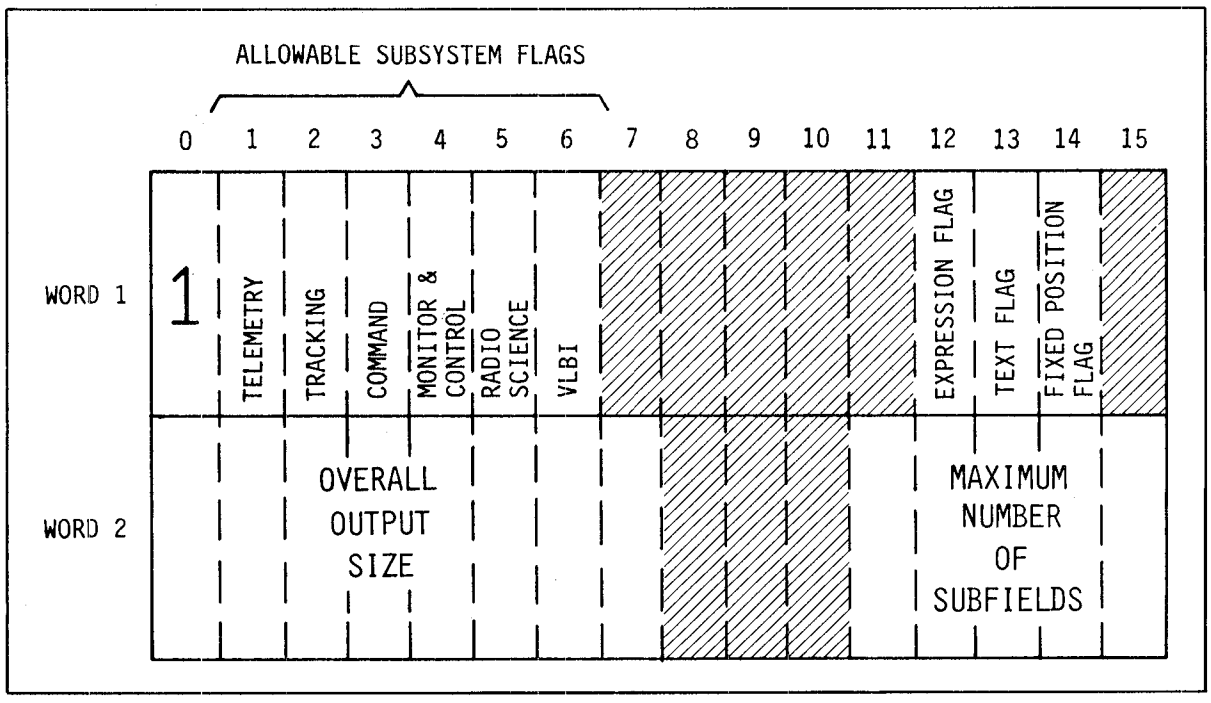


**Fig. 5. Directive characteristics table, parameter description entry**

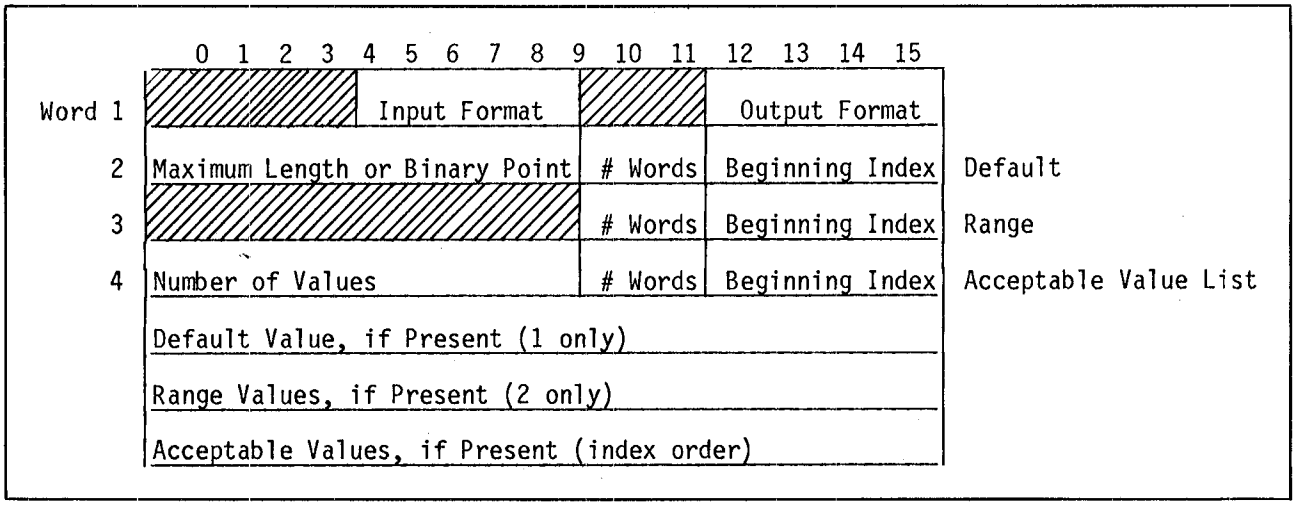


**Fig. 6. Parameter characteristics table**

```
*
*********************************************
* CAL Directive parameters                  *
*********************************************
PCAL1   PARCHR,2,,R     NUM,DF
        RANGES          1.0E1,1.0E3
*
PCAL2   PARCHR,2,A,,D   ALP,XX,2
        DEFAUL          1
        ACCVAL          "CFG","MON"
*
*********************************************
* CON Directive parameters                  *
*********************************************
PCON1   PARCHR,2,A      ALP,XX,4
        ACCVAL          "GET","SAVE","LIST","DEL"
*
PCON2   PARCHR,2,A      ALP,NP,1
        ACCVAL          "FILE"
*
PCON3   PARCHR          ALP,PT,,8
*


*
*********************************************
* CAL Directive                             *
*********************************************
        DIRNAM          CAL
        DIRCHR,T        11,2
        PARPTR,PCAL1,6  FS,R
        PARPTR,PCAL2,9  FS,D,A
*
*********************************************
* CON Directive                             *
*********************************************
        DIRNAM          CON
        DIRCHR,T        14,3
        PARPTR,PCON1,6  FS,SR,A
        PARPTR,PCON2,8  FS,SR,A
        PARPTR,PCON3,9  SR
*
```

**Fig. 7. Sample SPT syntax table generation macros**

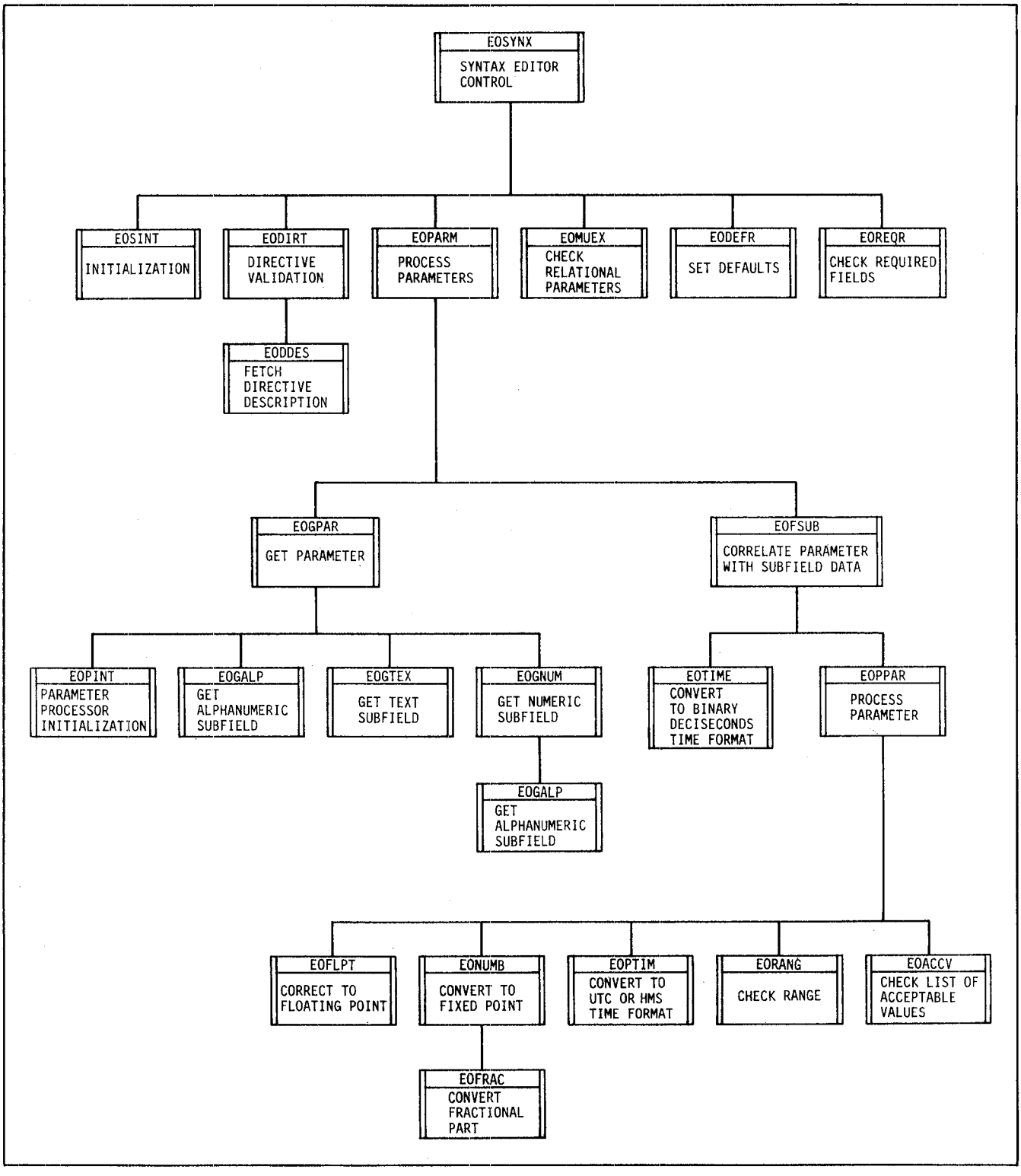


**Fig. 8. Syntax editor hierarchical tree**

IDP DESIGN CHECKLIST

1) Does IDP have to determine the particular case by checking to see which parameters or what values have been entered?

2) Should IDP perform directive error checks in addition to those that have been checked for by the Syntax Editor?

3) Is there any special processing (e.g., conversions, calculations) that the IDP must perform?

4) Should the IDP set flags or data in global or private common for the corresponding subsystem or task?

5) Should a semaphore (interlock) be checked and set before the data is setup?

6) Should IDP notify the subsystem or task of a new data entry or flag?

7) Should the IDP wait for a completion response from the subsystem or task?

8) Should the IDP check for abnormal returns from the subsystem or task (and then take appropriate action)?

9) Should the IDP provide default values for any of the subfields?

10) Is the IDP consistent with the interface as defined in the Syntax Output Buffer and Syntax Definition Forms?

11) Should the IDP issue an acknowledgement for completion of processing the directive?

12) Have the appropriate Syntax Output Buffer equivalences been defined and coded?

13) Are there any other functions the IDP should perform before exiting?

14) For assembly language IDPs, did the IDP preserve R10 and return to the Directive Processor via the address contained in R10?

**Fig. 9. IDP design checklist**

DIRECTIVE STATUS REPORT

| Directive | Programmer | Directive Description | Step | Status |
|---|---|---|---|---|
| EHL | M. BURNS | Enables or disables halting of procedure processing when a procedure error has occurred | 100 | **** |
| ELM | R. BILLINGS | Modifies a command file prior to transmission to the CPA | C070 | *** |
| END | T. OWENS | Terminates a test sequence | 050 | **** |
| ERA | S. MAK | Erases file directory | C120 | - |
| ESD | M. MACAULAY | Supplies the support data file name which is to be edited | L040 | ** |
| ESH | J. STICHT | Edits the header of the requested support data file name | L040 | ** |
| EST | J. STREIT | Enables or disables reporting, tolerance tests, status tests, or error rate tests and sets appropriate parameters | T080 | * |

Status:

- \- Proposed
- * Submitted
- ** Approved
- *** Implemented
- **** Demonstrated

**Fig. 10. Directive status report**

CDRR - ENABLE/DISABLE UDT/DDT OR ALL FOR GCF DSN BLOCK(S)

DESCRIPTION: The directive CDRR enables or disables GCF DSN block(s). The request enters into or removes from the routing table either 'all' prime CPA routing codes or a specific UDT/DDT code.

FORMAT: CDRR z, (<UDT=x, DDT=y>,ALL)

FIELDS: Three required field entries can be input in any sequence when specifying a UDT/DDT code. For this case the request is as follows:

CDRR z, UDT=x, DDT=y

Two fields in any sequence are required when requesting all prime CPA routing codes. The request is as follows:

CDRR z, ALL

NOTE: If the 'ALL' request is enabled, then the specifications for unique UDT/DDT pairs can not be requested. The 'ALL' request must be disabled before specific UDT/DDT pairs can be enabled. The converse is also true.

CAUTION: The UDT/DDT pairs entered are not checked for correctness or validity.

It is possible to lose a block if an identical enable request is entered. This occurs because the prior request is removed from the routing table to prevent reception of identical blocks.

PARAMETER CHARACTERISTICS:

| Parameter | Description | Input Type | Range Or Maximum Length | Input Status (Required, Optional, Mutually Exclusive, Acceptable Values, Default Values) |
|---|---|---|---|---|
| z | Enable or disable block(s) | Alpha | 1 Char. | Acceptable values:<br>E - for enable<br>D - for disable |
| UDT | User Dependent Type Identifier | | | Keyword for x |
| x | UDT Code | Integer | 0 -127 | Specifies unique UDT code |
| DDT | Data Dependent Type Identifier | | | Keyword for y |
| y | DDT code | Integer | 0 - 127 | Specifies unique DDT code |
| ALL | Self Identifying variable | | | Acceptable value:<br>ALL - indicates all prime CPA routing codes |

**Fig. 11. Sample SOM directive description**

```
EXAMPLES:
          Acceptable requests:
              CDRR E, UDT=#47, DDT=#66
              CDRR E, UDT=0107, DDT=0146
              CDRR E, UDT=71, DDT=102
              CDRR E, ALL
              CDRR D, UDT=#47, DDT=#66
          Rejected requests:
              CDRR E              ( One or more fields are missing. )
              CDRR E, UDT=ALL     ( All is not a specific UDT code.)
              CDRR E, UDT=#7A     ( A DDT code has not been specified.)
```

CDRR Directive Response Messages

| MESSAGE | REASON | OPERATOR RESPONSE |
|---|---|---|
| ALL INVALID, UDT/ DDT PAIR(S) ENABLED | The request to enable the prime CPA routing codes has been rejected because specific UDT/DDT routing codes were previously enabled. | Disable each UDT/ DDT previously entered, reenter the 'all' request |
| ERROR, CRUN NOT ENTERED | The CRUN directive must be entered prior to CDRR to identify the mission. | Enter the CRUN directive and reenter CDRR |
| REQUEST NOT ACCOMPLISHED | A status check has indicated that the SPT EXEC could not execute the request. | Reenter the request |
| UDT/DDT INVALID, ALL ENABLED | The request to enable the specific UDT/DDT routing code has been rejected because the prime CPA routing codes are enabled. | Disable the prime CPA routing codes with the 'all' request, and reenter the directive for the specific UDT/DDT |

**Fig. 11 (contd)**

# Radio Astronomy

P. R. Wolken and R. D. Shaffer
Control Center Operations Section

*This article reports on the activities of the Deep Space Network in support of Radio Astronomy Operations during May, 1983. A series of experiments sanctioned by the Radio Astronomy Experiment Selection Panel was supported.*

## I. Introduction

Deep Space Network (DSN) 26- and 64-meter antenna stations were utilized in support of Radio Astronomy Experiment Selection (RAES) Panel experiments. Within a time span of 10 days, in May 1983 (267.75 hours total), nine RAES experiments were supported. Most of these experiments involved multifacility interferometry using Mark III data recording terminals and as many as six non-DSN observatories.

## II. Radio Astronomy Operations

### A. RA 180. "The Nuclei of M81 and M104" (N. Bartel, MIT)

DSS 63 supported 3 hours of observations of these objects. Six non-DSN observatories also participated. This second epoch of observations of M81 would disclose any time variability and frequency dependence in the flux density and the structure of the nucleus of this compact source. Observations of M104, a galaxy seen edge-on, would disclose whether any alignment between axes of the optical image and the radio map exists.

### B. RA 181. "The Black Hole Candidate CYG X-1" (N. Bartel, MIT)

DSS 14 and DSS 63 supported this event in conjunction with RA 185 for a combined total of 33 hours. Two non-DSN facilities took part in this experiment. CYG X-1, an X-ray emitting binary system, is the best known candidate for containing a black hole. VLBI observations at a single epoch would allow conclusions to be drawn about the physical model of the source.

### C. RA 183. "SS-433 VLBI" (A. Niell, JPL)

DSS 13 and DSS 14 observed this object for a total of 46.5 hours. Five non-DSN observatories also acquired data. In addition to enhancing knowledge of the small-scale structure of SS-433, these VLBI observations would investigate the energy transport beams of the object, study the spectral properties of the core, and explore the structural similarities between this galactic object and extragalactic compact radio sources.

### D. RA 184. "VLBI Observations of 0957+561A, B and 1038+528A, B (Twin and Double QSOs, Second Epoch)" (M. V. Gorenstein, Harvard Center for Astrophysics)

The twin QSO phenomenon is an effect of a gravitational lens on a single source, while the double QSOs are observationally close together, but physically unrelated sources (see *TDA Progress Report 42-64, May and June 1981).* DSS 14 and DSS 63 supported 82.25 hours of observations. This large number of hours was requested because both sources are expected to have time-variable structure. Six non-DSN

observatories took part in this experiment. In the case of 0957+561A, B, the study of time variations would lead to a detection of the gravitational time delay. For 1038 + 528, the B quasar acting as a phase reference would provide a positional reference with which to study the motion of internal features of the A quasar.

### E. RA 185. "Observations of the Galactic Center" (J. Marcaide, MPIR)

DSS 14 and DSS 63 supported this event for 14.75 hours in addition to the 33 hours of observations combined with RA 181. Five non-DSN observatories also participated. Some continuing debate on the existence of a core in the compact nonthermal radio source (Sgr A-W-C) in the Galactic Center would be resolved by these highly sensitive observations. In addition, mapping the source, studying day-scale time variations in some observations, and refining the known position of the source would greatly improve existing information about the Galactic Center.

### F. RA 186. "The Compact Sources in M82" (N. Bartel, MIT)

The DSN 64-meter antenna stations at Goldstone and Madrid (DSS 14 and DSS 63) supported this experiment for 29.25 hours. Six non-DSN observatories also participated. This experiment would study the radio nuclei of nearby galaxies (M82 is an irregular galaxy at a distance of about 3.3 Mpc) by means of VLBI and hybrid mapping techniques.

### G. RA 187. "Mapping of the Galactic Center Compact Radio Science" (K. Y. Lo, CIT)

DSS 14 spent 12.25 hours in support of this activity. Six non-DSN observatories took part in these observations. This observation of Sgr A would determine the source structure via the mapping of its brightness distribution. Recent evidence suggests an asymmetric source structure. Clarifying any relationship of the source to other phenomena at the center would help in understanding not only the nature of this source, but extragalactic sources as well.

### H. RA 191. "A Search for Hyperfine Emission from Cosmic $^3He^+$" (G. M. Heiligman, CIT)

DSS 14 dedicated 20.75 hours to this spectroscopic experiment, which would determine an abundance of $^3He^+$ in the interstellar medium, which in turn would imply a helium mass-loss rate for stars and set a lower limit on the mean density of the universe. (The 64,000-channel Radio Frequency Interference Surveillance System (RFISS) was used to support this experiment. See *TDA Progress Report 42-66, September and October 1981*.)

### I. RA 192. "Weak Superluminal Quasar 3C179" (R. W. Porcas, MPIFR)

DSS 14 and DSS 63 each devoted 13 hours (total 26 hours) to VLBI observations of 3C179. This observation would measure the rate of separation of the bright components of the source and check on the frequency dependence of the separation.

# Planetary Radar

J. R. Bogan and R. D. Shaffer
Control Center Operations Section

R. M. Goldstein
Telecommunications Science and Engineering Division

R. F. Jurgens
Communications Systems Research Section

*This article reports on the radar astronomy activities supported by the Deep Space Network (DSN) during the unique close approaches of the comets IRAS-Araki-Alcock (1983d) and Sugano-Saigusa-Fujikawa (1983e) to Earth.*

## I. Introduction

The application of modern planetary radar techniques to a comet passing in close proximity to Earth has the potential to determine the nature of cometary origins, structure, and internal dynamics. Moreover, the understanding gained could very likely negate or corroborate one of the prevailing hypotheses regarding the origin of the solar system: that comets are the remainder of the primordial material out of which the planets coalesced approximately 4.5 billion years ago.

In 1983, two unique opportunities were presented to observe a comet very near to Earth. The last such encounter was several centuries ago.

## II. Observations

### A. IRAS-Araki-Alcock

The first event came in May with the arrival of the comet IRAS-Araki-Alcock (1983d). The Point of Closest Approach (PCA) was measured at about 0.03 Astronomical Units (AU). Two observing sessions were scheduled, amounting to ten hours of supported activity at DSS 14. Observations at S-band produced strong radar echoes and about seven viable spectra. Indeed, the return signals were monitored in real-time with a good signal-to-noise ratio, and subsequent observations at X-band were made at orthogonal circular polarizations.

Preliminary data analysis is speculative at best, but some conclusions can be drawn. The spectral features (see Fig. 1) indicate a rapid rotation of the comet's nucleus, and a spin period of 1.6 hours is suggested. Since the spectral bandwidths define the pole positions (north and south), one can then infer a radius of approximately 200 meters (m). Therefore, the geometric cross section corresponds to:

$$\sigma_g = \pi(200\text{m})^2 = 1.2 \times 10^5 \text{ m}^2$$

However, the measured radar cross section, $\sigma_r$, is about $5 \times 10^6$ m$^2$, leading to an albedo, $a$, of

$$a = \frac{\sigma_r}{\sigma_g} = \frac{5 \times 10^6 \text{ m}^2}{1.2 \times 10^5 \text{ m}^2} \cong 40$$

An albedo of 20-30 might be explained on the basis of cometary debris in the coma, but the residual discrepancy is difficult to account for. Alternatively, if the spectral features are *not* real, but due to speckle noise, one is forced to assume a much longer spin period. In that case, the surface albedo is unknown since the radius cannot be determined. The shape of the power spectrum and the depolarization ratio (~25%) of the return signals imply that the majority of the surface is rough on a large scale, but smooth on a scale comparable to a wavelength or smaller. Further analysis should yield a more definitive picture.

## B. Sugano-Saigusa-Fujikawa

In June, a second comet, Sugano-Saigusa-Fujikawa (1983e), neared Earth with a PCA of 0.06 AU. S- and X-band observations were performed at DSS 14 for a total of 40 hours. No signals were observed in real-time; however, further data reduction and analysis may provide a detectable echo. A future issue of this publication will contain more information pertaining to the investigation of this comet.

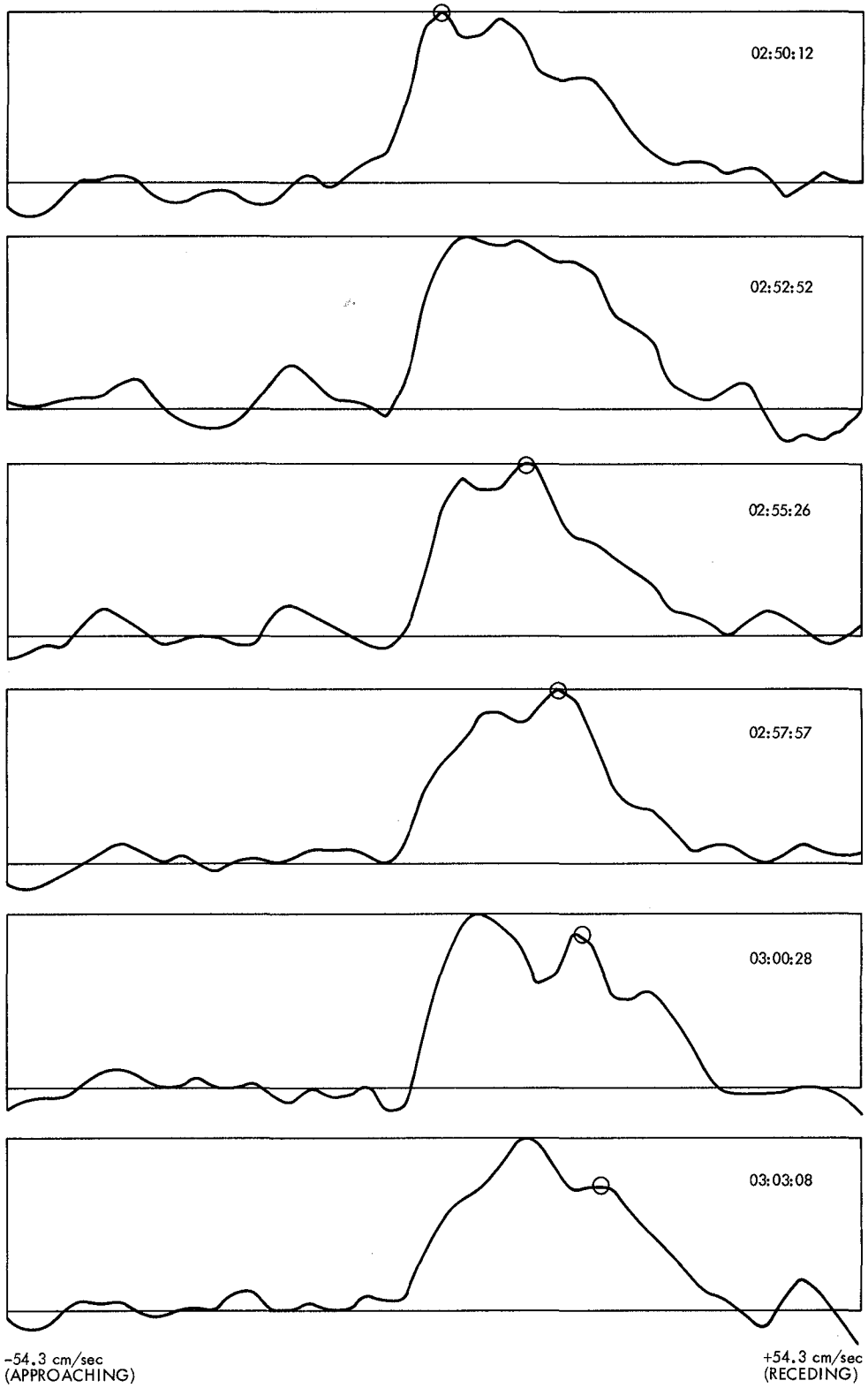


**Fig. 1. Successive X-band radar spectra of Comet 1983d, showing the transit of a suspected spectral feature (circled) with respect to time. Abscissa is limb velocity. Ordinate is intensity**

# Interagency Array Study Report

J. W. Layland (Study Team Leader) and A. M. Ruskin
TDA Planning

D. A. Bathker and R. C. Rydgig
Radio Frequency and Microwave Subsystems Section

D. W. Brown and B. D. Madsen
Telecommunications Systems Section

R. C. Clauss and G. S. Levy
TDA Technology Development

S. J. Kerridge
Mission Design Section

M. J. Klein
Atmospheric Sciences Section

C. E. Kohlhase
Voyager Project

J. I. Molinder
TDA Engineering

R. D. Shaffer
Control Center Operations Section

M. R. Traxler
TDA Mission Support

*The interagency array study was convened in early 1982 to determine which of the world's large radio reception facilities might be feasibly and beneficially enlisted to help support the Voyager encounters at Uranus (1986) and Neptune (1989), and also to examine the future for such similar events and options as might appear. A similar but more specific study of the Parkes Radio Telescope at Uranus Encounter was just then being completed with a strong positive recommendation, and formed the foundation of the broader study. This report describes the approach, driving considerations, and outcome of the interagency array study. The recommendations of the study team concentrated upon the Voyager Encounters: specifically to develop Parkes for the Uranus Encounter, while pursuing related Advanced Systems development work with the Owens Valley Radio Observatory, and to seek support for the Neptune Encounter from Parkes, the VLA, and the Japanese ISAS 64-meter station.*

# I. Introduction

The interagency array study formally began in early 1982 as a follow-on to the about-to-be-completed study of the support which could be provided by the Parkes Radio Telescope in Australia to the Voyager spacecraft at Uranus. That study had indicated that a quite significant benefit to the encounter could be obtained by arraying Parkes with the Australian DSN complex, and had displayed a technically feasible method of achieving it. The broader arraying study was charged with determining which other facilities might also be feasibly and beneficially employed for the support of Voyager at Uranus, and with examining the Voyager-Neptune Encounter, and such other future events and options as might appear.

There are three general reasons why the DSN is interested in the concept of interagency arraying. First and foremost is the desire on the part of NASA to increase telecommunications link performance for some very special events such as the encounters of Voyager with Uranus in 1986 and Neptune in 1989. The flight of the ISEE-3 (International Sun-Earth Explorer –3) past the comet Giacobini-Zinner in 1985 is a similar special event, although there are no present plans to support it by interagency arrays. Future missions can also be expected to be candidates for such support if they contain events for which the need for intense or high data-rate support is significantly larger than the average throughout the mission.

The second reason is to provide an opportunity for the U.S. to cooperate in international space exploration with those nations that are interested in joining that activity and have established a large radio reception facility. Participation by their scientists can engender support for exploration in general, thus broadening overall interest in international space exploration.

The third reason is to expand the options for the planning of future missions, to make it feasible to pursue missions which would otherwise be severely limited by the telecommunications link at their climax, and as a consequence be too expensive or impractical to develop.

Figure 1 shows the heliocentric trajectory of the two Voyager spacecraft from their launch in 1977 to their excursion beyond the orbit of Neptune, and it indicates the quite dramatic decrease in signal strength for the encounters at the two other planets relative to that at the Jupiter Encounter. These spacecraft were designed to provide superb coverage of the basic mission to Jupiter and Saturn, but with a trajectory option which could take one spacecraft past Uranus and Neptune many years later. The extended mission to Uranus and Neptune was not approved until after Saturn Encounter. Now work is underway both at the ground stations and with the spacecraft control software to make the data return at the outer planet encounters approach that of these first two encounters. Gains available from modifications to the spacecraft data system software are limited to about 3 dB, which means that a significant part of the 13.5-dB decrease in signal level must be compensated for on the ground. Since both money and time are limited, arraying with large apertures from outside the DSN appears to be the only open avenue.

Most of the world's large radio receiving antennas were at least considered in the early stages of the study, but the span of possible choices was narrowed as the study evolved. Table 1 represents the catalog of apertures which were given early consideration, together with their approximate location, and some of their pertinent characteristics. Figure 2 shows the 1986 configuration of the DSN, together with the most prominent candidate observatories for arraying for support of the Voyager at Uranus. These candidates include the Parkes Radio Telescope, the Bonn 100-meter antenna, the Japanese 64- and 45-meter antennas, and the large NRAO and OVRO antennas in the U.S.A. Arecibo is also shown, not because of Voyager, but because of its potential benefits to the ISEE-3 flyby of comet Giacobini-Zinner. The narrowing of options took place primarily because it was recognized that the resources are limited, both for study and for later accomplishment, and that the greatest benefits would accrue through arraying with the largest and best located of the available apertures. Further, the individual apertures had to be large enough so that a significant increment to the mission science return would be obtained without serious technical difficulties in arraying.

While arraying with non-DSN apertures is expected to provide a significant part of the increased reception capability needed for the Voyager, NASA is also looking for growth of its own internal ground network capabilities in the latter part of the 1980's. Several precepts guided the planning for the growth to the planned 1989 DSN configuration. First, the DSN must have the capability and capacity to adequately support all regular long-term mission operations, such as cruise operations and cruise science data gathering; any regular planetary orbiter science gathering, such as the Venus Radar Mapper, or any frequent repeated planetary satellite encounters such as will occur with the Galileo orbital operations around Jupiter. Second, the DSN by itself must be capable of ensuring at least a limited successful encounter for each planetary flight project under normal conditions. Interagency arraying is as yet untested, both technically and organizationally, and depending totally upon it for a flyby encounter is clearly unwise. Even for the stringent conditions of Voyager at Neptune, the DSN alone should be capable of capturing the needed near-continuous general science data and a part of the imaging return. Normal conditions are assumed, with the

Voyager's on-board tape recorder and image data compression software both operative. To justify their use, the interagency arrays must significantly enhance the support provided to the planetary encounters, or to other selected special events. Figure 3 shows a baseline 1989 DSN configuration that is consistent with these precepts and the most prominent of the candidate observatories for that time. Here, the Very Large Array (VLA) near Socorro, New Mexico, has replaced the NRAO antenna in the American longitude. Arecibo is again shown, in this case for its potential for following the Pioneer 10 out of the Solar System.

In looking at the other potential applications of interagency arraying, certain criteria were identified which could be used to select appropriate missions. First, missions to be enhanced through the participation of the radio astronomy observatories should be unique special events; not routine nor regular usage. This restriction does not necessarily apply, however, in the case of a non-DSN aperture sponsored by another space agency, where mutual benefit arrangements could be established to exchange support of flight projects, and perhaps ultimately lead to regular joint operations. Second, participation of another agency should substantially enhance the mission science return, by increasing data volume or mission reliability, and should also provide suitable benefits to the observatory or the agency sponsor of the non-DSN antennas. Such benefits could take the form of exchange of cross-support for other missions, enhanced capabilities which would be left in place after the arraying event concluded, or perhaps assistance in other scientific endeavors of mutual interest. It could also take the form of direct reimbursement. The catalog of suitable NASA candidate missions which were identified is not large, and whether this is due to the true uniqueness of this opportunity or merely to our myopia will only become clear with time.

The recognized suitable candidate missions are the two far outer planet encounters of the Voyager at Uranus (1986) and Neptune (1989), the encounter of ISEE-3 with Giacobini-Zinner (1985), and a potential future Mariner Mark-II mission, Titan Flyby/Titan Probe (1996). Other candidates are possible, and if, for example, some future spacecraft approached a flyby, or a probe release event or an orbit insertion with a severely degraded telecommunications capability, these events could qualify as suitable for interagency arraying support. Further into the future, exchange of mission support between NASA and other space agencies could become routine for peak load sharing, or for better viewing geometry.

This report provides a survey of the benefits of the Voyager and other missions which are obtainable by interagency arraying, and of the technical and organizational efforts needed to achieve these benefits.

## II. Missions Other Than Voyager

In addition to Voyager's needs which motivated this study, a number of other applications for interagency arraying were examined. These included both other possible flight projects and ground-based radio science observations of several kinds.

Table 2 summarizes the opportunities that were identified for ground-based observations. Planetary radar, for example, can be done using Goldstone for the transmitter, and one or more large observatories as receiving stations—if the needed frequency compatibility is maintained. Some work of this type has been done in the past at S-band, using DSS 14 as the transmitting and Arecibo as the receiving site. The table identifies the three main categories: Planetary Radar, SETI (Search for Extraterrestrial Intelligence), and Interferometry—either VLBI, or connected-element interferometry using the real-time links that would be installed to implement the interagency arrays. The table also indicates in each case the facilities which would be of greatest benefit, the science drivers for their use, and the main items of instrumentation which would be required.

The currently understood mission sets, as represented on Figs. 4 and 5, were examined for their potential need for interagency arrays. In general, the base mission set was designed to operate adequately into the antennas of the DSN alone, and nothing has really occurred to change that, or to create major benefits from substantially increased ground aperture beyond that planned for the DSN of the late 1980's. Voyager, of course, has encountered a change, because it was basically designed for the Jupiter and Saturn Encounters, much closer to Earth than Uranus and Neptune.

The ISEE-3 spacecraft has also undergone change, from its initial role as a solar wind observatory in the libration point between the Sun and Earth, to its planned usage in the close vicinity of the comet Giacobini-Zinner in 1985. At its design point, the spacecraft was 0.01 astronomical units (AU) away from Earth, and at the cometary encounter it will be about 50 times further at 0.46 AU away. It was supported with very high signal margins by the GSTDN at the libration point, but will be straining the DSN capabilities as a comet mission. The encounter with the comet will be at the northern declination of +23 degrees, so that the planned Japanese 64-meter antenna and Arecibo could both provide an excellent supplement to the support by the DSN.

The set of potential future missions was examined for candidates for support by interagency arrays which would be similar to that needed by Voyager. This mission set is dominated by Mariner Mark II missions, which are constrained in data rate, deployed to close-in targets, or both. The Mariner Mark II EEIS (End-to-End Information System) Team helped

in examining this mission set for benefits of interagency arraying. Of these missions, only one, the Titan Flyby/Titan Probe, showed even modest benefit from arrayed support. For this mission, it was found that "interagency array allows reduction of precious spacecraft power to telecom" (Ref. 1). The mission is characterized by two short intervals of fairly intense data gathering, the probe entry phase first, and then the radar mapping phase as the carrier spacecraft flies past Titan.

In addition to the examination of specific missions, the interagency array study team also spent some time in brainstorming about types of missions which could follow the present or presently planned missions. These mission types included intensive Mars or Venus exploration programs, as well as missions to small bodies, and orbital missions to the outer planets. If Voyager does the job expected of it in 1986 and 1989, there will probably not be another reconnaissance type mission to Uranus or Neptune. Even if there is such a mission to an outer planet, it will probably be *designed* directly for that usage, with a telecom capability which is consistent with support by the DSN's own apertures. Planetary orbital missions could motivate additional capability within the DSN, but would not be candidates for arrayed support by observatories because of the extensive coverage required.

In summary then, it appears unlikely that another U.S. mission will arise within the near future which will derive as great a benefit as Voyager from interagency arrays. Cross support, or the exchange of support between various space agencies for each others' missions, is a very different matter, and suitable arrangements with Japan's Institute of Space and Astronautical Sciences (ISAS), or with other space agencies of the world, would effect an increase in the pool of antenna facilities which can be called upon to support space missions. This would both enable better mission support during intervals of heavy support load and smooth the workload on individual facilities. Exchanges of support can also be beneficial in situations which are geometry-dependent, as in supporting a U.S. spacecraft at northerly declination from the Japanese 64-meter station and a Japanese spacecraft at southerly declination from the Canberra Deep Space Communications Complex (DSCC). Emergency situations are yet another matter, and if the various non-DSN facilities were easily configured to be capable of spacecraft observations, it would seem perfectly natural to seek their support in reacting to a greatly diminished spacecraft signal level.

## III. System Requirements and Performance for Voyager

The Voyager flight to Uranus and Neptune is the primary near-term driver for the expanded performance enabled by interagency arraying. The objectives of the missions to Uranus and Neptune are, generally, to extend the comparative studies of the outer planets to include the environment, atmosphere, surface and body characteristics of the planets and the characteristics of one or more of their satellites; to determine the nature of the rings of Uranus; and to search for rings at Neptune. Typical specific scientific objectives to be addressed include measurements of the gross morphological structures of the planets and satellites; determination of the atmospheric composition, structure, and dynamics of Uranus and Neptune; determination of the Neptune rotation period; detailed magnetospheric and plasma studies; a study of the satellite surface features, temperatures, and possibly the Triton atmosphere; a study of the Uranus ring system; and a study of the Neptune rings, if they exist. More detail on this subject may be found in the Voyager Project plans for Uranus (Ref. 2) and Neptune (Ref. 3).

The Voyager science data requirements for the Uranus encounter can be succinctly stated as (1) continuous general science data throughout the entire encounter period, in order to characterize the spatial and temporal variations of the fields and particles surrounding the target planet, and (2) imaging observations during the near-encounter period which are adequate to provide a basic characterization of Uranus, its satellites, and rings.

By assessing the specific imaging targets at Uranus, the project science office estimated that on the day of encounter, some 50 effective-full-frame-images (EFFI) should be allocated to the planet, 121 EFFI allocated to the satellites, and 157 EFFI allocated to the examination of the rings, for a total of approximately 330 EFFI. For several days immediately surrounding the encounter day, the image count requirement will also be in the neighborhood of 300 EFFI per day. During the observatory phase, a few months preceding encounter, a return of 30–50 EFFI each day would be considered satisfactory.

The specific target-based assessment has not yet been done for the Neptune encounter, but it is strongly believed that the required image count will be on the order of some 300 EFFI on the encounter day. Although there are no known rings at Neptune, the important search for rings, coverage of the planet Neptune itself and of the large satellite Triton will almost certainly require the 300 EFFI per day at encounter.

These needs can only in part be met by the support available through the capability the DSN will have in 1986 or 1989, in concert with the enhancements being made to the onboard Flight Data System software. The part of these needs which cannot be met by the DSN forms the primary driver for the interagency arraying system. That system must provide the capability to receive the Voyager's X-band signal at the selected

sites and to reduce these signals to baseband so that they may be transported to the DSN site in longitude. That system will further provide the capability to array the baseband signals from the non-DSN facilities with those of the DSN site in real-time via microwave or satellite link. It will also provide the capability to combine recorded baseband signals from each non-DSN site with concurrently recorded signals from the DSN site in longitude. Both real-time and recorded-signal arraying must be provided to ensure adequate reliability for the overall arrayed aperture.

Figure 6 shows the planned performance of the DSN as it would be when arrayed with a number of the plausible candidate observatories for the support of Voyager at Uranus Encounter. The horizontal axis of this figure is labeled in GMT hours on the encounter day, January 24, 1986. The left-hand axis is calibrated in dB-Hz of data power to noise spectral density. The solid arcs of the figure show the expected received signal-to-noise ratio for the X-band Voyager signal under 90% confidence conditions. This means that for at least 90% of possible situations, including predictable variations in the equipment parameters and weather as modelled by day-quarter and year-quarter, the Voyager's signal as it is received will be at least as strong as that indicated. The arrayed performance of Parkes with the DSN Australian complex is also shown as a solid line, because we are committed to bringing that capability into existence for the Uranus Encounter. The American longitude array of the Owens Valley Radio Observatory with the DSN's Goldstone Complex is being pursued by the DSN Advanced Systems Program as a possible demonstration vehicle for arraying technology, while the array with the Bonn 100-meter is not being actively pursued at this time.

The weather statistics assumed for Fig. 6 for each of the DSN sites are the standard MRI (Meteorological Research Incorporated) quarterly weather model which is documented in the DSN Interface document (Ref. 4). For the non-DSN sites, the weather statistics were approximated by those of a DSN site with similar rainfall and temperature averages, as represented by the Hammond world almanac, or by other data as available. As the DSN models are believed to be conservative, this should result in a conservative estimate of arrayed performance. Work is needed to refine these estimates prior to encounter. In all cases, the statistical independence of the weather patterns at the DSN and non-DSN arrayed sites was included, and modestly increased the arrayed performance. The functional availability of the various array elements was also included.

At each longitude, the DSN performance shown corresponds to the arrayed performance achievable with the full DSN configuration as it will be in 1986. At Madrid, the array is the same as it was for the Saturn Encounter, with the 64-meter and the standard-performance 34-meter antennas. At Canberra and Goldstone, the array consists of three antennas at each site, which includes the preceding two, plus a new, specially shaped high-efficiency 34-meter antenna. It should be noted that the arraying configuration being developed will also be capable of non-real-time arraying of the different longitudes of the DSN, should it prove operationally desirable to do so. The performance of such an array during the overlap between Goldstone and Canberra would rise to a peak at the equi-power points of the Goldstone and Canberra performance curves. It would rival the Canberra-Parkes arrayed performance at peak value, but provide only a few short hours of coverage.

The right-hand axis of Fig. 6 is labeled at the threshold levels of signal-to-noise ratio for the data rates which will be used at the Uranus encounter. Table 3 is a partial catalog of these data rates, together with their contents in terms of science data return. The data rates of 29.9 kbps, 19.2 kbps, and 7.2 kbps exist today and were available at the Saturn encounter. The other data modes are under development now by the Voyager Project to improve the return from the Uranus and Neptune encounters. The full catalog of applicable data rates and modes may be found in Ref. 5. The new data rates involve the use of an onboard Reed-Solomon encoder to provide very low bit error rates with only modest redundancy. For the true rate of 3.6 kbps of the general science data, this means that a transmitted data rate of 4.8 kbps can be used instead of the 7.2-kbps data rate which was the primary coded data rate when the Voyager was launched. The penalty of the Reed-Solomon code is in greater complexity, in both spacecraft encoder and ground-based decoder. The new imaging data rates all involve use of image data compression, which is established in the Voyager spacecraft by operating the redundant Flight Data System (FDS) processors as a dual parallel processor. Since the dual processors were initially provided to give adequate assurance that at least one of them would be functioning at the Saturn encounter, the availability of that dual processor mode is an item of some concern. Nevertheless, with the exception of a few minor components, all four FDS units on the two spacecraft are operable today, giving rise to a current assessment of a 80-85% likelihood that the dual processor operation will be available at Uranus, and a 65-75% likelihood that it will work for Neptune.

The fulfillment of the requirement for continuous general science data can be assessed from Fig. 6. It is fully satisfied if the 4.8-kbps data rate is operative. If the existing 7.2-kbps data rate must be employed instead, there are coverage gaps totalling approximately four hours at the edges of the Madrid pass. Arraying with the Bonn Observatory would fill in only a small part of that.

Assessment of the imaging return from a planetary encounter is a considerably more complex process, involving as it does

more than a half-dozen possible data rates, plus the option of recording either compressed or uncompressed images onto the spacecraft digital tape recorder. The assessment was carried out for the Voyager Mission Planning Office by S.J. Kerridge by using a linear programming technique to optimize the predicted return within the constraints of the telecommunications performance curves of Fig. 6, the available data rates, and the available storage capacity of the digital tape recorder. Details of this process are beyond the scope of this document, and may be found in Ref. 5.

The results of this assessment for the return from the Uranus encounter appear in Table 4. The most favorable and least favorable spacecraft state are indicated here. The most favorable state, with both Image Data Compression (IDC) and the Digital Tape Recorder (DTR) operable has an estimated 72% likelihood, while the least favorable state, with neither IDC nor DTR has an estimated likelihood of less than 2%. Encounter day differs from the steady-state operations in that the DTR, if operable, will be filled to capacity with the irreplaceable data from the closest approach period, and played back on succeeding days. The steady-state condition represents the operation on the days approaching encounter when any data recorded on the DTR must soon be played back to leave the DTR empty for filling at closest approach. Without the DTR operable, all images must be returned in real-time, so that the only difference between encounter day and steady-state results is the specific data modes which are used based upon science criteria.

As can be seen from this table, the addition of Parkes Radio Telescope to the Australian array effects a 10% to 15% increase in the images returned by a healthy Voyager, and brings the encounter day return up to almost the target level of 330 EFFI. The benefit from Parkes support is more dramatic if neither IDC nor DTR are available. For this very unfavorable but possible condition, the addition of Parkes more than doubles the image return to an estimated 90 EFFI. The benefits from augmenting Goldstone with the Owens Valley Radio Observatory or Madrid with the Bonn 100-meter telescope are neither one as significant to the objectives of the Voyager encounter with Uranus, but are shown in Table 4 for comparison

The baseline plan for the DSN configuration of 1989 is shown in Fig. 3, together with the largest of the candidate observatories for support of the Voyager Neptune encounter. The arrayed performance of this network is shown in Fig. 7, together with that available through arraying with the primary candidate observatories. Similar to Fig. 6, this figure indicates the 90% confidence telecommunication performance curves for the day of Neptune encounter on August 24, 1989. For this encounter, arraying with Parkes is needed to support the 14.4-kbps IDC data rate. As was the case at Uranus, almost continuous general science is supportable by the DSN at the 4.8-kbps data rate, but not if the 7.2-kbps data rate must be used.

The assessment of imaging return from Neptune was performed by the same linear programming algorithm as was used for Uranus, and is shown in Table 5. There are clear benefits in terms of image return for all spacecraft states from arrayed configurations involving Parkes, the Japanese ISAS 64-meter facility, and at least the "partial" configuration of the Very Large Array (VLA). The step-up to the maximum VLA configuration also has substantial benefit for the weakened-spacecraft condition. At Neptune, the anticipated likelihood of both IDC and DTR being available is 54%, and the likelihood of neither being operable is less than 7%.

There is, in addition, a need to retain some measure of protection against deterioration in the spacecraft telecommunications link in ways not covered by potential failure modes of the Flight Data System. Such deterioration can result from degradation in the spacecraft's high power X-band transmitter, or its RTG power supplies, or from antenna pointing losses resulting from accommodating the unrelated problems with the instrument scan platform. Link deterioration can be on the order of 1-3 dB with a risk level of perhaps 5% for each of several sources; much larger losses are possible but with lower risk. Such concern is best accommodated by providing at least one receiving facility which is capable of satisfactory support despite the 1-3 dB potential deterioration. The Parkes-Canberra array fulfills this need for the Uranus encounter. The VLA with maximum capability would be ideal for the Neptune encounter if it were readily achievable. The Japan-Parkes-Canberra array appears to provide another effective and achievable answer to this concern for Neptune. As shown on Fig. 7, the array of Goldstone with the VLA at approximately half maximum capability will extend the duration of Voyager coverage at this level.

Figure 8 shows the functional block diagram for the interagency arraying capability. Both real-time and near-real-time operation are included as outlined previously. The preferred mode of operation is to use the real-time array as the primary path, with the near-real-time as a backup. This operating mode requires wideband analog RF links, but provides continuous real-time imaging, even if the DSN site alone cannot, by itself, support the spacecraft link. It also does not require the transport or processing of the tape recordings unless the real-time intersite link is inoperative.

The high cost of the intersite link would be eliminated if we chose to use near-real-time combining only. However, there would be no real-time science data and thus no visibility to enable experimenters to adjust instrument parameters, unless

the weather were exceptionally benign and the telecommunications link into DSN site alone were of itself above threshold. This mode of combining also requires the operational burden of regular transport and processing of the tape recordings, and inserts a new single-point-of-failure in the form of the recorders which would not themselves have backup. Furthermore, our experience in establishing correct operation of dual-site non-real-time support operations in VLBI (Very Long Baseline Interferometry), without concurrent real-time verification of the configuration, has been dismal and would be thoroughly inadequate for support of vital planetary encounter telemetry. Instrumentation of the arrayed sites to provide adequate visibility and verification without the real-time link is being explored as part of the Parkes/Uranus activity in an attempt to make the near-real-time-only mode into a workable option.

As outlined above, substantial evidence has been gathered that both real-time and near-real-time capability must exist to provide adequate support to the Voyager encounters (Ref. 6), and until demonstrated otherwise, this combination will continue to be the basis for all interagency array planning.

## IV. Organizational Interfaces

It was clear from many considerations that there was no uniform and absolute rule which could be used to characterize the organizational aspects of each instance of interagency arraying. While a generalized model is possible, the details of the interfaces will in each instance be specialized to the needs of the involved agency. In establishing the arrangements for interagency arraying, we must and will seek to establish associations and interfaces that are beneficial to all agencies involved. Permanent ties will be sought with other space agencies, such as Japan's ISAS. Shorter-term relationships focussed by a specific goal such as the support of Voyager at Uranus, or the making of a ground-based interferometric radar map of Venus, or other astronomical measurements, seem more appropriate for the radio astronomy observatories.

There are four distinct categories of agencies which operate the primary candidates for interagency arraying operation. Each of these has special needs, which must be considered in establishing the organizational interfaces, and special strengths which can be relied upon. These four agency types are catalogued below:

U.S. National Observatory . . . . . NRAO-VLA

U.S. Academic Observatory . . . . . OVRO

Non-U.S. Radio Observatory . . Parkes/Bonn/Nobeyama

Non-U.S. Space Agency . . . Japan-64-m/Weilheim-30-m

The interfaces to non-U.S. agencies will require formal agreements tailored to fit under the umbrella of pre-existing international agreements, as is the case for the Parkes array. For all of these, management and administrative interfaces will involve NASA Managers, the JPL Assistant Laboratory Director for Telecommunication and Data Acquisition (TDA), and the TDA office managers in interaction with their counterparts at the operating, or host agencies. These interfaces are supported by the current TDA structure and procedures.

The engineering interfaces for establishing an interagency array are formally managed via the TDA Engineering Office. The applicable procedures, however, are necessarily very different from those usually used in DSN implementation, and are streamlined and respectful of both the capabilities and interests of the host agencies. The engineering interfaces with each agency are focussed during development by a project engineer/task manager who is responsible for the success of that particular array element. Because each candidate host is unique, significant interaction will be required between the engineers of the JPL technical divisions and those of the host agencies. This will need at least good electronic communication, as well as increased travel or personnel exchanges.

Operations interfaces for the flight projects are similar to those which exist now. The "TDS Manager for Project" is the focal point for all joint mission support. The coordination of operational events and activities will be performed by DSN operations, within the constraints of the agreements negotiated with each host agency. Operational coordination of the arrays will occur via the combining center at the DSCC in-longitude. Communication and coordination for both operation and implementation can be facilitated by in-longitude visits between DSN and host-agency personnel. A global forum would also be useful in this regard, similar to, or perhaps as a part of the Station Director's (STADIR) Conference.

## V. The Tidbinbilla-Parkes Array for Uranus

The array of the Australian DSN complex with the Parkes Radio Telescope is being established for the support of the Voyager at Uranus. It is the pathfinder project for interagency arraying, as it will be the first time that such support will be provided for a major planetary encounter. The overall requirements for configuring an interagency array were described in section III. The Parkes array is being implemented as a straightforward extension of current DSN technology in order to assure support for the Voyager data return at Uranus. Specific items of equipment design will be new for this application, such as the telemetry recording subsystem utilizing VLBI recorders, but the real-time system design follows that which was experimentally developed in the early 1970's, demonstrated with arrayed reception of Mariner 73 at Gold-

stone, and more recently implemented throughout the DSN and used to support the Voyager Saturn encounter (Ref. 7).

The implementation process for the Parkes array is expected to be much streamlined as compared to conventional DSN practice for long-term implementations. Specific details of this process are still to be negotiated. In considering this, it should be remembered that the Parkes array will not be implemented and then left in place to be operated and maintained by a long series of different operational personnel; it will instead be established and operated for a short (but important) event under the guidance of its designers. Rationale and general guidance for the steamlined implementation process may be found within the reports of the "Parkes-Canberra Telemetry Array" Task (Ref. 8). This process is aimed at providing cost-effective implementation and operation of a unique installation, which nevertheless is of adequate quality to assure viable spacecraft support. It is assumed throughout this report that this steamlined implementation process will be applied to all of the non-DSN facilities which are instrumented for arraying support.

The timetable for on-site activities at Parkes is shown on Fig. 9. Radio astromony, shown on the bottom line of this figure, is the primary business of the observatory, and naturally dominates the overall time, except for intervals surrounding the two Voyager encounters plus the test and demonstration interval in late 1984. In addition to the Voyager, the Parkes Radio Telescope will be supporting the Giotto spacecraft, which is being sent by the European Space Agency (ESA) to Halley's Comet. The support interval in 1985-86 will be shared between these spacecraft, with Voyager dominating near its encounter in January 1986, and Giotto dominating near its encounter a few weeks later. The intersite link between the Parkes Observatory and the DSN Complex, which is about 350 km to the south, will be installed to provide real-time arraying capability, but will be available for radio astonomy use also, and retained for that purpose following the Uranus encounter. Figure 10 shows the relative locations of Parkes, the Australian DSN complex, and the planned intersite link. The agreements which enable the support of Voyager by the Parkes Radio Telescope also provide for a significant amount of support for the Australian radio astronomy community by the DSN, which is anticipated to be used for real-time interferometry employing Parkes, the DSN antennas of the Canberra Complex, and the intersite link.

Figure 11 shows the functional elements of an interagency array as typified by the Parkes-Canberra array. Two elements of this drawing were added to generalize it, and are not part of the Parkes configuration: the satellite communication link for real-time arraying with large intersite distances, and the non-real-time combining via the VLBI correlator in Pasadena. The satellite link is applicable to an array between the Japanese 64-meter station and the Australian DSN site. The non-real-time arraying via the VLBI correlator is being explored under the DSN Advanced Systems Program, but is not critical to the operation of the array. It could be used for arraying between longitudes, or as an off-line backup for the real-time/near-real-time systems. At Parkes, the low-noise amplifier, the receiver front-end, and an upgrading of the antenna surface for X-band operation are being provided by ESA as part of their preparation to support Giotto.

The elements shown in the upper left one-third of Fig. 11 reside at the observatory, while the rest of the mainline elements are at the DSN complex in-longitude. At the observatory, the spacecraft signal is coherently detected to produce a baseband signal consisting of the subcarrier (360 kHz for Voyager) modulated by data, which is then both transmitted over the real-time link to the DSN site, and simultaneously recorded. At the DSN site, this signal is treated virtually the same as a signal from a DSN antenna, in that it and the combined signal of the DSN subarray are delay-adjusted into agreement and then coherently added before subsequent demodulation of the subcarrier, decoding, and telemetry processing.

With the configuration shown, we have the option of replaying the recorded tapes via the intersite link for near-real-time backup operation, as well as the operation of transporting the observatory tape recording, should there have been problems with arraying during the pass. Technical performance of the array is expected to be excellent, with an allowed degradation budget of 0.2 dB for the combiner itself, and another 0.2 dB allotted for either the intersite link or the recording and playback processes.

## VI. DSN Advanced Systems Program Plans for Arraying

The DSN Advanced Systems Program Office has defined plans for development of arraying technology which will be applicable to the Neptune encounter. The Owens Valley Radio Observatory (OVRO) is to be approached as a test bed for the demonstration of the potential improvements in both technology and cost, and for field demonstration of this capability through support to the Voyager at Uranus on a best-efforts basis. Specific negotiations for this work are now in process.

The Advanced Systems Program intends to provide a complete receiving system, including telemetry equipment, which is suitable for arraying a radio observatory site with the DSN. This effort will include developing fieldworthy R&D equipment for demonstration at the OVRO site prior to the Voyager Uranus encounter. It will provide a focus and a schedule

driver for selected advanced systems activities. Equipment developed will be transportable to other facilities for future encounters or demonstrations, if needed. The proposed demonstration is an R&D activity with no formal commitment to the Voyager project.

In general, technology planned for demonstration with an OVRO array is already planned or under development by the Advanced Systems Program for future use by the DSN. To reduce costs, existing or surplus equipment will be outfitted for the OVRO installation wherever possible. For the front-end area, a new focal point feed will be employed which has the potential for achieving an efficiency of 60-65% with a 17 kelvin system temperature. A surplus R&D X-band traveling wave master (TWM) will be modified to achieve dual-channel operation for polarization diversity and to fit within the package design recently employed to install a K-band (22-GHz) TWM at OVRO. The dual-channel TWM can accommodate a switch to the alternative polarization of the Voyager spacecraft's backup transmitter by simply switching inside the receiver instead of the microwave area. Existing support equipment for the K-band TWM will be used for the X-band TWM. If the conversion to a Cassegrainian feed system, which is currently being considered, occurs prior to the arraying demonstration, then the new focal point feed will not be needed, and other parts of the task will also be simplified.

The back-end of the array of Goldstone and OVRO will provide the opportunity to demonstrate symbol-stream combining, and also applicable technology from the advanced receiver development, including digital phase-locked loops, ephemeris aided tuning, etc. For symbol stream combining, the received signal at each site is processed through the subcarrier demodulation and symbol detection processes before being sampled and transported to the common combining point for decoding. Preliminary analysis indicates that symbol stream combining is not only feasible, but may also be able to perform better than the predetection combining currently employed. The initial rationale for exploring symbol stream combining is still valid: to reduce the bandwidth of the signal to be transported by intersite link or on tape from a remote site to the DSN combining location, in order to reduce the cost of such electronic or physical transport.

The schedule goal of the Advanced Systems Program is to demonstrate the arraying with OVRO prior to the Voyager Uranus encounter. In fact, the basic demonstration should be by the spring of 1985, so that it could be accommodated into project planning, if appropriate. The non-real-time demonstration is totally within the Advanced Systems Program resources. A real-time demonstration will require the provision of a 224-kbps digital link from Owens Valley to Goldstone, which is not within the Advanced Systems funding. The detailed milestone schedule leading to this demonstration will be established during the program planning negotiations which are occurring in early 1983. Both funding and schedule for this activity are subject to the usual review by JPL and NASA management as the details of the Advanced Systems Program are refined.

## VII. Instrumentation of Other Facilities for Voyager at Neptune

Other major antenna facilities of the world were examined to determine the effort and equipment needed to instrument them for arraying with the DSN in a configuration analogous to that being used to connect Parkes with the Canberra complex. Chief among these were the Bonn 100-meter telescope, the Japanese ISAS agency's 64-meter station, and the National Radio Astronomy Observatory's Very Large Array. In each case, the arraying configuration and functional block diagram is the same as that employed for Parkes: including both real-time and near-real-time arraying, and using the VLBI recorders for the backup recordings. Engineering for this design is a routine step forward from that of the Parkes array, which establishes a reference mode in which we can be well assured of success. But as we assume there will be success within the Advanced Systems development work on arraying, so then we should expect the details of the arraying design for Neptune to change to absorb the improvements demonstrated there. Until such demonstration, however, prudence dictates that the main pathway plan for Neptune arraying should directly follow the Parkes design.

In general, the equipment configuration for each installation is based upon a JPL design, even though when all details of in-place or planned equipment are known, the better course may be to utilize equipment developed by the facility itself. The engineering process is assumed to be the streamlined one being pioneered with Parkes.

The Bonn 100-meter telescope and the Japanese 64-meter antenna are both very similar to Parkes in that each is a large single reflector which by itself would contribute a significant addition to the array aperture. Loss of that addition would result in either a direct loss of data, or a change in Voyager data rate. To reduce the risk of loss to an acceptable level, independent redundant components are required in the cryogenic front-end amplifiers, and perhaps elsewhere in the system. Traveling wave maser (TWM) amplifiers are appropriate to the Japanese station, where the Voyager is visible for almost 8 hours per day. Other spacecraft will be subsequently supported by this antenna, and will benefit from the very low system temperatures which are achievable by TWMs. It is unfortunately true that the Bonn 100-meter telescope is

far enough north that it can only observe the Voyager spacecraft for approximately 5 hours per day, and then only through a significant amount of atmosphere. While it is true that under clear dry conditions a TWM will provide substantially better performance than any other known amplifier, missions are not designed to operate only in clear conditions, but must accommodate (at least) the 90% weather condition. Under 90% conditions, as we today perceive the Bonn weather statistics for August 1989, there is only a very modest benefit to Voyager for choosing a TWM over a (much cheaper) cryogenic FET amplifier with a 40-50 kelvin clear-weather system temperature.

Our engineering assessment proceeded under the assumption that all equipment which is specialized to X-band operation for tracking of spacecraft would be JPL-supplied. This includes the feed, the microwave plumbing, the applicable low noise amplifiers, the receivers, the recording and communication interfaces, and applicable instrumentation and monitor/control equipment. A VLBI recorder is also anticipated to be needed for the Japanese station. It should be noted that there is presently no commitment to JPL supplying any specific components, and that in fact cooperative agreements would be sought for the equipment development. The generalized schedule for the implementation is analogous to that being pursued for Parkes, and assumes a significant amount of contracting for fabrication of needed equipment. The overall effort occupies on the order of four years, and for the Neptune encounter in August of 1989, significant in-depth engineering work must start by FY 85. Onsite demonstration of arraying with the in-longitude DSN facility is strongly recommended for mid 1988, about a year in advance of the Neptune encounter.

The major agreements needed to enable the Voyager support at Neptune should be in place by mid 1985 in order to avoid potential problems in the engineering process. Figure 12 shows a generalized schedule applicable to the Bonn 100-meter telescope, to the Japanese 64-meter station, or to most other single-antenna facilities which might be considered for Neptune support.

The approach considered for the Very Large Array near Socorro, New Mexico, follows the Parkes design to the extent that such is possible with an array of modest-sized antennas. The back end of the system which performs phase locked detection and demodulation of the spacecraft signal to baseband in preparation for combining, the combining process at Goldstone, including both real-time and near-real-time options, the recording on the VLBI recorders, and the phase-lock receiver/coherent detection processes are all directly derived from those of the Parkes array. As will be discussed shortly, there are a number of options available for the front end of the VLA system, each with a different capability and complexity.

The VLA is an array of twenty-seven 25-meter antennas in a triradial configuration in the high New Mexico desert. Each of these antennas could be equivalent to about 18% of the DSN's 64-meter antenna aperture, if the VLA antenna were outfitted with a TWM. The primary role of this array is developing maps of radio-bright objects in the sky, and it incorporates a large mapping processor which is capable of cross-correlating the 351 (= 27*26/2) baselines of the array in real-time. One of the optional products of this mapping processor is a combined output which represents the coherent sum of the signals being received at each of the antennas. This combined output of the mapping processor would represent about four of the DSN's 64-meter apertures if all of the VLA antennas were outfitted with TWMs, or about two apertures if cryogenic FETs were installed. Because of the atmospheric noise effects, as noted earlier with the Bonn observatory, the effective performance of the VLA with FETs is expected to be better than 70% of that with the same number of TWMs for the Voyager encounter. Also, an improvement of about 1 dB in effective performance for the reception of spacecraft signals should be possible with either low noise amplifier if a specialized combiner and parallel signal path is installed. While this improvement potential is interesting, our current estimate of the costs involved makes this a nonviable option.

While there are conceptually very many options to choose from for the VLA configuration, they are all categorizable into a few option families, and only a few specific options need be examined to adequately characterize the entire collection. Our study approach was based upon the assumption that the maximum configuration should be protected and made available to be implemented if it became clear after the Uranus encounter that there was significant risk that the Voyager's image data compression would not be available at Neptune. This capability would have required TWMs in all VLA antennas, plus the specialized combiner and also would have required significant start by mid 1983 to remain viable. A schedule consistent with this approach is shown in Fig. 13. On this schedule, the actual decision between maximum capability and approximately half-capability would be deferred until just after the Uranus encounter, and could be based then upon an updated estimate of the likelihood that data compression would be operable at Neptune.

However, assuming that we can safely base the decisions regarding the Neptune encounter support upon the estimates available today for the viability of the data compression at Neptune, then the rational choice for a VLA configuration is one which can provide approximately half the maximum capability. Strong gains exist for Voyager's image return by provid-

ing this capability over the American longitude, whether the data compression is operative or not. As noted earlier, stepping upward to the maximum capability at the VLA will also reap significant benefits in the absence of data compression, but will only provide mild benefits if the Voyager is in its "most likely" state with both the data compression and the onboard tape recorder operative. The recommendations of the study team, to be discussed in section IX, are for a VLA configuration with the half-maximum capability.

The VLA can be configured to about half of its maximum overall capability for Voyager signal reception by installing cryogenic FET amplifiers in all of the antennas. The FETs are significantly less expensive and easier to build and maintain than the same number of TWMs, and it is believed that major work for an FET-configured VLA can begin in FY 85. Such a delay will, however, virtually foreclose the option of achieving the maximum configuration with TWMs.

Figure 14 shows the VLA configuration for Voyager support as we envision it today, together with the option for a specialized combiner which would bypass both the quantization in the VLA's mapping processor and the 1.6-ms gap in signal reception per 52 ms which is used in the VLA to calibrate and control its front-end systems. As noted above, the current assessment is that this option is too expensive relative to its expected benefit to pursue seriously, so that the only items to be added to the VLA are the X-band low-noise amplifiers and down-converters at the front-ends, and the phase-locked receiver and coherent detector at the combined output of the VLA processor. Two channels of the VLA signal transmission and processing equipment are used: one with a 6-MHz bandwidth to carry the spacecraft signal at roughly full precision, and a second with narrower bandwidth to be used to control the differential phase and delay in the system.

Should the X-band TWM be chosen for installation into the VLA, the design of choice could be expected to be a dual-channel maser identical to that to be installed at OVRO, except for the packaging and instrumentation. Figure 15 is a sketch of this design, incorporating a cryogenically cooled orthomode coupler and a dual-channel TWM derived from the DSN TWM design by segmenting it into two independent halves, and supplementing the gain of each half by an output FET amplifier. As shown in Fig. 16, the standard DSN X-band TWM consists of four quasi-independent structures which are usually cabled end-to-end to provide the gain and noise figure specified for the DSN. Splitting it into two independent units can be effected by a cabling change, along with providing the additional input/output couplers. There should be no problem in achieving an effective zenith system temperature below 20 kelvins with this configuration, which is virtually the same as that of the original DSN configuration.

The X-band FET was not explored to the same level of detail as was the TWM, but related NRAO experience was considered. In the currently planned development of the transcontinental Very Long Baseline (VLB) Array by NRAO in collaboration with Caltech (Ref. 9), cryogenic FETs are included for X-band coverage. The anticipated system temperature is on the order of 50 kelvins with amplifiers built today, or about 40 K by 1986. Clearly, then, it will pay to delay commitment to hardware if FETs are to be chosen. Also, if FETs are to be chosen, there may be some benefit to NRAO or JPL, or both, if the design for the X-band amplifiers of the VLA shares common elements with that for the VLB Array.

## VIII. Operations Scenario

The interagency array study team also sought to identify a reasonable operations scenario for arraying which would be consistent with that to be employed for Parkes, and also be applicable to the other facilities. The identified scenario depends upon several assumptions, derived from the Parkes planning, which are listed here:

(1) Data will be acquired and combined in both real-time and near-real-time.

(2) A member of the implementation team will remain "in-longitude" after the system is operational to serve as consultant to the operations team.

(3) The dividing line between non-DSN and DSN maintenance and operations functions will be at the receiver IF, as indicated in Fig. 17—this implies that host-agency personnel will maintain and operate the site-dedicated equipment, even if supplied by JPL, and that DSN-associated personnel will maintain and operate the "back end".

(4) Sustaining engineering will be via a suitable mechanism like the Equipment Support Agreement (ESA), instead of via full transfer.

(5) Operations of each array will be coordinated from the Deep Space Communications Complex in-longitude.

(6) All operations personnel for the array-specific operation will be recruited by the local DSCC.

These assumptions and the following notes define a general model for the operations scenario. It is recognized that each specific non-DSN facility which we will approach for the support of Voyager will be different in its interests and capabilities, and that details of the operations scenario will differ in

each case, in ways that will be defined in specific agreements with the non-DSN facility and its sponsoring agency.

Figure 17 is an operations-oriented functional block diagram of a non-DSN facility configured for arraying with a DSN site. The general dividing line between the two main spheres of responsibility is shown explicitly. Implicit in this division is the assumption that each non-DSN facility will have a VLBI Mark III Data Acquisition Terminal (DAT). Staff support for the arraying operation involves three personnel in addition to the implementation engineer, who will remain in-longitude as the arraying consultant and general troubleshooter. At the DSCC, a dedicated station operator will be assigned responsibility for actual array monitor and control. At the non-DSN facility, an on-site Leadman will be assigned the overall maintenance and operation (M&O) responsibility for the DSN sphere of responsibility, and will perform in addition some operations monitoring. He will be supported by one M&O Tech whose responsibilities include the M&O of DSN equipment, providing backup to the Leadman, and tape operations. At the DSCC, the M&O of the array equipment will be by station personnel, as defined in the Equipment Support Agreement. Sustaining engineering of the equipment items at both the DSCC and the non-DSN facility will be specified in agreements with the facility managers.

Some support to the array will be required from the operations organization at JPL. This support includes coordination functions for additions to the operations plan as related to interagency arraying, coordination of predicts and communications, and general operation coordination and scheduling. Predicts are needed for the pointing of the non-DSN antenna and for specifying tuning for the receivers and time-delay for the arraying process. Some sustaining engineering will also be required, including at least maintaining the interface between various parties to the Equipment Support Agreements as well as Subsystem-Cognizant-Operations-Engineer support for System Performance Tests (SPTs) for the total array.

The nominal timetable for deployment of operations personnel at the non-DSN site is shown in Fig. 18. Two high-activity periods are indicated: one at encounter and an earlier one for SPTs about 20 weeks in advance of encounter. The actual duration and intensity of these periods is a negotiable item, but it should encompass the intervals surrounding encounter when the data of greatest intrinsic value would be obtained. As permitted by the equipment configuration, radio astronomy operation would continue throughout this period except during the agreed-upon intervals specifically dedicated to Voyager support. A large part of the installation and checkout of the arraying configuration and equipment could and would take place on a noninterference basis with respect to other activities at both the non-DSN and DSN sites.

## IX. Summary and Recommendations

The interagency array study was brought to its conclusion in an open review on Friday, February 25, 1983. The primary decision needed at that time was for those items to be included in the DSN budgets and implementation planning for the years 1984-89. One decision which was particularly urgent was also painful—the choice between a pathway for the VLA which would protect the option of achieving its maximum capability for Voyager, but which needed an immediate start, and an alternative set of pathways which could achieve approximately half-maximum capability. Other decisions, whether to seek support from the Bonn or the Japan antennas or both, or perhaps from other facilities, would impact FY 85 and later budgets, but not require immediate starts.

The study team brought to this review a set of recommendations which were cognizant not only of the needs of the Voyager for Neptune, but also of the preparations in process for the support of the Uranus encounter, and of the ongoing need within the DSN to provide service to a substantial number of other missions. It became clear in this consideration that initiating the significant effort in FY 83-84, as needed for the maximum capability at the VLA, could jeopardize the near term work of the Network. Accordingly, such near-term start of detailed engineering work was not considered feasible, and the maximum-capability option was not recommended.

The recommendations of the study team, generally supported by the study steering committe, were as follows:

(1) Continue on present course with preparations for the Voyager Uranus encounter, including both the implementation of Parkes according to the planned streamlined process and the Advanced Systems demonstration of arraying technology at the Owens Valley Radio Observatory.

(2) Plan to seek support for the Voyager Neptune encounter from the Parkes Radio Telescope, from the VLA—configured to approximately half maximum capability (2.5 equivalent 64-meter aperture units), and from the Japanese ISAS 64-meter station.

(3) Retain the option to seek support for Voyager at Neptune from the Bonn 100-meter Observatory, should it become feasible and appropriate to do so.

(4) Establish interagency agreements and begin engineering on a schedule which is consistent with the chosen course of action. As noted earlier, the schedule for the recommended pathway requires implementation engineering to start by the beginning of FY 85.

The rationale upon which these recommendations are based can be seen in part in Figs. 19 and 20, which assess, each in different ways, the value of various interagency arrays to the Voyager as a function of their relative funding cost to DSN. Figure 19 shows the "capture value" of the various antenna options, as projected to the position of the Voyager spacecraft at its 1989 encounter with Neptune. Capture value is indicative of the total signal-energy-to-noise-density ratio that can be acquired from the Voyager during any one support pass by the identified antenna at one (optimum) realizable data rate. A capture value of unity could represent a mythical antenna offering 24-hour coverage equivalent to the current DSN 64-meter stations: 64-meter reflector with 50% efficiency and a 25-kelvin system temperature. The actual DSN 64-meter dishes are significantly less than unity capture value because they can only see the Voyager for a fraction of the day, and because their system temperature is degraded (for 90% confidence weather) to above 25 kelvins by the atmosphere the Voyager signal must penetrate.

On Fig. 19, the three DSN 64-meter stations are shown with zero incremental cost, to configure them for Voyager support, and with their capture value scaled to that which they will offer to Voyager at its position of -23° declination at the outer planet encounters. Identical in intrinsic capability, they differ in this figure due to their differing latitudes, and also to the different weather statistics peculiar to their site. The capture value for the various non-DSN facilities was derived with the same assumed weather statistics used earlier in Fig. 6. Their relative cost was derived from the engineering evaluation described in section 7, utilizing where applicable the analogy to the Parkes-Canberra array implementation. The Parkes cost itself is that applicable to the Uranus encounter, and does not include the TWMs and receiver components which are being supplied by ESA. The three straight lines on this figure for the VLA are approximations to the stairstep lines which would represent varying numbers of low noise amplifiers (FETs or TWMs) installed into the VLA antennas.

Figure 20 shows the potential imaging return for the Voyager at Neptune encounter for various interagency array options. The data portrayed on the vertical axis of this figure corresponds to Table 5 of section 3, but represents only the encounter-day strategy. Reference 5 may be consulted for more detail. The cost assigned to the Parkes array on this figure corresponds to only the replacement of the TWMs and receiver components which were supplied by ESA for the Uranus time frame. The costs assigned to the other arrays correspond to those of Fig. 19, including the partial VLA options which are shown as if achieved by TWMs. The various line segments of Fig. 20 serve merely to connect the points which represent specific arraying options. As in Table 5, Parkes is assumed to be a first step, to which can be added the Japan-ISAS 64-meter, the VLA in any of several possible configurations, or the Bonn 100-meter telescope. The slope of each line segment of Fig. 20 represents the "pictures-per-dollar" that can be obtained via the inclusion of the associated option.

Considering the Voyager imaging return in isolation, it is clear from Fig. 20 that the single most cost-effective interagency array for the Neptune encounter is that which was previously implemented for Uranus support; i.e., the Parkes Radio Telescope in Australia. That would still be true even if the full cost (Uranus + Neptune) of the implementation were considered. That is also true regardless of whether the spacecraft is healthy, with both image data compression (IDC) and the onboard tape recorder (DTR) operable, or whether it is weakened by one or more failures. The four probable states of the spacecraft data system are shown on Fig. 20, annotated by the current assessment of their relative likelihoods (Ref. 5). Argument can be made using the data on this figure that any one of the three primary alternatives should be considered as next after Parkes. The Japan 64-meter station is preferred because it provides the greatest imaging gain for the healthy spacecraft (the most probable state). The next best investment for the healthy spacecraft is the partial VLA configuration. Benefits in Neptune encounter data return continue to be obtained from adding capability to the VLA for all spacecraft states up to approximately the half-maximum capability level. Beyond this point, we are buying insurance that adequate support can be achieved despite deterioration of the spacecraft condition. The Bonn Observatory also is in the nature of insurance, in that its greatest benefits for Voyager imaging are obtained under conditions of a partially weakened spacecraft.

In summary, the Interagency Array Study team recommends that the arraying configuration for the Neptune encounter should consist of the full DSN aperture, plus Parkes, the VLA (at half-maximum capability), and the Japanese 64-meter station. This configuration will provide good imaging support of the Voyager at Neptune under current project expectations, as well as resilience to unanticipated deterioration in the space-to-earth telecommunications link.

# References


1. Noreen, G. K., "Mariner Mark II EEIS Report #6," IOM 3171-82-321, August 25, 1982; Material presented at Interagency Array Study Team Meeting, Jet Propulsion Laboratory, Pasadena, Calif., August 13, 1982 (JPL internal document).

2. *Voyager Project Plan, Part 2: Voyager Uranus/Interstellar Mission*, PD 618-5, Part 2, Jet Propulsion Laboratory, Pasadena, Calif., July 22, 1981.

3. *Voyager Project Plan, Part 3: Voyager Neptune/Interstellar Mission*, PD 618-5, Part 3, Jet Propulsion Laboratory, Pasadena, Calif., Sept. 1, 1982.

4. DSN Document 810-5, Rev. D, *Deep Space Network/Flight Project Interface Design Handbook*, Module TCI-40, Rev. A, Sept. 1980, "Atmospheric and Environmental Effects," Jet Propulsion Laboratory, Pasadena, Calif.

5. Kerridge, S. J., "Imaging Science Returns from Uranus and Neptune and Their Sensitivity to DSN Augmentation Planning," IOM-Voyager-SJK-83-1, Feb. 4, 1983 (JPL internal document).

6. Stevens, R. "Consideration of Combining Methods for the Parkes-Tidbinbilla Array for Voyager 2 Uranus Encounter," IOM-RS-82-2120B, Jet Propulsion Laboratory, Pasadena, Calif., Sept. 2, 1982 (with attachments) (JPL internal document).

7. Stevens, R. "Applications of Telemetry Arraying in the DSN," *TDA Progress Report 42-72*, pp. 78-82, Jet Propulsion Laboratory, Pasadena, Calif., Feb. 15, 1982.

8. Brown, D. W., et al., "PCTA System Requirements and Design Including Subsystem Requirements," (Draft 5, April 14, 1983; JPL internal document).

9. *The Very Long Baseline Array Radio Telescope*, National Radio Astronomy Observatory, May 1982.

10. Layland, J. W., *Potential VLA/DSN Arrayed Support to the Voyager at Neptune*, May 12, 1983 (JPL internal document).

**Table 1. Catalog of radio observatories**

| Institution | Location | East longitude | Latitude | Aperture | Area, $m^2$ | Current Efficiency | Current $T_{op}$ | Improved Efficiency | Improved $T_{op}$ | % equivalent, 64-m | Remarks |
|---|---|---|---|---|---|---|---|---|---|---|---|
| 64-m DSS | Standard for 86 | | | 64 | 3,217 | 50 | 25 | 50 | 25 | 100 | |
| 70-m DSS | Standard for 89 | | | 70 | 3,848 | | | 60 | 25 | 145 | |
| Nuffield R.A.L. | Jodrell Bank, U.K. | 358 | +53 | 76 | 4,536 | 20 | 50 | 20 | 25 | 56 | Old-inefficient far north |
| Franco-German | Spain | 359 | +38 | 30 | 707 | | | 60 | 25 | 26 | mm-wave R/A instrument |
| MPIR | Effelsberg, FRG | 006 | +50 | 100 | 7,854 | 45 | 90 | 45 | 25 | 220 | Needs LNA |
| | Bologna, Italy | 012 | +43 | 32 X 2 | 1,609 | | | 60 | 25 | 60 | mm-wave; not built |
| CC-1 | Yevpatoriya | 033 | +45 | 70 | 3,848 | 50 | N/A | 50 | 25 | 120 | Needs TWM |
| CC-2 | Ussurijsk | 134 | +44 | 70 | 3,848 | 50 | N/A | 50 | 25 | 120 | Needs TWM |
| Japan 64m | Usuda, Japan | 138 | +35 | 45 | 1,590 | 60 | N/A | 60 | 25 | 59 | Needs TWM |
| Japan 45m | Nobeyama, Japan | 138 | +35 | 64 | 3,217 | | | 60 | 25 | 120 | Needs TWM |
| CSIRO | Parkes, NSW | 148 | −33 | 64 | 3,217 | 35 | 100 | 40 | 25 | 80 | Needs TWM |
| OVRO | Big Pine, CA | 242 | +37 | 40 | 1,257 | 50 | 150 | 50 | 25 | 39 | Needs TWM |
| NRAO-VLA | Socorro, NM | 253 | +34 | 25 X 27 | 13,253 | 60 | N/A | 60 | 25 | 494 | Needs 27 TWMs |
| NRAO | Greenbank WV | 281 | +38 | 43 | 1,452 | 45 | 85 | 45 | 25 | 41 | |
| Algonquin Park | Algonquin Park, Ont. Canada | 282 | +45 | 46 | 1,661 | 50 | N/A | 50 | 25 | 52 | Needs |
| Haystack | Haystack, MA | 289 | +42 | 37 | 1,075 | 40 | 100 | 40 | 25 | 27 | Lose 1 dB to Dome |
| Arecibo | Arecibo, PR | 294 | +18 | 305 | 73,062 | 40 | N/A | 40 | 25 | 1817 | Useful only ±20 LHA and $\delta$ = −2 to +39 |

**Table 2. Additional potential users**

| Radio and radar astronomy | | | |
|---|---|---|---|
| Classification | Potential observatories | Science driver | Required instrumentation capability |
| Planetary radar | GDSCC with:<br>VLA, OVRO, Arecibo (S-band), Australia telescope, Japan | Venus mapping<br>Outer planet satellites and rings | X-band (8.45 GHz transmitter at GDSCC) |
| SETI | All | Confirmation, including position-finding<br>Search special frequency bands<br>RFI avoidance, e.g., interferometry | Receiver tunability (1–10 GHz)<br>Data link to SETI processor at DSN facility |
| Interferometry | | | |
| VLBI | VLBI-consortium | Additional U-V plane coverage | RF frequency compatibility (including 22 GHz) |
| | VLBI-TDRS | Greater sensitivity for VLBI net | VLBI system compatibility, e.g., Mark III DAT at all 64-m DSN stations |
| Real-time | GDSCC-OVRO | Greater positional accuracy | Link bandwidth $\geq$ 6 MHz<br>X-band link phase stability |
| | CDSCC-Parkes | Improved mapping | $\frac{\Delta f}{f} < 3 \times 10^{-3}$ rms and hourly drift rate<br>RF frequency compatibility |

**Table 3. Voyager Uranus and Neptune data rates**

| Data rate, kb/s | Data type | Coding | Equivalent full images/hr |
|---|---|---|---|
| 29.9 | Full frame imaging | Convolutional | 13 |
| 21.6 | Compressed imaging + playback | Convolutional + Reed-Solomon | 13 + 6 |
| 19.2 | Half frame imaging | Convolutional | 6 |
| 14.4 | Compressed imaging | Convolutional + Reed-Solomon | 13 |
| 11.2 | Compressed imaging | Convolutional + Reed-Solomon | 9 |
| 8.4 | Compressed imaging | Convolutional + Reed-Solomon | 5 |
| 7.2 | General science and engineering | Convolutional + Golay | None |
| 4.8 | General science and engineering | Convolutional + Reed-Solomon | None |

**Table 4. Voyager Uranus picture return/day**

| Aperture | Spacecraft state: IDC, DTR — Encounter day | Spacecraft state: IDC, DTR — Steady state | Spacecraft state: No IDC, No DTR |
|---|---|---|---|
| Baseline<br>GDSCC = 64, 34 S, 34 H<br>CDSCC = 64, 34 S, 34 H<br>MDSCC = 64, 34 S | 290 | 205 | 40 |
| Δ for augment "Australia"<br>Parkes | 30 | 30 | 50 |
| Total (planned) | 320 | 235 | 90 |
| Δ for augment "Goldstone"<br>OVRO | 10 | 10 | 25 |
| Δ for augment "Spain"<br>Bonn | 10 | 40 | 15 |

Notes: Daily return depends on DTR strategy and imaging constraints.

If S/C roll pointing is substituted for azimuth slewing, reduce numbers by 25%; additional telecom losses also likely.

H = high efficiency S = standard efficiency

**Table 5. Voyager Neptune picture return/day**

| Aperture | Spacecraft state: IDC, DTR — Encounter day | Spacecraft state: IDC, DTR — Steady state | Spacecraft state: No IDC, No DTR |
|---|---|---|---|
| Assumed<br>GDSCC = 70, 34 S, 34 H<br>CDSCC = 70, 34 S, 34 H<br>MDSCC = 70, 34 S, 34 H | 255 | 95 | 35 |
| Parkes | 20 | 30 | 20 |
| Total (planned) | 275 | 125 | 55 |
| Δ for augment "Australia"<br>Japan | 20 | 25 | 5 |
| Δ for augment "Goldstone"<br>VLA 2.5 aperture units | 30 | 55 | 30 |
| VLA 5.0 aperture units | 35 | 60 | 65 |
| Δ for augment "Spain"<br>Bonn | 0 | 25 | 10 |

Notes: Daily return depends on DTR strategy and imaging constraints.

If S/C roll pointing is substituted for azimuth slewing, reduce numbers by 25%; additional telecom losses also likely.

H = high efficiency. S = standard efficiency.

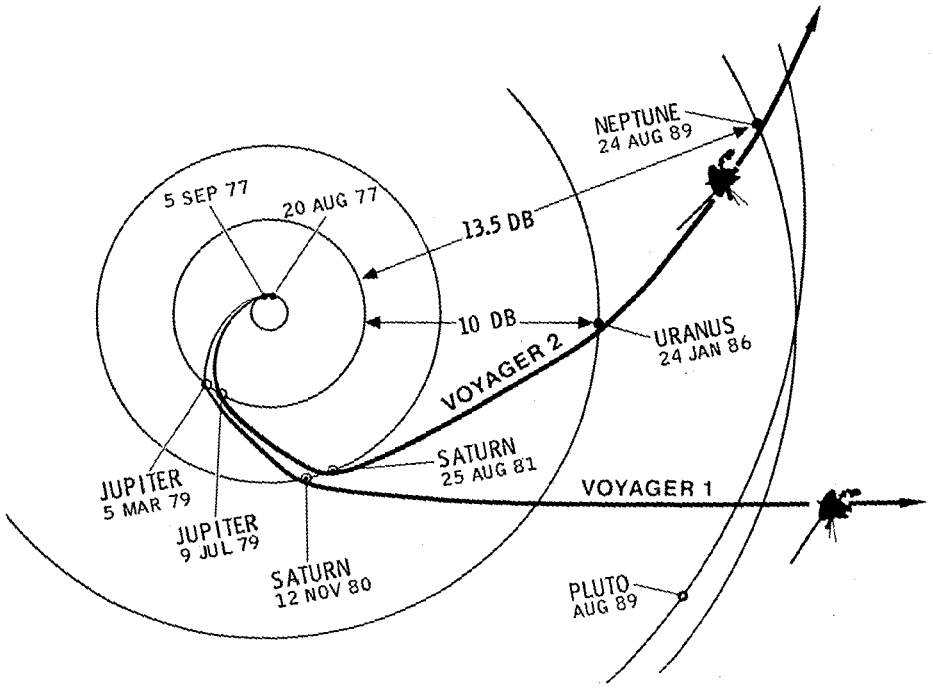


**Fig. 1. Voyager heliocentric trajectory**

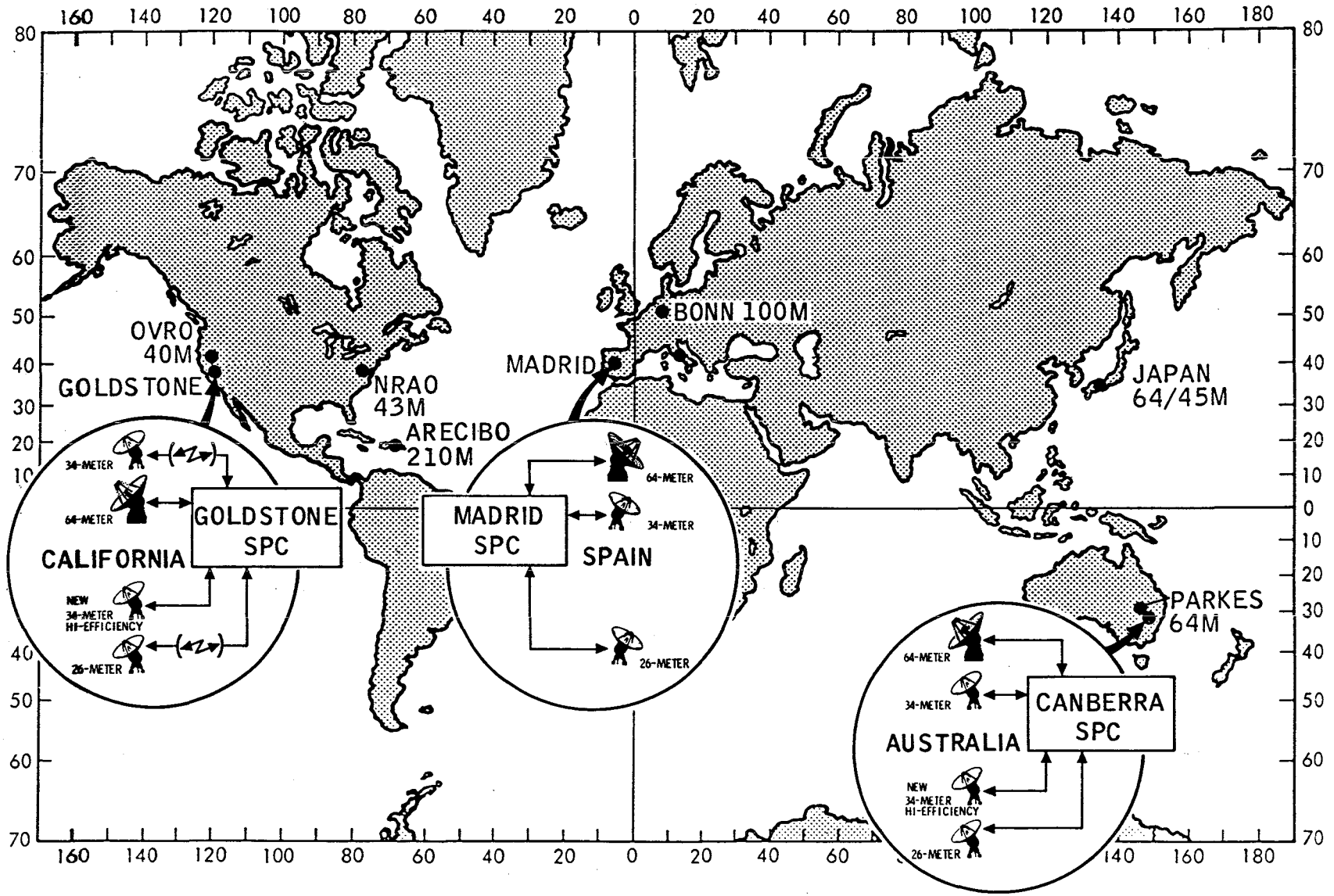


Fig. 2. 1986 Network configuration + candidate facilities

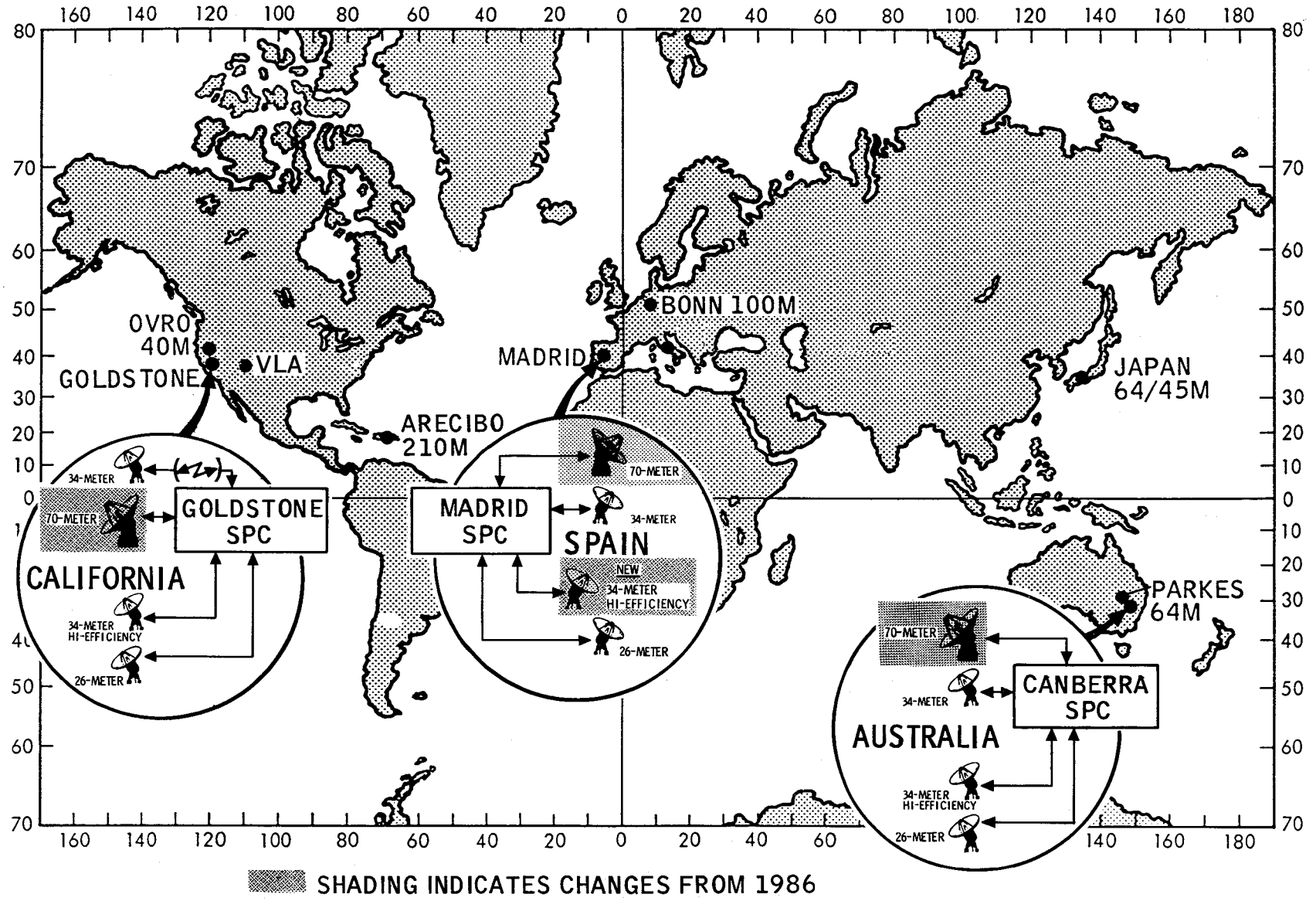


**Fig. 3. Baseline 1989 network configuration + candidate facilities**

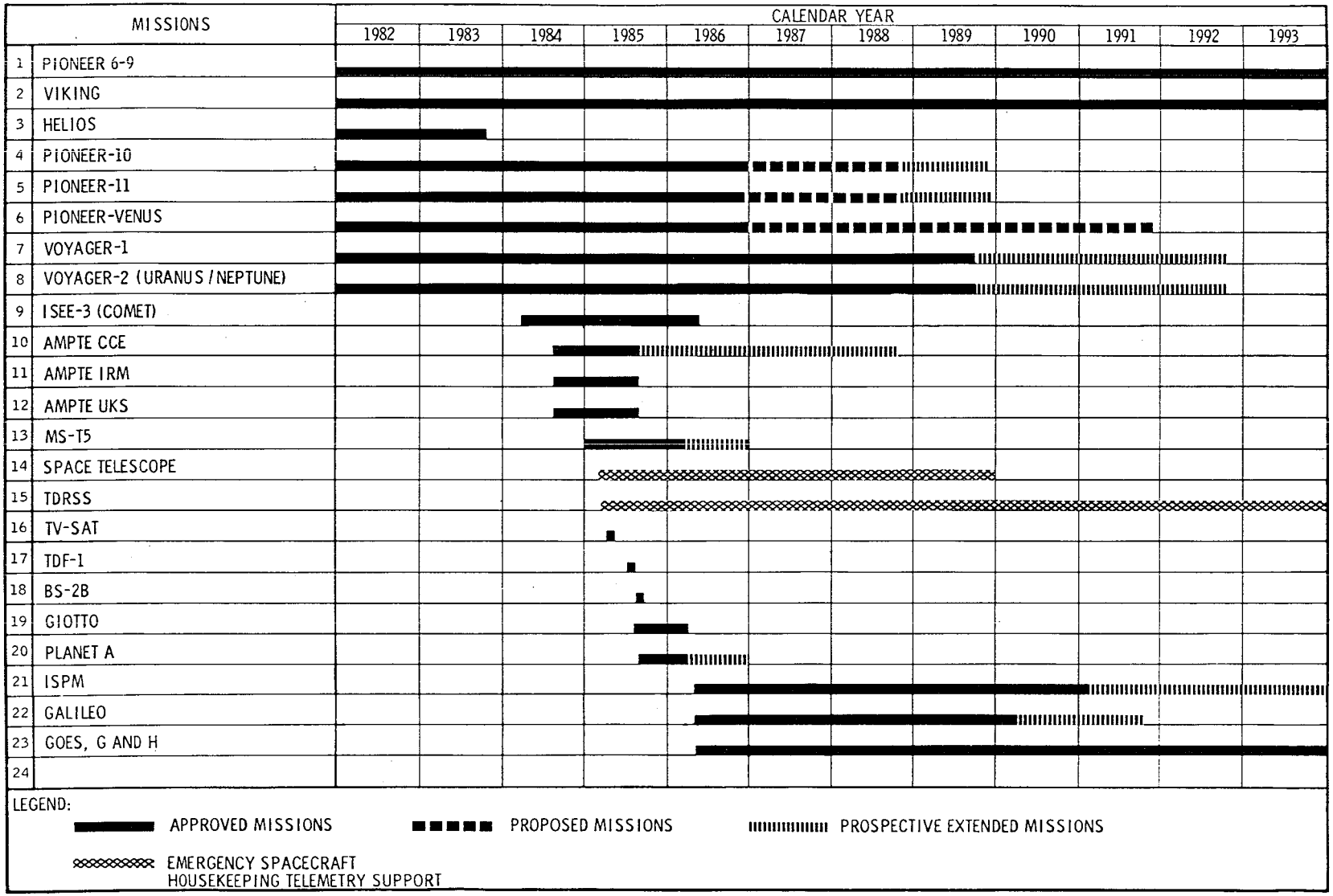


**Fig. 4. Flight project support: mission set**

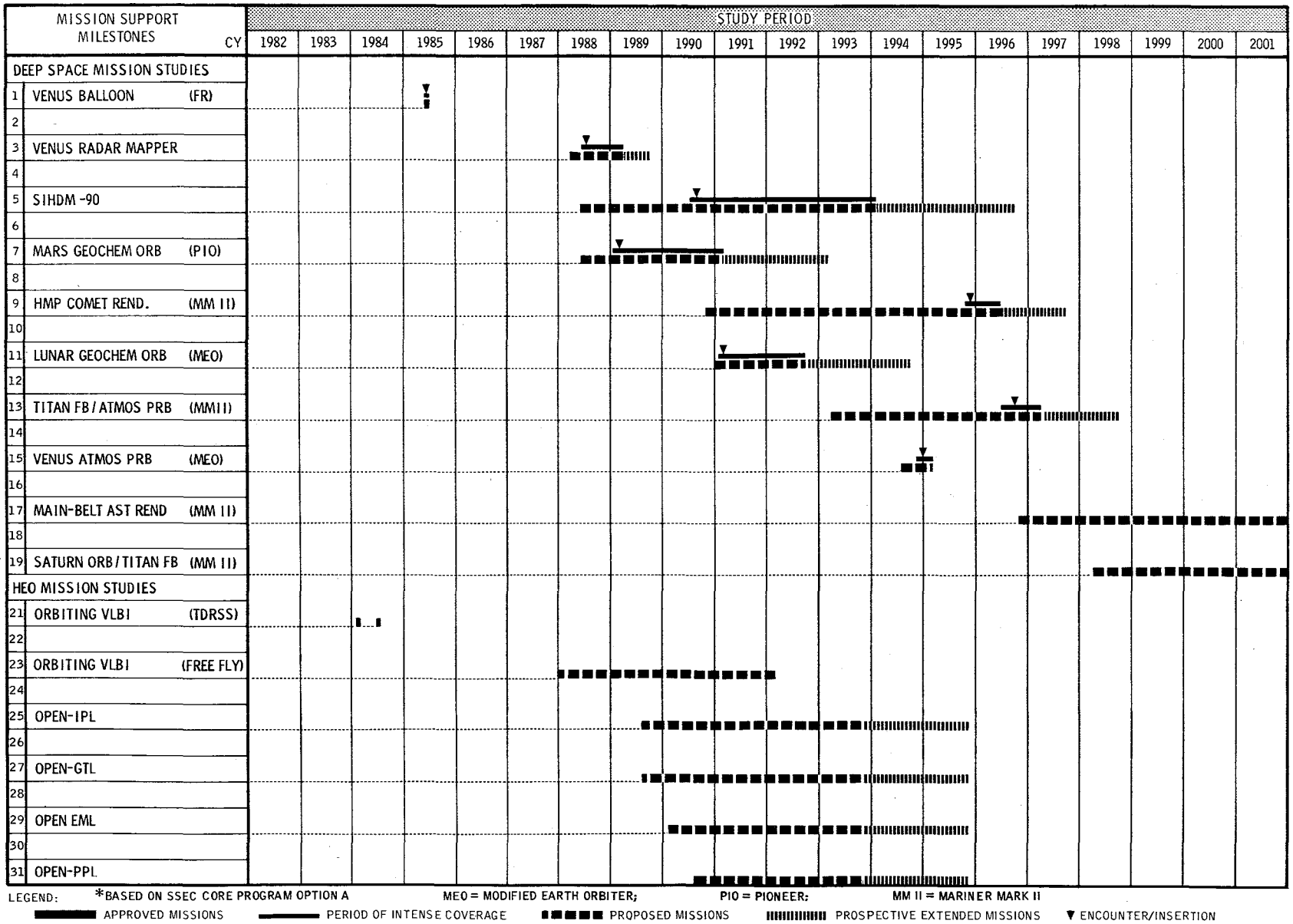


**Fig. 5. Advanced planning missions: mission set**

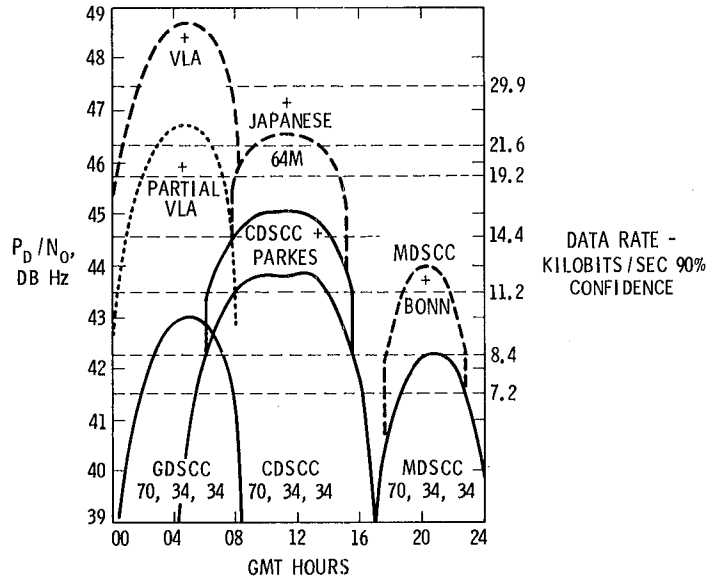


**Fig. 6. Enhanced link performance at Uranus**

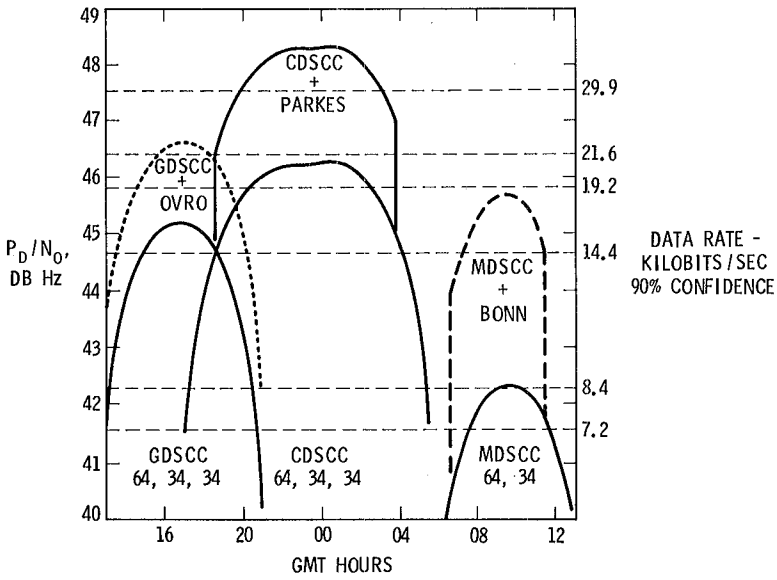


**Fig. 7. Enhanced link performance at Neptune**

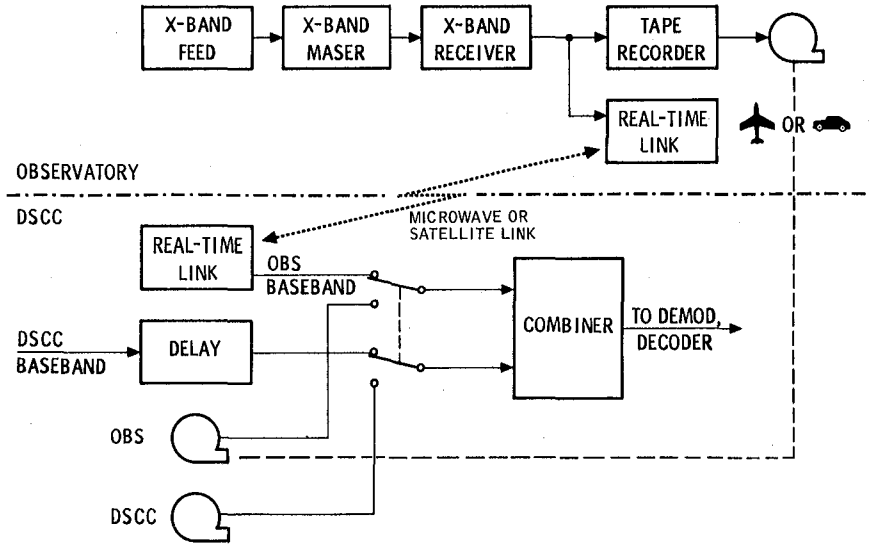


**Fig. 8. Interagency arraying capability, functional block diagram**

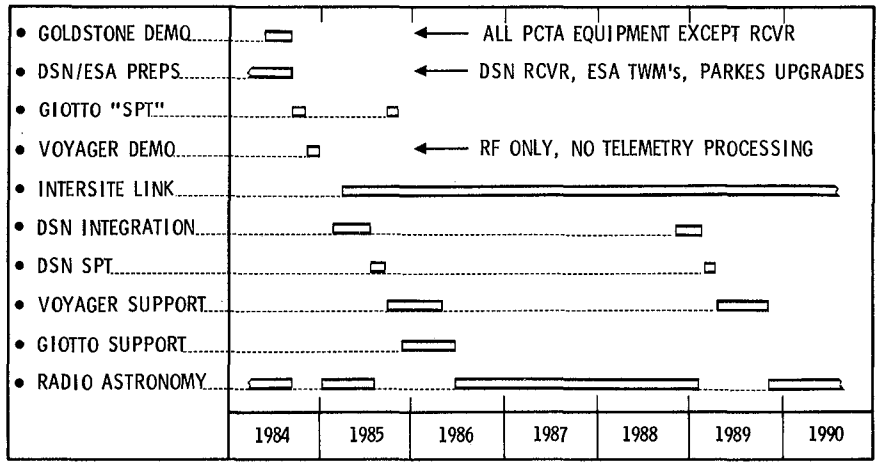


**Fig. 9. Parkes on-site activity**

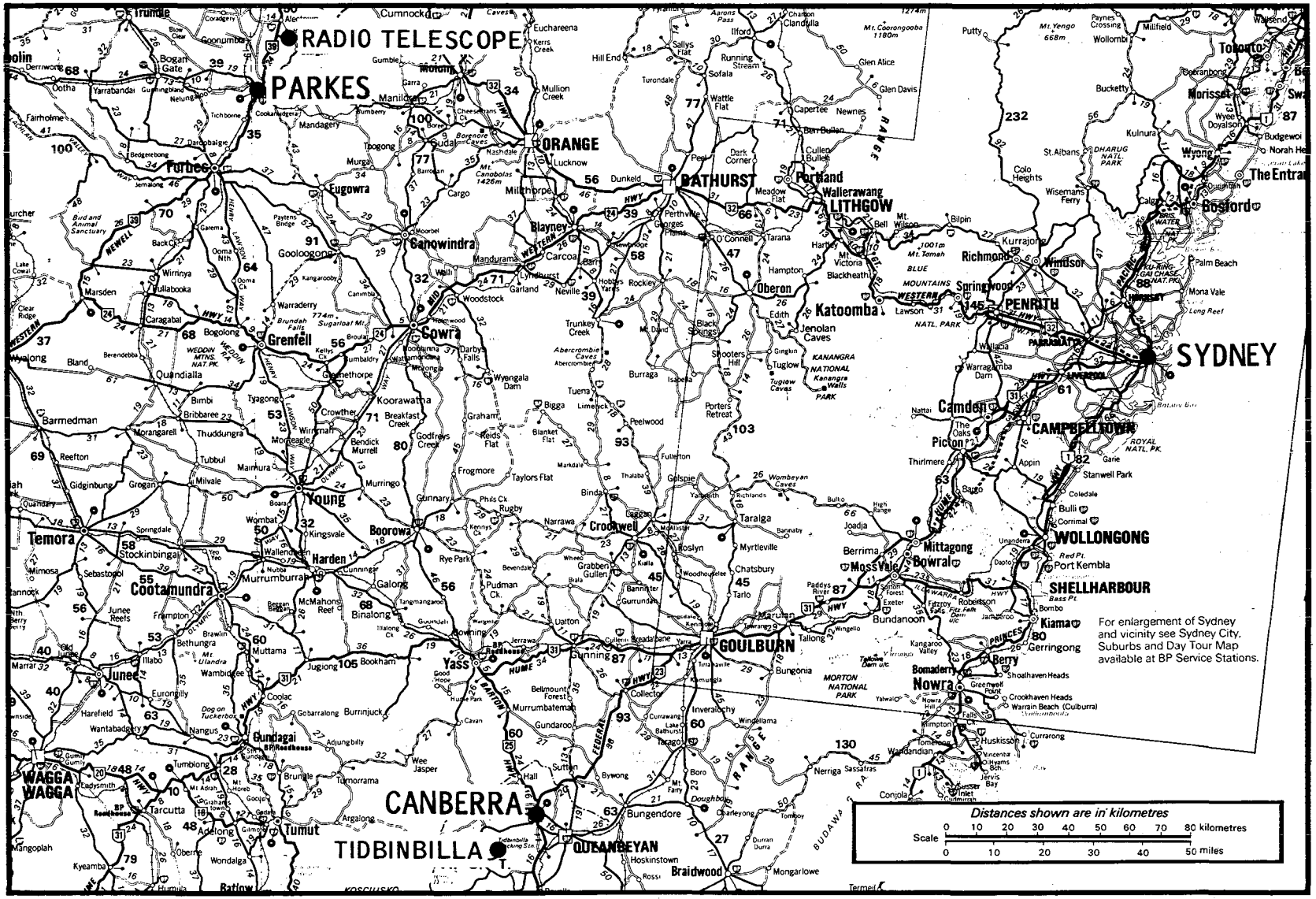

Fig. 10. Parkes-CDSCC telemetry array: site locations

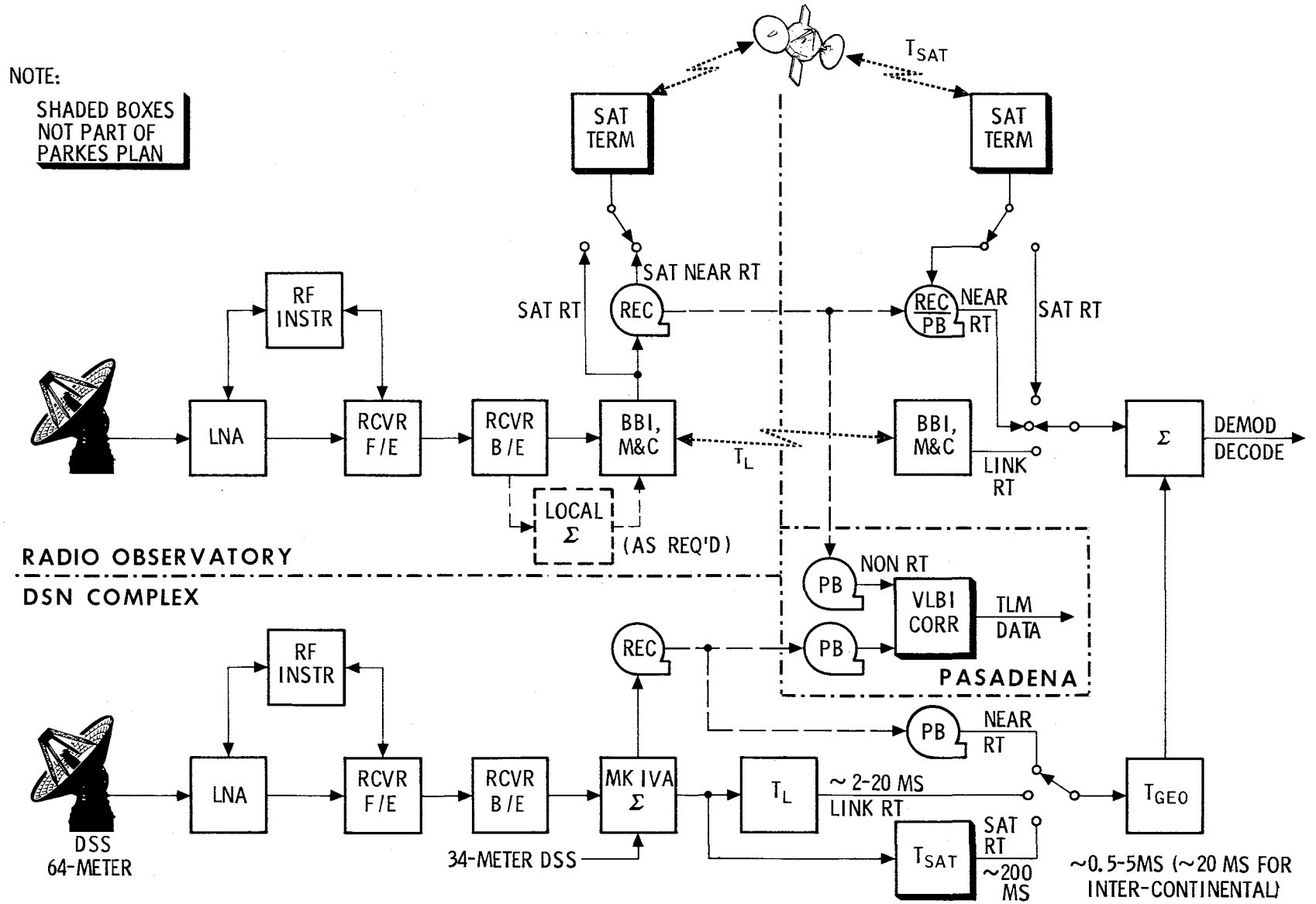


**Fig. 11. Functional elements of array**

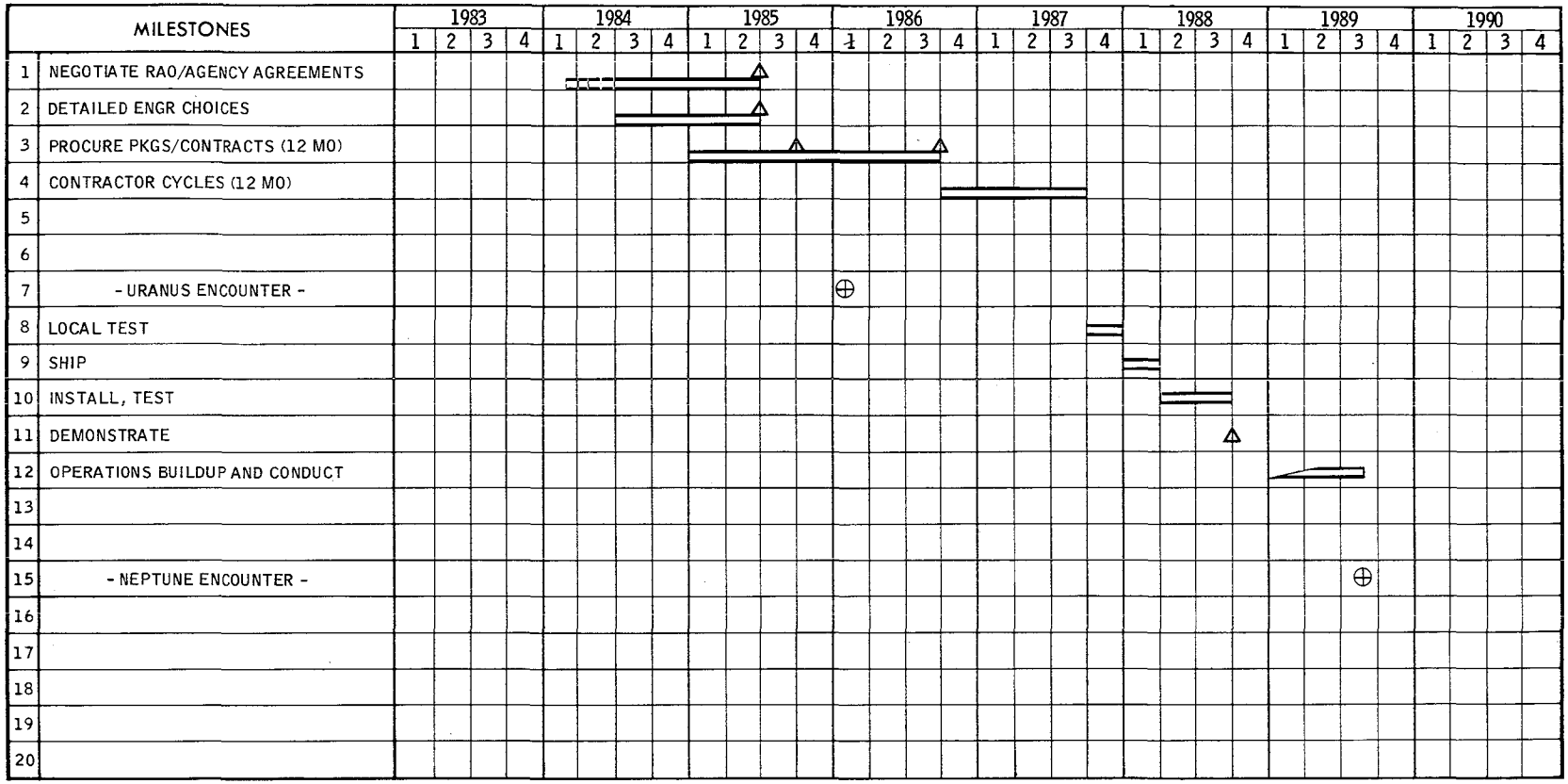


**Fig. 12. Bonn/Japan 64-meter general schedule, late CY 1988 demos**

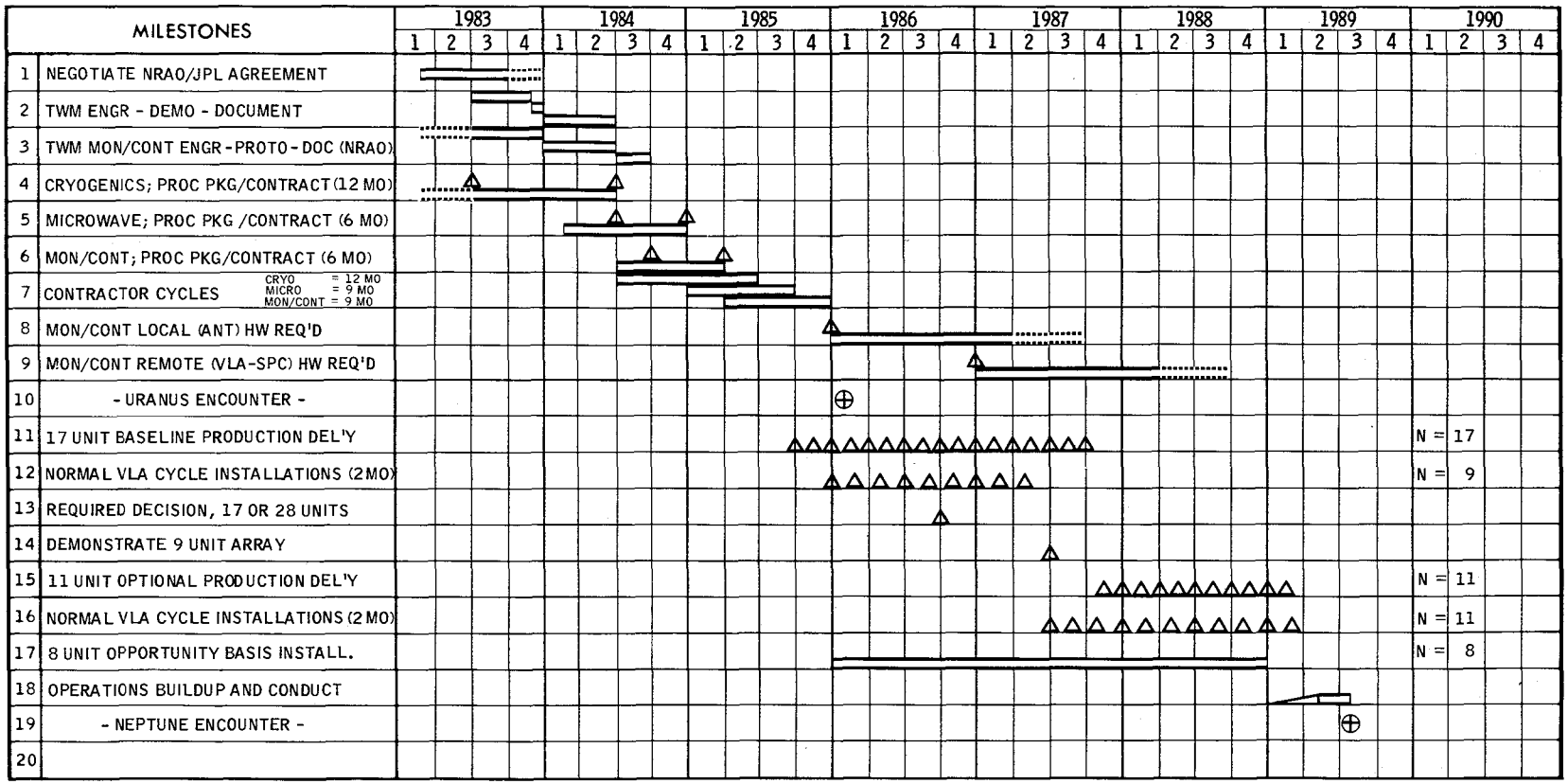


**Fig. 13. Full capability schedule, NRAO/JPL for VLA**

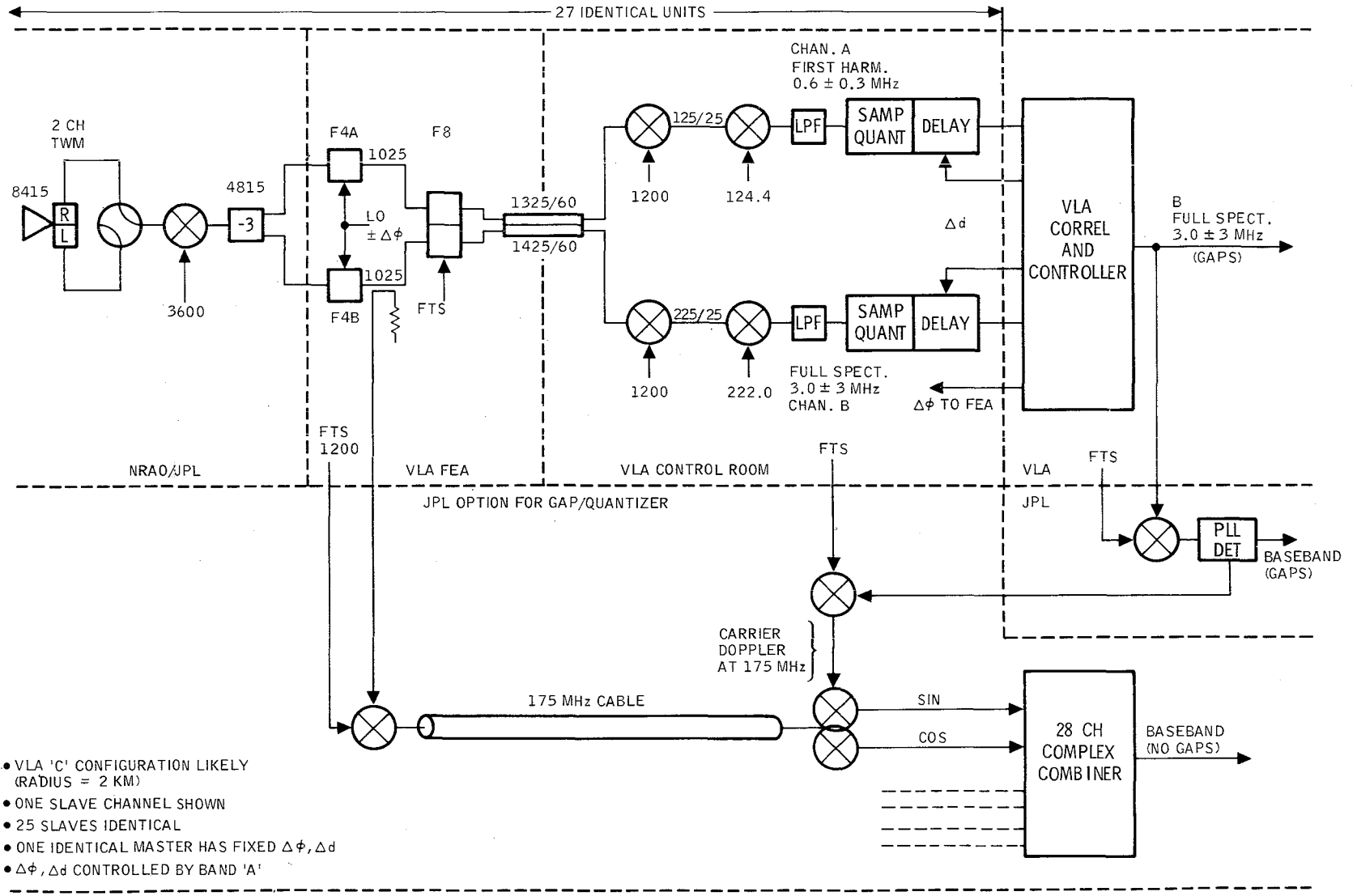


**Fig. 14. General VLA configuration for Voyager support**

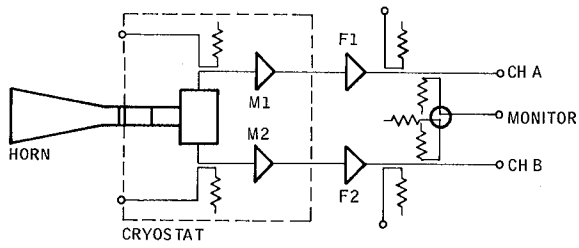


- INTEGRAL TO 3 WATT CRYOSTAT:
  - TWO TWM STRUCTURES, EACH 1/2 OF DSN TYPE (M1, M2)
  - CIRCULAR POLARIZER AND ORTHOMODE
  - INPUT CALIBRATION DIRECTIONAL COUPLERS
- EXTERNAL TO CRYOSTAT:
  - TWO F.E.T. AMPLIFIERS (F1, F2)
  - OUTPUT CALIBRATION DIRECTIONAL COUPLERS

**Fig. 15. Proposed Block III X-band dual-channel TWM NRAO/JPL**

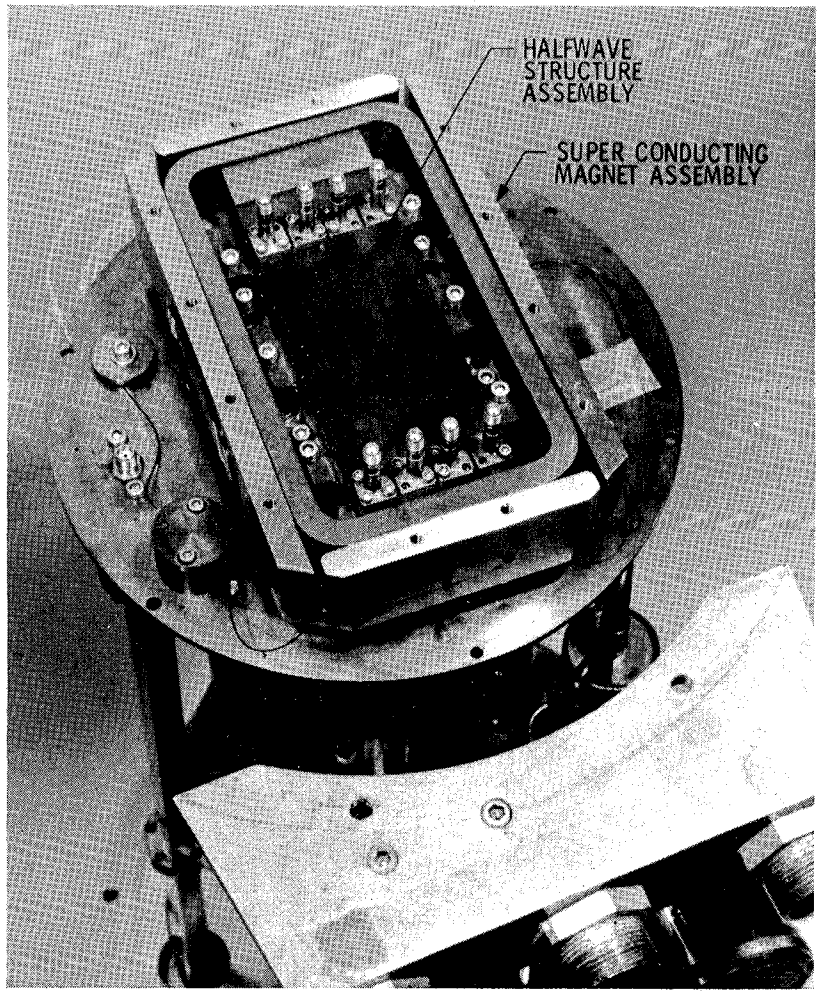


**Fig. 16. X-band half-wave structure assembly mounted in superconducting magnet**

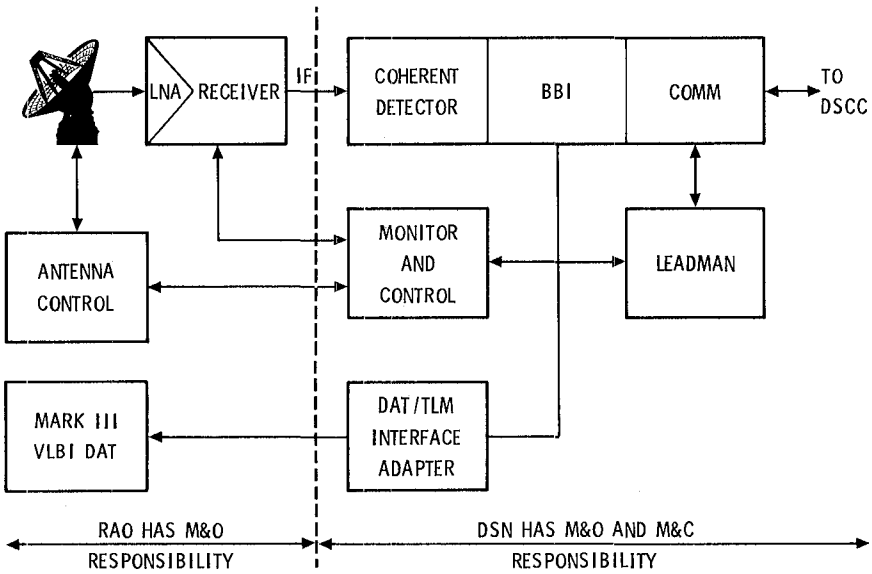


**Fig. 17. Operations scenario: RAO basic functional block diagram**

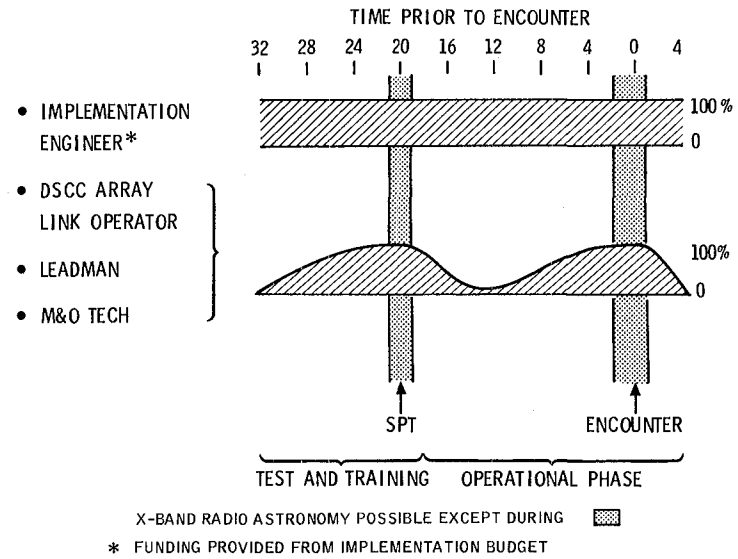


**Fig. 18. Operations scenario: conceptual personnel deployment plan**

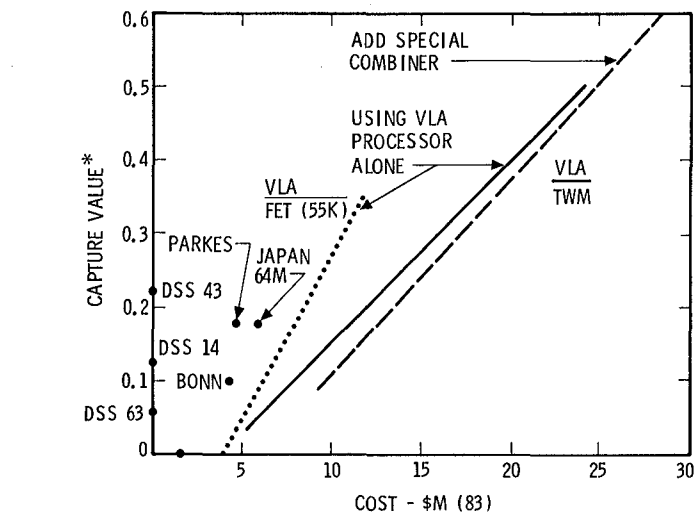


*CAPTURE VALUE = (APERTURE-UNITS) • (PASS-TIME DAYS) • $\left(\frac{25\ \text{KELVIN}}{\text{SYSTEM TEMP AT EL (90°)}}\right)$

**Fig. 19. Voyager signal capture vs cost**

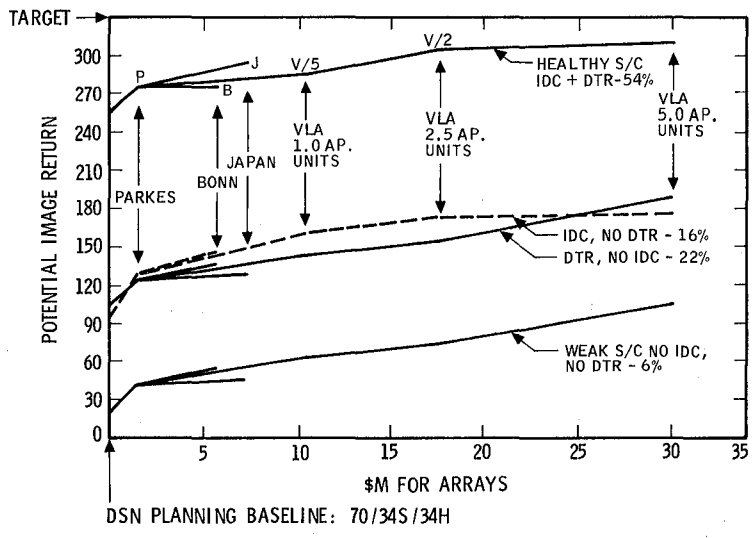


**Fig. 20. Neptune imaging potential vs cost by spacecraft state at encounter**

# SETI Pulse Detection Algorithm: Analysis of False-Alarm Rates

B. K. Levitt
Communications Systems Research Section

*This report extends some earlier work by the Search for Extraterrestrial Intelligence (SETI) Science Working Group (SWG) on the derivation of spectrum analyzer thresholds for a pulse detection algorithm based on an analysis of false-alarm rates. The algorithm previously analyzed was intended to detect a finite sequence of i periodically spaced pulses that did not necessarily occupy the entire observation interval. This algorithm would recognize the presence of such a signal only if all i-received pulse powers exceeded a threshold T(i): these thresholds were selected to achieve a desired false-alarm rate, independent of i. To simplify the analysis, it was assumed that the pulses were synchronous with the spectrum sample times.*

*This analysis extends the earlier effort to include infinite and/or asynchronous pulse trains. Furthermore, to decrease the possibility of missing an ETI signal, the algorithm has been modified to detect a pulse train even if some of the received pulse powers fall below the threshold. The analysis employs geometrical arguments that make it conceptually easy to incorporate boundary conditions imposed on the derivation of the false-alarm rates. While the exact results can be somewhat complex, simple closed form approximations are derived that produce a negligible loss of accuracy.*

## I. Introduction

Just as a flashing light commands more attention than constant illumination for the same average power, a sequence of pulses is a more likely extraterrestrial intelligence (ETI) beacon than a continuous wave (CW) signal. Oliver has shown that there is a signal-to-noise-ratio (SNR) advantage in detecting pulse trains over CW signals (Ref. 1, p. 39). Furthermore, pulsed signals are less likely to be confused with natural phenomena. So the pulse detection algorithm is an important element of SETI.

In both the sky and target survey modes of operation, the received signals will be processed by a multichannel spectrum analyzer (MCSA), which generates a temporal sequence of observed powers in a large number of contiguous frequency bins. For real-time operation, it would be impractical to apply an ETI detection algorithm directly to this frequency-time matrix of analog powers. So each power is compared with a set of thresholds to create a reduced observation space of soft-quantized powers: the algorithms then search this simplified space for signals of interest.

Suppose we are interested in detecting a sequence of narrowband periodic pulses. For simplicity, assume we do not have to compensate for frequency drifts, so that if one of the pulses is observed in a particular frequency bin, subsequent pulses will be observed in the same bin: the analysis that follows will isolate the operation of a pulse detection algorithm on a single representative frequency cell corresponding to a particular MCSA resolution.

The detection problem is complicated by the largely unknown nature of the signal of interest. The only certainty under our hypothesis is that the signal is periodic. We do not have a priori knowledge of the received power, center frequency, bandwidth, pulse duration, period, or time of occurrence of the first observed pulse, nor do we have statistical distributions for these parameters. We also do not know the likelihood of observing an ETI pulse train, although the presumption is that such an event is extremely rare. Because of this last consideration, we tend to select an algorithm that ensures tolerable false-alarm rates, without regard for the probability of missing an ETI event: this paper adheres to that premise.

The analysis that follows will focus on the false-alarm rate for a particular pulse detection algorithm that searches for patterns of $i$ periodically spaced hits in a threshold detected record of finite duration for a given frequency bin, where $i$ is an unknown variable. We will assume that the duration of each pulse is no larger than the inverse resolution bandwidth, which is the time required to generate each spectral measurement: so each pulse affects at most two adjacent temporal observations if it starts in the first and ends in the second, and if the pulse duration is small enough, most of the power will impact a single time cell. In analyzing false-alarm rates, the desired signal is absent: it is only the internal system noise that can cause a particular measurement to exceed the operating threshold. If the detection algorithm demands that all $i$ hypothetically observed pulses cause the corresponding temporal measurements to exceed a selected threshold $T(i)$, the likelihood of this occurring due to noise alone decreases with $i$. Conversely, if we want to maintain a desired false-alarm rate independent of $i$, we must employ a sequence of thresholds $\{T(i)\}$, where $T(i)$ decreases with $i$. This last approach was adopted by Cullers based on a preliminary false-alarm analysis for "regular" (periodic) pulses (Ref. 1, pp. 12-19).

This paper extends that earlier work, and the initial thinking that went into it provided a welcome opportunity for Cullers and me to collaborate in the evolution of the SETI pulse detection algorithm. In the course of this effort, we agreed on some useful terminology. In particular, a "finite" pulse train refers to a signal of limited duration that may begin and/or end within a given observation interval, whereas an "infinite" pulse sequence is assumed to extend indefinitely before and after that interval. For computational convenience it was useful to introduce the mathematical artifice of a "synchronous" pulse train wherein each received pulse coincides with a spectral time cell. Of course, the probability of this serendipitous occurrence is strictly zero, and realistically we should consider the situation in which the pulses are "asynchronous" with the measurement times. Cullers' ground breaking analysis was restricted to the finite/synchronous category, whereas this paper examines all four cases and ultimately favors the more credible infinite/asynchronous assumption.

Finally, Cullers and I both recognized the need to modify the pulse detection algorithm to allow it to indicate the reception of a sequence of $i$ pulses even if some of those pulses do not exceed the power threshold $T(i)$. This has the effect of lowering the probability of missing a potential ETI signal at the expense of a higher false-alarm rate. We agreed that for a given $i$, the number of pulses allowed to fall below $T(i)$ would be kept small enough to permit the period of the detected pulse train to be uniquely determined.

## II. The Algorithm

As mentioned earlier, the SETI equipment uses a spectrum analyzer to generate a frequency-time matrix of received powers. The pulse detection algorithm investigates the hypothesis that embedded in that data record is a sequence of $i$ periodically spaced pulses, where $i$ is an unknown parameter that in general can be any integer between 1 and the number of time cells $N$. Because of the desire to process a given data record in real time, the two-dimensional array of received powers is soft quantized by tagging each frequency-time cell according to the largest power threshold exceeded in the preselected set $\{T(i)\}$.

To simplify the analysis, we will assume that a received pulse train does not drift in frequency during the observation interval, and focus on the operation of the detection algorithm on a single frequency channel. Furthermore, although the algorithm simultaneously searches for pulse trains with many values of $i \geqslant 1$, we will consider a particular value of $i$ and compute the corresponding $T(i)$ that produces a desired false-alarm rate.

So the observation space of interest is a sequence of $N$ spectral power measurements that have been hard quantized by a threshold $T(i)$. As stated earlier, we assume that the power in each pulse is largely contained within a single time cell (this is not meant to imply the synchronous restriction). Even within these constraints, there are still two important degrees of freedom to resolve—the phase and period of the received pulse train. The phase is defined by the integer $k \in [1, N]$, which

denotes the time cell containing the first pulse within the observation window. In the synchronous case, the period is the integer spacing $m \geq 1$ between cells containing consecutive pulses. However, in the asynchronous case, the period $m$ is noninteger, so the second degree of freedom is defined by the integer spacing $\ell \cong (i-1)\,m$ between the cells containing the first and last received pulses. Depending on whether the pulse train is assumed to be finite or infinite, these degrees of freedom will have some constraints or boundary conditions. For the four cases of interest (e.g. infinite/synchronous), the domain of allowable degrees of freedom defines $g(i)$ *distinct* subsets of $i$ cells within the $N$ cell data record where the received pulses could be located. The boundary conditions and the parameters $g(i)$ are derived in the next two sections.

Consider a *particular* group of $i$ cells that is a member of the subset of $g(i)$ potential pulse train locations. A very restrictive pulse detection algorithm might insist that the power levels in *all* $i$ cells exceed $T(i)$, while the remaining $(N-i)$ cells fail the threshold test. While such an algorithm would have a low false-alarm rate, it would be at the expense of a higher probability of missing a received pulse train. A more reasonable criterion is to declare that a sequence of $i$ periodically spaced pulses has been detected whenever *any* $(i-J)$ of them or more satisfy the threshold test, and allow up to a small number $K$ of the other $(N-i)$ cells to exceed the power threshold erroneously due to thermal noise. Of course, $J$ and $K$ would be kept small enough to ensure unambiguous determinations of $i$ and $m$, and to maintain a sufficiently low false-alarm rate.

To compute the false alarm probability $P_{FA}$, we assume that the $N$ spectral power measurements represent internal system noise only. The power in each cell is then a central chi-square random variable with two degrees of freedom. If the cell powers and the threshold $T(i)$ are normalized by dividing each by the mean cell power, the probability that a given cell erroneously satisfies the threshold test is

$$p = e^{-T(i)} \tag{1}$$

Then, for the modified pulse detection algorithm described above,

$$P_{FA} = g(i)\sum_{j=0}^{J}\binom{i}{j}p^{i-j}(1-p)^{j}\sum_{k=0}^{K}\binom{N-i}{k}p^{k}(1-p)^{N-i-k} \tag{2}$$

If $p \ll 1$, $P_{FA}$ will be dominated by the $j = J$, $k = 0$ terms, so that a good approximation that avoids having to select a particular $K$ is

$$\begin{aligned} P_{FA} &\cong g(i)\binom{i}{J}p^{i-J}(1-p)^{N-i+J} \\ &= g(i)\binom{i}{J}e^{-(i-J)\,T(i)}\left[1-e^{-T(i)}\right]^{N-i+J} \end{aligned} \tag{3}$$

In the next two sections, we will compute $g(i)$ according to whether the pulse train is assumed to be synchronous or asynchronous, and finite or infinite. In all four cases, the first degree of freedom represented by the integer location $k$ of the first received pulse is trivially constrained by

$$1 \leq k \leq N \tag{4}$$

In the special case $i = 1$, only a single pulse is observed and $m$ cannot be determined from the available data. Then there is only the single degree of freedom given by Eq. 4, and in all four cases,

$$g(1) = N \tag{5}$$

We shall now derive boundary conditions on the second degree of freedom, and compute $g(i)$ for $i \geq 2$.

## III. Synchronous Case

Here the second degree of freedom is the integer period $m$. Since the last of the $i$ pulses must lie within the $N$ observed cells, we must have $k + (i-1)\,m \leq N$, or

$$m \leq \frac{N-k}{i-1}; \quad i \geq 2 \tag{6}$$

for both the finite and infinite cases. The infinite assumption further demands that the number of cells prior to the first pulse and following the last one within the span of $N$ be strictly less than the period $m$: that is, $k, -N-k-(i-1)m+1 \leq m$, or equivalently

$$m \geq k, \frac{N-k+1}{i} \tag{7}$$

In the finite/synchronous case previously analyzed by Cullers, the domain of $(k, m)$ defined by Eqs. 4 and 6 is illustrated in Fig. 1. Every integer pair within this triangular domain corresponds to a distinct member of the $g(i)$ possible pulse train locations, so that

$$\begin{aligned} g(i) &= \sum_{m=1}^{\mu}\left[N-(i-1)m\right]; \quad \mu \equiv \left\lfloor \frac{N-1}{i-1} \right\rfloor \\ &= N\mu - \frac{1}{2}(i-1)\,\mu\,(\mu+1); \quad i \geq 2 \end{aligned} \tag{8}$$

where $\underline{x}$ denotes the integer part of $x$. As an approximation, if we ignore the requirement that $\mu$ be an integer and substitute $\mu \cong (N-1)/(i-1)$ into Eq. 8, we find that $g(i)$ reduces to the approximation

$$g(i) \cong \frac{(N-1)(N-i+2)}{2(i-1)}; \quad i \geq 2$$
$$\cong \frac{N^2}{2(i-1)}; \quad N \gg 1, i \tag{9}$$

These are the same results obtained by Cullers in Ref. 1.

Note that the series summation of Eq. 8 looks like a numerical integration of the area of the triangular domain of $(k, m)$ in Fig. 1. A loose approximation to $g(i)$ is simply the area of that triangle:

$$g(i) \cong \frac{(N-i)^2}{2(i-1)} \cong \frac{N^2}{2(i-1)}; \quad i \geq 2, N \gg i \tag{10}$$

In the infinite/synchronous case, the domain of $(k, m)$ must be modified to include the additional boundary conditions of Eq. 7, as illustrated in Fig. 2. Let $\overline{x}$ denote the smallest integer greater than or equal to $x$: then defining

$$\mu_1 \equiv \left\lceil \frac{N+1}{i+1} \right\rceil \quad \mu_2 \equiv \left\lfloor \frac{N}{i} \right\rfloor \quad \mu_3 \equiv \left\lfloor \frac{N-1}{i-1} \right\rfloor \tag{11}$$

allows us to write

$$g(i) = \sum_{m=\mu_1}^{\mu_2} [(i+1)m - N] + \sum_{m=\mu_2+1}^{\mu_3} [N - (i-1)m]$$
$$= N(\mu_1 - 2\mu_2 + \mu_3 - 1)$$
$$+ \frac{i}{2}(\mu_1 - \mu_1^2 + 2\mu_2 + 2\mu_2^2 - \mu_3 - \mu_3^2)$$
$$+ \frac{1}{2}(\mu_1 - \mu_1^2 + \mu_3 + \mu_3^2); \quad i \geq 2 \tag{12}$$

Ignoring the integer constraints in Eq. 11, and substituting the noninteger expressions for $\mu_1$, $\mu_2$, and $\mu_3$ into Eq. 12 yields the approximation

$$g(i) \cong \frac{N^2 + i^3 - i^2 - i}{i(i^2-1)}; \quad i \geq 2$$
$$\cong \frac{N^2}{i(i^2-1)}; \quad N \gg i \tag{13}$$

As a check, the area of the trapezoidal domain in Fig. 2 gives the approximation

$$g(i) \cong \frac{(N-i)^2}{i(i^2-1)} \cong \frac{N^2}{i(i^2-1)}; \quad i \geq 2, N \gg i \tag{14}$$

## IV. Asynchronous Case

Now the second degree of freedom is the integer spacing $\ell$ between the cells containing the first and last received pulses. The nominal or *observed* period is therefore

$$\hat{m} = \frac{\ell}{i-1} \cong m; \quad i \geq 2 \tag{15}$$

Assuming that the duration of each pulse is much smaller than the width of each time cell, the actual locations of these pulses can deviate from the centers of the cells containing them by up to half a cell width in either direction. Therefore, the true, noninteger period lies in the range

$$\frac{\ell - 1}{i-1} < m < \frac{\ell + 1}{i-1}$$
$$\Downarrow$$
$$|m - \hat{m}| < \frac{1}{i-1} \tag{16}$$

which becomes negligible for large $i$.

In both the finite and infinite cases, clearly $k + \ell \leq N$, or

$$\ell \leq N - k \tag{17}$$

Because of the uncertainty as to the true value of $m$, we shall use the *approximate* boundary modifications

$$k, \; N - k - \ell + 1 \lesssim \hat{m}$$

for the infinite case, which implies that

$$\ell \gtrsim (i-1)k, \left(\frac{i-1}{i}\right)(N-k+1); \quad i \geq 2 \tag{18}$$

The domains for both sets of boundary conditions are illustrated in Figs. 3 and 4. Unlike the synchronous cases, there is not a one-to-one correspondence between integer pairs $(k, \ell)$ in these domains and distinct subsets of $i$ cells containing the received pulses. Although the cell locations of the first and last pulses are fixed for a given $(k, \ell)$, because the pulse sequence is asynchronous with the time cells, each of the $(i-2)$ intermediate pulses can often occupy one of two adjacent cells. For example, if $i = 3$ and $\ell$ is an odd integer, $\hat{m}$ is a half-integer, and the middle pulse could lie in either the $[k + (\ell - 1)/2]^{\text{th}}$ cell or the $[k + (\ell + 1)/2]^{\text{th}}$ cell: under these conditions, a particular integer pair $(k, \ell)$ in the domain (with $\ell$ odd) corresponds to two distinct patterns of $i$ cells. On the other hand, if $i = 3$ and $\ell$ is even, each integer pair represents a single pattern of $i$ cells. If $\ell$ is equally likely to be even or odd, *on the average* each $(k, \ell)$ represents 3/2 distinct $i$-cell subsets of the $N$ observations. Denoting the number of integer pairs within an asynchronous domain by $f(i)$, we can represent the average number of $i$-cell pulse location patterns by

$$g(i) \equiv c(i) f(i) \tag{19}$$

where $c(2) = 1$ and we have argued above that $c(3) = 3/2$. A more rigorous derivation of $c(i)$ is given in the Appendix; we show that

| $i$ | $c(i)$ |
|---|---|
| 3 | 1.5 |
| 4 | 3 |
| 5 | 5.25 |
| 6 | 13 |
| 7 | 17.5 |

There remains the computation of $f(i)$. In the finite case of Fig. 3,

$$f(i) = \sum_{\ell=1}^{N-1} (N - \ell) = \frac{1}{2} N(N-1); \quad i \geq 2$$

$$\cong \frac{N^2}{2}; \quad N >> 1 \tag{20}$$

which is *independent of i.* In the infinite case, remembering that the lower boundaries in the domain of Fig. 4 are approximate,

$$f(i) \cong \sum_{\ell=\lambda_1}^{\lambda_2} \left[ \left( \frac{i+1}{i-1} \right) \ell - N \right] + \sum_{\ell=\lambda_2+1}^{N-1} (N - \ell)$$

$$= (\lambda_2 - \lambda_1 + 1) \left[ \frac{1}{2} \left( \frac{i+1}{i-1} \right) (\lambda_2 + \lambda_1) - N \right]$$

$$+ \frac{1}{2} (N - \lambda_2)(N - \lambda_2 - 1); \quad i \geq 2 \tag{21a}$$

where

$$\lambda_1 \equiv \left\lceil \left( \frac{i-1}{i+1} \right) (N+1) \right\rceil$$

$$\lambda_2 \equiv \left\lfloor \left( \frac{i-1}{i} \right) N \right\rfloor \tag{21b}$$

Ignoring the integer restrictions on $\lambda_1$ and $\lambda_2$, Eq. 21 simplifies to

$$f(i) \cong \frac{N^2 + i}{i(i+1)}; \quad i \geq 2$$

$$\cong \frac{N^2}{i(i+1)}; \quad N >> i \tag{22}$$

## V. Example

Suppose $N = 100$ and we want to determine a set of thresholds $\{T(i)\}$ such that $P_{FA} = 2 \times 10^{-12}$ independent of $i$. We will assume that the pulse detection algorithm is looking for infinite/asynchronous pulse trains, and we will allow $J = 1$ of the $i$ pulses to fail the threshold test for $i \geq 4$, keeping $J = 0$ for smaller $i$. From Eqs. 3, 5, 19, and 22, we have

$$P_{FA} = N e^{-T(1)} \left[ 1 - e^{-T(1)} \right]^{N-1}; \quad i = 1$$

$$P_{FA} = c(i) \left[ \frac{N^2 + i}{i(i+1)} \right] \binom{i}{J} e^{-(i-J)T(i)} \left[ 1 - e^{-T(i)} \right]^{N-i+J};$$

$$i \geq 2 \tag{23}$$

The resulting thresholds, normalized in terms of the mean cell power, are

| $i$ | $T(i)$ | |
|---|---|---|
| 1 | 31.5 | $J = 0$ |
| 2 | 17.2 | |
| 3 | 11.4 | |
| 4 | 11.9 | $J = 1$ |
| 5 | 9.0 | |
| 6 | 7.3 | |
| 7 | 6.1 | |

## VI. Postscript

This work was recently presented at the SETI SWG meeting at Ames Research Center. It became evident from the audience's questions that the actual operation of the pulse detection algorithm using a superposition of thresholds $\{T(i): 1, 2, \cdots\}$ was not clear. To alleviate this problem, the synchronous example illustrated in Fig. 5 was used. The example considers a single data record of $N = 25$ time cells for an arbitrary frequency bin. The algorithm first searches for a single pulse exceeding the power threshold $T(1)$, then for two cell powers exceeding $T(2)$, then for three periodically spaced pulses exceeding $T(3)$, and so on. This is a special case of the algorithm described earlier with $J = 0$.

In the particular example of Fig. 5, there are no cell powers that exceed $T(1)$, only one exceeds $T(2)$, and, although three do exceed $T(3)$, they are not periodically spaced; so the algorithm does not see a sequence of $i$ periodic pulses for $1 \leqslant i \leqslant 3$. However, six cell powers exceed $T(4)$, including the periodic sequence consisting of cells 4, 10, 16, and 22, so the algorithm flags that 4-cell subset.

## References


1. Cullers, D. K., Oliver, B. M., Day, J. R., and Olsen, E., "Signal Recognition," in Appendix III of *1983 Report of the SETI Science Working Group*, edited by F. Drake, J. H. Wolfe, and C. L. Seeger. NASA/Ames Research Center, Moffett Field, California, February 1983.

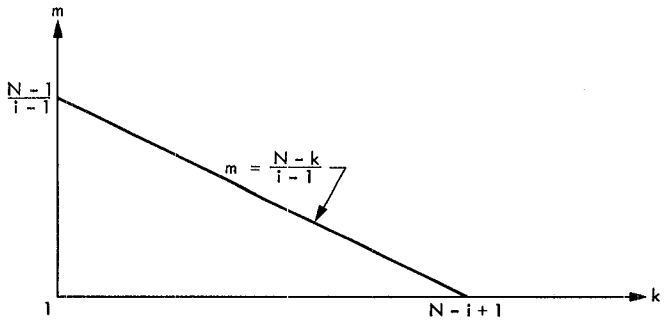


Fig. 1. Domain of $(k, m)$ for finite/synchronous case, where $i \geq 2$

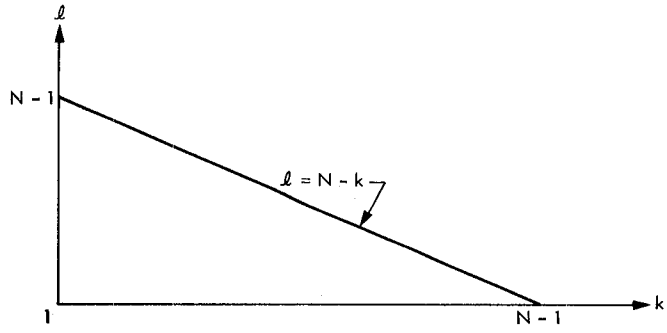


Fig. 3. Domain of $(k, \ell)$ for finite/asynchronous case, where $i \geq 2$

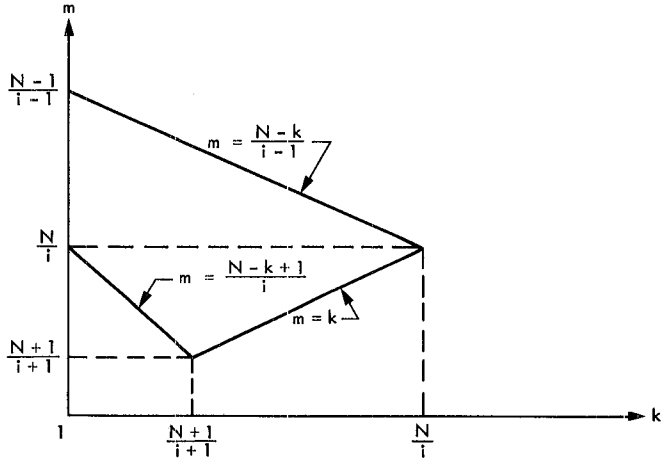


Fig. 2. Domain of $(k, m)$ for infinite/synchronous case, where $i \geq 2$

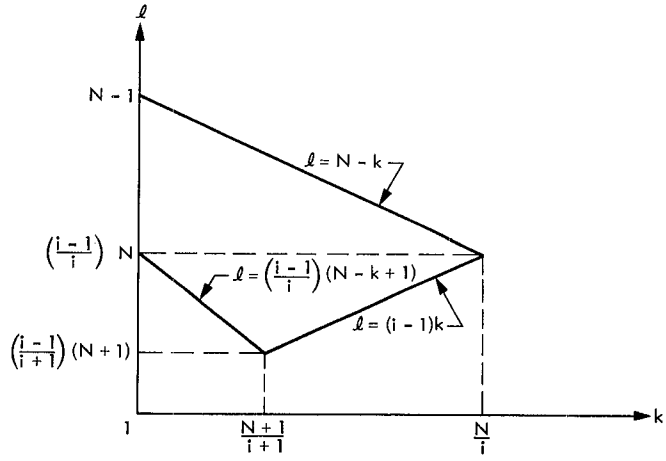


Fig. 4. Domain of $(k, \ell)$ for infinite/asynchronous case, where $i \geq 2$

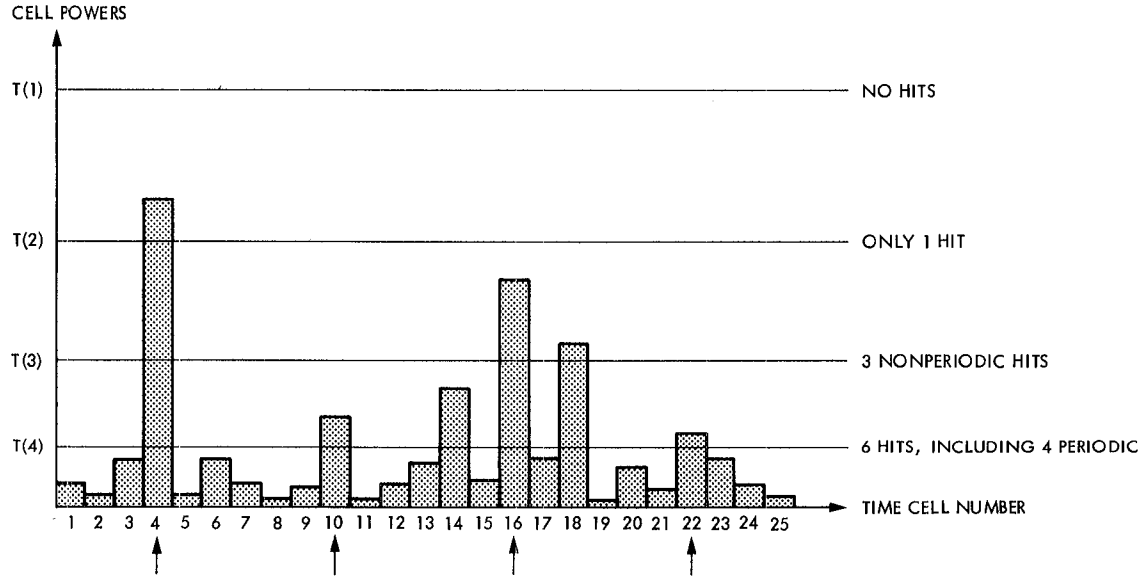


Fig. 5. Example of sequential investigation of hypothesis that a sequence of $i$ periodic pulses is present in data record of $N = 25$ time cells, $i = 1, 2, \ldots$. The $(J = 0)$ algorithm demands that $i$ periodically spaced cell powers exceed $T(i)$. The synchronous case is assumed

# Appendix

# Computation of c(i) for Asynchronous Pulse Trains

Consider a sequence of $i$ periodic pulses received within a data record of $N$ time cells. The duration of each pulse is assumed to be much smaller than a cell interval, so we can essentially regard it as occuring at a single point in time. Furthermore, all time measurements below are in time cell units, so that the normalized sample times are the integers $1, 2, \cdots, N$. In the asynchronous case, the pulse period $m$ and the times of occurrence of the pulses $x_1, x_2, \cdots, x_i$ are noninteger. The $j^{\text{th}}$ pulse is received in the $y_j^{th}$ cell, where

$$x_j = y_j + \Delta_j ; \quad |\Delta_j| < \frac{1}{2} \tag{A-1}$$

and $y_j$ is integer. In Section IV, we defined the observed period (Eq. 15)

$$\hat{m} \equiv \frac{\ell}{i-1} = \frac{y_i - y_1}{i-1} \tag{A-2}$$

whereas the actual period is

$$m = \frac{x_i - x_1}{i-1} = \hat{m} + \frac{\Delta_i - \Delta_1}{i-1} \tag{A-3}$$

which satisfies Eq. 16.

For particular first and last observed pulse locations, $y_1$ and $y_i$, which fix $\ell \equiv y_i - y_1$, we want to investigate the range of observed intermediate pulse locations $y_2, y_3, \cdots, y_{i-1}$, for $i \geq 3$. The actual noninteger location of the $j^{\text{th}}$ intermediate pulse $(2 \leq j \leq i-1)$ satisfies

$$\begin{aligned} x_j &= x_1 + (j-1)m \\ &= y_1 + \frac{i-j}{i-1}\Delta_1 + \left(\frac{j-1}{i-1}\right)(\ell + \Delta_1) \end{aligned} \tag{A-4}$$

If we denote

$$\ell_0 \equiv \left\lfloor \frac{\ell}{i-1} \right\rfloor$$

and $\ell_1 \equiv \ell \bmod (i-1)$, then $\ell = \ell_0 (i-1) + \ell_1$, where $\ell_0$ and $\ell_1$ are integers and $0 \leq \ell_1 \leq i-2$. In the analysis that follows, we will assume that $\ell_1$ is uniformly likely to assume any value within its range. We can express Eq. A-4 as

$$x_j = \underbrace{y_1 + \ell_0(j-1)}_{\text{integer}} + \underbrace{\left(\frac{i-j}{i-1}\right)\Delta_1 + \left(\frac{j-1}{i-1}\right)(\ell_1 + \Delta_i)}_{\text{noninteger, } z_j} \tag{A-5}$$

Since $y_j$ is the integer closest to $x_j$, the range of $z_j$ determines the number of possible $y_j$'s. Let $\vec{y} \equiv (y_1, y_2, \cdots, y_i)$ and $D$ denote the number of distinct $\vec{y}$'s consistent with the given values of $i, y_1, y_i$. Then $D$ equals the number of possible $y_2$'s times the number of possible $y_3$'s times $\cdots$ times the number of possible $y_{i-1}$'s, and

$$c(i) = E[D] \tag{A-6}$$

where the expectation is over the discrete uniform random variable $\ell_1$. Since $|\Delta_1|$, $|\Delta_i| < 1/2$, and $\Delta_1$ and $\Delta_i$ are independent parameters,

$$\left|\left(\frac{i-j}{i-1}\right)\Delta_1 + \left(\frac{j-1}{i-1}\right)\Delta_i\right| < \frac{1}{2}$$

$$\Downarrow$$

$$\left| z_j - \left(\frac{j-1}{i-i}\right)\ell_1 \right| < \frac{1}{2} \tag{A-7}$$

If

$$\left(\frac{i-1}{i-1}\right)\ell_1$$

is an integer, which is always true when $\ell_1 = 0$, then there is only one possible value of $y_j$:

$$\begin{aligned} y_j &= y_1 + \ell_0 (j-1) + \left(\frac{j-1}{i-1}\right)\ell_1 \\ &= y_1 + \left(\frac{j-1}{i-1}\right)\ell \end{aligned} \tag{A-8}$$

However, if

$$\left(\frac{j-1}{i-1}\right) \ell_1$$

is noninteger, then $y_j$ can have one of two possible values:

$$\begin{aligned} y_j &= y_1 + \ell_0 (j-1) + \left\lfloor \left(\frac{j-1}{i-1}\right) \ell_1 \right\rfloor \\ y_j &= y_1 + \ell_0 (j-1) + \left\lfloor \left(\frac{j-1}{i-1}\right) \ell_1 \right\rfloor + 1 \end{aligned} \qquad \text{(A-9)}$$

So, for a given $i$ and $\ell_1$, $D$ is simply 2 raised to the number of noninteger members of the set

$$\left\{ \left(\frac{j-1}{i-1}\right) \ell_1 \; ; 2 \leqslant j \leqslant i-1 \right\};$$

in particular

$$1 \leqslant D \leqslant 2^{i-2} \qquad \text{(A-10)}$$

Table A-1 illustrates the calculation of $c(i)$ for $i \geqslant 3$.

**Table A-I. Calculation of parameter c(*i*)**

| $i$ | $\varrho_1$ | $j$ | $\left(\frac{j-1}{i-1}\right)\varrho_1$ | $D$ | $c(i)$ |
|---|---|---|---|---|---|
| 3 | 0 | 2 | 0 | 1 | 1.5 |
| | 1 | 2 | noninteger | 2 | |
| 4 | 0 | 2 | 0 | 1 | 3 |
| | | 3 | 0 | | |
| | 1 | 2 | noninteger | 4 | |
| | | 3 | noninteger | | |
| | 2 | 2 | noninteger | 4 | |
| | | 3 | noninteger | | |
| 5 | 0 | 2 | 0 | 1 | 5.25 |
| | | 3 | 0 | | |
| | | 4 | 0 | | |
| | 1 | 2 | noninteger | 8 | |
| | | 3 | noninteger | | |
| | | 4 | noninteger | | |
| | 2 | 2 | noninteger | 4 | |
| | | 3 | 1 | | |
| | | 4 | noninteger | | |
| | 3 | 2 | noninteger | 8 | |
| | | 3 | noninteger | | |
| | | 4 | noninteger | | |

# Gain Stability Measurements at S-Band and X-Band

S. Gulkis and E. T. Olsen
Atmospheric Sciences Section

*The Search for Extraterrestrial Intelligence (SETI) requires low noise broadband total power radiometers of high gain stability. We report here preliminary results of SETI field tests for a variety of receiver configurations at DSS 13. The power spectra of DSN low noise receiving systems exhibit 1/F noise whose spectral index is significantly smaller than unity. The gain stability of the S-band and X-band systems tested is almost $10^{-4}$. An appendix presents a derivation of the power spectrum of the output of a square law detector.*

## I. Introduction

Many physical phenomena exhibit low frequency fluctuations whose power spectral density varies inversely with frequency. These fluctuations are commonly referred to as "1/F noise". In general, the power spectrum of this noise follows the form, $F^n$, where $F$ is the frequency of the fluctuations and $n$ is the spectral index. The spectral index varies from system to system, but is always near unity. This phenomenon has been observed in the current output from junction diodes, zener diodes, and schottky diodes, in the frequency of quartz oscillators, and in the voltage gain of amplifiers.

In a total power radio astronomy receiving system, the detected power exhibits 1/F noise in combination with thermal ("white") noise which has a spectral index of zero. The frequency dependent noise is generally attributed to gain variations in the amplifiers arising from a number of physical sources, such as variations in the power supplies, temperature, pump power levels, and mechanical vibrations. The contribution of the atmosphere to the fluctuations in system temperature is also important at X-band and higher frequencies. Under certain circumstances, the 1/F noise in these systems will dominate the thermal noise, and the system sensitivity can be severely degraded from what is predicted based on the system temperature.

The rms temperature fluctuations of the output of a total power receiver is given approximately by the expression (Ref. 1):

$$\Delta T = T\left[(B\tau)^{-1} + (\Delta G/G)^2\right]^{1/2} \quad (1)$$

where $T$ is the system temperature, $G$ is the average predetection power gain, $\Delta G$ is an effective value of the power gain variation, $B$ is the predetection bandwidth and $\tau$ is the integration time. The first term of the expression in the square brackets is due to the thermal noise (Johnson noise). The second term is due to the gain fluctuations. It is clearly seen from equation (1) that the gain fluctuations assume greater significance as $B\tau$ is increased. A more complete discussion of Equation (1) is given in Appendix A.

The frequency at which the 1/F noise becomes equal to the white noise is sometimes referred to as the "knee fre-

quency". This "knee frequency" is a function of the predetection bandwidth, and hence needs to be specified in order to provide a complete description. At frequencies lower than the knee frequency, the 1/F noise dominates the system fluctuations; at frequencies higher than the knee frequency, the thermal noise dominates. It is important to know where the transition occurs in order to be able to estimate the sensitivity of a receiving system.

The SETI program intends to utilize the NASA Deep Space Network receiving systems over a wide range of bandwidths, integration times, and microwave frequencies. As a first step toward understanding the nature of the noise in DSN receiving systems, we measured the power spectra of S-band and X-band receiving systems situated at DSS 13, the 26m R&D (Venus) station located at Goldstone, California. From these measurements, we were able to obtain both the spectral index of the 1/F noise and the knee frequency. The results of these measurements are reported here.

## II. Experiment Configuration

We tested the three different system configurations shown in Fig. 1. Configuration A is known as the S-band VLBI receiver configuration. The instantaneous bandpass of this receiver was measured to be 14 MHz between the 3 dB points. Configuration B is the S-band R&D receiver in combination with the microwave link from DSS 13 to DSS 14. The instantaneous bandpass of this receiver configuration was set by the 5 MHz bandpass of the microwave link. Configuration C is the X-band VLBI receiver. The instantaneous bandpass of this receiver was measured to be 25 MHz between the 3 dB points. The system noise temperatures of these systems are approximately 30 K at S-band and 33 K at X-band.

Figure 2 shows a block diagram of the instrumentation used to measure the gain stability. The receiver intermediate frequency (IF) is input to a broadband (1 MHz to 130 MHz) square law detector. The detector DC output is then converted to frequency in the analog to digital (A/D) converter by a fast VCO (Analog Devices 460L V/F converter). This frequency is then counted and sampled by an HP 9825A desk top computer at a 210 Hz rate. The accumulation times are selectable and the power spectra are computed as described in the following section.

## III. Experimental Procedure

The complete system was turned on and allowed time to stabilize; subsequently the system noise temperature was calculated by switching the receiver input from the sky to an ambient load of known temperatures. The A/D converter linearity and offset had already been measured prior to its arrival at Goldstone. With the IF from the receiving system connected, the power level output from the detector was adjusted so that the digital voltmeter which monitored the system displayed a reading of 0.5 volts. This value was chosen because it is in the middle of the dynamic range of the A/D converter. The output of the converter was then sampled and analyzed using the HP 9825A. The time constant for the sampling, the number of points in the fast fourier transform (FFT), and the number of integrations to be added together were specified in response to prompts from the HP 9825A. Following the completion of a data sampling run, the power spectrum is computed and the result displayed on the HP plotter. In order to obtain a wide range of frequencies in the power spectrum, we combined the results of several data runs with different integration times. The power spectral density was computed for each run and the results of several runs were combined in a single plot. The FFT algorithm utilized is based on one given for real functions by Brigham (Ref. 2). The input to the FFT is $2^N$ $(1 < N < 10)$ points, and the power spectrum output is:

$$P(n/T) = (a_n^2 + b_n^2)/2 \tag{2}$$

where $n = 1, 2, 3, \ldots, 2^{N-1}$ and the input time series may be written as a Fourier series:

$$D(t) = a_o/2 + \sum_n [a_n \cos(2\pi nt/T) + b_n \sin(2\pi nt/T)] \tag{3}$$

over the interval $0 < t < T$.

Each point in the power spectrum is normalized by the total power contained within the spectrum. Thus the output is a normalized power. An average power spectrum is produced by accumulating the power spectra from many individual runs.

## IV. Experimental Results

Figure 3 shows the power spectrum of the S-band VLBI receiver (configuration A). The frequency range spanned by the data is 0.1 Hz to 10 Hz. The data represented by open circles were acquired while the receiver system was looking out the horn; the data represented by filled circles were acquired while the receiver system was connected to an ambient temperature load. The power spectrum increases rapidly for temporal frequencies below 1 Hz, and we identify this rapid increase with the 1/F noise component. The spectral index of the 1/F noise component is $n = -0.83$, and the knee frequency is 1.3 Hz. Since the open and filled circles are

nearly coincident, we conclude that the measured 1/F noise spectrum is dominated by the receiving system itself and not by the atmosphere. We note that there is a slight increase in the noise power of the system when it is viewing the sky; this may be due to the atmosphere being less stable than the ambient load.

Figure 4 shows the power spectrum of the S-band VLBI receiver over a much wider range ($2 \times 10^{-4}$ Hz to 50 Hz) than is shown in Fig. 3. While the signal-to-noise ratio of this spectrum is poor due to the small number of individual power spectra which were combined, it nevertheless shows that the 1/F noise component extends to $2 \times 10^{-4}$ Hz with little change in slope.

Figures 5 and 6 show power spectra for the X-band VLBI receiver (configuration C). These figures correspond to Figs. 3 and 4 respectively. The 1/F noise component spectral index is $n = -0.78$, and the knee frequency is 1.5 Hz.

Thus there is no significant difference apparent in the gain stability of the two VLBI receiving systems at DSS 13. Both exhibit a spectral index of approximately −0.8 and a knee frequency of 1.4 Hz.

Figure 7 shows the power spectrum for the S-band R&D receiver (configuration B) as seen at the end of the microwave link at DSS 14. The 1/F noise component spectral index is $n = -0.8$ and the knee frequency is 1.2 Hz. Aside from the fact that the bandwidth of the link is 5 MHz (which should make the thermal noise component larger, shifting the knee frequency to a slightly lower frequency), we can see that no additional fluctuations were imposed by the link. The spectral index of this system is within the experimental uncertainty of the measurements of the values for configurations A and C.

## V. Conclusions

The gain of the S-band and X-band receiving systems is stable to approximately three parts in $10^4$. The spectral index of the 1/F noise for the three configurations tested is 0.8 ±0.03, significantly smaller than unity. This exceeds the requirements of the 1 kHz resolution leg of the SETI target survey for an accumulation time of 1000 seconds. It is very close to meeting the radio astronomy requirements of the SETI all sky survey. The high gain stability is required for a continuum survey which utilizes the full 256 MHz bandpass and may accumulate for as long as 3 seconds.

The authors suggest that a standardized procedure be implemented on a trial basis to determine if monitoring the gain stability might provide an early warning that a receiving system is beginning to deteriorate.

## VI. Future Work

The tests reported here were by no means exhaustive. Listed below are some of the areas where future studies would be useful.

(1) The knee frequency for a system is expected to vary with the bandwidth of the system. We did not explore this variation in our experiments. Some tests should be carried out using varying bandpasses.

(2) Some small broad features were apparent in power spectra accumulated overnight. Investigations with increased signal-to-noise should be made to determine if these features are indeed present and to understand them if they are.

(3) Increase the sampling rate beyond the 50 Hz limit imposed by our equipment. We just missed the expected 60 Hz feature, and it would be useful to trace this out, as well as to look for its higher harmonics.

(4) Extend the measurements to even lower frequencies to see if there is a break in the 1/F spectrum. This would mean that another component, with 1/F noise of a different slope, has become predominant.

(5) Repeat the tests for the R&D receiver and VLBI receiver with the detection setup on each side of the microwave link.

(6) Extend the tests to DSS 14 receivers, and in particular make measurements of the K-band system.

(7) Repeat the tests over different times to sort out diurnal effects and the effects of the atmosphere.

(8) Extend the work to include cooled and room temperature FET systems, as these systems are likely to show a spectral index different than those of the maser systems.

## Note

After this paper was written, the authors became aware of another treatment of this topic for the case of a 94-GHz receiver in a laboratory environment (see Ref. 4).

## References


1. Kraus, J. D., *Radio Astronomy*, McGraw-Hill, 1966, pp 247-248.
2. Brigham, E. O., *The Fast Fourier Transform*, Prentice-Hall, New Jersey, 1974.
3. Campbell, "Mathematical Analysis of Random Noise," in *Noise and Stochastic Processes*, N. Wax, ed., Dover Publications, 1954, p. 281.
4. Hersman, Michael S., and Poe, Gene A., "Sensitivity of the Total Power Radiometer with Periodic Absolute Calibration," in *IEEE Transactions on Microwave Theory and Techniques*, Vol MITT-29, pp. 32-40, Jan. 1981.

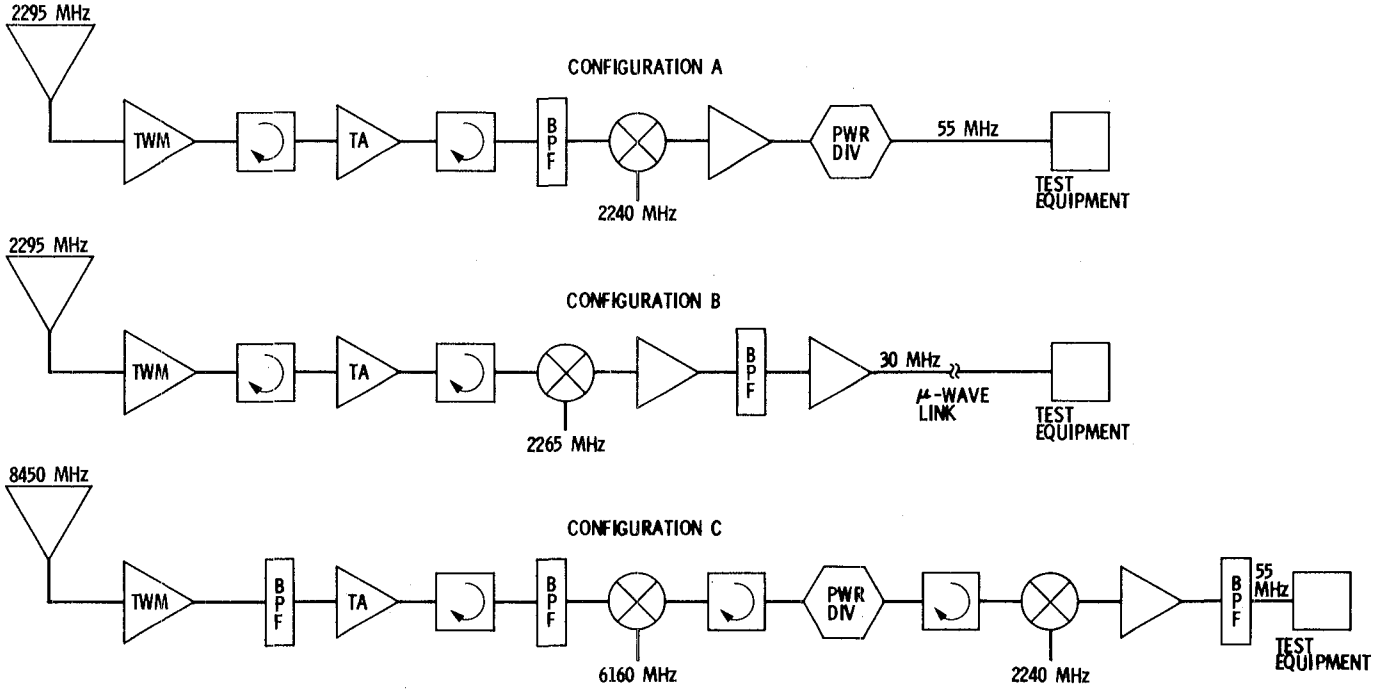


**Fig. 1. The three receiver configurations tested: Configuration A is the DSS 13 S-band VLBI receiver; Configuration B is the DSS 13 S-band R&D receiver in combination with the microwave link from DSS 13 to DSS 14; Configuration C is the DSS 13 X-band VLBI receiver**

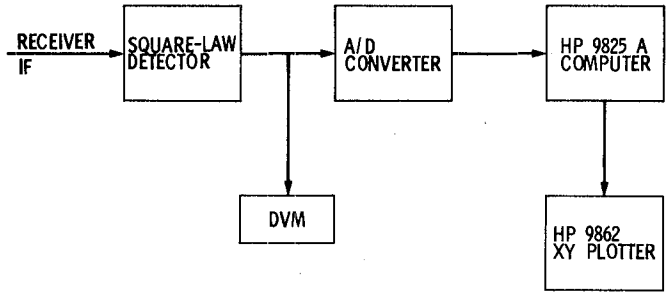


**Fig. 2. The block diagram of the instrumentation used to measure the gain stability**

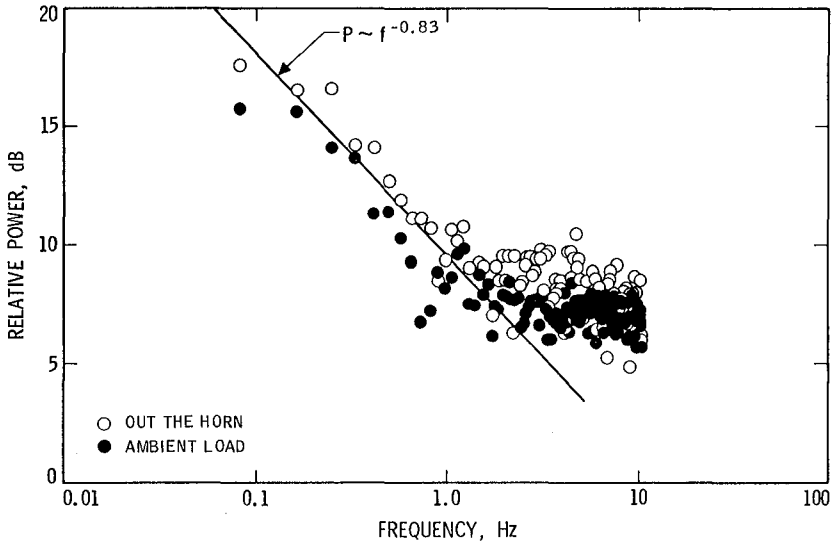


**Fig. 3. The power spectrum of the gain fluctuations of the S-band VLBI receiver (Configuration A) over the frequency range 0.1 to 10 Hz. Open circles represent data taken looking out the horn with the antenna pointed at the zenith. Filled circles represent data taken looking at an ambient load**

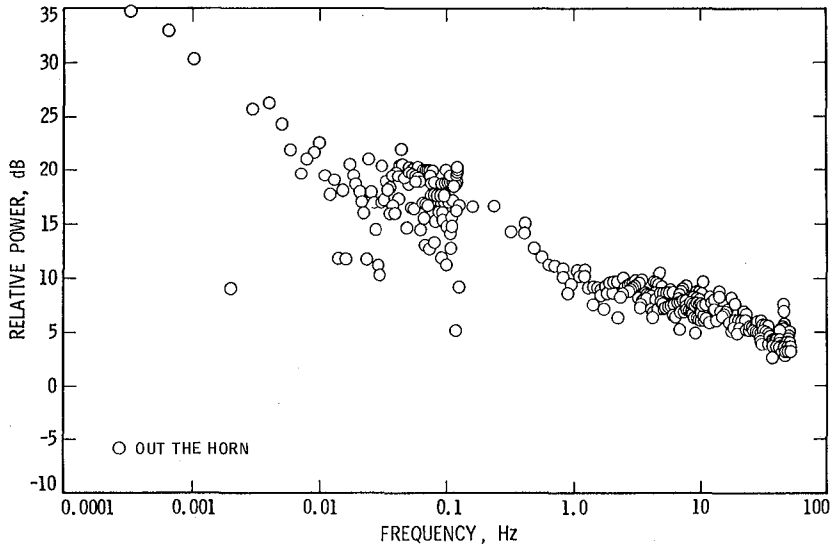


**Fig. 4. The power spectrum of the gain fluctuations of the S-band VLBI receiver (Configuration A) over the frequency range $10^{-4}$ to 50 Hz. The receiver was looking out the horn while the antenna was pointed at the zenith**

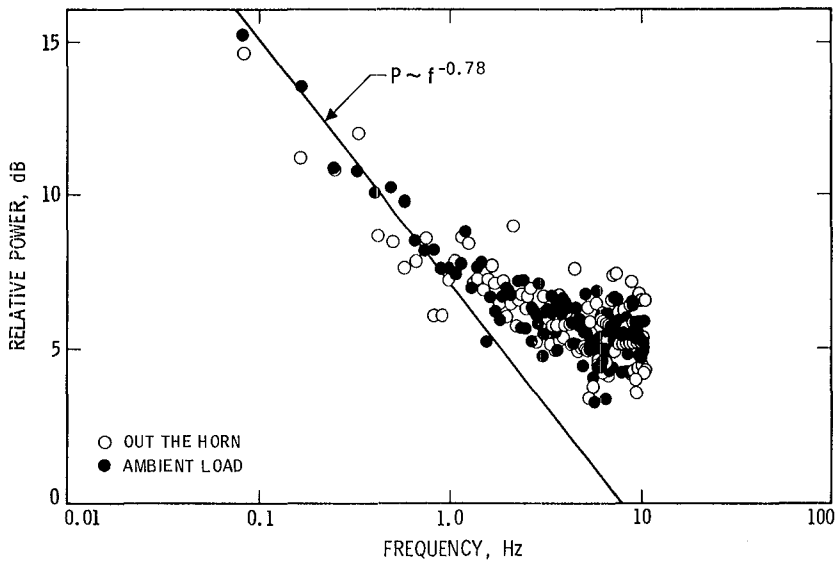


**Fig. 5. The power spectrum of the gain fluctuations of the X-band VLBI receiver (Configuration C) over the frequency range 0.1 to 10 Hz. Open circles represent data taken looking out the horn with the antenna pointed at the zenith. Filled circles represent data taken looking at an ambient load**

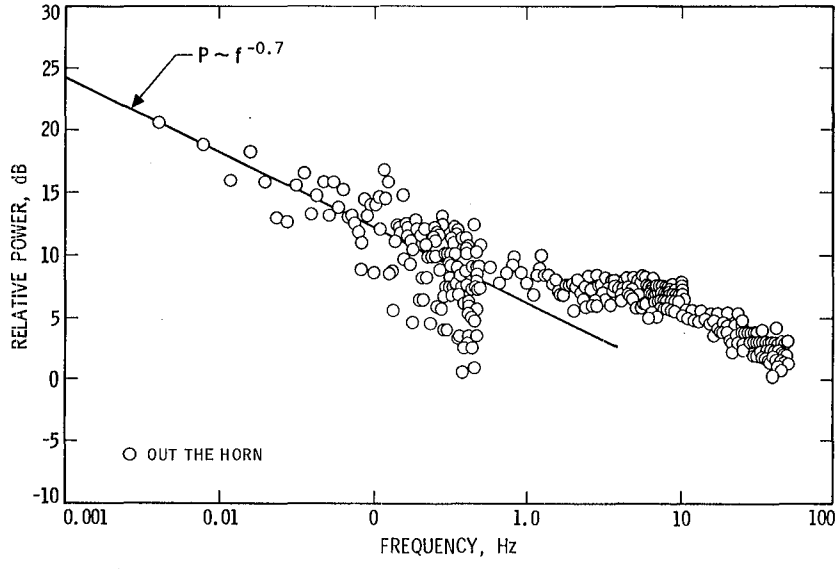


**Fig. 6. The power spectrum of the gain fluctuations of the X-band VLBI receiver (Configuration C) over the frequency range $10^{-4}$ to 50 Hz. The receiver was looking out the horn while the antenna was pointed at the zenith**

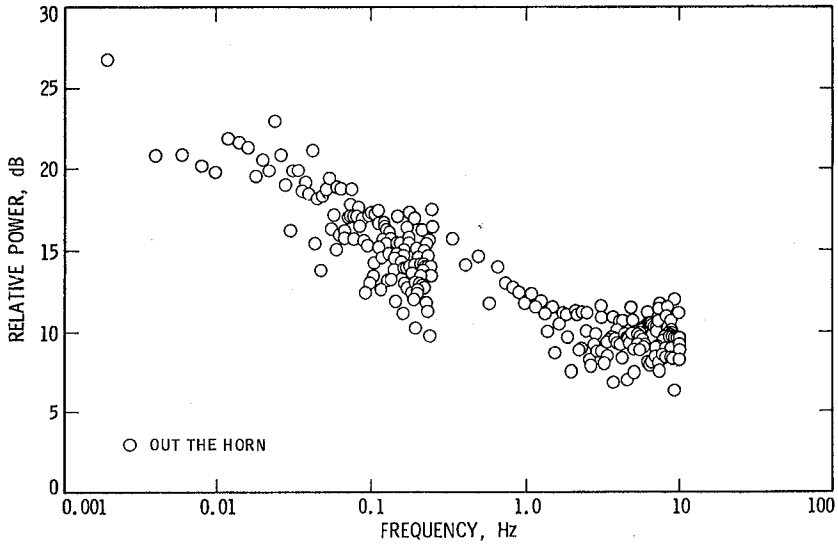


**Fig. 7. The power spectrum of the gain fluctuations of the S-band R&D receiver as seen at the end of the microwave link at DSS 14. The receiver was looking out the horn while the antenna was pointed at the zenith**

# Appendix

## The Power Spectrum of a Square Law Detector with Gain Variations

We present in this appendix a derivation of the power spectrum of the output of a square law detector which exhibits gain fluctuations. Let us first consider the power spectrum of the output of a square law detector whose gain, $G$, is constant. Assume that the output from the detector is given by:

$$D(t) = G\,V^2\,(t) \tag{A-1}$$

where $V(t)$ is the input voltage as a function of time. The correlation function of $D(t)$ when $V(t)$ is the result of thermal noise only is given by:

$$\psi(\tau) = G^2\,[\psi_0^2 + 2\,\psi_\tau^2] \tag{A-2}$$

where $\psi_\tau$ is the correlation function of the noise voltage, $V(t)$ (Ref. 3).

In the frequency domain, the power spectrum of the detector output is given by:

$$\phi(f) = G^2\,[\psi_0^2\,\delta\,(f) + 2\int_{-\infty}^{\infty} w(f)\,w(f-z)\,dz] \tag{A-3}$$

where

$$w(z) = \int_{-\infty}^{\infty} \psi_\tau\,e^{-i2\pi z\tau}\,d\tau \tag{A-4}$$

is the power spectral density of $V(t)$ and $\delta(f)$ is the unit impulse at $f = 0$. Fig. A-1 shows the power spectral density of bandlimited thermal noise; Fig. A-2 shows the power spectrum which corresponds to the bandlimited thermal noise spectrum shown in Fig. A-1.

Let us assume that the gain is a fluctuating quantity, but that $\Delta G/G \ll 1$, so that it may be written:

$$G(t) \cong G_0 + \Delta G(t) = G_0\,[1 + \Delta G(t)/G_0] \tag{A-5}$$

Substituting this approximation for $G(t)$, we may rewrite Eq. (A-1) in the following form:

$$D(t) = G_0\,[1 + \Delta G/G_0]\,V^2\,(t) \tag{A-6}$$

and the correlation function for $D(t)$ is:

$$\psi_G(\tau) = G_0^2\,\psi(\tau)\,\overline{[(1 + \Delta G(t)/G_0)\,(1 + \Delta G(t+\tau)/G_0)]} \tag{A-7}$$

where the term in brackets is the autocorrelation function of the normalized gain.

Since the power spectrum is the Fourier transform of the correlation function, the product relationship in Eq. (A-7) implies that the power spectrum of $D(t)$ is derived by convolving the power spectrum given by Eq. A-3 with the power spectrum of the gain fluctuations. This convolution leads to the following approximate expression for the power spectrum of the output of a square law detector which suffers gain fluctuations:

$$\phi_G(f) = (kTB)^2\,\delta(f) + (kT)^2\,(B - f) + (kTB)^2\,g(f) \tag{A-8}$$

where $g(f)$ is the power spectrum of the gain fluctuations. The convolution of $g(f)$ with the distributed part of $\phi(f)$ has been dropped in this expression because it is generally small.

The part of Eq. (A-8) which contains a delta function in frequency, $\delta(f)$, represents the DC power in the spectrum. The variance around the mean of $D(t)$ is:

$$\Delta P^2 = \int_0^{\infty} [(kT)^2\,(B - f) + (kTB)^2\,g(f)]\,df \tag{A-9}$$

Equation (A-9) leads directly to Eq. (1) if we realize that the total system power is $P = kTB$ and the frequency interval is the reciprocal of the integration time, $\tau$. Thus we may rewrite Eq. (A-9):

$$\Delta P^2/P^2 = (B\tau)^{-1} + \int_0^{f_{max}} g(f)\,df \tag{A-10}$$

and since we recognize:

$$\int_0^{\infty} g(f)\,df = \psi_G(0) = \overline{(\Delta G/G)^2} \tag{A-11}$$

we see that Eq. (A-10) is just another way of writing Eq. (1):

$$\Delta P^2/P^2 = (B\tau)^{-1} + \overline{(\Delta G/G)^2} \tag{A-12}$$

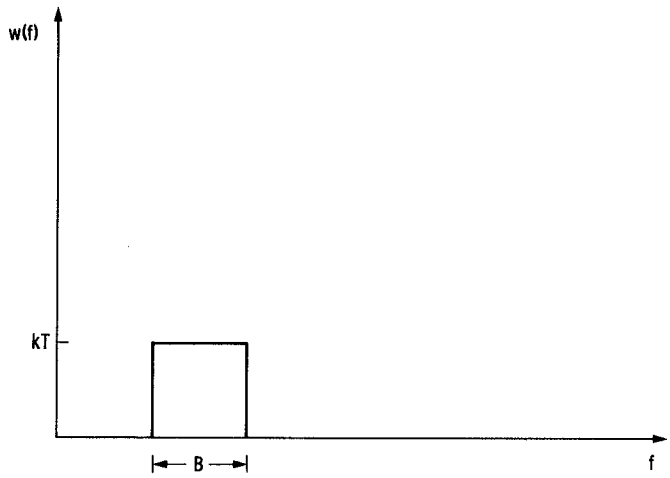


**Fig. A-1. The power spectral density of bandlimited thermal noise**

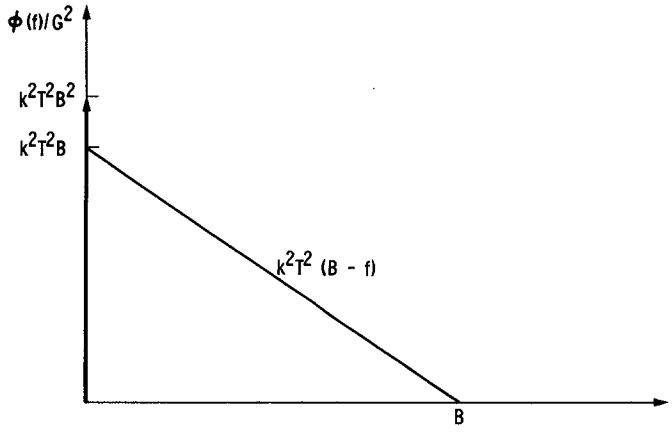


**Fig. A-2. The power spectrum of the bandlimited thermal noise spectrum shown in Fig. A-1**

# The SETI Interpreter Program (SIP) – A Software Package for the SETI Field Tests

E. T. Olsen and A. Lokshin
Atmospheric Sciences Section

*The SETI (Search for Extraterrestrial Intelligence) Interpreter Program is an interactive software package designed to allow flexible off-line processing of the SETI field test data on a PDP 11/44 computer. The user can write and immediately execute complex analysis programs using the compact SIP command language. The software utilized by the SETI Interpreter Program consists of FORTRAN - coded modules that are sequentially installed and executed.*

## I. Introduction

The objective of the SETI SR&T Program is the development of efficient means by which a large-scale microwave search for signals of extraterrestrial intelligent origin may be accomplished. A key element of the approach is the field test of hardware, search strategies, and signal-detection algorithms.

The SETI Science Team perceived the necessity for software that can be exploited by a large number of users to accomplish a wide range of analyses without requiring extensive new-code generation. The SETI Interpreter Program (hereafter referred to as the SIP) is the result.

A deliberate decision was made to sacrifice speed for flexibility, for it is planned to identify the optimum signal detection algorithms, which will then be implemented in custom high-speed hardware. The SIP is not expected to be capable of performing real-time data analysis so long as all processing is accomplished in software alone. Short bursts of raw data will be dumped on magnetic tape, which will then be analyzed in the field in near-real time or brought back to JPL or NASA/Ames.

The SETI SR&T Program will employ the Radio Frequency Surveillance System (RFISS) 65-kbin pipeline FFT device as well as its own 74-kbin multichannel spectrum analyzer (MCSA) to collect spectral data. The RFISS and the MCSA will both be used at DSS 13, the 26-meter R&D antenna at Goldstone, California; the MCSA will also be used at the 305-meter antenna at Arecibo Observatory in Puerto Rico.

## II. Data Format

A necessary prerequisite to the development of software for data analysis is the specification of the format and content of the data records themselves. If such a standardization of the data records had not been made, the SIP would have been

impossible, and all software would perforce be stand alone and thus entail a duplication of effort.

The SIP works with data in the standard SETI processed data format. This format defines a spectrum to be made up of 4-kword physical records, the first of which is a header record. Although the MCSA will be able to output data in several different formats, the SIP presently works with only one format, assuming data are unsigned 16-bit integers. This format was chosen because it is common to both the MCSA and the RFISS. At present, the SIP is configured to manipulate spectra as large as 32 kbins, but this limit is imposed only by the 512-kbyte memory of the PDP 11/44. When the memory is upgraded to a full 1 Mbyte, the SIP can be easily configured to handle 74-kbin spectra.

The MCSA will be equipped with an interface to allow direct data transfer to disk or tape of the PDP 11/44. The RFISS will be so equipped at some time in the future. During the next year, the only interface will be via magnetic tape transferred between the Modcomp in the RFISS van and the PDP 11/44. Software has been written to translate the Modcomp tape data into SETI processed data format on disk.

## III. Features of the SETI Interpreter Program

The presently implemented SIP reads spectra in SETI processed data format from disk files and accepts commands from the user console. There are three major parts of the SIP:

(1) A memory-resident Task Manager, which parses keyboard input, keeps track of task names and the numerical parameters and character parameters to be passed to the tasks, and schedules the spawning of independent tasks.

(2) A memory-resident Data Region, amounting to 108 kwords, which is large enough to hold three 32-kword spectra and their respective 4-kword headers.

(3) A disk-resident SETI Task Library, which holds most of the executable tasks that the Task Manager will spawn. A few frequently utilized tasks are incorporated into the manager to speed the SIP execution.

All SIP software has been coded in FORTRAN 77, even the part of the task manager, which parses the keyboard input. Some readers may consider the choice of language unfortunate, arguing for an assembly code where high-speed computations are required and a character-string friendly code (like PASCAL, for example) where the parsing occurs. The answer is that the SETI program stipulated some time ago that all software should be coded in FORTRAN to forestall the building of another Tower of Babel when the attempt was made to merge the products of JPL, NASA Ames, and Stanford University.

The PDP 11/44 is not a virtual memory machine and so it is not possible for a program to address more than 32 kwords of memory. The SIP utilizes a 4-kword window that can be mapped around data and headers of the spectra, and so each task can really address no more than 28 kwords plus the window. It is this memory constraint that forced us to use disk-resident tasks, despite the fact that the time required to simply install a disk-resident task for execution is approximately one second.

Some readers who are familiar with PDP 11s may wonder why we went the route of spawning independent tasks, rather than utilizing the task overlay features of this machine. We actually started out along that road, but soon came to the point where the overlay tree became so impossibly complex that it was a major undertaking to modify a task or add a new task. We switched over to spawning independent tasks to make maintenance and modification of the SIP humanly possible!

Communication between separate spawned tasks is accomplished by means of a special common block and the headers of the spectra. Thus every task includes in its code a standard preamble that keeps it informed as to the state of the data and its analysis.

Due to the memory restriction, there are limits to the size of the task stack, numerical stack, character stack, and typed command line. A data analysis program may not exceed any one of the following constraints:

(1) A typed line may contain no more than 120 characters

(2) A command line (made up of one or more typed lines) may contain no more than 30 tasks

(3) A program may contain a maximum of 25 command lines, 100 tasks, 200 numerical parameters, 300 character parameters, 25 dynamically variable parameters, and 10 macro commands

(4) A macro command may contain a maximum of 15 tasks, 30 numerical parameters, and 100 character parameters.

The above tabulation of constraints has introduced some concepts that have not been previously defined. A "typed line" is whatever the investigator has typed in response to the SIP prompt. A "command line" is a unit that can be repeat-

edly executed. A "program" is a complete data analysis algorithm. A "macro command" is a convenient feature that allows the investigator to identify an often-used series of tasks with a name; in effect it is a user-defined task made up of many SIP tasks. A "dynamically variable parameter" is one of a special set of numerical parameters that can be changed by the program during execution and used as a numerical parameter input to a task.

The SIP has already undergone several revisions, for we identified new requirements as we began field-test data analyses. Some especially useful facilities we added are:

(1) Dynamically variable parameters and primitive logical IF and GO TO commands to allow program execution to be controlled by the results of the analysis

(2) Input of stored ASCII files in response to the SIP prompt. Thus we may use any text editor to compose a program file that can then be read and executed by the SIP

(3) The capability to heavily comment the ASCII file so that the analysis program is well documented

(4) Debugging features.

A full list of the tasks presently implemented and planned is given in the Appendix.

## IV. An Example Analysis Program

The contemplated bimodal search strategy (see Ref. 1) for the microwave search includes an all-sky survey. Such a survey would rapidly scan the sky with an antenna, looking for excessive narrowband power coming from a direction fixed to the celestial sphere. Since the antenna is being moved, the power will vary because of changing sidelobe pickup, maser gain, and troposphere, among others. Thus the power in each spectrum bin will vary even though no narrowband signal is present. It will be necessary to use some reference spectrum to remove the changing ripples and overall bias of the newly acquired spectrum before applying a threshold to look for excessive power. This is a process that SETI personnel call "baselining," and it is a high-priority item in the field-test investigations. If we are fortunate (and careful), the ripples should be rather broad, and thus the required reference spectrum will be of very coarse resolution. In the worst case, the reference spectrum will have the same resolution as the newly acquired spectrum.

Of course, the reference spectrum will also vary with time. The current plans require that the reference spectrum be updated with some smoothing in time. In the worst case, each spectrum bin will be baselined using a value that reflects its recent history. The example that follows shows how this algorithm may be implemented in the SIP for testing.

Figure 1 is an overall logical flow diagram of the algorithm, which does not include SIP peculiar steps. A new spectrum is acquired and it is compared to a reference spectrum. If any bins exceed a preset threshold, the hits are reported. The reference spectrum is then updated and the cycle begins anew.

Figure 2 is the flow diagram, which includes the SIP peculiar steps. Recall that there are presently three spectra allowed in memory (V1, V2, and V3) and up to 25 dynamical variables ($P(n)$).

Figure 3 is the analysis program itself as read by the SIP. These are four ASCII files that were composed using a text editor and stored. The first file initializes some parameters, the second file defines macros, the third file makes a first guess at the reference spectrum, and the fourth file is the actual analysis program. If a first guess at the reference spectrum is already on disk, the third file need not be executed. These four files demonstrate how a program file may be documented for future users. As an indication of the (lack of) speed of the SIP, the master loop of the fourth file requires approximately one minute and twenty seconds. Note that this program contains an extra calculation that keeps track of the number of times a particular bin exceeded threshold. This is an attempt to identify local radio frequency interference (RFI) that is not variable in frequency.

This analysis program has in fact been executed using some data taken with the RFISS at X-band using DSS 14. Figure 4 shows what an individual raw spectrum looks like. Figure 5 shows the first guess baseline. Figure 6 is a representative report on an individual spectrum. Figure 7 is the accumulated RFI report. Figure 8 is the plot output of this accumulated RFI report.

## V. Software Portability

The SIP would be portable to any machine supporting FORTRAN 77 with minor changes except for two PDP 11/44 system features that have been incorporated in it. The first is the spawning of independent tasks. Any target machine must allow an executable element resident on the disk to be installed, run, and removed under software calls to the system. The second and more serious is the memory mapping which is built into the SIP. Any machine of the PDP 11 series that supports memory mapping is a good target, but even a VAX requires some major modifications of the software. The SETI program does plan to make the SIP run on a VAX, but we have not yet scoped the magnitude of the task.

The SIP Task Manager can be easily modified to allow a totally different library of tasks and data structure to be installed. Thus any potential user can customize the SIP for a specialized analysis task, building upon the basic structure already in place.

## VI. Future Work

As the reader can see by looking at the tasks listed in the Appendix, not all desired tasks have been implemented yet. These and tasks yet to be identified shall be added to those currently available as time and need dictate. Once the memory of the PDP 11/44 is upgraded to 1 Mbyte, the SIP data area in memory will be set up to handle four vectors to minimize disk I/O. There will very likely be two installed versions of the SIP. The smaller should handle up to 32-kbin spectra so that two investigators may execute in the PDP 11/44 concurrently. The larger will handle 74-kbin spectra, and only one investigator will fit in the memory at a time.

## References

1. Gulkis, S., Olsen, E. T., and Tarter, J., "A Bimodal Search Strategy for SETI," *Strategies for the Search for Life in the Universe*, edited by M. D. Papagiannis. The Proceedings of the IAU General Assembly, Vol. 83, pp. 93-105. D. Reidel, Dodrecht, Holland, the Netherlands, 1980.

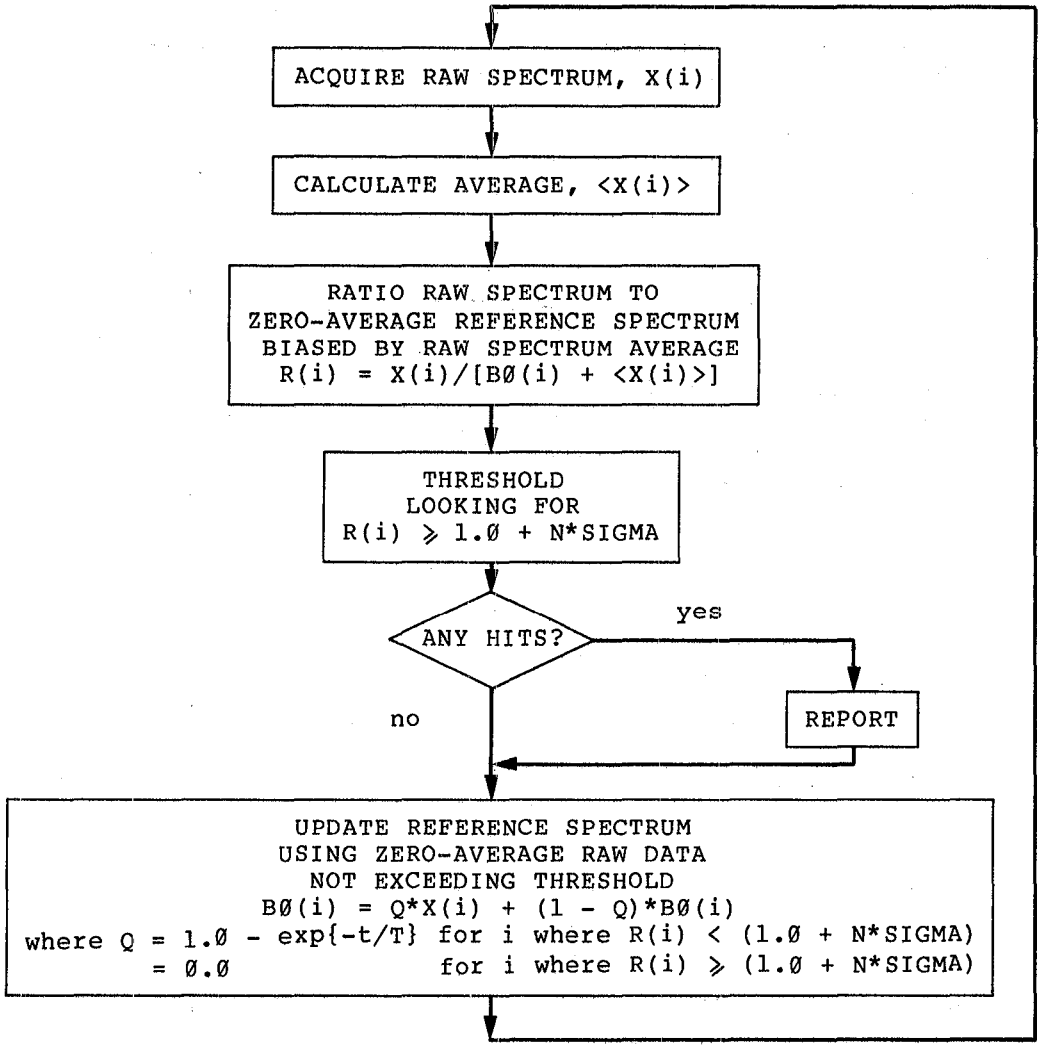


**Fig. 1. A candidate signal-detection algorithm for an all-sky SETI. Because of the rapid movement of the antenna, the reference spectrum must be continuously updated**

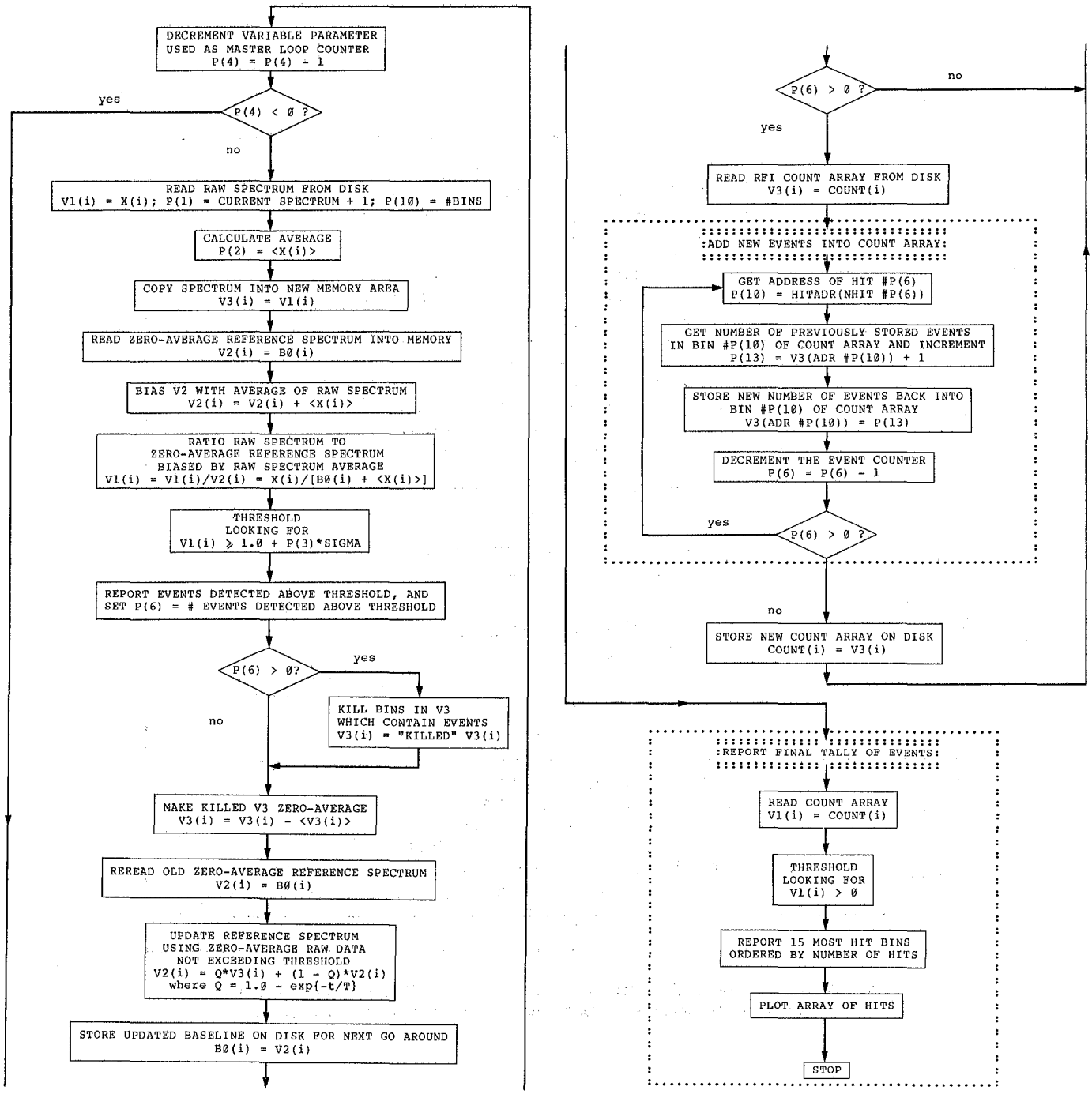


**Fig. 2. Implementation in the SIP of the candidate all-sky SETI signal-detection algorithm shown in Fig. 1. Note that an extra report has been added that shows the investigator how many times the power in a bin has exceeded the threshold**

```
PAR,1,'=',6       (FIRST SPECTRUM USED IN LOOP)
PAR,2,'=',Ø       (AVERAGE OF SPECTRUM, CALCULATED IN LOOP)
PAR,3,'=',4       (THRESHOLD LEVEL IN UNITS OF SIGMA ABOVE AVERAGE)
PAR,4,'=',1Ø4     (NUMBER OF TIMES MAJOR LOOP IS EXECUTED)
PAR,5,'=',3       (NUMBER OF SPECTRA EQUAL TO E-FOLDING TIME)
PAR,6,'=',Ø       (NUMBER OF HITS, CALCULATED IN PROGRAM)
PAR,7,'=',Ø       (INCREMENTAL COUNTER USED IN PROGRAM)
PAR,8,'=',Ø       (HIT ADDRESS, SET IN PROGRAM)
(THE FOLLOWING VARIABLE PARAMETERS ARE ALSO USED IN PROGRAM)
PAR,9,'=',Ø;PAR,1Ø,'=',Ø;PAR,11,'=',Ø;PAR,12,'=',Ø;PAR,13,'=',Ø
PAR,Ø,'?'         (DISPLAY ALL THE PARAMETERS NOW)
%
PARAMETER SETUP FOR SIPØØ2 --- SKY SURVEY RFI ANALYSIS PROGRAM
WHICH LOOPS THROUGH ACCUMULATED SPECTRA AND THRESHOLDS
ON THE QUANTITY
                    P/[<P> + D]

WHERE :
          P = POWER IN INDIVIDUAL BINS OF SPECTRUM
        <P> = AVERAGE OF ALL P
          D = ZERO-AVERAGE REFERENCE SPECTRUM USED IN
              EXPONENTIALLY UPDATED BASELINE

THIS PROGRAM ACCUMULATES THE HITS INTO A NEW SPECTRUM WHICH
ALLOWS THE INVESTIGATOR TO SEE HOW MANY TIMES A PARTICULAR
BIN HAS BEEN HIT OVER THE ENTIRE OBSERVATION PERIOD.


-------------------------------------------------------------------------


FILE'DM1:[31Ø,3Ø1]X1ØSEC.CH1;1'=XF              (DEFINE RAW DATA VECTOR NAME)
FILE'DM1:[31Ø,3Ø1]SIPØØ2.BLV;1'=DF            (DEFINE ZERO AVERAGE BLV NAME)
DF$;GET,2,'K'=DG                                   (READ BLV INTO VECTOR #2)
FILE'DM1:[31Ø,3Ø1]HITCNT.CH1;1'=DC                  (DEFINE HITCOUNT VECTOR)
AVER,1;PAR,2,'A'=APAR            (CALCULATE #1 VECTOR AVERAGE AND SET PAR 2)
APAR$;PAR,2,'*',-1=MAPAR            (CALCULATE -1*VECTOR AVERAGE SET PAR 2)
AVER,1;THRESH,1,,,3&,'HSG'=THR                        (THRESHOLD VECTOR #1)
CLEAR;REPORT,5,'H';REPORT,1,1,1Ø,5,'D'=RPT      (MAKE HIT REPORT ON CONSOLE)
DC$;SCALE,1,,,Ø,Ø;PUT,1                          (ZERO THE HITCOUNT VECTOR)
?$                                          (DISPLAY ALL DEFINED MACRO NAMES)
%
MACRO COMMAND DEFINITIONS FOR SIPØØ2 --- SKY SURVEY RFI ANALYSIS PROGRAM
```

**Fig. 3. The four files that comprise the actual SIP statements implementing the all-sky signal- detection algorithm shown in Fig. 2. The time required to execute one cycle of the major loop is approximately one minute, twenty seconds**

```
CLEAR;MSG,5,'BUILDING FIRST GUESS AT ZERO-AVERAGE BASELINE'    (START MESSAGE)
PAR,13,'=',2                                          (SET ITERATION COUNTER = 2)
XF$;NEWVER,1&;GET,1,'K';FILE'?'                (READ THE FIRST RAW DATA VECTOR)
PAR,13,'-',1;IF'LE',13;GOTO,11 (DECRIMENT ITER CNTR;GET OUT IF LOOPED ENOUGH)
COPY,1,2;COPY,1,3                        (COPY VECTOR #1 INTO VECTORS #2 AND #3)
SMOOTH,2;BLN2,1,2,'/'             (SMOOTH #2 BY 65 CHANNELS AND RATIO #1 TO #2)
AVER,1;THRESH,1,,,3.Ø,'HSB'           (LOOK FOR SPIKES IN BASELINED VECTOR #1)
COPY,1,3,'H';KILL,3,1Ø,'HN'          (COPY HEADER TO #3 AND KILL SPIKES IN #3)
COPY,3,1;MAPAR$;SCALE,1,,,2&    (COPY ALL FROM #3 TO #1; MAKE #1 ZERO-AVERAGE)
DF$;PUT,1;GOTO,4                      (STORE THE FIRST GUESS ZERO-AVERAGE BLV)
PLOT,1,'G:FIRST GUESS AT ZERO-AVERAGED BASELINE';CLEAR          (END MESSAGE)
%
FIRST BASELINE SETUP FOR SIPØØ2 --- SKY SURVEY RFI ANALYSIS PROGRAM
GET FIRST GUESS AT ZERO-AVERAGE BASELINE FROM FIRST SPECTRUM


-------------------------------------------------------------------------


PAR,4,'-',1;IF'LT',4;GOTO,12                                (MASTER LOOP COUNTER)
XF$;NEWVER,1&;GET,1,'K';APAR$;COPY,1,3;PAR,1,'+',1;PAR,1Ø,'N' (READ RAW DATA)
PAR,1,'?','NEXT VECTOR';DG$;SCALE,2,,,2&;BLN2,1,2,'/' (CALCULATE   X/[D+<X>])
THR$;RPT$;PAR,6,'HN';IF'LE',6;GOTO,6 (THRESH; DIRECTLY UPDATE BLV IF NO HITS)
COPY,1,3,'H';KILL,3,1,'HN'             (KILL HITS IN RAW DATA FOR BLV UPDATE)
AVER,3;PAR,2,'A';PAR,2,'*',-1;SCALE,3,,,2&  (MAKE KILLED VECTOR ZERO-AVERAGE)
DG$;EXP,2,3,,,5&;DF$;PUT,2          (UPDATE BLV WITH KILLED VECTOR AND STORE)
AREA,1;PAR,6,'HN';IF'LE',6;GOTO,1    (SKIP REST AND CONTINUE LOOP IF NO HITS)
DC$;GET,3                                    (READ IN THE HIT COUNT ARRAY)
AREA,1;PAR,1Ø,'HA',6&;AREA,3;PAR,13,'C',1Ø&;PAR,13,'+',1;-
PAR,13,'P',1Ø&;PAR,6,'-',1;IF'GT',6;GOTO,1Ø            (COUNT HITS INTO BINS)
DC$;PUT,3;GOTO,1             (STORE UPDATED HITCOUNT ARRAY AND CONTINUE LOOP)
DC$;GET,1;THRESH,1,,,Ø,'G';CLEAR;MSG,5,'REPORT OF 15 MOST FREQUENTLY HIT CHANNELS
REPORT,1,1,15,,5,'D';WAIT;PLOT,1,'G:HIT COUNT ARRAY';CLEAR     (FINAL REPORT)
%
ACTION PROGRAM FOR SIPØØ2 --- SKY SURVEY RFI ANALYSIS PROGRAM
EXECUTE THE FOLLOWING FILES IN THE ORDER SPECIFIED:

              SIPØØ2.ØØ1    ---    PARAMETER SETUP
              SIPØØ2.ØØ2    ---    MACRO DEFINITION
              SIPØØ2.ØØ3    ---    INITIAL BASELINE CALCULATION
              SIPØØ2.ØØ4    ---    THIS FILE
```

**Fig. 3 (contd)**

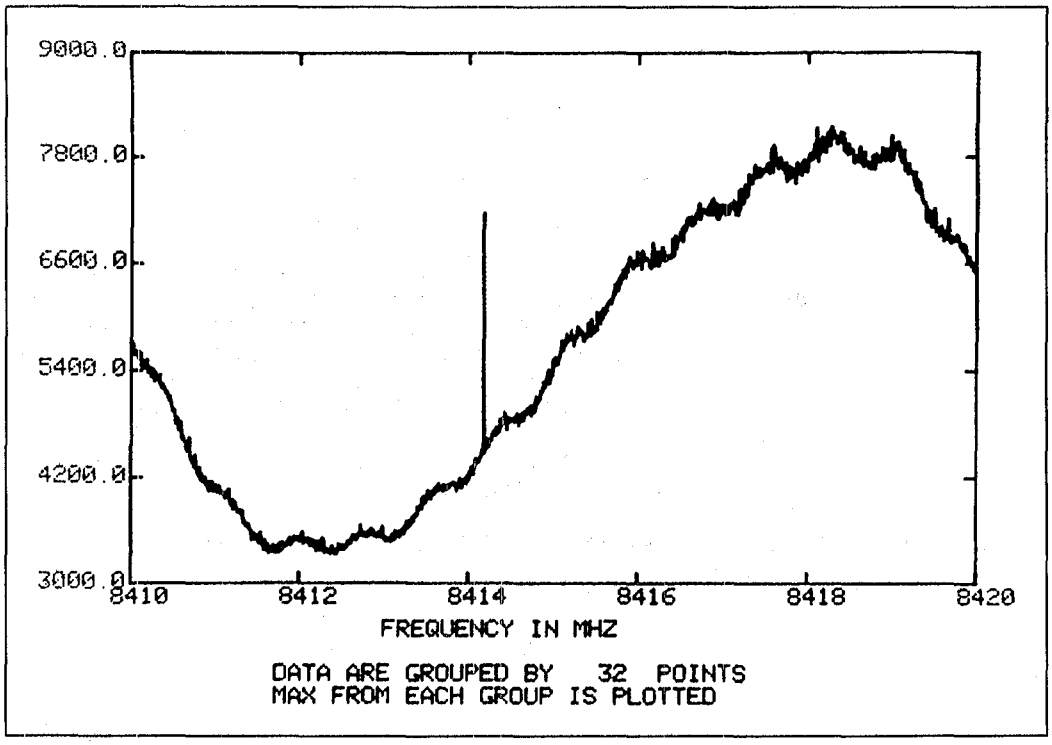


**Fig. 4. A 32-kbin spectrum before application of a baseline. Note the RFI at 8414.3 MHz**

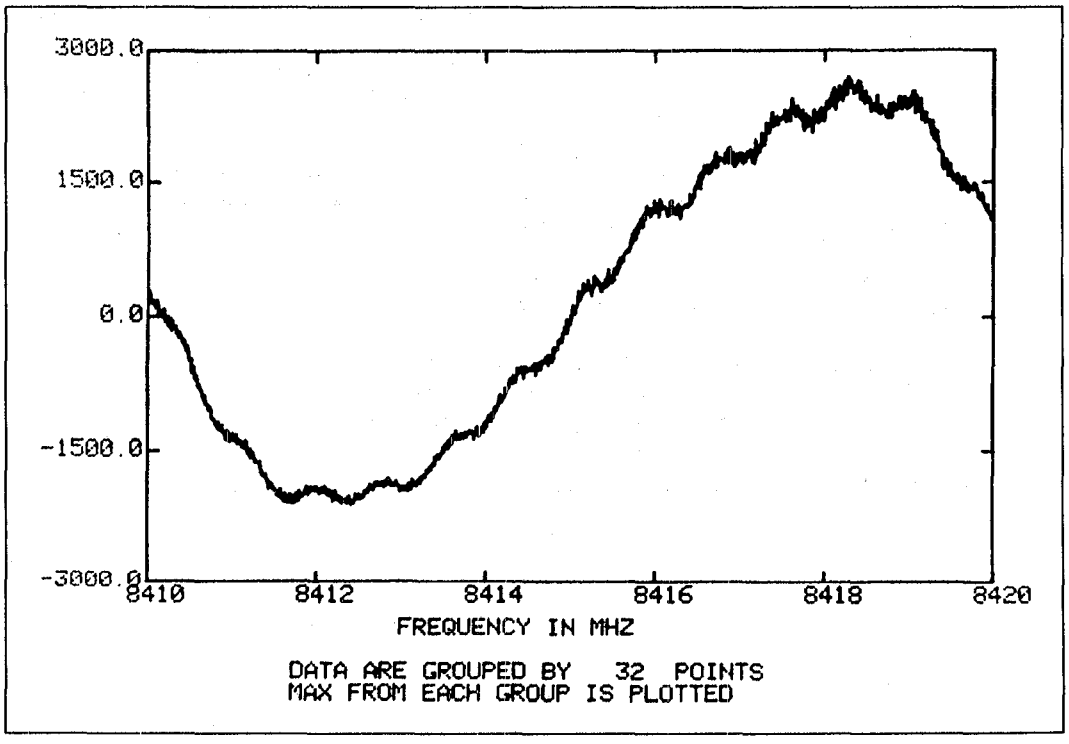


**Fig. 5. The first derived zero-average reference spectrum. Note that the structure present in Fig. 4 is preserved, with the exception of the narrowband feature at 8414.3 MHz**

```
    DATE-TIME        RA [H/M/S]   DEC[DG/M/S]   #HITS   ABV SG   AVERG   SIGMA

83/ 86/11:27:59.70   0/ 0/ 0.0     0/ 0/ 0.0        4     3.99    999.7   19.58
       BIN#          FREQ [MHZ]      AMPLITUDE    SIGM LEV
      13292      8414.356,080,750         1470       24.02
      15864      8415.140,991,            1098        5.02
       6334      8412.232,673,250         1081        4.15
      22882      8417.282,709,            1079        4.05
```

**Fig. 6. A representative report after thresholding a baselined spectrum at a level of 4*SIGMA above its average**

```
83/ 96/11:19:18.36   0/ 0/ 0.0     0/ 0/ 0.0     205        0   XXXX     XXXX
       BIN#          FREQ [MHZ]      AMPLITUDE    SIGM LEV
      13292      8414.356,080,750         104      XXXXX
      13291      8414.355,775,500           2      XXXXX
      15541      8415.042,419,500           2      XXXXX
      28869      8419.109,792,              2      XXXXX
      32429      8420.196,215,              1      XXXXX
      32422      8420.194,078,              1      XXXXX
      32245      8420.140,062,              1      XXXXX
      31853      8420.020,434,              1      XXXXX
      31544      8419.926,135,              1      XXXXX
      31343      8419.864,794,              1      XXXXX
      31155      8419.807,422,              1      XXXXX
      30788      8419.695,422,              1      XXXXX
      30725      8419.676,196,              1      XXXXX
      30649      8419.653,003,              1      XXXXX
      30543      8419.620,654,              1      XXXXX
```

**Fig. 7. The accumulated RFI report showing the 15 most frequently hit bins after baselining and thresholding 104 spectra at the level of four standard deviations above their means. The interference at 8414.3 MHz was detected in all spectra**

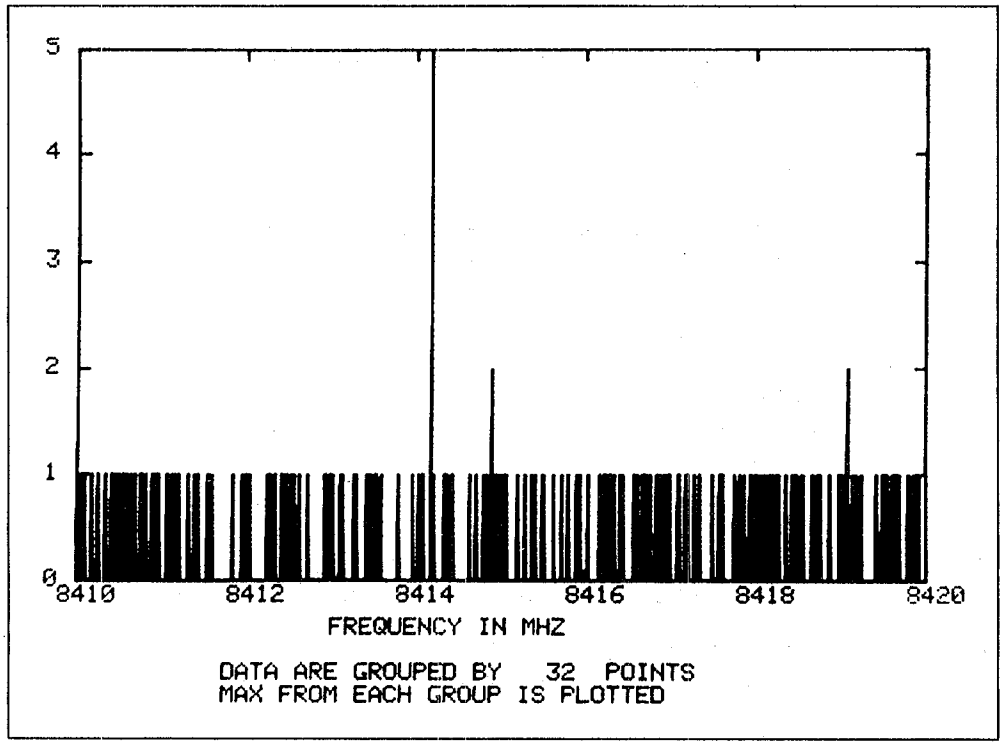


**Fig. 8. The accumulated RFI report for the entire 10-MHz frequency interval. The RFI at 8414.3 MHz has been arbitrarily set to 5 so that the distribution of the events due to random noise is visible. A power spectral analysis shows the events to be randomly distributed over the 32 Kbins**

# Appendix

## Alphabetical Listing of SIP Tasks

| TASK # | TASK NAME AND PARAMETERS AND SUMMARY DESCRIPTION |
|---|---|
| 1 | ACCUM[,NAREA,NBIN1,NBIN2][,'CHAR']<br>Performs floating point accumulation and averaging of spectra. |
| 2 | AREA,NAREA<br>Sets spectrum area for PAR command. |
| 3 | AVER,[NAREA,NBIN1,NBIN2,LU][,'?']<br>Calculates statistics of spectrum. |
| 4 | BELL<br>Sounds tone at user console. |
| 5 | BLN2[,NAREA1,NAREA2,NBIN1,NBIN2,SCALE][,'CHAR']<br>Calculates quotient or difference of two spectra. |
| 6 | BYE<br>Exits SIP. |
| 7 | CLEAR<br>Erases Tektronix terminal screen. |
| 8 | CLIP[,NAREA,NBIN1,NBIN2,R1][,R2][,'CHARs']<br>Limits range of amplitudes in spectra. |
| 9 | CMT[,NAREA,NWORD,LU],'CHARACTER_STRING'<br>Places ASCII comment into spectrum header. |
| 10 | COPY[,NAREA1,NAREA2][,'CHARs']<br>Copies spectrum from one memory area to another. |
| 11 | CURRNT[,LU]<br>Displays SIP parameters for debugging purposes. |
| 12 | DATE[,LU]<br>Displays current date and time on user console. |
| 13 | DB[,NAREA,NBIN1,NBIN2,NSCALE]<br>Makes spectrum amplitudes logarithmic. |
| 14 | EXP[,NAREA1,NAREA2,NBIN1,NBIN2][,R][,'CHAR']<br>Exponentially updates baseline spectrum using current spectrum. |
| 15 | FFT[,NAREA,NBIN,N]<br>Calculates power spectrum of spectrum amplitudes. |

| TASK # | TASK NAME AND PARAMETERS AND SUMMARY DESCRIPTION |
|---|---|
| 16 | FILE'NEWFILENAME'[,LU]<br>Defines disk file name used by GET and PUT. |
| 17 | *FIT[,NAREA,NBIN1,NBIN2,NORDER,LU][,'CHAR']<br>Makes Least-squares fit to features of spectrum. |
| 18 | FRQ[,NAREA,R,LU][,'CHAR']<br>Makes conversion between bin number and frequency and displays on user console. |
| 19 | GET[,NAREA,NBLK1,NBLKS][,'K']<br>Reads spectrum from disk file into memory. |
| 20 | GOTO,LINE<br>Passes program control to new command line. |
| 21 | GROUP[,NAREA,NBIN1,NBIN2,NGROUP][,'CHAR']<br>Compresses spectrum by combining adjacent bins. |
| 22 | HELP<br>Invokes facility which describes commands in detail. |
| 23 | HIST[,NAREA,NBIN1,NBIN2]<br>Invokes statistical analysis package. |
| 24 | HRDCPY<br>Triggers Tektronix console hardcopy. |
| 25 | IF,NPAR,'COND'[,VALUE]<br>Logically compares value of dynamical variable to a value and skips rest of command line if false. |
| 26 | KILL[,NAREA,NVAL][,'CHARs'][,NBIN1,NBIN2,NBIN3,...]<br>Adjusts amplitude in identified bins. |
| 27 | LEVEL,R[,'S']<br>Sets amplitude for CLIP, KILL, and THRESH |
| 28 | MSG,LU,'CHARACTER_STRING'<br>Sends message to console. |
| 29 | NEWVER[,NVAL,'CHAR']<br>Changes file name version. |
| 30 | PAR,NPARM[,R1][,'OP1'][,R2,'OP2',  ,RN,'OPN']<br>Calculate value and set dynamical variable equal to it. |
| 31 | PEEK,NAREA,NBIN1,NBIN2[,LU][,'H']<br>Displays amplitudes of bins or values in header of spectrum on user console. |

| TASK # | TASK NAME AND PARAMETERS AND SUMMARY DESCRIPTION |
|---|---|
| 32 | PICK[NAREA,NBIN1,NBINS,NSTEP]<br>Compresses spectrum by selecting equally spaced bins. |
| 33 | PLOT[,NAREA,R1,R2,'CHARs:heading character string']<br>Display spectrum on Tektronix terminal. |
| 34 | POKE,NAREA,NBIN1[,NBIN2],K1[,K2, ,Kn][,'H']<br>Places values into bins or header of spectrum. |
| 35 | PUT[,NAREA,NBLK1,NBLKS]<br>Writes spectrum from memory into disk file. |
| 36 | RANGE,NBIN1,NBIN2<br>Specifies range of bins in spectrum over which all other tasks will operate. |
| 37 | RASTR,NAREA,NBIN,N<br>Places time history of a bin into single spectrum. |
| 38 | REPORT[,NAREA,NHIT1,NHIT2,LU][,'CHAR']<br>Writes report of events crossing threshold on console. |
| 39 | SCALE[,NAREA,NBIN1,NBIN2,ADD,SCALE]<br>Rescales amplitudes of bins of spectrum. |
| 40 | SIGNAL[,NAREA,NBIN1,NBIN2,LU][,'CHAR']<br>Generates artificial signal and writes into spectrum. |
| 41 | SKIP[,NSKIP,LU][,'P']<br>Controls line printer pagination. |
| 42 | SMOOTH[,NAREA,NBIN1,NBIN2,NHALF]<br>Smooths amplitudes in bins of spectrum with boxcar filter. |
| 43 | THRESH[,NAREA,NBIN1,NBIN2,T1][,T2][,'CHARs']<br>Applies threshold to spectrum and records events which exceed it. |
| 44 | TIME[,LU]<br>Times SIP tasks. |
| 45 | WAIT<br>Pauses SIP execution until console key is pressed. |

* Task not yet implemented.
Parameters enclosed by [ ] may be omitted
if default values apply.

# A Southern Hemisphere VLBI Survey on a 275-km Baseline

D. D. Morabito, R. A. Preston, J. Faulkner, and A. E. Wehrle
Tracking Systems and Applications Section

D. L. Jauncey, M. J. Batty, R. F. Haynes, and A. E. Wright
C.S.I.R.O., Division of Radiophysics, Epping, Australia

*A VLBI survey at 2.29 GHz has been conducted using a 275-km baseline consisting of the NASA DSN tracking site in Tidbinbilla, Australia, and the 64-m antenna located at Parkes, Australia. The purpose of this survey was to identify sources in the southern sky possessing strong compact cores (< 0.1 arcseconds). Such sources will be used to form a reference frame for conducting VLBI geodesy experiments in the southern hemisphere. The 70 candidate sources were chosen to be south of -39 degrees declination, and only four had been previously observed from the northern hemisphere. Of the observed sources, 49 were found to have compact structure. In addition to determining correlated flux densities, the delay and delay rate observables of several detected sources were used to determine an estimate of the three-dimensional location of the Parkes antenna relative to the Tidbinbilla site with a 1-sigma accuracy of < 10 meters.*

## I. Introduction

Prior to April 1980, there had been very few sources observed with VLBI in the southern polar region due to the dearth of antennas in the southern hemisphere with built-in VLBI capabilities. From 24-28 April 1980 a VLBI experiment at 2.29 GHz was performed between the NASA DSN site at Tidbinbilla, Australia, and the 64-m antenna at Parkes, Australia, for the purpose of identifying sources possessing compact components and hence useful for southern hemisphere VLBI geodesy experiments. This paper discusses the results of that survey.

The candidate sources were selected from the Parkes survey (Refs. 1-10). The selection criteria were (1) catalog total flux density > 1.0 Jy at 2.7 GHz, (2) spectral index >-0.7 ($S=kf^{\alpha}$), and (3) declination south of -39 degrees. Of 95 sources meeting these criteria, 70 sources were observed. Of these sources, 49 were found to have a compact core on the Tidbinbilla to Parkes baseline (~0.1 arcsec fringe spacing). Selected sources from these 49 new VLBI detections combined with sources previously detected by VLBI (mostly with declinations north of -39 degrees) (Ref. 11), and sources detected in future VLBI surveys will be used to construct a celestial reference frame for performing southern hemisphere VLBI geodesy experiments. The advent of southern hemisphere VLBI will be of great value to both the geodynamic and astrophysics communities. The seismically quiet Australian continent will serve as a stable platform for testing long-term reliability and repeatability of VLBI-determined geodetic relative positions, and as a base for using VLBI to measure the crustal motions of the very seismically active regions near Australia.

## II. Experiment Configuration

Right circular polarization was employed. The NRAO Mark II VLBI recording system was used to record a 1.8-MHz data bandwidth by digitally sampling at 4 Mbs (Ref. 12). Digital sampling and phase stability of the receiver chain were controlled by a rubidium atomic oscillator at Parkes and a hydrogen maser at Tidbinbilla. Each source was observed for three minutes. The Tidbinbilla/Parkes interferometer has a length of 275 km, corresponding to a minimum fringe spacing of 98 milliarcsec at 2.29 GHz.

Total flux densities for most of the sources were measured during the experiment with the 64-m antennas at Parkes and Tidbinbilla. The rms errors were $[(0.05\,S)^2 + (0.03)^2]^{0.5}$ Jy for Tidbinbilla and $[(0.1\,S)^2 + (0.03)^2]^{0.5}$ Jy for Parkes, where $S$ is the measured total flux density.

## III. Data Reduction

Matching tapes from both sites were cross-correlated using the Caltech/JPL VLBI Block 0 Processor (Mark II). Computer manipulation of the correlator output yielded the correlation coefficient for each observation. The tapes were correlated over a range of relative tape delay and delay rate offsets to compensate for a priori source position uncertainties. The sky was searched within 2 arcmin of all a priori source positions.

The correlation coefficients were then converted into correlated flux densities or the VLBI source strength for each celestial radio source observation using the procedure discussed in a previous paper (Ref. 13) with a scaling constant of 2.5 ±0.1 Jy. The 5-sigma detection limit for each observation was about 0.1 Jy. Correspondingly, the uncertainty in detected source strength due to random noise was about 0.02 Jy. However, in practice, systematic errors at about the 7% level dominate the random contributions for most sources.

The delay and delay rate observables of 31 detected sources were used to solve for the DSS 42 to Parkes baseline. Most of the source positions used in this solution were determined from VLBI experiments between Australia and South Africa performed during the same week (Ref. 14). The rest of the positions were obtained from Fanselow et al. (Ref. 15). The delays were bit stream alignment delays yielding post-fit residuals of about 10 ns. Post-fit residuals in delay rates were about 0.5 mHz.

## IV. Results and Discussion

Table 1 lists the total flux densities, the correlated flux densities, and the number of observations for each source. For cases where multiple observations of correlated flux density differ by more than 1 sigma (probably due to source structure effects), both the lowest value (denoted by L) and the highest value (denoted by H) are listed in the table. Undetected sources are denoted by 5-sigma upper bound.

Figure 1 shows a sky distribution plot of the detected sources. This plot along with the results given in Table 1 can serve as a useful tool in creating an optimum observing schedule for conducting VLBI geodesy experiments. Figure 2 shows a correlated flux density histogram of the detected sources. Note that there are 10 sources with mean flux densities greater than or equal to 2 Jy.

The baseline vector from DSS 42 to Parkes was determined as a by-product of this survey. By assuming the previously determined position of DSS 42 (Ref. 16), the new position of the Parkes antenna intersection of axes is

$X$ = -4554229 m
$Y$ = 2816762 m
$Z$ = -3454050 m

where $X$ is the vector component aligned along the Greenwich meridian on the equatorial plane, $Y$ is the vector component aligned 90 degrees east of Greenwich on the equatorial plane, and $Z$ is the vector component aligned along the earth's spin axis defined positive north. The 1-sigma accuracy of the baseline measurements is $< 10$ meters in each coordinate.

This result agrees with a recent ground survey (Ref. 17), but differs from the position published in the 1981 American Ephemeris by -140 m in $X$, 46 m in $Y$, and 133 m in $Z$. This solution is a fourteenfold improvement over the previously known Parkes antenna position.

## V. Conclusion

A 2.29-GHz VLBI survey of 70 southern polar sources on a 275-km baseline found 49 of these sources to have compact cores. These sources will be useful for future VLBI geodesy experiments in the southern hemisphere. As a by-product of this survey, the position of the Parkes antenna was determined with a 1-sigma accuracy of $< 10$ meters.

## Acknowledgments

We are indebted to the instrumentation and observing assistance supplied by L. J. Skjerve of JPL and to the staffs of the Tidbinbilla and Parkes observatories.

## References

1. Shimmins, A.J., and Bolton, J.G., *Aust. J. Phys. Astrophys. Suppl.*, No. 26,1, 1972.
2. Bolton, J.G., and Butler, P.W., *Aust. J. Phys. Astrophys. Suppl.*, No. 34,33, 1975.
3. Wall, J.V., Shimmins, A.J., and Bolton, J.G., *Aust. J. Phys. Astrophys. Suppl.*, No. 34,55, 1975.
4. Wright, A.E., Savage, A., and Bolton, J.G., *Aust. J. Phys. Astrophys. Suppl.*, No. 41,1, 1977.
5. Shimmins, A.J., *Aust. J. Phys. Astrophys. Suppl.*, No. 21,1, 1971.
6. Bolton, J.G., and Shimmins, A.J., *Aust. J. Phys. Astrophys. Suppl.*, No. 30,1, 1973.
7. Ekers, J.A., *Aust. J. Phys. Astrophys. Suppl.*, No. 7,1, 1969.
8. Shimmins, A.J., Manchester, R.N., and Harris, B.J., *Aust. J. Phys. Astrophys. Suppl.*, No. 8,1, 1969.
9. Shimmins, A.J., and Bolton, J.G., *Aust. J. Phys. Astrophys. Suppl.*, No. 23,1, 1972.
10. Wills, B.J., *Aust. J. Phys. Astrophys. Suppl.*, No.. 38,1, 1975.
11. Preston, R.A., et al. (to be published in the *Astrophysical Journal*).
12. Clark, B.G., *Proc. IEEE*, 61,1242, 1973.
13. Preston, R.A., et al., *DSN Progress Report 42-46*, Jet Propulsion Laboratory, Pasadena, Calif., Aug. 15, 1978.
14. Morabito, D.D., et al., *Astronomical Journal* (in press).
15. Fanselow, J.L., et al. (private communication).
16. Moyer, T.D. (private communication).
17. Allman, J.S. (private communication) 1983.

**Table 1. Table of observations**

| SOURCE NAME | TOTAL FLUX DENSITY (Jy) | | CORRELATED FLUX DENSITY (Jy) | NUMBER OF OBSERVATIONS |
|---|---|---|---|---|
| P 0003-56 | 0.86+/- 0.09 | | <0.07 | 1 |
| P 0003-42 | 1.3 +/- 0.1 | | 0.15+/- 0.02 | 1 |
| P 0036-62 | 0.79+/- 0.08 | | <0.07 | 1 |
| P 0043-42 | 4.8 +/- 0.5 | | <0.07 | 1 |
| P 0047-579 | 2.7 +/- 0.3 | | 1.5 +/- 0.1 | 1 |
| P 0131-522 | 1.4 +/- 0.1 | | 0.96+/- 0.07 | 1 |
| P 0153-410 | 1.6 +/- 0.2 | | 1.21+/- 0.09 | 1 |
| P 0202-76 | 1.9 +/- 0.2 | | 0.28+/- 0.03 | 1 |
| P 0208-512 | 3.5 +/- 0.4 | | 2.3 +/- 0.2 | 1 |
| P 0214-48 | 1.4 +/- 0.2 | | <0.07 | 1 |
| P 0302-623 | 1.7 +/- 0.2 | | 1.4 +/- 0.1 | 1 |
| P 0332-403 | 1.2 +/- 0.07 | L | 0.66+/- 0.05 | 2 |
| | | H | 1.28+/- 0.09 | |
| P 0354-48 | 0.39+/- 0.05 | | <0.07 | 1 |
| P 0427-53 | 3.5 +/- 0.4 | | <0.07 | 1 |
| P 0437-454 | 0.71+/- 0.08 | | 0.62+/- 0.05 | 1 |
| P 0438-43 | 3.9 +/- 0.2 | L | 2.3 +/- 0.2 | 2 |
| | | H | 3.2 +/- 0.2 | |
| P 0454-46 | 2.1 +/- 0.2 | | 1.30+/- 0.09 | 1 |
| P 0506-61 | 1.8 +/- 0.2 | | <0.07 | 1 |
| P 0511-48 | 2.5 +/- 0.3 | | <0.07 | 1 |
| P 0514-459 | | | 0.72+/- 0.05 | 1 |
| P 0517-56 | 1.0 +/- 0.1 | | <0.07 | 1 |
| P 0535-66 | 1.2 +/- 0.1 | | <0.07 | 1 |
| P 0537-441 | 3.3 +/- 0.3 | | 2.6 +/- 0.2 | 1 |
| P 0616-48 | 0.66+/- 0.07 | | <0.07 | 1 |
| P 0637-75 | 5.1 +/- 0.5 | | 3.6 +/- 0.3 | 1 |
| P 0658-65 | 0.86+/- 0.09 | | <0.07 | 1 |
| P 0719-55 | 1.2 +/- 0.1 | | <0.07 | 1 |
| P 0743-67 | 3.0 +/- 0.3 | | 1.15+/- 0.08 | 1 |
| P 0748-44 | 1.4 +/- 0.1 | | <0.07 | 1 |
| P 0842-75 | 2.6 +/- 0.3 | | 0.14+/- 0.02 | 1 |
| P 0903-57 | 1.7 +/- 0.2 | | 0.11+/- 0.02 | 1 |
| P 1046-409 | 1.8 +/- 0.2 | | 0.52+/- 0.04 | 1 |
| P 1104-445 | 2.1 +/- 0.2 | | 1.8 +/- 0.1 | 2 |
| P 1105-680 | | | 0.75+/- 0.05 | 1 |
| P 1148-671 | | | 1.6 +/- 0.1 | 1 |
| P 1215-45 | 3.7 +/- 0.4 | | 2.0 +/- 0.1 | 1 |

| SOURCE NAME | TOTAL FLUX DENSITY (Jy) | | CORRELATED FLUX DENSITY (Jy) | NUMBER OF OBSERVATIONS |
|---|---|---|---|---|
| P 1302-49 | 4.9 +/- 0.3 | | <0.08 | 1 |
| P 1416-49 | 1.63+/- 0.09 | | 0.09+/- 0.01 | 1 |
| P 1421-49 | 7.4 +/- 0.4 | L | 1.7 +/- 0.1 | 6 |
| | | H | 3.3 +/- 0.2 | |
| P 1424-41 | 2.6 +/- 0.1 | L | 1.4 +/- 0.1 | 8 |
| | | H | 1.8 +/- 0.1 | |
| P 1540-82 | 1.20+/- 0.07 | | 1.12+/- 0.09 | 1 |
| P 1549-79 | 5.4 +/- 0.3 | L | 2.5 +/- 0.2 | 2 |
| | | H | 3.0 +/- 0.2 | |
| P 1602-63 | 2.2 +/- 0.1 | | 0.05+/- 0.01 | 1 |
| P 1610-77 | 4.4 +/- 0.2 | | 3.7 +/- 0.2 | 2 |
| P 1619-680 | 1.8 +/- 0.1 | | 1.9 +/- 0.1 | 5 |
| P 1637-77 | 4.3 +/- 0.2 | | 0.14+/- 0.01 | 1 |
| P 1655-77 | 1.74+/- 0.09 | | <0.04 | 1 |
| P 1718-649 | 4.2 +/- 0.2 | | 3.8 +/- 0.2 | 2 |
| P 1733-56 | 5.8 +/- 0.3 | | 1.18+/- 0.06 | 2 |
| P 1806-458 | 1.26+/- 0.07 | | 0.43+/- 0.02 | 2 |
| P 1815-554 | 1.12+/- 0.06 | | 1.06+/- 0.08 | 1 |
| P 1831-711 | 1.12+/- 0.06 | | 0.85+/- 0.06 | 1 |
| P 1933-58 | 1.9 +/- 0.1 | | 0.31+/- 0.02 | 2 |
| P 1936-623 | 1.37+/- 0.07 | | 0.86+/- 0.05 | 2 |
| P 1951-50 | 0.94+/- 0.06 | | <0.07 | 2 |
| P 2002-50 | | | 0.24+/- 0.02 | 1 |
| P 2005-489 | | | 0.96+/- 0.07 | 1 |
| P 2052-47 | | | 1.26+/- 0.06 | 2 |
| P 2106-413 | | | 1.8 +/-0.1 | 2 |
| P 2153-69 | 20.8 +/- 2.1 | | 0.75+/- 0.05 | 1 |
| P 2204-54 | 1.09+/- 0.1 | | <0.07 | 1 |
| P 2207-45 | | | <0.07 | 1 |
| P 2213-45 | | | 0.69+/- 0.05 | 1 |
| P 2227-399 | 0.41+/- 0.05 | | 0.53+/- 0.04 | 1 |
| P 2311-452 | 2.0 +/- 0.2 | | 1.4 +/- 0.1 | 1 |
| P 2326-477 | 2.8 +/- 0.3 | | 2.4 +/- 0.2 | 2 |
| P 2333-528 | 1.7 +/- 0.2 | | 1.32+/- 0.09 | 1 |
| P 2338-58 | 1.8 +/- 0.2 | | <0.07 | 1 |
| P 2355-534 | | | 1.5 +/- 0.1 | 1 |
| P 2356-61 | 16.9 +/- 1.7 | | <0.08 | 2 |

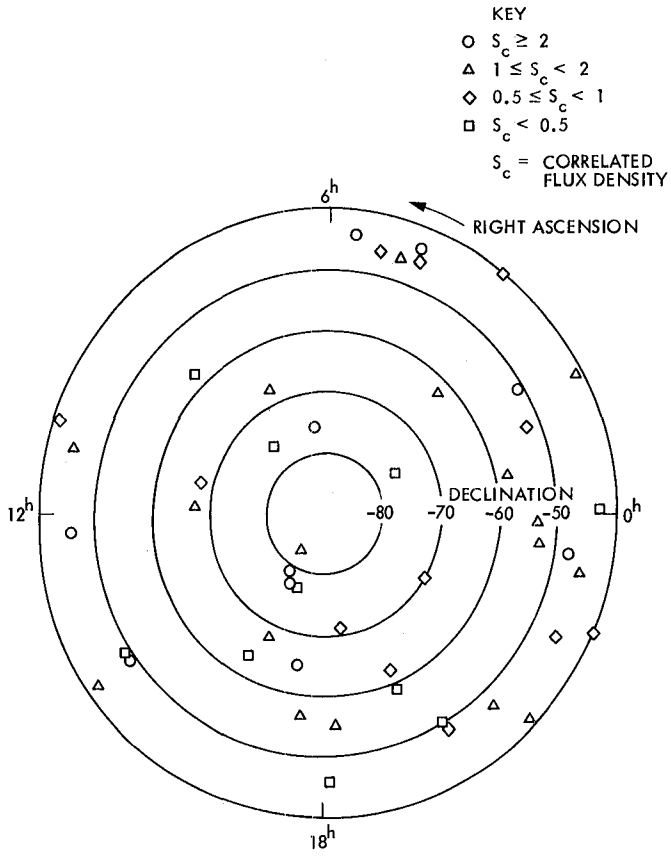


**Fig. 1. Sky distribution plot**

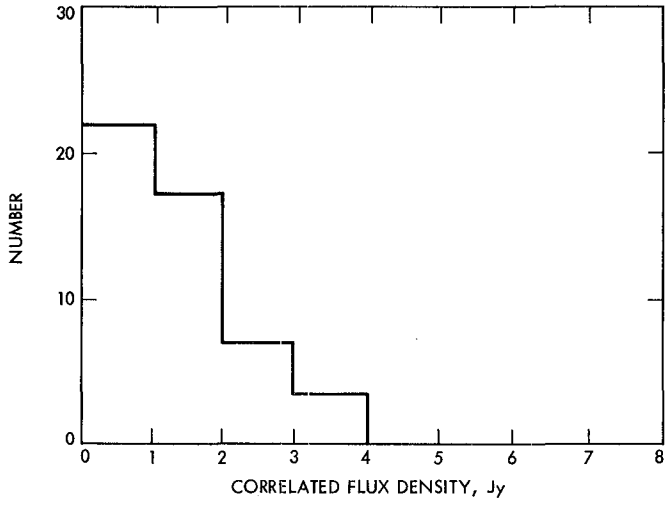


**Fig. 2. Correlated flux density histogram**

# Two-Dimensional Finite Element Modeling for Modeling Tectonic Stress and Strain

G. A. Lyzenga and A. Raefsky
Tracking Systems and Applications Section

*Techniques of finite element analysis in two-dimensional plane strain have been applied in this study to problems of geophysics and tectonics. More specifically, the flexibility of the finite element method has been employed to address problems involving geological complexity and fault interactions. In this work the modeling of effective anisotropy in material elastic properties has proven useful in describing the deformation of faulted crustal blocks. The applications of this modeling work to problems of actual tectonics in southern California have been explored. Preliminary models show encouraging agreement with measured tectonic strain in this region, and modeling work has been done to gain an understanding of the stress state in a "locked" fault region with future seismic potential.*

## I. Introduction

Understanding the tectonic processes which govern the evolution and present state of continental plate boundary regions such as that in Southern California requires the modeling of crustal deformation. In most instances, whether such modeling addresses broad scale "average" tectonic features of a region, or seeks to understand the detailed processes governing single faults or seismic events, it is important to consider the effects of material heterogeneities in influencing the problem.

In practice, the complications of contrasts and variations in geology and rock properties throughout a region may present formidable challenges for modeling crustal stress and strain. While the application of analytic techniques contributes much, and usually provides physical insight into the general features of a given problem, often numerical techniques are required in order to adequately characterize such complex models. In the work described here, one such numerical method, the finite element method, has been employed. In this work, the finite element method is used in a two-dimensional approximation to construct models of Southern California crustal deformation for correlation with geophysical observations, including geodetic strain measurements and seismicity.

By using finite elements, it is possible to solve for stress distributions in problems of linear elasticity and viscous deformation. In the latter case, both steady, time-independent deformation (Stokes flow) and time-dependent viscoelastic deformation are amenable to treatment by these methods. A particular specialization of this technique which is useful in considering strike slip tectonics of the style observed in Southern California, and which is one of the novel contributions of the present study, is the introduction of anisotropic material constitutive properties into the models. As discussed

below, anisotropic properties allow the modeling of regions characterized by many parallel faults in a diffuse "shear zone," using a continuum finite element model.

Also outlined in this report is the relevance of these modeling results to problems of crustal rheology and earthquake-related transient deformation. The interaction of the current modeling with such studies is in both directions, with independent crustal stress/strain studies both supporting and being augmented by the current finite element work. As an example of the former case, crustal effective viscosities derived from seismic deformation studies serve as input to viscous stress models. In the latter case, finite element modeling has been used in the work described below to address the problem of anomalous stresses in the Anza, California, seismic gap.

## II. Modeling Techniques

The finite element method has found increasing applications in problems of modeling tectonic stress and strain. Beyond the solution of simple elasticity problems, the utilization of algorithms for the treatment of viscoelastic stress relaxation (e.g., Refs. 1-3) has allowed the consideration of dynamic problems such as post-seismic rebound and rheological flow.

In general terms, the finite element technique is used to solve a given boundary value problem by breaking the problem domain up into a number of smaller elements. The problem of solving for the continuous field of unknown variables reduces to the discrete problem of solving for function values at the nodal points in the element grid. In this discretization, the task of solving the governing differential equations thus becomes a problem of solving simultaneous linear algebraic equations. Therefore, a central feature of standard finite element analysis is the requirement of obtaining the inverse of a large matrix, which has a rank equal to the total number of nodal degrees of freedom, and is generally symmetric and banded.

In principle, the finite element method allows solution of problems in arbitrary complex geometries, with resolution determined by the (variable) grid spacing in a given region. In practice, limitations of two types are evident. Most obvious is that, as the grid grows in size and complexity, the computer time and storage required for assembly and solution of the matrix equations grows intractable. Furthermore, even if extremely complex grids can be handled on a given machine, the complexity of the model may preclude its being useful to constrain observable quantities in terms of a few unique parameters. The former limitation is imposed by computer capability, while the latter reflects the need for methodical modeling procedure.

When considering three-dimensional models of geological problems, both storage and time constraints become serious. This is a result of the matrix column-storage method used for solving the system. For a number of nodal degrees of freedom, the number of operations required for matrix reduction and back-substitution varies as the square of matrix column height (Ref. 4) while storage varies as the first power.

Since two-dimensional grids display such a lower degree of interconnectivity between nodes than a three-dimensional problem of comparable size, the computation time restriction may be largely avoided by considering 2-D problems. In this case, focusing upon methods of expanding the effective memory available to the program can pay off in allowing the solution of very large two-dimensional problems.

In the discussion which follows, we concentrate on the two-dimensional modeling techniques which have been useful in this tectonic simulation work. Among the principles which make up the paradigm of current plate tectonics is the idea that the lithospheric "plates" behave as relatively rigid entities, coupled in a quasi-viscous manner to an underlying asthenosphere. To first order then, on time scales sufficiently long, the lithosphere is considered to be weakly coupled to the underlying mantle. As a result many problems, especially those involving steady deformation and long-term response, may be considered in a two-dimensional "plane stress" approximation.

If the problem to be considered is one of elastic strain, the standard equations governing stress $\sigma_{ij}$ in linear elasticity apply:

$$\sigma_{i\mu.\mu} = 0 \tag{1a}$$

$$\sigma_{ij} = \lambda u_{\mu,\mu}\,\delta_{ij} + \mu(u_{i,j} + u_{j,i}) \tag{1b}$$

On the other hand, steady Newtonian viscous flow ($R \gg 1$) is governed by the set of equations,

$$\sigma_{i\mu,\mu} = 0 \tag{2a}$$

$$\sigma_{ij} = (-P + \lambda u_{\mu,\mu})\,\delta_{ij} + \eta(u_{i,j} + u_{j,i}) \tag{2b}$$

where

$$P = f(\rho) \text{ (equation of state)} \tag{2c}$$

and

$$\frac{\partial \rho}{\partial t} + (\rho u_{\mu}),\mu = 0 \text{ (continuity)} \tag{2d}$$

In conventional usage, these steady flow equations are used in the case of divergenceless flow, in which case $U_{\mu,\mu} = 0$ and $\rho$ and $P$ are constants. It is apparent through comparison of Eqs. (1) and (2) that in this limit the Newtonian flow equations are identical with those describing incompressible elasticity. Carrying this comparison further, we can see that if $U_{\mu,\mu} \neq 0$ is permitted in the flow equations, perhaps through use of a special form of the equation of state which limits the growth of $P$ with increasing $\rho$, we obtain equations essentially identical to general linear elasticity, with only the addition of a hydrostatic pressure term to the stress tensor.

How can this be interpreted in terms of physical behavior in the tectonic model? In considering two-dimensional deformation of the lithosphere, the horizontal divergence $u_{\mu,\mu}$ need not in general vanish, this case corresponding to the occurrence of crustal shortening (or extension). While such areal dilatations in the lithospheric plate are resisted by restoring forces, these are not forces which increase without limit as crustal shortening or thickening occur. Rather, these resisting forces are related to the equilibrium height of topography induced by crustal area changes, and for constant (or slowly changing) topographic distributions they are adequately represented by constant (in time) pressure terms ($P$ in equation (2b)).

Thus in this type of lithospheric deformation model, there exists a complete analogy between the Lame parameters of elasticity, $\lambda$ and $\mu$, and the bulk and shear viscosities $\lambda$ and $\eta$ of Newtonian flow. It is thus asserted that given appropriate choices of these parameters and a priori topographic pressure distribution, elastic stress/strain solutions can provide a good approximation to the field of plastic deformation in the lithosphere. Moreover, the parallel work of England and McKenzie (Ref. 5) indicates that the magnitudes of topography-induced stresses are probably such that they do not exert a dominating influence on the pattern of horizontal flow.

A major part of the work reported here consists of such crustal deformation models, which seek to explain spatial variations in stress and strain, as they are observed to occur in Southern California. While such models may be interpreted as giving elastic strains, we emphasize here their interpretation as models of irreversible plastic strain. This remark applies to the following discussion of anisotropic models.

As is emphasized in the work of Ivins et al. (Ref. 6), which has proceeded in collaboration with this work, it may be important in tectonic deformation models to take into account the effect of numerous subparallel minor faults which define a tectonic "fabric" of shear deformation in a given region. The effect of numerous parallel joints or faults is to introduce an effective material anisotropy in the model when treating it as a homogeneous continuum.

Both analytic results and finite element calculations have shown that directional variations in effective shear modulus (or shear viscosity) by factors of $\sim 10$ occur in media with freely slipping fault densities, which are reasonable for a shear zone like that in the vicinity of the San Andreas fault.

In the case of a general anisotropic body, the matrix of stiffness constants relating stresses and strains (strain rates) contains 21 independent entries. If, however, we restrict ourselves to a two-dimensional case in which the anisotropy takes the form of parallel stratification in material properties (orthotropic plates), four elastic constants are required. In practice, the orthotropic stiffness matrix is evaluated in a coordinate system aligned with the direction of stratification and is subsequently rotated by coordinate transformation into the appropriate model orientation (Ref. 7). The accuracy of anisotropic finite element solutions obtained with this program have been checked by comparison with analytic results, such as those of Lekhnitskii (Ref. 8).

In addition to the above mentioned models of two-dimensional continuum deformation, the work included in this study has also included models of elastic fault interactions. Central to this work has been the development and utilization of "roller" elements for the accommodation of arbitrary slip on a dislocation surface.

Whereas a priori specified fault motions may be input into a model via the split node technique (e.g., Ref. 9), the roller technique described here allows the solution for the fault dislocation as an implicit part of the finite element solution. As Fig. 1 shows schematically, the rollers consist of incompressible bar or "truss" elements which are positioned between pairs of nodes spanning a gap or "crack" in the material grid which represents the fault. In practice, this fault width is made small in comparison with the typical element spacing along its length. For the study of stress relief on a fault, the desired stress drop is applied as tractions on the fault walls. On the other hand, fault creep accompanying regional deformation is modeled by application of boundary conditions to the grid as a whole.

The above descriptions summarize the salient specific techniques in finite element analysis used in the accomplishment of this research. In addition to these developments, work was performed to write a program for automatic finite element grid generation in problems involving roller faults and cracks. This software development effort resulted in the program GRIDX (see Appendix). The following section summarizes the scientific results of the application of the techniques for tectonic modeling so far described.

## III. Results and Implications

### A. Block Deformation Models and Correspondence with Southern California

A common feature of modern tectonic models of continental regions such as Southern California is the breaking up of such regions into a number of discrete "blocks" within each of which geological and tectonic features are largely homogeneous. One end member in a family of such block tectonic models is of a type described by Hill (Ref. 10). In this picture, blocks interact mainly through frictional forces at block boundaries, and overall regional deformation is accommodated by thrust, normal, and transform slip on the polygonal network of boundary faults.

A contrasting model framework takes the view that continuously distributed deformation occurs throughout the blocks, and that such continuous inelastic deformation makes a major contribution to long-term tectonic motions. In this view, therefore, block boundaries would be largely defined by contrasts in constitutive properties, rather than by the location of major bounding faults, as is the former class.

Clearly, the second type of model also corresponds to slip on discrete faults, if only scrutinized on a small enough scale. The distinction is that the distribution, both in time and space, of fault slip is assumed in this view to be so nearly continuous as to be modeled by continuum deformation. It is perhaps obvious that each of these two extreme views have strengths and weaknesses when compared with reality.

The models from this work seek to correlate features of Southern California tectonics with a continuum deformation model. While geodetic strain rates in California may be strongly perturbed by transient strain associated with great earthquake cycles on the San Andreas, Thatcher (Ref. 11) presents data which suggest that in the southern segment, on which $\sim 120$ years has elapsed since the last great event, earthquake-related strain has decayed to a low level compared with the average interseismic rate. Thus, distributed shear within $\sim 100$ km of the main trace of the San Andreas may be a useful model of present-day strain accumulation in the region, as well as explaining the apparent deficit between plate motion rates and geologic slip rates on the main fault.

Figure 2 is a map diagram of Southern California block tectonics, taken from Luyendyk et al. (Ref. 12). Highlighted in this figure are the "transverse" crustal blocks, which in addition to having generally east-west striking fault and structural trends, have experienced large ($\sim 70^\circ$) clockwise block rotations since Miocene time, as determined from paleomagnetism. It is significant for this discussion to note that the "big bend" of the San Andreas fault coincides with its encounter with the western transverse block, and apparently offsets it from its eastern counterpart. This observation provides the point of departure for our discussion of the finite element models.

We consider as the prototypical block model the simple case of an elliptical inclusion in an infinite (two-dimensional) medium. This geometry has the virtue of being amenable to analytic solution in certain cases. All models discussed in this work have the elliptical block with a 3:1 aspect ratio and oriented with the major axis along the abscissa (east-west). Although somewhat arbitrary, this choice yields a geometric similarity with the case of the Southern California Transverse block.

Calculations using simple isotropic material descriptions immediately show that very large contrasts in moduli are required to obtain stress field perturbations of the magnitude implied by the Big Bend and local variations in geodetic strain. Unless order-of-magnitude contrasts in strength between the block and surrounding medium are assumed, the resulting stress field is very nearly homogeneous.

Interestingly, this seemingly implausible requirement of strength contrasts is fulfilled by considering a faulted anisotropic continuum model. As discussed earlier, a 10:1 directional anisotropy in shear stiffness is reasonably accommodated by such a model. Thus, we are led to ask whether judicious choices of crustal anisotropy can lead to plausible patterns of model stress and strain.

Figure 3 presents, in graphical form, the stress (a) and strain (b) fields resulting from a transverse (east-west-faulted) block imbedded in a NW-SE trending faulted medium. The entire model is subjected to uniform pure shear by imposing N-S compressive and E-W tensile stresses at the distant boundaries. Other than differing in grain orientation the two regions have identical properties with 10:1 stiffness ratios. In coordinates for which $x$ lies along the faults, the stiffness constants are given by

$$\begin{bmatrix} \sigma_{xx} \\ \sigma_{yy} \\ \sigma_{xy} \end{bmatrix} = \begin{bmatrix} C_{11} & C_{12} & 0 \\ C_{12} & C_{22} & 0 \\ 0 & 0 & C_{66} \end{bmatrix} \begin{bmatrix} \epsilon_{xx} \\ \epsilon_{yy} \\ \epsilon_{xy} \end{bmatrix} \tag{3}$$

In the isotropic case, $C_{11} = C_{22} = \lambda + 2\mu$, while $C_{66} = \mu$. In the orthotropic case just described, we let $C_{66}$ relax to 0.1 of its isotropic value, leaving all other constants unchanged. It is easily verified that this leads to a material with two "weak

directions" at 90° to one another, normal and parallel to the direction of faulting. The "strong" directions for shear are at 45° to these directions.

The effect of the choice of orientations in Fig. 3 is to shear the "block" along its "strongest" direction while the surrounding medium shears along its most compliant direction. Immediately evident in the stress plot is a symmetric pattern of rotation in the orientation of principal stresses around the periphery of the inclusion (the plots show the directions and magnitudes of principal stresses/strains, with outward directed heads denoting extension). The sense of rotation is clockwise in the NW and SW. The sense of stress is predominantly compressive along the north and south sides of the inclusion, and tensile at the "ends." Accentuated east-west tensile stresses also characterize the block interior, where there is no rotation in orientation.

The plot of model strains (or strain rates in the visous interpretation) shows a somewhat different picture. No strong pattern of differential rotations is seen as in the stress plot. Aside from a slight global clockwise rotation, the strain directions are not influenced by the block. Although the stress field shows significant regions of compressive stress, the net effect in this model is *not* to produce any significant crustal shortening, as all observed *strains* are either isovolumetric, or slightly extensional.

In Fig. 4, adapted from Savage et al. (Ref. 13) geodetically measured strain rates in Southern California are shown along with a suggested analogy between the Western Transverse block and the elliptical inclusion model. Since this correspondence places much of the block's western end in the ocean, all the geodetic results apply to the eastern half of the model.

These USGS trilateration results show a general correspondence with the rotation of stresses in the model. In the NE quadrant (Tehachapi/Palmdale, for example) strain orientations are rotated counterclockwise along with the fault strike of the Big Bend. SE quadrant networks (e.g., Anza) appear to show a slight clockwise complementary rotation, relative to the direction of shear in the more distant Salton network.

This apparent success of the simple inclusion model is not satisfactory for a number of reasons. First, and perhaps most important, the model predicts rotation of stresses but not strains, which are the observed quantities. In addition, the finite element model displays a marked degree of symmetry (because of its symmetry of boundary conditions), which may not be reflected in the real situation. Whereas the model is formally indifferent as to whether the deformation is primarily right lateral on NW trending structures, or left lateral on NW trends, the actual tectonics of Southern California is manifestly dominated by dextral shear. The predominance of clockwise block rotations and counterclockwise strain axis rotations in conjunction with the Big Bend reflect this fundamental asymmetry.

Figure 5 gives the strain field resulting from modifying the finite element model to more realistically represent the actual situation. In this model, rather than imbedding the inclusion in a faulted medium of infinite extent, the anisotropic medium is confined to a NW-SE trending band or "shear zone," just wide enough to contain the elliptical block. Outside this band, the material has the isotropic properties of unfaulted material ($C_{66} = 1/3\ C_{11}$). Besides more accurately emulating the zone of diffuse shear deformation which surrounds the San Andreas Fault, this modification has two evident effects on the pattern of deformations (or flow). First, it effectively "channels" deformation, restricting it to regions which must interact with the inclusion. This has the effect of amplifying the perturbing effect of the block on strains, which were formerly only weakly affected. Secondly, the presence of the diagonal channel introduces a preferred direction in the model, thus providing a basis for breaking the symmetry of the earlier solutions.

The results of this model are to bring the strain field into somewhat better agreement with our expectations of the real situation. As expected, shear strain amplitudes are enhanced in the channel relative to the outer regions. Also, the orientation of the principal strains is rotated slightly counterclockwise in the NE quadrant, in agreement with the location and sense of fault strike and strain rotation in the Big Bend region. This rotation no longer has a complementary opposite rotation in the NW quadrant in this unsymmetric model, although it does predict comparable counterclockwise rotations in the SW quadrant. This prediction of the anisotropic block model could in principle be checked by geodetic network measurements in the Channel Islands region.

While the qualitative pattern of strain distributions is improved in this channel model, the magnitude of rotations predicted is quantitatively small compared with the strike rotation observed on the San Andreas. This in turn suggests that further narrowing of the channel could be used to obtain closer agreement. The suggestion that the shear zone may be actually narrower than the proto-Transverse Ranges block receives some support from reconstructions, such as those of Luyendyk et al. (Ref. 12) which suggest that the offset eastern and western Transverse blocks formed a single unit prior to the inception of motion on the modern (bent) trace of the San Andreas fault.

In Fig. 6, the modeled situation is as in Fig. 5, except that the shear zone now has a width of about 40% of that of the

inclusion major axis (the ratio of widths projected along the fault strike is 56%). As anticipated, large amplitude strain rotations are obtained in a fairly narrow boundary zone coincident with the interpreted position of the fault bend. Evidently, this rotation is a sensitive function of shear zone width, and within the context of this model, suggests that the actual situation in Southern California should be modeled with a shear band approximately 100-150 km in width. In reality, the transition from "weak" faulted medium to more nearly isotropic crustal material is probably gradational, rather than steplike as in this simple model. Therefore, this 100-150 km scale might be regarded as a "halfwidth" of distributed shear deformation in the diffuse plate boundary region. This agrees fairly well with the lateral extent of strike slip faulting in the Salton trough and surrounding regime.

As has been emphasized above, the models considered thus far represent generalized pictures of certain processes which may be important in determining the overall tectonic pattern in specific regions, such as Southern California. It is through the methodical construction of such "long-wavelength" tectonic models that progress is made toward meaningfully modeling the tectonics of the real situation on finer spatial scales. The areas in which future research promises to further the achievement of this goal include consideration of gradients in constitutive properties (which may be inferred from geologic fault-slip data), and the relative influence of topographic stresses in controlling secular deformation. In the remainder of this report, we discuss modeling problems of finer scale, examining the interactions of small numbers of faults and their immediate local effects.

## B. Seismic Gap Fault Models and Applications to Anza, California

The states of stress and strain occurring near the focal region of an impending earthquake are of great importance for studies of earthquake prediction. Information of this kind may come from a variety of sources, including seismological, geodetic, and in situ monitoring. The finite element method offers the potential of modeling these results in situations where geometric or geologic complexities may be important influences. During this study, attention has been focused upon the inferred seismic gap near Anza, California, in which the occurrence of a magnitude 5 earthquake is considered likely.

Figure 7 shows a map of the region of the San Jacinto fault near Anza. Plotted are the surface traces of mapped faults, with major active strands of the San Jacinto shown as heavy lines. Small crosses show the epicenter locations of earthquakes with $M > 2$ between January 1977 and July 1981. The seismic "gap" is visible here as a paucity of small earthquakes between the outlined strands of the fault. The relative absence of events extends uniformly to ~ 20 km depth, where all seismicity ceases. The seismological data for this world have come from Sanders et al. (Ref. 14).

The evidence for anomalous stress in this gap region comes from the two small earthquake swarms indicated on Fig. 7. Focal mechanism studies of these events show a consistent clockwise rotation of the inferred axis of maximum compression, from its expected north-south azimuth. The effect is larger for the swarm closest to the fault, and in that case amounts to about a 20° clockwise rotation of stress axes.

The goal of finite element modeling in this study has been to determine whether this indication of anomalous stress may be understood in terms of strain accumulation on the "locked" segment of the fault, or other processes associated with the seismic gap. Figure 8 is typical of plane stress models constructed for this region. The faults indicated by heavy lines have been modeled as freely slipping dislocations (using the "roller" elements) within an elastic continuum. Principal stresses are plotted, and as before, boundary loading of the problem is achieved with application of surface forces to yield pure shear parallel to the fault strike, in the absence of any perturbing stresses.

In such models, it is found that appreciable stress field rotation occurs, but only relatively near the tips of the modeled dislocations. As may be seen, clockwise rotations of the observed magnitude occur just south of the northwest strand of the fault; however, within the gap, corresponding to the locations of the anomalous swarms, essentially no rotation is obtained. This result remains qualitatively unchanged as we consider, in more detail, different combinations of slipping fault strands outside the locked gap.

Several approaches were tried to obtain models in which the region of rotated stress axes was drawn out into the gap. Among these was a set of models based upon the conjecture that nonlinear effects preceding seismic failure (such as strain hardening or dilatancy) might introduce a zone of anomalous elastic properties within the gap. The results of such models have been uniformly negative, with the finding that even large contrasts in elastic moduli within an elongated body centered on the gap fail to modify the orientation of stresses.

In further work, it was suggested that significant asymmetry might be necessary in the models in order to obtain a preponderance of clockwise rotation over the otherwise symmetric field. Using mapped geological contrasts across the San Jacinto Fault as a general guide, lateral variations in constitutive properties were included in the elastic gap models. Once again, no plausible distribution of material contrasts across the fault(s) provided significant rotations.

The possibility of anisotropy providing an answer, as in the case of the larger scale regional models discussed above, is unsatisfactory for a number of reasons. First of all, in this model configuration, the stress field is found to be dominantly influenced (in the near field) by the major modeled faults. Such models when calculated, yield little or no improvement of the rotation picture.

It could be argued that if anisotropy were important, that the direction of compression and tension axes derived from earthquake focal mechanisms would reflect increments in strain (displacement field) rather than stress. If true, it would indeed be easier to obtain agreement between the strain field and the observed mechanisms. However, this would mean simply assuming ad hoc that a region of strong anisotropy of just the right orientation exists within the gap, and nowhere else. This makes for a very unconvincing and unsatisfying physical model, in light of its arbitrary nature. Moreover, even though we have argued for the existence of strong crustal anisotropy for deformation on *long* time scales, there exists no observational evidence for anisotropy on seismic time scales of the magnitude required for this purpose.

As a general conclusion, it appears difficult to explain the observed stresses as a direct result of rigidly locking the quiet segment of the fault. It may be worthwhile to consider, however, a different physical model for the seismic gap. In particular, we consider the description of this gap as a "geometric asperity," in which a bend or kink in the fault zone inhibits uniform slip locally.

In a left-stepping (dextral sense of slip) kink of the kind illustrated in the model of Fig. 9, compressive stresses are generated in the bent region. These large compressive stresses could provide an increase in internal friction, thus locally inhibiting shear failure and producing a seismically quiet gap. Most importantly, careful examination of Fig. 9 shows that modest clockwise axis rotations occur near the center of the asperity.

While this model enjoys some success in explaining stress rotations, it makes no prediction (except indirectly) about the relation between rotation magnitudes and the likelihood of eventual failure in the geometrically hindered gap. Elucidation of this question will require the consideration of cases in which a friction model determines the transition from locked to sliding fault segments. Ultimately, the glaring weakness of this hypothesis for explaining the observations is that there is no evidence from the morphology of the relevant faults or the distribution of seismicity that any left-stepping fault kink of the kind required actually exists. Unless geophysical data suggesting the occurrence of such a bend are forthcoming, this model agreement must remain an interesting but probably irrelevant coincidence.

In the absence of any compelling explanation for the observations described, we report to the consideration of possible alternatives. It is possible, but difficult, to verify that the observed behavior is due to an anomalous region of preferentially assigned preexisting fractures, which give rise to the observed axes. In this case, the rotated stresses have nothing to do (directly) with the potential for seismicity in the gap, and their association is coincidental. Alternatively, some more subtle aspect of the time-dependent accumulations of stress and strain in the gap needs to be addressed in the finite element model. This is the current state of our understanding of this problem, and new answers await either renewed efforts in modeling, or further geophysical data on the Anza region, or both.

# References


1. Melosh, H. J., and Raefsky, A., "Anelastic Response of the Earth to a Dip Slip Earthquake," *J. Geophys. Res., 88*, 515-526, 1983.

2. Yang, M., and Toksoz, M. N., "Time Dependent Deformation and Stress Relaxation after Strike Slip Earthquakes," *J. Geophys. Res.*, 86, 2889-2901, 1981.

3. Cohen, S. C., "Postseismic Rebound Due to Creep of the Lower Lithosphere and Asthenosphere," *Geophys. Res. Lett*, 8, 493-496, 1981.

4. Bathe, K. J. and Wilson, E. L., *Numerical Methods in Finite Element Analysis*, Prentice-Hall, Englewood Cliffs, New Jersey,1976.

5. England, R., and McKenzie, D., "A Thin Viscous Sheet Model for Continental Deformations," *Geophys. J. R Astr. Soc. 70*, 295-321, 1982.

6. Ivins, E. R., Lyzenga, G. A., Sanders, R. S., and Raefsky, A., "Mechanics of the Neogene Rotation of the Transverse Ranges, California," in preparation 1983.

7. Zienkiewicz, O. C., *The Finite Element Method*, McGraw-Hill, London, 1977.

8. Lekhnitskii, S. G. (translated by S. W. Tsai and T. Cheron) *Anisotropic Plates*, Gordon and Breach Publishers, 1968.

9. Melosh, H. J., and Raefsky, A., "A Simple and Efficient Method for Introducing Faults into Finite Element Computations," *Bull. Seismol., Soc. Am., 71*, 1391-1400, 1981.

10. Hill, D. P., "Contemporary Block Tectonics: California and Nevada," *J. Geophys. Res., 87*, 5433-5450, 1982.

11. Thatcher, W., "Nonlinear Strain Buildup and the Earthquake Cycle on the San Andreas Fault," preprint submitted (1983).

12. Luyendyk, B. P., Kamerling, M. J., and Terres, R., "Geometric Model for Neogene Crustal Rotations in Southern California," *Geol. Soc. Am. Bull., 91*, 211-217, 1980.

13. Savage, J. C., Prescott, W. H., Lisowski, M., and King, N. E., "Strain Accumulation in Southern California, 1973-1980," *J. Geophys. Res.*, 86, 6991-7001, 1981.

14. Sanders, C., McNally, K., and Kanamori, H., "The State of Stress near the Anza Seismic Gap, San Jacinto Fault Zone, Southern California," *Trans. Am. Geophys. U.*, 61, 957 (1981).

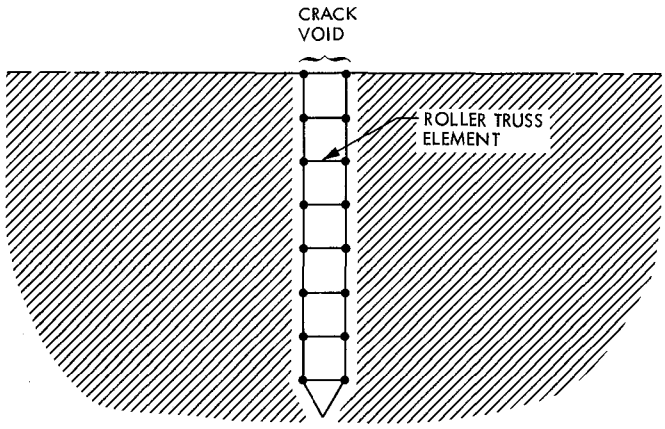


**Fig. 1. Schematic representation of roller elements used to model a slipping dislocation in faulted model**

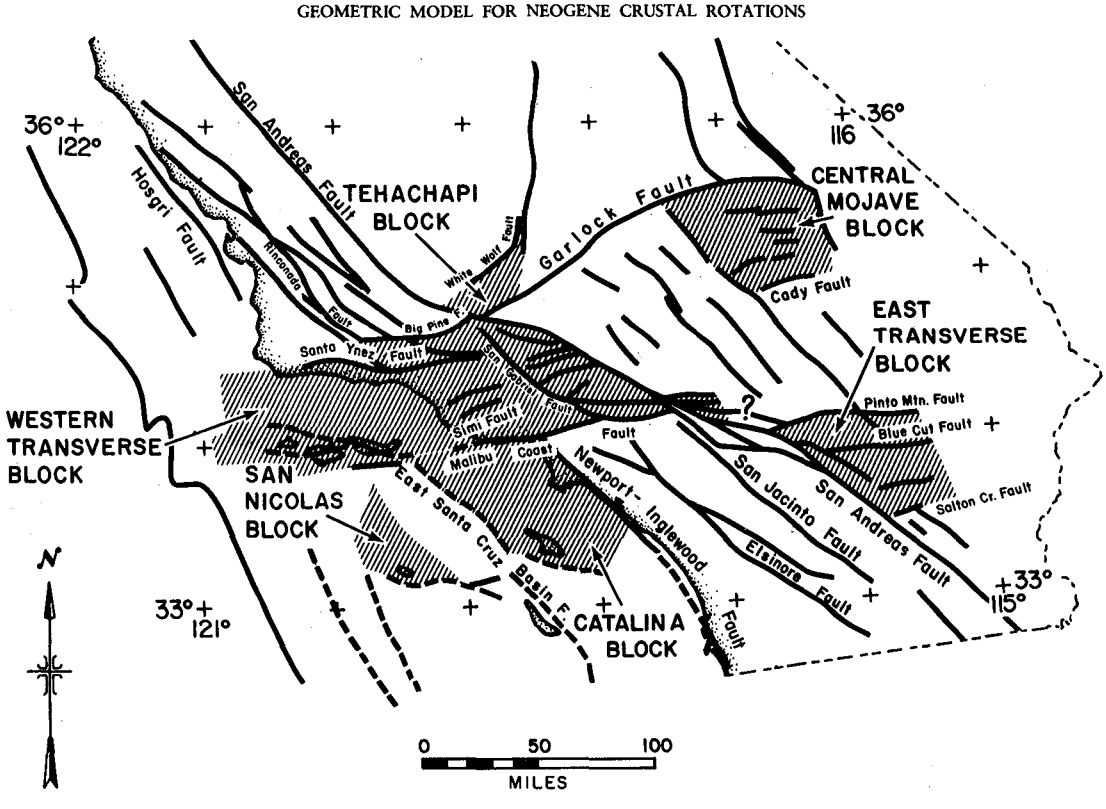


**Fig. 2. Map from Luyendyk et al. (Ref. 12) showing Southern California faults and tectonic blocks, for some of which rotations have been inferred from paleomagnetic data**

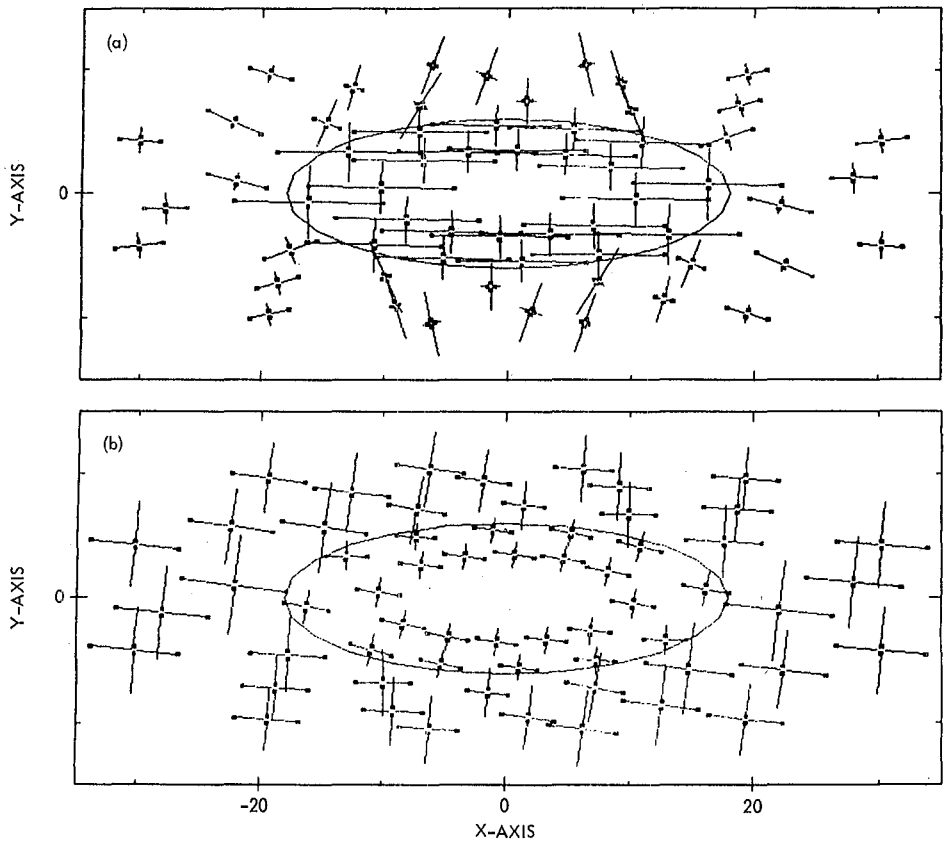


**Fig. 3. (a) Stress field obtained in finite element model with anisotropic faulted block whose grain is rotated with respect to surrounding medium orientation; (b) strain field for same model.**

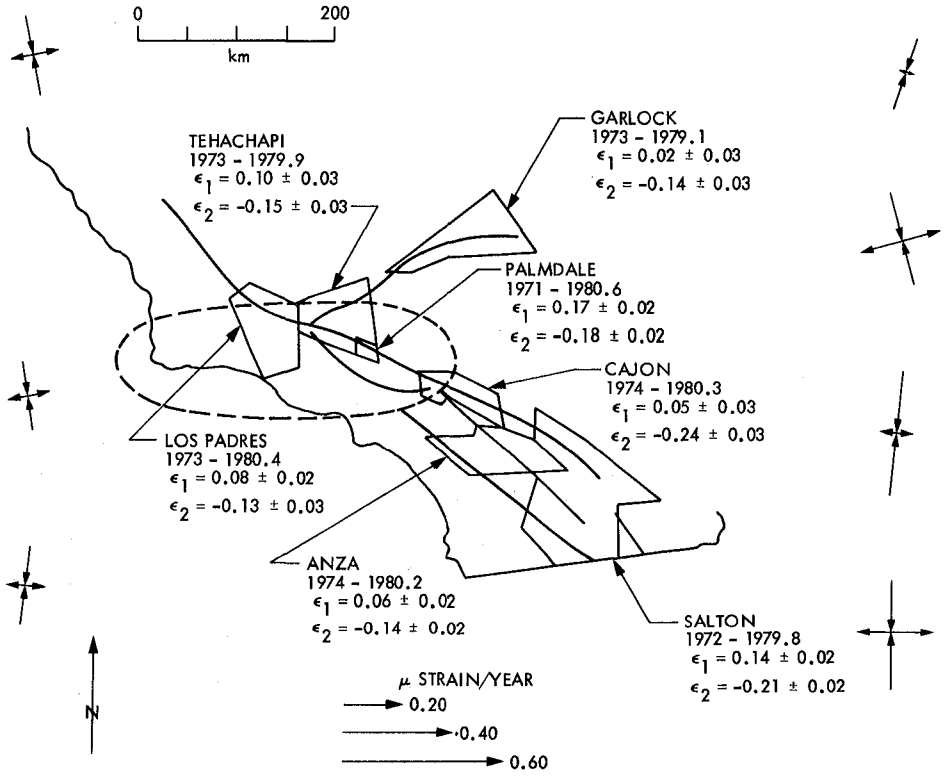


**Fig. 4. Map from Savage et al. (Ref. 13) showing measured strain accumulation in Southern California near inferred Transverse block (dashed line)**

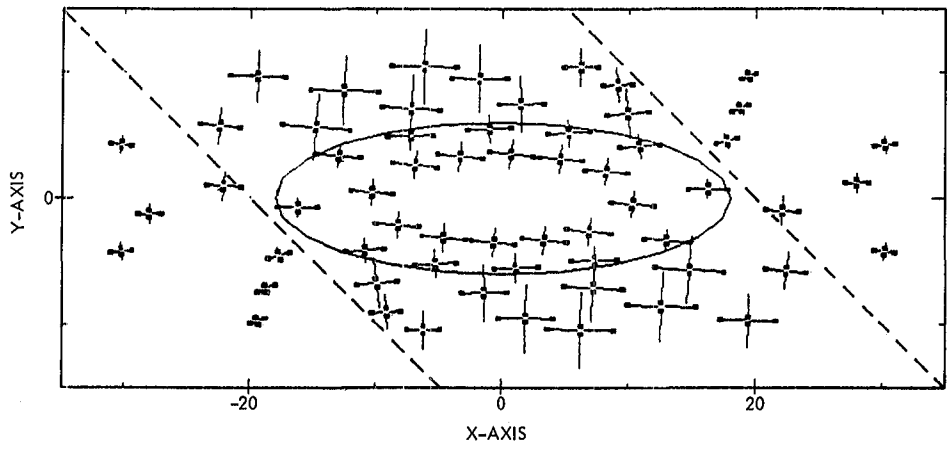


**Fig. 5. Strain field in model for which anisotropy in surrounding medium is restricted to a "channel" (dashed line)**

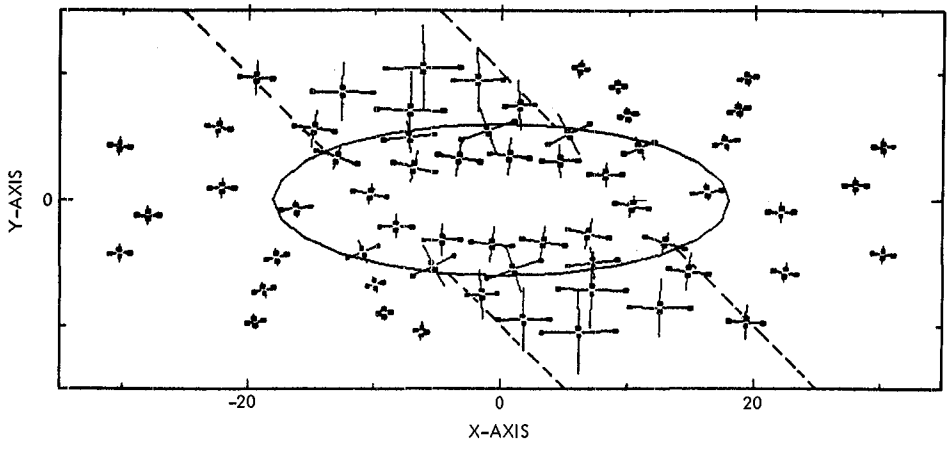


**Fig. 6. Strains for channel model as in Fig. 5, but with channel width one half that of the previous case**

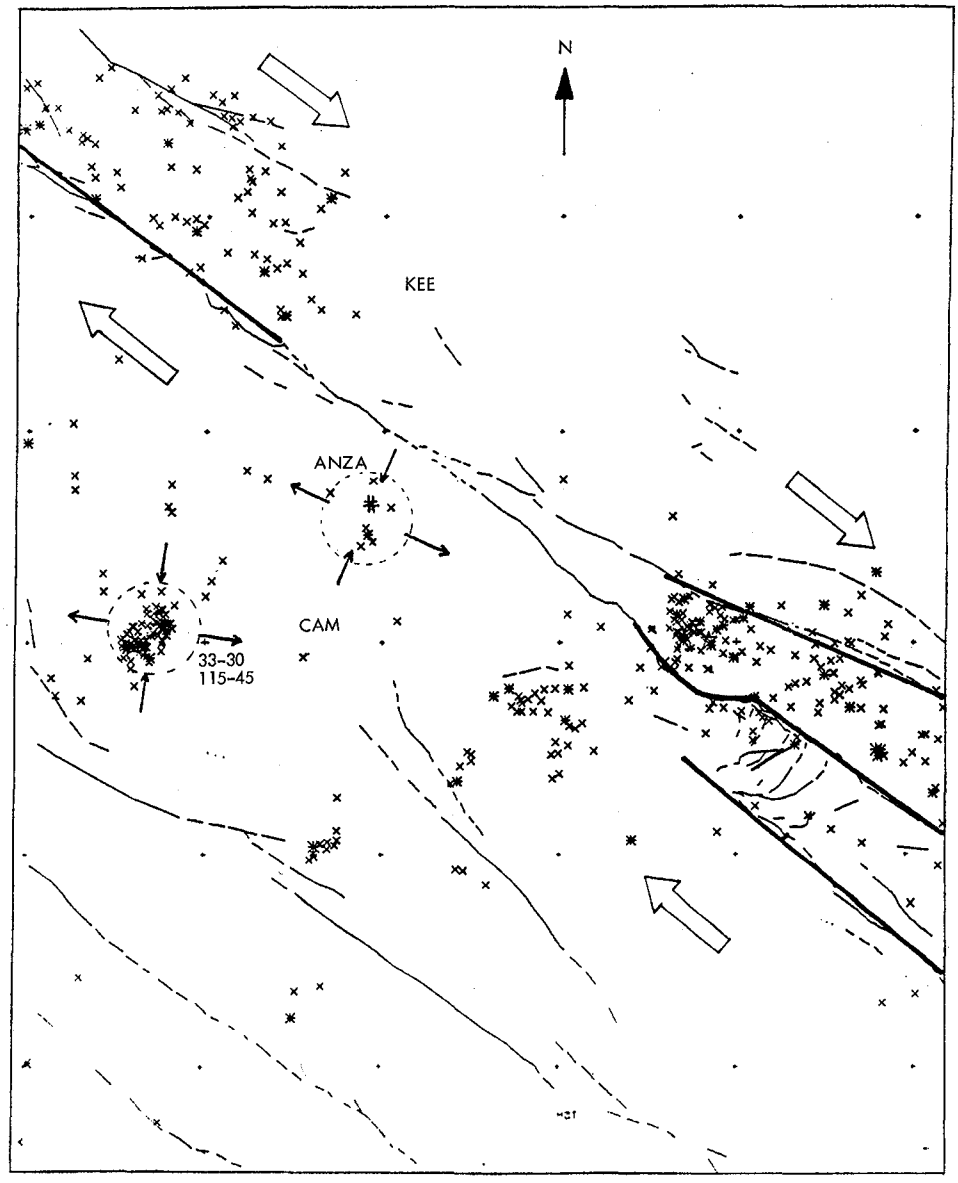


**Fig. 7. Map of Anza region, showing distribution of seismicity, mapped faults, and orientation of stress axes for two anomalous swarms of earthquakes. Data taken from work of Sanders et al. (Ref. 14)**

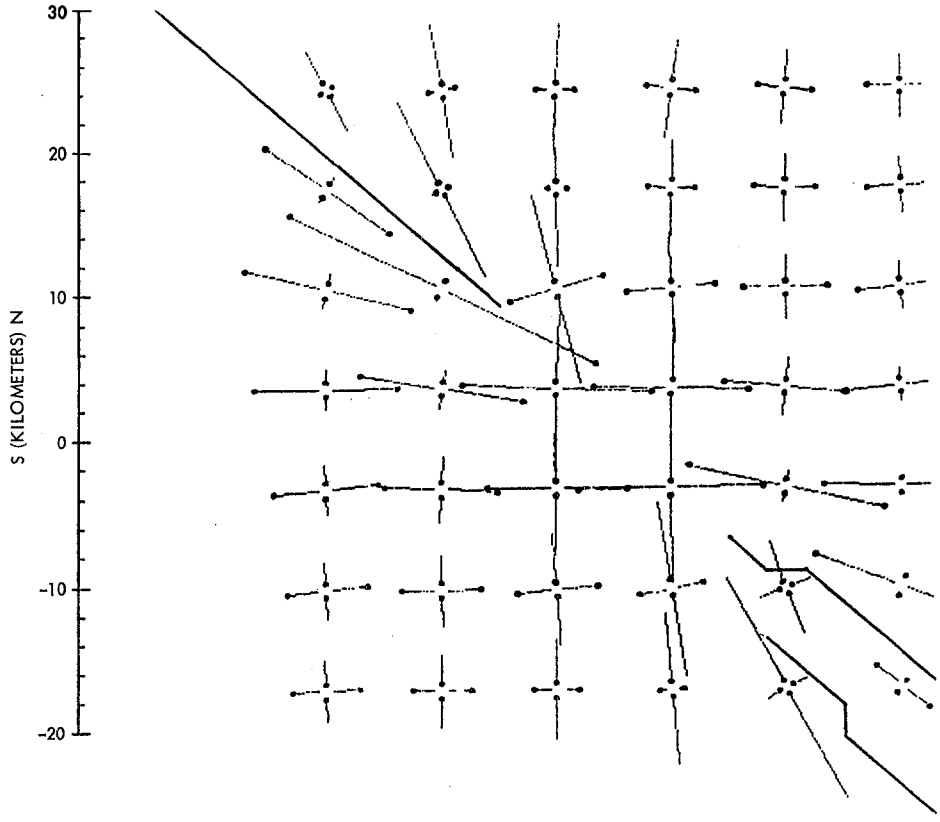


**Fig. 8. Elastic dislocation model of stress field in vicinity of a locked fault gap with shown distribution of active faults (heavy lines)**

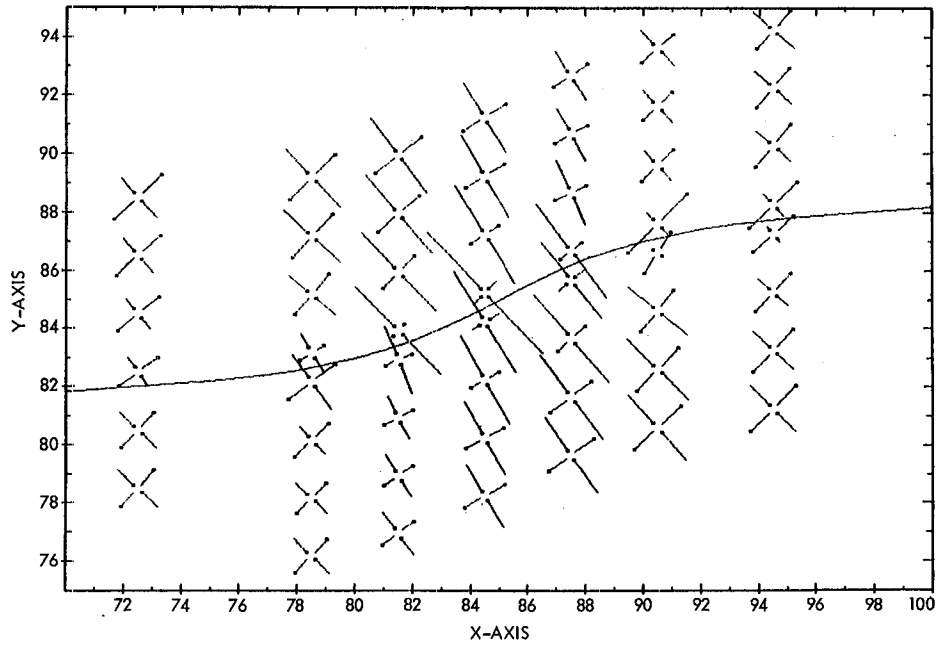


**Fig. 9. Stress distribution near left-stepping bend in an elastic fault model for a geometric asperity**

# Appendix

## Brief Descriptive Summary of Program GRIDX

The following is a brief description of the purpose and use of FORTRAN program GRIDX. This program was developed to provide a utility for the generation of complex finite element computational grids incorporating faults, as are required in many tectonics problems. GRIDX is intended as a flexible routine for the generation of nodal coordinates and element global node assignment (IEN array), with a simplified input format. A listing and detailed description of GRIDX is available from G. Lyzenga (JPL, extension 6920).

Input to GRIDX consists of parameters which control the size and spacing of elements in a rectangular grid. Following this input, the program accepts codes describing the boundary conditions to be applied to the particular problem. Finally, input is read which generates fault roller elements of the required spacing and orientation to model faults. The input of a few lines of generation parameters allows the immediate assembly of a finite element grid and all the necessary nodal information for a complex grid which would require many hours to assemble and number manually.

Output from GRIDX is provided in two forms. The first and most important is the output file, containing the nodal coordinates and numbering, as well as the boundary conditions and element arrays in ready-to-use format for the finite element program. Secondly, the program provides (optionally) a plot display of the generated grid in order to provide the user with easy verification that the desired grid has been properly generated. The program is intended to be generally applicable to the types of problems discussed in this report, but is also adaptable to other finite element modeling or software requirements.



NASA—JPL—Coml., L.A., Calif.

End of Document